

Cotton Textile-Enabled Flexible Energy Storage Systems

A Dissertation Proposal

Submitted to the Faculty

of

University of Virginia

In Partial Fulfillment of the

Requirements for the Degree

Of Doctor of Philosophy in **Mechanical & Aerospace Engineering**

By

Zan Gao

November 2018

APPROVAL SHEET

The dissertation is submitted in partial fulfillment of the
requirements for the degree of
Doctor of Philosophy

Zan Gao, Author

This dissertation has been read and approved by the examining Committee:

Xiaodong (Chris) Li, Advisor

Baoxing Xu, Committee Chair

Lin Ma, Committee Member

David L. Green, Committee Member

Sen Zhang, Committee Member

Accepted for the School of Engineering and Applied Science:

Craig H. Benson, Dean

School of Engineering and Applied Science

November 2018

Abstract

With rising energy concerns, efficient energy conversion and storage devices are urgently required to provide a sustainable, green energy supply. Electrochemical energy storage devices, such as supercapacitors and batteries, have been proven to be the most effective energy conversion and storage technologies for practical application. Supercapacitors and lithium-based batteries are particularly promising because of their excellent power density and energy density. However, further development of these energy storage devices is hindered by their poor electrode performance. The carbon materials used in supercapacitors and batteries, such as graphite, activated carbons and various nanostructured carbon materials (ordered porous carbon, CNT, graphene etc.), are often derived from non-renewable resources under relatively harsh environments. Natural abundant biomass is a green, alternative carbon source with many desired properties to derive renewable carbon materials for supercapacitors and lithium-based batteries. Therefore, it has been of great social and economic significance to develop renewable carbon materials from natural abundant biomass materials in order to realize sustainable battery materials sourcing.

It has also been predicted that next-generation electronics will be flexible and wearable. Many efforts have been devoted to developing safe, lightweight and flexible power sources with the goal of meeting the increasing need for future wearable/flexible electronics. This dissertation aims to study the mechanism and technologies for converting cotton textile into renewable, flexible and conductive carbon substrate at a low cost, high throughput way for flexible energy storage applications. In this dissertation, cotton textile, as the commonly overlooked everyday households, has been chosen as the starting precursor materials to prepare renewable flexible conductive substrates for different energy storage systems.

Specifically, in Chapter 2 & 3, natural abundant cotton textiles were first converted to flexible, conductive activated cotton textile (ACTs). The obtained ACT was further chosen as a flexible substrate to design flexible supercapacitor. In order to push up the energy storage capability, high energy density metal oxides, such as core/shell $\text{NiCo}_2\text{O}_4@ \text{NiCo}_2\text{O}_4$, 3D porous $\text{CoO}@ \text{NiO}$, were controllably deposited on the ACT fiber with desired microstructure. Both symmetric and asymmetric supercapacitors were assembled and tested. Inspired by using flexible ACTs for supercapacitors application, in Chapter 4, NiS_2 nanobowls wrapped with conductive

graphene sheets (ACT/NiS₂-graphene) were deposited on ACT fibers by a simple two-step heat treatment method to fabricate binder-free electrode for flexible lithium-ion battery. When used as a binder-free electrode, the ACT/NiS₂-graphene electrode exhibited an exceptional electrochemical performance. Encouraged by the success of the design of flexible lithium-ion batteries with flexible ACTs, in Chapter 5, we extended the application of flexible ACTs for lithium-sulfur (Li-S) battery applications. The assembled lithium-sulfur cell also exhibited exceptional rate capability and durable cyclic performance (with a well-retained capacity of ~1016 mAh g⁻¹ even after 200 cycles). A flexible Li-S cell with ACT/S-rGO as a cathode was also assembled to demonstrate its superior potential as flexible power sources. In Chapter 6, a new built-in magnetic field enhanced polysulfide trapping mechanism was discovered by introducing ferromagnetic iron/iron carbide (Fe/Fe₃C) nanoparticles with a graphene shell (Fe/Fe₃C/graphene) onto a flexible activated cotton textile (ACT) fiber to prepare the ACT@Fe/Fe₃C/graphene sulfur host. The novel trapping mechanism is demonstrated by significant differences in the diffusion behaviour of polysulfides in a custom-designed liquid cell compared to a pure ACT/S cathode. In Chapter 7, we proposed a scalable roll-to-roll manufacturing approach to integrating a flexible solar cell with a flexible home-made flexible supercapacitor to fabricate self-sustainable power pack, which demonstrates huge potential for future off-grid and micro-grid application.

These research activities not only brought new insights on the deriving renewable carbon materials from natural abundant biomass resources but also boosted the design and fabrication of next-generation flexible energy-storage devices, which hold great promise for future wearable/flexible electronics.

Table of Contents

Abstract	i
Table of Contents	iii
Acknowledgments	vi
List of Figures	vii
List of Tables	i
Chapter 1. Introduction	1
1.1 Background and Motivation	1
1.2 Current Challenges of the Biomass-derived Carbon Materials for Energy Storage Applications	3
1.3 Biomass Resources for Renewable Carbon Materials	5
1.4 Typical Methods and Mechanism for the Biomass Conversion	6
1.4.1 Physical Activation	7
1.4.2 Chemical Activation	8
1.4.3 Hydrothermal Carbonization	10
1.5 Biomass-Derived Carbon Materials for Energy Storage Applications	11
1.5.1 Biomass-Derived Carbon Materials for Supercapacitors	12
1.5.2 Biomass-Derived Carbon Materials for Lithium-Sulfur Battery	14
1.6 Specific Research Objectives	16
References:	19
Chapter 2. Cotton Textile-Enabled Flexible Symmetric Supercapacitors	33
2.1 Introduction	33
2.2 Experimental Section	36
2.3 Results and Discussion	38
2.3.1 Structural and Morphological Characterization	38
2.3.2 Electrochemical Performance	42
2.4 Conclusions	52
Reference	52
Chapter 3. Cotton Textile-Enabled Flexible Asymmetric Supercapacitors	56
3.1 Introduction	56
3.2 Experiment Section	59
3.3 Results and Discussion	61

3.3.1 Positive Electrode Materials.....	61
3.3.2 Negative Electrode Materials	66
3.3 Electrochemical Performance.....	68
3.4 Conclusion	75
References.....	76
Chapter 4. Cotton Textile Enabled Flexible Lithium-ion Batteries	81
4.1 Introduction.....	81
4.2 Experimental Section	83
4.3 Results and Discussion	85
4.4 Conclusion	99
Reference	100
Chapter 5. Cotton Textile-Enabled Flexible Lithium-Sulfur Battery	105
5.1 Introduction.....	105
5.2 Experimental Section	107
5.3 Results and Discussion	109
5.3.1 Structural and Morphological Characterization	109
5.3.2 Electrochemical Performance of Lithium-Sulfur Batteries with the KOH-activated Porous ACT Interlayer.....	116
5.4 Conclusion	123
References.....	124
Chapter 6. Cotton-Textile-Enabled, Ferromagnetic Nanoparticle-Assisted Polysulfide New Trapping Mechanism	131
6.1 Introduction.....	131
6.2 Experimental Sections	133
6.3 Results and Discussion	135
6.3.1 Microstructure Characterization	135
6.3.2 Electrochemical Performance.....	140
6.4 Conclusion	146
Reference	146
Chapter 7. Cotton-Textile-Enabled Self-Sustaining Flexible Power Packs via Roll-to-Roll Fabrication. 150	150
7.1 Introduction.....	150
7.2 Experimental Section	152
7.3 Results and Discussion	155

7.3.1 Positive Electrode Materials.....	155
7.3.2 Negative Electrode Material.....	157
7.3.3 Cell Performance.....	160
7.4 Conclusion.....	168
References.....	169
Chapter 8 Summary and Recommendations.....	174
8.1 Summary of Contribution and Significance.....	174
8.2 Recommendations for Future Research.....	177

Acknowledgments

Firstly, I would like to express my heartfelt gratitude to my advisor Professor Xiaodong Li, for advising me through my years of Ph.D. study, for supporting me to pursue various scientific opportunities, for encouraging me to always aim high and do things patiently. His energy, enthusiasm and strong mentality always encourage me to do better. Without his guidance and constant supervision, it would be impossible for me to complete this dissertation. I am truly grateful for these valuable years, which certainly will benefit my career and life in the long run. I would also like to thank other committee members, Prof. Baoxing Xu, Prof. Lin Ma, Prof. David L. Green, and Prof. Sen Zhang, for their valuable time and guidance.

Secondly, I would like to thank all the members of the Li group who have created such a diverse, welcoming and supportive atmosphere. To Ningning, Yunya, Clifton, Yospy and Brendan *et al.*, thanks for the help from all of you through my Ph.D. study. Wherever I will be in the future, UVa will be my life-long memory. I also would like to thank all my friends at UVa, Chao Liu, Naiming Liu, Spring Dong, Serena Luo, Qingyun Wu, Fulin Wang, Bin Wang *et al.* for your accompanying, which makes my Ph.D. life so memorable.

Thirdly, I would like to acknowledge the financial support from the National Science Foundation (NSF) CMMI-1418696, CMMI-1728042 and Department of Energy (DOE), which necessarily make this dissertation study possible.

Lastly, I would like to express my deepest gratitude to my parents and family, thanks for raising me and supporting me to pursue my dream. Here, I give my special thanks to my lovely wife, Xiaohan Chen, thanks for the understanding and continuous supporting. The meaning of life is becoming different because of you.

List of Figures

Figure 1.1 Indicative roadmap of future energy scenario.

Figure 1.2 (a) Schematic illustrations of working principles of LIB (charging) [5] and (b) a two-cell supercapacitor made of nanoporous electrode and the corresponding EDL structure based at a positively charged electrode surface [6].

Figure 1.3 (a) Ragone plots for various electrical energy storage devices. Adapted from Simon *et al.* [8]; (b) Prediction of next-generation high energy batteries. Adapted from Van Norrden. [9]

Figure 1.4 (a) Biomass resources in nature; (b) Various microstructures from biomaterials in nature; (c) Overview of biological templates, placed on a length scale according to their critical dimensions. On the left-hand side are the original biological structures, whereas on the right-hand side are the corresponding synthesized templated structures. (b,c) Adapted from Zhou *et al.*[26]

Figure 1.5 (a) Weight loss in carbonization of (Δ) almond shells, (\square) olive stones, and (\circ) peach stones and evolution of bulk density (\bullet) for peach stones. Adapted from Reinoso *et al.* [36]; (b) Activation mechanism above 1000 K by the penetration of metallic potassium into the lattice of the carbon, the expansion of the lattice by the intercalated potassium, and the rapid removal of the intercalation from the carbon matrix. Adapted from Romanos *et al.* [41]; (c) Transformation of various natural biomass-derived materials into activated carbons. Adapted from Wang *et al.* [16]

Figure 2.1 Illustration of the fabrication process of hierarchical $\text{NiCo}_2\text{O}_4@ \text{NiCo}_2\text{O}_4$ core/shell nanostructure on activated carbon textiles (ACTs).

Figure 2.2 (A) Optical photographs of (a) a commercial cotton T-shirt, (b) a piece of ACT and (c) a piece of ACT under folding condition, showing its super flexibility; (d) SEM image of ACT, inset is the amplified SEM image; (e-f) SEM images of NiCo_2O_4 nanowires grown on the ACT microfibers by a hydrothermal method; (g) and (h) SEM images of $\text{NiCo}_2\text{O}_4@ \text{NiCo}_2\text{O}_4$ core/shell nanostructure on the ACT fibers, inset is the SEM image of $\text{NiCo}_2\text{O}_4@ \text{NiCo}_2\text{O}_4$ nanoflake at high magnification. **(B)** EDS spectrum and element mapping images of C, O, Co and Ni elements of NiCo_2O_4 nanowire/ACT.

Figure 2.3 (a) TEM image of Ni-Co hydroxide precursor nanowires; (b) TEM image of NiCo_2O_4 nanowires grown on ACTs after the annealing process; (c) TEM image of $\text{NiCo}_2\text{O}_4@ \text{NiCo}_2\text{O}_4$

core/shell nanostructure precursor; (d) TEM image of NiCo₂O₄@NiCo₂O₄ core/shell nanostructure after the annealing process; (e) HRTEM image of NiCo₂O₄@NiCo₂O₄ nanostructure, inset is the amplified region; (f) Selected area electron diffraction (SAED) pattern of NiCo₂O₄@NiCo₂O₄ nanostructure.

Figure 2.4 (a) Illustration of the assembled flexible all-solid-state asymmetric supercapacitor; (b) XRD patterns of the as-obtained ACT, NiCo₂O₄ nanowire/ACT, and NiCo₂O₄@NiCo₂O₄/ACT; (c) Co 2p and (d) Ni 2p XPS spectra of NiCo₂O₄@NiCo₂O₄/ACT.

Figure 2.5 (a) Cyclic voltammetry (CV) curves of ACT at different scan rates in 6 M KOH aqueous solution; (b) Specific capacitances of ACT at different scan rates derived from the CV curves; (c) CV curves of NiCo₂O₄ nanowire/ACT at different scan rates in 6 M KOH aqueous solution. (d) Specific capacitances of NiCo₂O₄ nanowire/ACT derived from the CV curves.

Figure 2.6 (a) CV curves of NiCo₂O₄@NiCo₂O₄/ACT at different scan rates in 6 M KOH aqueous solution; (b) Galvanostatic (GV) constant-current charge/discharge curves of NiCo₂O₄@NiCo₂O₄/ACT in 6 M KOH aqueous solution at different current densities; (c) Specific capacitances of NiCo₂O₄@NiCo₂O₄/ACT in 6 M KOH aqueous solution at different current densities; (d) Nyquist plots of electrochemical impedance spectra of NiCo₂O₄@NiCo₂O₄/ACT in 6 M KOH aqueous solution in the frequency range of 100 kHz to 0.05Hz.

Figure 2.7 (a) Comparative CV curves of ACT, NiCo₂O₄ nanowire/ACT and NiCo₂O₄@NiCo₂O₄/ACT at a scan rate of 25 mV/s in 6 M KOH aqueous solution; (b) Comparative Nyquist plots of electrochemical impedance spectra of ACT, NiCo₂O₄ nanowire/ACT and NiCo₂O₄@NiCo₂O₄/ACT in 6 M KOH aqueous solution within the frequency range from 100 kHz to 0.05 Hz; (c) Cycling performance of NiCo₂O₄@NiCo₂O₄/ACT in 6 M KOH aqueous solution at a current density of 20 mA/cm², inset is a part of the charge/discharge curve of NiCo₂O₄@NiCo₂O₄/ACT during the GV constant-current test.

Figure 2.8 (a) CV curves of the symmetric supercapacitor with NiCo₂O₄@NiCo₂O₄/ACT as both the positive electrode and negative electrode, PVA/KOH as polymer gel electrolyte; (b) CV curves of the asymmetric supercapacitor with NiCo₂O₄@NiCo₂O₄/ACT hybrid as the positive electrode, ACT as the negative electrode, and PVA/KOH as polymer gel electrolyte, respectively; (c)

Charge/discharge curves of the symmetric supercapacitor with $\text{NiCo}_2\text{O}_4@\text{NiCo}_2\text{O}_4/\text{ACT}$ as both the positive electrode and negative electrode, PVA/KOH as polymer gel electrolyte; (d) Charge/discharge curves of the asymmetric supercapacitor with $\text{NiCo}_2\text{O}_4@\text{NiCo}_2\text{O}_4/\text{ACT}$ hybrid as the positive electrode, ACT as the negative electrode, and PVA/KOH as polymer gel electrolyte, respectively; (e) Specific capacitances and coulombic efficiency of the symmetric supercapacitor with $\text{NiCo}_2\text{O}_4@\text{NiCo}_2\text{O}_4/\text{ACT}$ as both the positive electrode and negative electrode, PVA/KOH as polymer gel electrolyte at different current densities; (f) Specific capacitances and coulombic efficiency of the asymmetric supercapacitor with $\text{NiCo}_2\text{O}_4@\text{NiCo}_2\text{O}_4/\text{ACT}$ hybrid as the positive electrode, ACT as the negative electrode, and PVA/KOH as polymer gel electrolyte, respectively.

Figure 2.9 (a) CV curves of $\text{NiCo}_2\text{O}_4@\text{NiCo}_2\text{O}_4/\text{ACT}//\text{ACT}$ asymmetric supercapacitor with PVA/KOH polymer gel electrolyte under the voltage windows of 1, 1.2, 1.4 and 1.6 V at the scan rate of 50 mV/s; (b) Nyquist plots of the ACT//ACT symmetric supercapacitor with PVA/KOH polymer gel electrolyte, $\text{NiCo}_2\text{O}_4@\text{NiCo}_2\text{O}_4/\text{ACT}//\text{ACT}$ asymmetric supercapacitor with PVA/KOH polymer gel electrolyte and $\text{NiCo}_2\text{O}_4@\text{NiCo}_2\text{O}_4/\text{ACT}//\text{NiCo}_2\text{O}_4@\text{NiCo}_2\text{O}_4/\text{ACT}$ symmetric supercapacitor with PVA/KOH polymer gel electrolyte; (c) charging/discharging curves of asymmetric supercapacitor with PVA/KOH polymer gel electrolyte at different current densities; (d) Ragone plots of the as-assembled $\text{NiCo}_2\text{O}_4@\text{NiCo}_2\text{O}_4/\text{ACT}//\text{ACT}$ asymmetric supercapacitor with PVA/KOH polymer gel electrolyte, and $\text{NiCo}_2\text{O}_4@\text{NiCo}_2\text{O}_4/\text{ACT}//\text{NiCo}_2\text{O}_4@\text{NiCo}_2\text{O}_4/\text{ACT}$ symmetric supercapacitor with PVA/KOH polymer gel electrolyte (inset is a red light-emitting diode (LED) lighted by two asymmetric supercapacitors under folded state); (e) Radar plot of the symmetric supercapacitor and asymmetric supercapacitor, inset is a lighted LED by two asymmetric supercapacitors connected in series; (f) Cycling performance of $\text{NiCo}_2\text{O}_4@\text{NiCo}_2\text{O}_4//\text{ACT}$ asymmetric supercapacitor with PVA/KOH polymer gel electrolyte under normal, bent and twisted state at a current density of 15 mA/cm^2 (inset is the SEM image of $\text{NiCo}_2\text{O}_4@\text{NiCo}_2\text{O}_4/\text{ACT}$ obtained after 1000 cycles).

Figure 2.10 (a) Digital photograph of the as-prepared solid-state electrolyte film and polymer gel electrolyte; (b) and (c) SEM images of the $\text{NiCo}_2\text{O}_4@\text{NiCo}_2\text{O}_4/\text{ACT}$ dipped with the polymer gel electrolyte; (d) Tensile stress-strain curves of the $\text{NiCo}_2\text{O}_4@\text{NiCo}_2\text{O}_4/\text{ACT}$ dipped with the polymer gel electrolyte and pure ACT, respectively.

Figure 3.1 Schematic illustration of the formation processes of CoO nanostructures of different morphologies and the core/shell CoO@NiO nanocomposite on ACT.

Figure 3.2 (a-c) SEM images of sheet-like CoO on ACT fibers at different magnifications; (d-f) SEM images of petal-like CoO on ACT fibers at different magnifications; (g-h) SEM images of urchin-like CoO on ACT fibers at different magnifications.

Figure 3.3 (a-b) SEM images of core/shell CoO@NiO nanostructure on ACT fibers at different magnifications; (c) TEM image of core/shell CoO@NiO precursor; (d-f) TEM and HRTEM images of core/shell CoO@NiO nanostructure, inset of (f) is the corresponding FFT pattern.

Figure 3.4 Typical XRD patterns of sheet-like CoO (a), petal-like CoO (b), urchin-like CoO (c) and the as-prepared hierarchical core/shell CoO@NiO nanocomposite (d).

Figure 3.5 (a) Optical photographs of a cotton T-shirt, insets are a piece of ACT and a piece of ACT under folding state, showing its high flexibility; (b) SEM image of ACT, inset is the amplified SEM image; (c and d) SEM images of ACT coated with graphene sheets; (e) AFM image of graphene oxide with highlighted profile; (f) TEM image of graphene oxide nanosheet, inset is the TEM image of ACT.

Figure 3.6 (a) Typical XRD patterns of cotton textile, ACT, ACT/graphene oxide and ACT/graphene; (b) Raman spectra of ACT/graphene oxide, and ACT/graphene.

Figure 3.7 (a) Illustration of the assembled flexible all-solid-state asymmetric supercapacitor; (b) CV curves of sheet-like CoO/ACT//ACT/graphene asymmetric supercapacitor with PVA/KOH polymer gel electrolyte under the voltage windows of 0.8, 1.0, 1.2 and 1.4 V at the scan rate of 50 mV s⁻¹; (c) CV curves of petal-like CoO//ACT/graphene asymmetric supercapacitor with PVA/KOH polymer gel electrolyte under the voltage windows of 0.8, 1.0, 1.2 and 1.4 V at the scan rate of 50 mV s⁻¹; (d) CV curves of urchin-like CoO//ACT/graphene asymmetric supercapacitor with PVA/KOH polymer gel electrolyte under the voltage windows of 0.8, 1.0, 1.2 and 1.4 V at the scan rate of 50 mV s⁻¹; (e) CV curves of core/shell CoO@NiO//ACT/graphene asymmetric supercapacitor with PVA/KOH polymer gel electrolyte under the voltage windows of 1, 1.2, 1.4 and 1.6 V at the scan rate of 50 mV s⁻¹; (b) CV curves of core/shell CoO@NiO//ACT/graphene asymmetric supercapacitor with PVA/KOH polymer gel electrolyte under the voltage windows of 1.6 V at different scan rates.

Figure 3.8 (a) Charging/discharging curves of sheet-like CoO/ACT//ACT/graphene asymmetric supercapacitor with PVA/KOH polymer gel electrolyte at different current densities; (b) Charging/discharging curves of petal-like CoO/ACT//ACT/graphene asymmetric supercapacitor with PVA/KOH polymer gel electrolyte at different current densities; (c) Charging/discharging curves of urchin-like CoO/ACT//ACT/graphene asymmetric supercapacitor with PVA/KOH polymer gel electrolyte at different current densities; (d) Charging/discharging curves of core/shell CoO@NiO/ACT//ACT/graphene asymmetric supercapacitor with PVA/KOH polymer gel electrolyte at different current densities.

Figure 3.9 (a) Specific capacitances and Coulombic efficiency of the core/shell CoO@NiO/ACT//ACT/graphene asymmetric supercapacitor with PVA/KOH as polymer gel electrolyte, inset shows a lighted LED by two asymmetric supercapacitors connected in series; (b) Nyquist plots of the sheet-like CoO/ACT//ACT/graphene supercapacitor, petal-like CoO/ACT//ACT/graphene, urchin-like CoO/ACT//ACT/graphene and core/shell CoO@NiO/ACT//ACT/graphene asymmetric supercapacitors with PVA/KOH polymer gel electrolyte; (c) Ragone plots of the as-assembled sheet-like CoO/ACT//ACT/graphene supercapacitor, petal-like CoO/ACT//ACT/graphene, urchin-like CoO/ACT//ACT/graphene and core/shell CoO@NiO/ACT//ACT/graphene asymmetric supercapacitors with PVA/KOH polymer gel electrolyte, inset shows the lighted LED by the asymmetric supercapacitor even under totally folded state; (d) Cyclic performance of the sheet-like CoO/ACT//ACT/graphene supercapacitor, petal-like CoO/ACT//ACT/graphene, urchin-like CoO/ACT//ACT/graphene and core/shell CoO@NiO/ACT//ACT/graphene asymmetric supercapacitors with PVA/KOH polymer gel electrolyte under different working condition; (e) Surface/volume ratios and specific capacitances of sheet-like CoO, petal-like CoO, urchin-like CoO and the as-prepared hierarchical core/shell CoO@NiO nanocomposite; (f) Fitting result and corresponding mathematical expression of the relationship between surface/volume ratio and specific capacitance.

Figure 4.1 (a) Schematically Illustration of the fabrication process of porous ACT/NiS₂-graphene composite; (b) Optical photograph of a commercial cotton T-shirt, a piece of ACT/Ni-graphene under normal and folded state, showing its high flexibility; (c) SEM image of cotton textile, inset is the amplified SEM image of a cotton fiber; (d) XCT images of ACT/Ni-graphene composite after removing the Ni nanoparticles by using 2 M HNO₃, inset is the amplified region; (e) SEM

image and (f) corresponding size distribution of porous ACT fibers after removing the Ni nanoparticles; (g) XRD patterns of cotton T-shirt textile and ACT/Ni-graphene composite.

Figure 4.2 SEM images of ACT/Ni-graphene composites obtained at various $\text{Ni}(\text{NO}_3)_2$ concentrations: (a) and (b) 0.01 M, (c) and (d) 0.5 M, (e) and (f) 1 M, (g) and (h) 2 M.

Figure 4.3 XRD patterns of ACT/Ni-graphene composites obtained at the $\text{Ni}(\text{NO}_3)_2$ concentration of 0.01 M, 0.5 M, 1 M, and 2 M, respectively.

Figure 4.4 Raman spectra of ACT/Ni-graphene composites obtained at the $\text{Ni}(\text{NO}_3)_2$ concentration of 0.01 M, 0.5 M, 1 M, and 2 M, respectively.

Figure 4.5 (a) and (b) SEM images of ACT/Ni-graphene-0.5 composite at different magnifications; (c) and (d) Cross-sectional SEM images of ACT/Ni-graphene-0.5 composite at different magnifications, insets are the corresponding amplified regions; (e) TEM image of ACT alone; (f) TEM image of ACT/Ni-graphene-0.5; (g) AFM height and (h) corresponding phase images of ACT/Ni-graphene-0.5 composite; (i) Raman spectrum of ACT/Ni-graphene-0.5.

Figure 4.6 (a) and (b) SEM images of ACT/ NiS_2 -graphene composite at different magnifications, inset of b is the corresponding amplified region; (c) TEM images of ACT/ NiS_2 -graphene, inset of c is amplified region; (d) and (e) TEM images of NiS_2 nanobowls on ACT; (f) Selected area electron diffraction (SAED) pattern of the NiS_2 nanobowl; (g) AFM height and corresponding phase (h) images of ACT/ NiS_2 -graphene; (i) Raman spectrum of porous ACT/ NiS_2 -graphene.

Figure 4.7 (a)-(d) SEM image and the corresponding EDS maps of the obtained ACT/ NiS_2 -graphene-0.5 composite; (e) Relative element ratio of C, O, S, Ni in the ACT/ NiS_2 -graphene composite; (f) XRD pattern of ACT/ NiS_2 -graphene composite.

Figure 4.8 (a) BET measurement-isothermal curve of ACT/ NiS_2 -graphene composite; (b) BJH pore size distribution of ACT/ NiS_2 -graphene composite.

Figure 4.9 (a) Schematically illustration of the assembled flexible lithium-ion battery; (b) Initial cyclic voltammogram profiles of ACT/ NiS_2 -graphene; (c) Initial charge/discharge voltage-specific capacity curves of porous ACT/ NiS_2 -graphene at 0.01 C; (d) Cyclic voltammogram profiles of ACT/ NiS_2 -graphene after 10 charge/discharge processes; (e) 10th charge/discharge voltage-specific capacity curves of ACT/ NiS_2 -graphene at 0.01 C.

Figure 4.10 (a) 20th, 50th, 150th and 400th charge/discharge voltage-specific capacity curves of ACT/NiS₂-graphene at different charge/discharge rates; (b) Cyclic voltammogram profiles of ACT/NiS₂-graphene after 400 charge/discharge processes; (c) Nyquist plots of ACT/NiS₂-graphene at the 1st and 100th charge/discharge processes; (d) Cycling and rate performance of porous ACT/NiS₂-graphene, inset is the open circuit potential of the assembled flexible battery cell under bent state; (e) 1st (0.1 C), 5th (0.1C), and 15th (0.3C) charge/discharge voltage-specific capacity curves at normal state and the 50th charge/discharge voltage-specific capacity curve at the bent state of the flexible cell; (f) the cyclic performance of the flexible cell at normal and bent states; Insets of (c) and (e) are optical photograph of a yellow light-emitting diode (LED) lighted by the assembled flexible cell under normal and folded states, respectively.

Figure 4.11 SEM images of ACT/Ni-graphene composite electrode after repeated charge/discharge processes at normal and bent states, cross-section (a,b) and surface with the amplified region (c,d).

Figure 5.1 Schematic illustration of the fabrication process of hollow ACT/S-rGO composite.

Figure 5.2 Nitrogen adsorption/desorption isotherms (a) and pore size distribution (b) curves of the prepared ACT. Nitrogen adsorption/desorption isotherms (c) and pore size distribution (d) curves of the prepared porous ACT treated by KOH.

Figure 5.3 (a) Digital photograph of a commercial cotton T-shirt, and a piece of ACT under normal and folded state, showing its excellent flexibility; (b) SEM image of ACT, inset is the TEM image of ACT; (c) SEM image of ACT fiber, inset is the amplified cross-section of ACT fiber. (d) SEM image of ACT/S composite; (e) the amplified SEM image ACT/S composite; (f) AFM height image of graphene oxide nanosheet; (g,h) SEM images of ACT/S-rGO composite at different magnifications; (i) TEM image of graphene oxide (GO) nanosheet, inset is the HRTEM image and SAED of rGO nanosheet.

Figure 5.4 (a-d) EDS maps of the obtained ACT/S composite; (e) Relative element ratio of C, O, S in the ACT/S composite; (f) XRD pattern of the used S and its corresponding standard peaks.

Figure 5.5 (a) Raman spectra of ACT, GO, and ACT/S-rGO; (b) XRD patterns of the cotton textile, ACT, ACT/S composite; (c) XRD patterns of GO and ACT/S-rGO composite.

Figure 5.6 (a,b) TEM images of ACT/S at different magnifications; (c) HRTEM image of ACT/S, inset of d is the amplified region; (d) the corresponding FFT pattern of ACT/S; (e) Illustration of the conversation of cotton textile to porous ACT; (f-h) SEM images of porous ACT treated with KOH during the activation process.

Figure 5.7 (a) Initial charge/discharge voltage-capacity profiles of porous ACT/S graphene at the current density of 0.1 mA cm^{-2} ; (b) Initial charge/discharge voltage-capacity profiles of ACT/S-rGO cathode with porous ACT interlayer at the current density of 0.3 mA cm^{-2} ; (c) Nyquist plot of ACT/S cathode; (d) Nyquist plots of ACT/S-rGO cathode with porous ACT interlayer.

Figure 5.8 (a) Initial cyclic voltammogram profile of ACT/S-rGO cathode without porous ACT interlayer; (b) Nyquist plots of ACT/S-rGO cathode without porous ACT interlayer; (c) 4th, 8th, and 12th charge/discharge voltage-capacity profiles of ACT/S-GO without porous ACT interlayer at different current densities; (d) Stepwise cycling performance of ACT/S-rGO cathode without porous ACT interlayer and its Coulombic efficiency.

Figure 5.9 (a) Schematic illustration of the systematic effects of a Li-S battery with ACT/S-rGO as a cathode and porous ACT as an interlayer to manipulate the “shuttle effect”; (b) 11th, 21th, 25th, 31th and 100th charge/discharge voltage-capacity profiles of ACT/S cathode at different current densities; (c) 5th, 10th, 15th, 30th, 40th and 50th charge/discharge voltage-capacity profiles of ACT/S-GO with porous ACT interlayer at different current densities; (d) Cyclic voltammogram profile of ACT/S-rGO cathode with porous ACT interlayer after 50 charge/discharge cycles; (e) Stepwise cycling performance of ACT/S cathode and its Coulombic efficiency; (f) Stepwise cycling performance of ACT/S-rGO cathode with KOH-activated porous ACT as an interlayer and its Coulombic efficiency.

Figure 5.10 (a) Schematic illustration of the assembled flexible lithium-sulfur battery; (b,c) Digital photographs of a yellow light-emitting diode (LED) lighted by the assembled flexible Li-S cell under normal and bent states, respectively; (d) The 1st, 5th and 25th charge/discharge voltage-capacity profiles under the normal state and the 50th charge/discharge voltage-capacity profile under a bent state of the flexible Li-S cell at the current density of 1.2 mA cm^{-2} ; (e) Cyclic performance of the flexible lithium cell under normal and bent states at the current density of 1.2 mA cm^{-2} .

Figure 6.1 Schematic illustration of the synthesis of ACT@Fe/Fe₃C nanoparticles (ACT@Fe/Fe₃C NPs) composite and its hybridization with sulfur to prepare ACT@Fe/Fe₃C/S composite.

Figure 6.2 (a,b) Scanning electron microscopy (SEM) images of the ACT@Fe/Fe₃C NPs at different magnifications; (c,d) Transmission electron microscopy (TEM) images of the ACT@Fe/Fe₃C NPs at different magnifications; (e,f) High resolution transmission electron microscopy (HRTEM) images of the ACT@Fe/Fe₃C NPs at different magnifications, inset of (f) is the corresponding fast Fourier transform (FFT) pattern; (g) Selected area electron diffraction (SAED) pattern of the ACT@Fe/Fe₃C NPs; (h) Atomic force microscopy (AFM) height and corresponding phase (i) images of ACT@Fe/Fe₃C NPs.

Figure 6.3 XRD patterns of the as-prepared (a) cotton textile and activated cotton textile (ACT); (b) ACT@Fe/Fe₃C NPs and ACT@Fe/Fe₃C/S composite.

Figure 6.4 (a,b) SEM images of the ACT@Fe/Fe₃C/S composite at different magnifications; (c) TEM image of the ACT@Fe/Fe₃C/S composite; (d) HRTEM images of the core/shell nanostructures in ACT@Fe/Fe₃C/S composite with Fe/Fe₃C NP core and multilayered graphene shell; (e) the corresponding amplified region of (d); (f) HRTEM image of the ACT@Fe/Fe₃C/S composite with random distributed sulfur nanograins; (g) selected area electron diffraction (SAED) pattern of the ACT@Fe/Fe₃C/S composite; (h) AFM height and corresponding phase (i) images of ACT@Fe/Fe₃C/S composite.

Figure 6.5 Raman spectra of the as-prepared ACT@Fe/Fe₃C NPs and ACT@Fe/Fe₃C/S composite.

Figure 6.6 (a-e) The EDS element mapping images of the ACT@Fe/Fe₃C/S composite and (f) the elemental spectrum and the relative element ratio of C, O, S, Fe, scale bar 5 μm .

Figure 6.7 (a) Close-up HRTEM image and (b) the corresponding elemental spectrum of the ACT@Fe/Fe₃C/S composite.

Figure 6.8 (a) Cyclic voltammogram (CV) profile of the prepared ACT@Fe/Fe₃C/S cathode; (b) 1st, 2nd, 11th, 21st, 31st and 61st charge/discharge profiles of ACT@Fe/Fe₃C/S cathode at different current densities (1 C = 3 mA cm⁻²); (c) Electrochemical impedance spectroscopy (EIS) of the prepared ACT@Fe/Fe₃C/S cathode at 1st and 600th cycle; (d) rate performance of ACT@Fe/Fe₃C/S

cathode at different current densities in the first 50 cycles; (e) stepwise cycling performance of ACT@Fe/Fe₃C/S cathode and its Coulombic efficiency; (f) XRD pattern and SEM images (g-i) of the ACT@Fe/Fe₃C/S cathode after the cyclic tests.

Figure 6.9 (a) The initial charge/discharge curves of the ACT@Fe/Fe₃C/S composite; (b) Cyclic and Coulombic efficiency of the ACT@Fe/Fe₃C/S composite.

Figure 6.10 Digital images of the ACT/S composite (a) and ACT@Fe/Fe₃C/S composite (b) electrodes during the first discharge cycle in the liquid cell at the current density of 0.1 mA cm⁻²; (c) Illustration of the possible polysulfides trapping mechanism by introducing of Fe/Fe₃C NPs in the ACT@Fe/Fe₃C/S cathode.

Figure 7.1 (a) Schematic illustration of the formation processes of Co-Al LDH nanostructure on the ACT; (b) Photographs of a cotton T-shirt, a piece of ACT and a piece of ACT under folded state; (c-e) SEM images of Co-Al LDH nanosheets on ACT fibers at different magnifications. Scale bars, 20 μm for (c), 5 μm for (d) and 1 μm for (e).

Figure 7.2 (a) TEM image of Co-Al LDH (scale bar, 1 μm), inset is the illustration of LDH; (b-d) HRTEM images of Co-Al LDH and the corresponding SAED pattern. Scale bars, 10 nm for b, 5 nm for c and 5 1/nm for d; (e) Schematic illustration of the molecular structure of Co-Al LDH; (f) XRD patterns of ACT/Co-Al LDH and the standard peaks of Co-Al LDH (JCPDS # 510045).

Figure 7.3 (a) SEM image of ACT (scale bar, 250 μm), inset is the amplified SEM image (scale bar, 5 μm); (b) SEM image of graphene oxide, inset is the AFM image of graphene oxide nanosheets (with a height profile showing a step of 1.1 nm marked by the red arrows); (c,d) SEM images of ACT/graphene composite at different magnifications (scale bars, 10 μm for c and 2 μm for d), insets of d are the HRTEM image (scale bar, 5 nm) and corresponding SAED pattern of graphene nanosheets; (e) Schematic illustration of the ACT fiber with graphene coating, inset is the TEM image of ACT fiber (scale bar, 25 nm); (f) XRD patterns of pure cotton textile, ACT, ACT/graphene oxide, and ACT/graphene composite.

Figure 7.4 Raman spectra of ACT/graphene oxide (a) and ACT/graphene (b) composites.

Figure 7.5 (a) CV curves of the ACT, ACT/graphene, and ACT/Co-Al LDH electrodes with the 6 M KOH electrolyte in the potential window of -0.2-0.6 V at a scan rate of 25 mV s⁻¹; (b)

Charge/discharge curves of the ACT, ACT/graphene, and ACT/Co-Al LDH electrodes with the 6 M KOH electrolyte in the potential window of 0-0.44 V at a current density of 2.5 A g⁻¹; (c) CV curves of ACT/Co-Al LDH electrode with the 6 M KOH electrolyte in the potential windows of -0.2-0.6 V at different scan rates; (d) Charge/discharge curves of ACT/Co-Al LDH electrode with the 6 M KOH electrolyte in the potential windows of 0-0.44 V at different current densities.

Figure 7.6 (a) CV curves of ACT/graphene//ACT/graphene and ACT/Co-Al LDH//ACT/Co-Al LDH symmetric cells as well as ACT/Co-Al LDH//ACT/graphene asymmetric cell with PVA/KOH polymer gel electrolyte in the voltage window of 1.0 V at a scan rate of 25 mV s⁻¹; (b) Charge/discharge curves of ACT/graphene//ACT/graphene and ACT/Co-Al LDH//ACT/Co-Al LDH symmetric cells as well as ACT/Co-Al LDH//ACT/graphene asymmetric cell with PVA/KOH polymer gel electrolyte in the voltage window of 1.6 V at a current density of 12.5 mA cm⁻² (X-axis has been transformed to time/mass, based on the mass of the electrode); (c) CV curves of ACT/Co-Al LDH//ACT/graphene asymmetric cell with PVA/KOH polymer gel electrolyte under the voltage windows of 1, 1.2, 1.4 and 1.6 V at the scan rate of 25 mV s⁻¹, respectively; (d) CV curves of ACT/Co-Al LDH//ACT/graphene asymmetric cell with PVA/KOH polymer gel electrolyte in the voltage windows of 1.6 V at different scan rates.

Figure 7.7 (a) Charge/discharge curves of ACT/Co-Al LDH//ACT/graphene asymmetric cell; (b) Specific capacitances and Coulombic efficiency of the ACT/graphene//ACT/graphene and ACT/Co-Al LDH//ACT/Co-Al LDH symmetric cells as well as ACT/Co-Al LDH//ACT/graphene asymmetric cell; (c) Ragone plots of the ACT/graphene//ACT/graphene and ACT/Co-Al LDH//ACT/Co-Al LDH symmetric cells as well as ACT/Co-Al LDH//ACT/graphene asymmetric cell; (d) Nyquist plots of the ACT/graphene//ACT/graphene and ACT/Co-Al LDH//ACT/Co-Al LDH symmetric cells as well as ACT/Co-Al LDH//ACT/graphene asymmetric cell; (e) Representative charge/discharge curve of ACT/Co-Al LDH//ACT/graphene asymmetric cell; (f) Cyclic performance of the ACT/graphene//ACT/graphene and ACT/Co-Al LDH//ACT/Co-Al LDH symmetric cells as well as ACT/Co-Al LDH//ACT/graphene asymmetric cell with PVA/KOH polymer gel electrolyte.

Figure 7.8 (a) The digital photograph of the assembled flexible asymmetric cell under normal state; (b) The digital photograph of the assembled flexible asymmetric cell under folded state, demonstrating its excellent flexibility.

Figure 7.9 (a) Schematic illustration of the roll-to-roll manufacturing process for integrating a flexible solar cell with the supercapacitor into a self-sustaining power pack; (b) Digital photograph of the assembled solar cell/supercapacitor hybrid energy conversion and storage system, insets are the photographs of the open circuit potential of the ACT/Co-Al LDH//ACT/graphene asymmetric cell before charging and after charging with solar cell; (c) Charging curve of the ACT/Co-Al LDH//ACT/graphene asymmetric cell with solar cell, and discharging curve of the ACT/Co-Al LDH//ACT/graphene asymmetric cell at a current density of 5 mA cm^{-2} ; (d) Digital photograph of the assembled solar cell/supercapacitor hybrid power pack worked under the light, inset shows schematically the working circuit connection; (e) Digital photograph of the assembled solar cell/supercapacitor hybrid power pack worked without the light, inset shows schematically the working circuit connection.

List of Tables

Table 1.1 Summary of various biomass-derived carbon materials by different activation methods for supercapacitor application as well as their specific surface area, pore volume, and specific capacitance

Table 1.2 Summary of various biomass-derived carbon materials by different activation methods for lithium-sulfur battery application as well as their specific surface area, pore volume, and cyclic capacitance

Table 7.1. Comparison of the as-prepared Co-Al LDH asymmetric supercapacitor with previously published results.

Chapter 1. Introduction

1.1 Background and Motivation

Energy is one of the most important topics in the 21st century. Unfortunately, current power supplies are mainly based on the non-renewable fossil fuels. With growing energy demand in many urbanizing nations, particularly in India and China, the threat of depleting the planet's fossil fuel reserves is of increasing concerns. Therefore, it is essential to explore natural and renewable energy sources, such as solar, wind, geothermal and tidal energy, in order to build a sustainable future [1]. Figure 1.1 shows a well-considered roadmap for the near future energy scenario, which demonstrates the development trend of energy technologies with the goal of replacing fossil-based energy through renewable energy sources [2]. However, one of the key issues in the application of these renewable energy sources is their non-continuous and unstable power output. Therefore, it is necessary to develop efficient energy storage devices to mitigate the power fluctuations of renewable energy source, making them become a reliable source of energy.

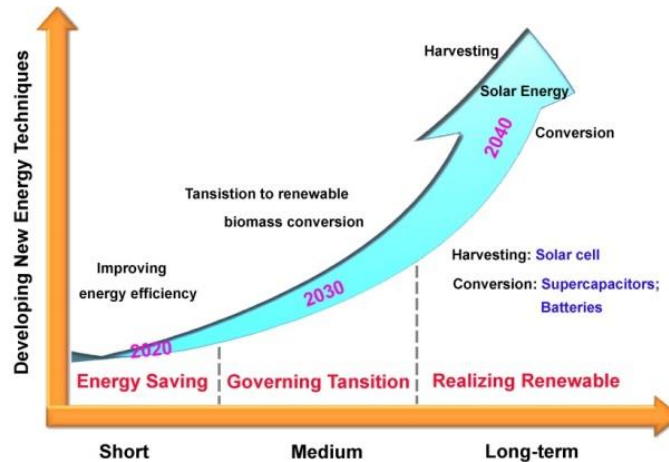


Figure 1.1 Indicative roadmap of future energy scenario.

To date, batteries and supercapacitors have been proven to be the most effective electrochemical energy storage devices for practical applications, which have completely revolutionized our lifestyle by providing power for portable electronics. In the past decades, significant progress has been made on the improvement of the performances of energy storage devices, however, the current batteries and supercapacitors are still suffered from limited energy density and power density, which cannot satisfy our increasing needs on high energy batteries. Furthermore, these traditional energy storage devices are rigid and fragile and thus cannot meet

the requirements of the next-generation flexible/wearable electronics. Therefore, it is imperative to fabricate flexible energy storage devices with superior flexibility and durability for future flexible/wearable electronics.

On the other hand, the rapidly swelling of electric vehicles (EVs) and portable/wearable electronics market is straining the supply of raw electrode materials [3]. Considering their combined detrimental effects of toxicity, non-renewable nature, and a limited supply of raw materials used in current battery/supercapacitor technologies, material sustainability is another critical consideration [4]. As the key components used in current batteries/supercapacitors, carbon materials, such as graphite and activated carbon, are often derived from nonrenewable resources under relatively harsh environments. Therefore, a different approach to battery material sourcing is urgently required for continued sustainable development.

To tackle these ground challenges, in my Ph.D. research, I will focus on using natural abundant cotton textiles to derive renewable, flexible and conductive carbon substrates at a low cost, high throughput way for the design and fabrication of next-generation flexible energy storage devices. The following key scientific questions will be investigated: (1) How to derive flexible conductive substrates from natural abundant cotton textiles? (2) What are the fundamental mechanisms behind the materials conversion? (3) How to improve their electrochemical performance by well-defined materials design strategy? (4) What is the potential of these biomass-derived renewable flexible substrates?

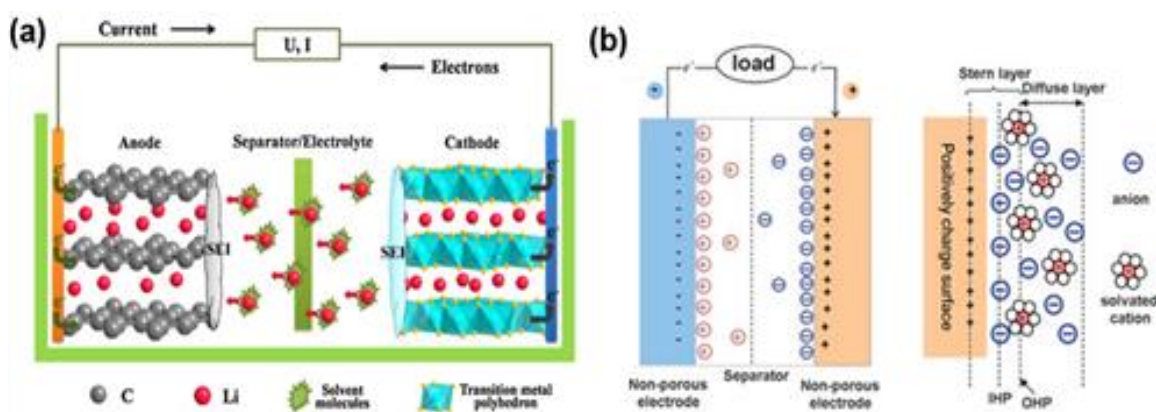


Figure 1.2 (a) Schematic illustrations of working principles of LIB (charging) [5] and (b) a two-cell supercapacitor made of nanoporous electrode and the corresponding EDL structure based at a positively charged electrode surface [6].

1.2 Current Challenges of the Biomass-derived Carbon Materials for Energy Storage Applications

Batteries and supercapacitors are currently the most widely used electrochemical energy storage devices for power portable electronics, hybrid or electric vehicles (EVs), as well as stationary and mobile instruments. In order to design a better battery or supercapacitor, we need to thoroughly understand the energy storage mechanisms of different energy storage devices. Figure 1.2 shows the different energy storage mechanisms for traditional lithium-ion batteries and supercapacitors. Briefly, supercapacitors can store charge at the electrode/electrolyte interface via electrical double layer or reversible faradic reactions, while lithium-ion batteries convert chemical energy into electrical energy by exothermal redox reactions, in which lithium-ions are served as energy carrier, transporting back and forth between the anode and cathode during charge/discharge processes [7].

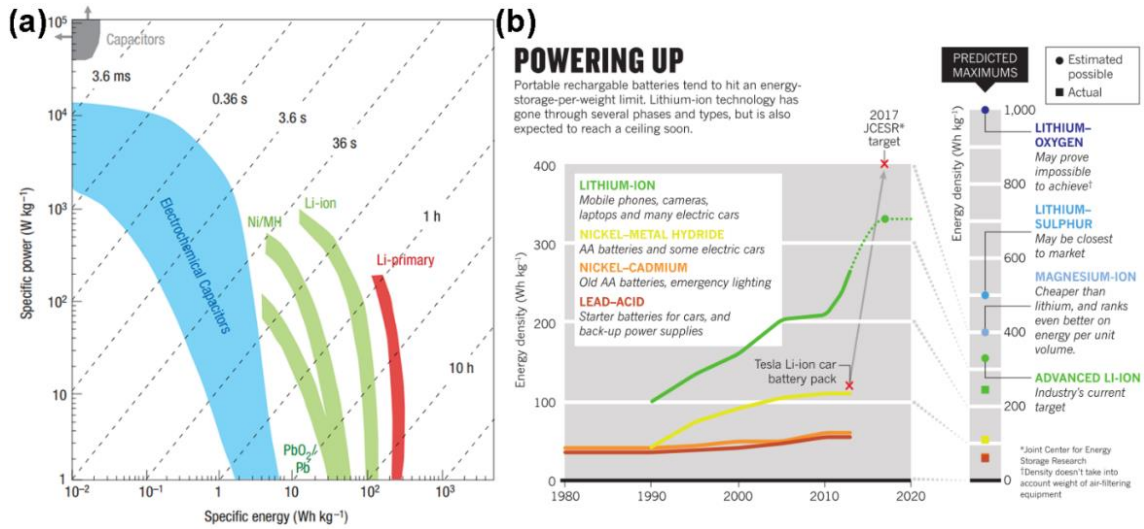


Figure 1.3 (a) Ragone plots for various electrical energy storage devices. Adapted from Simon *et al.* [8]; (b) Prediction of next-generation high energy batteries. Adapted from Van Norrden. [9]

However, the energy density of traditional lithium-ion battery almost reaches its theoretical limit, which cannot satisfy the increasing needs for higher storage capability, such as electric vehicles and grid energy storage. At the same time, the poor power density of lithium-ion battery also hinders battery's further application in the fields that need fast power deliver, for example, the accelerating and braking of electric vehicles. Therefore, it is in urgent need to develop next-generation energy storage devices to provide higher energy storage and faster power deliver using less or without using any nonrenewable graphite materials. In this context, high energy density

lithium-sulfur batteries and high-power density supercapacitors have demonstrated the unprecedented potential for next-generation energy storage devices that can directly address the aforementioned challenges (Figure 1.3).

Even with so many merits, lithium-sulfur batteries and supercapacitors still encounter many roadblocks for scale-up commercialization. For example, the insulating nature of sulfur and the dissolution of polysulfide intermediates often lead to fast capacity decay of lithium-sulfur system, on the other hand, supercapacitors have shown poor energy density. [10] To explore the potential of the sulfur cathode, various carbon materials (including expensive nanostructured carbons, such as CNTs, graphene, and ordered porous carbon) with high conductivity and suitable porosity have been used to host sulfur to leverage the poor conductivity of sulfur cathode and trap the dissolved lithium polysulfides. [11-13] In addition, plenty of carbon materials ranging from traditional activated carbons (ACs) to nanostructured carbons have also been used as electrode materials for supercapacitors to push up their energy densities. [14] Unfortunately, the reserves of graphite and petroleum coke-derived ACs are limited and non-renewable, and the mining process is hazardous and contaminative, which brings an increasing pressure for high throughput production of graphite-based lithium-ion batteries and traditional AC-based supercapacitors. Furthermore, considering the increasing demands of energy storage devices for electronics and EVs and the nonrenewable nature of the currently widely electrode (such as graphite and metal cobalt), it is urgently needed to explore renewable alternative electrode materials for next-generation supercapacitor and lithium-sulfur applications.

Ideally, we hope energy storage materials can be produced via simple, low cost and environmentally friendly methods from renewable resources. Considering the whole cycle life of carbon materials, from the precursor, manufacturing process, to the end-of-life, nature renders us unlimited inspirations. On the other hand, biomass resources are recyclable and highly accessible across the earth, which can be not only transformed into biofuel (e.g. bioethanol and biodiesel) to replace the fossil fuels but also converted into renewable carbon materials by physical activation, chemical activation or hydrothermal carbonization (HTC) methods [15-17]. In fact, various biomass resources, including all kinds of wood and plant tissues, agricultural wastes, even industrial wastes, and municipal wastes have been used as precursor materials to derive renewable carbon materials with desired properties for both supercapacitors and batteries applications [18-

19]. However, due to the different microstructure and complicated composition of biomass precursors, there is still lack of fundamental understanding of the conversation mechanisms of biomasses to realize optimized microstructure, porosity, surface area and functionality of the final renewable carbon materials.

1.3 Biomass Resources for Renewable Carbon Materials

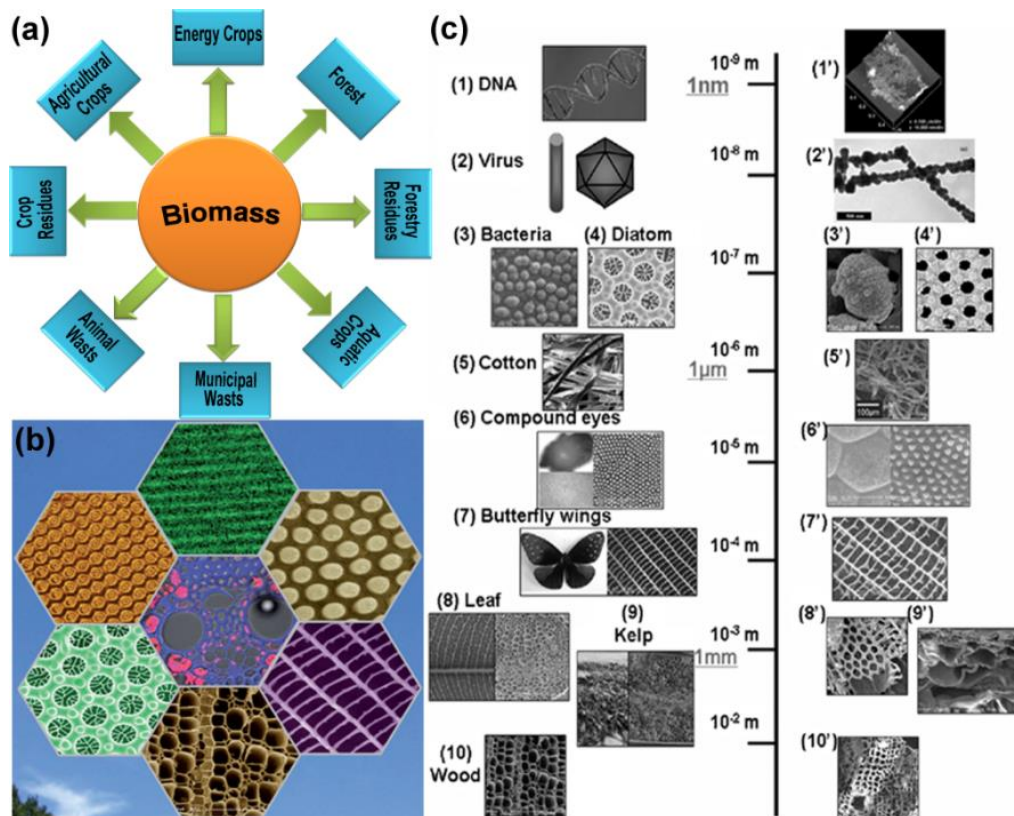


Figure 1.4 (a) Biomass resources in nature; (b) Various microstructures from biomaterials in nature; (c) Overview of biological templates, placed on a length scale according to their critical dimensions. On the left-hand side are the original biological structures, whereas on the right-hand side are the corresponding synthesized templated structures. (b,c) Adapted from Zhou *et al.* [26]

Biomass materials, including all of the biologically produced materials, generally indicate the living matters on earth. As shown in Figure 1.4a, the biomass resources are abundant, including energy crops, agricultural crops, and their residues, wood and wood wastes, municipal wastes and animal wastes, aquatic plants and algae. [20] Typically, biomass can store chemical energy transformed from solar energy in the plant tissues by the photosynthesis process. Therefore, biomass energy is also considered to be an important renewable energy source, like solar, wind, hydroelectricity and geothermal, and more significantly, utilizing this energy will not add CO₂ into

the environment. [21] To date, energy from biomasses has been widely used to meet the increasing energy needs, for instance, heating and cooling, electricity generating, and vehicle fueling.

Biomass materials not only can be directly used by burning or indirectly be used by converting into liquid or gas fuel, such as bioethanol or biodiesel, [22] but also can be used to derive many important chemicals, which is also a challenging topic in chemistry and biology for green and sustainable utilization of biomass wastes. [23] Biochar and activated carbons are the most common products from biomass materials. Briefly, biochar usually can be obtained by burning or pyrolysis (low oxygen) of biomass materials, which often produced a highly porous structure with high specific surface area. Such special porous structure is beneficial to absorbing nutritive cations and anions for the growth of soil-beneficial micro-organisms, improving the fertility of the soil and bringing great agricultural benefits. [24] ACs are another kind of by-products that can be obtained from the pyrolysis of biomass materials, usually possessing high specific surface area and rich porosity, which have been widely used for gas separation, water purification, catalyst supports, electrodes for supercapacitor and fuel cells. [25] More interestingly, biomass materials usually show intriguing structures, such as hierarchical organization, periodic pattern, or some special nano-architectures, which endow them with certain unique functionalities, such as anti-reflection, super-hydrophobicity, structural coloration, and biological self-assembly. As illustrated in Figures 1.4b and c, [26] these amazing structures can be inherited by choosing appropriate processes, producing morphology-controllable materials with structural specificity, complexity, and unique functionality for energy and environment applications. [27] Although the applications of biomass materials are different, the fundamental challenge is always the same - how to improve performance by optimizing their structures. A thorough understanding of the conversation mechanisms is needed to obtain high-performance chemical feedstocks which will help us to solve those energy and environmental challenges.

1.4 Typical Methods and Mechanism for the Biomass Conversion

To date, various methods have been tried to obtain energy from biomass. Typically, all of those methods can be grouped into two categories, namely thermochemical process (e.g. combustion, gasification, and pyrolysis) and biochemical process (e.g. fermentation and anaerobic digestion), which have been carefully summarized in previous report. [28] Pyrolysis is one important form of energy recovery process, which has the potential to produce products of different

kinds such as char, oil and gas. [29] During the thermal pyrolysis, the moisture and the volatile matter contents of biomass are removed and the remaining solid char often displays properties different from the pristine biomass materials. Therefore, the by-product char from biomass can be used to produce various carbon materials including activated carbon, porous carbon, even nanostructured carbons such as fullerenes, CNTs and graphene by well-designed synthesis routes. [30-33] The texture and surface functional groups of the obtained carbon materials can be further modified by employing appropriate activation methods and agents. [34] The final products from biomass have demonstrated potential in various fields, including air pollution control, wastewater treatment, catalyst support, hydrogen storage, and energy conversion and storage. Generally, there are three major synthesis methods to obtain carbon materials from renewable biomass materials, namely, physical activation, chemical activation and hydrothermal carbonization, based on different experimental conditions and conversion mechanisms. The following section presents a brief summary of these conversion methods.

1.4.1 Physical Activation

Physical activation is a widely used two-step process to activate carbon precursors, which involves pyrolysis carbonization process of raw materials (below 1000 K) followed by a controlled gasification process at relatively higher temperatures (>1150 K) in the presence of oxidizing gases such as carbon dioxide, steam, air or their mixtures. [35] In the first stage of carbonization process, raw materials were carbonized into chars with rudimentary pore structure in an inert atmosphere at a moderate temperature. Figure 4a demonstrates the evolution of weight loss during the carbonization process for three different lignocellulosic precursors: almond shells, olive, and peach stones. [36] The three materials show very similar weight loss trend with increasing temperature. Three distinct stages appear to exist: (I) fast weight loss between ~300 and ~470 K corresponding to water loss; (II) slow weight loss between ~470 and ~770 K corresponding to the primary pyrolysis, accompanying with evolution of most gases and tars as well as the formation of the basic structure of char; and (III) small weight loss in the range of ~770 ~1120 K, ascribing to the consolidation of char structure. However, the char pores are often filled with disorganized carbon from the decomposition of tars during the carbonization process, which in turn leads to inaccessible pores and low specific areas, retarding its practical application. Therefore, a subsequent activation process is necessary to enable the as-obtained chars undergone a partial and controlled gasification process at a higher temperature to achieve a well-developed and accessible interconnected porous

structure. The high-temperature activation process (~1100 - ~1250 K) helps to remove the disorganized material while enabling the elementary crystallites exposed to activating agents, facilitating porosity development.

Physical activation uses either CO₂ or H₂O as an activation gas, which is clean and easy to handle. [37] Rice husk, rice straw, corn cob, corn hulls, peanut hulls, pecan shells, coconut shells, and almond shells have been used as raw materials to produce activated carbon materials by physical activation method. [38-40]

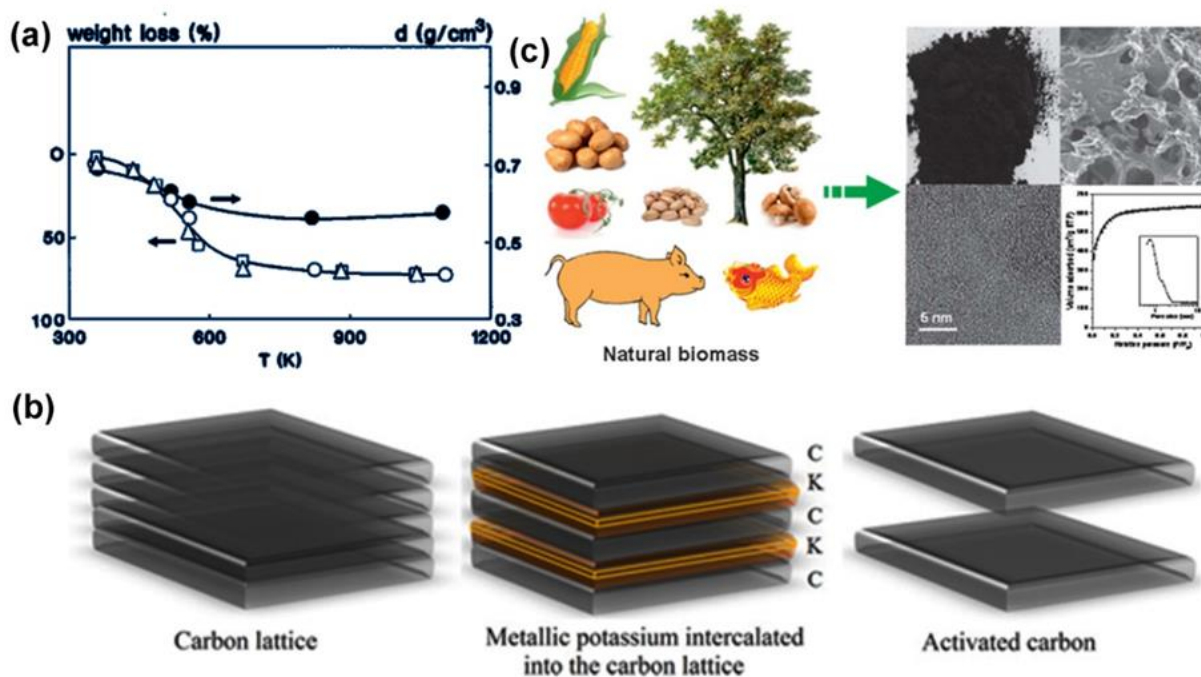
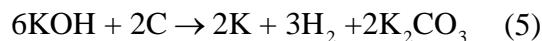
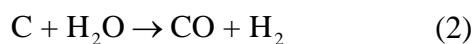
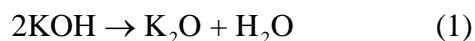


Figure 1.5 (a) Weight loss in carbonization of (Δ) almond shells, (◻) olive stones, and (◊) peach stones and evolution of bulk density (●) for peach stones. Adapted from Reinoso *et al.* [36]; (b) Activation mechanism above 1000 K by the penetration of metallic potassium into the lattice of the carbon, the expansion of the lattice by the intercalated potassium, and the rapid removal of the intercalation from the carbon matrix. Adapted from Romanos *et al.* [41]; (c) Transformation of various natural biomass-derived materials into activated carbons. Adapted from Wang *et al.* [16]

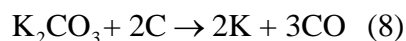
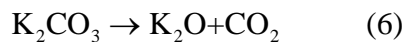
1.4.2 Chemical Activation

Chemical activation has been well established, which usually performs in a single step at ~700 - ~1200 K combining the carbonization and activation, with the precursor mixed with chemical activating agents (ZnCl₂, H₃PO₄, KOH, K₂CO₃ etc.). [42-45] The porous carbon materials from chemical activation often show a high specific surface area (>2000 m² g⁻¹) and large pore volume. Compared with physical activation, chemical activation has several superior merits, such as lower conversion temperature, shorter activation time, higher carbon yield, larger specific surface area, and porosity.

It is noteworthy that, among various activating reagents for chemical activation, KOH is the most popular one and has been widely used since 1978, because of its lower activation temperature and higher yield. The KOH-activated carbons often exhibit well-defined pore size distribution and super-high specific surface area (up to 3000 m² g⁻¹). [46] The activation mechanism, however, is still not completely understood because of the involvement of various experimental variables and different precursors. Here, we summarize state of the art of KOH-activated carbons, with a focus on the activation mechanism. Generally, the reaction between KOH and precursors starts from a solid-solid reaction, followed by a series of solid-liquid reactions, while the potassium compound is eventually reduced to metallic potassium. The KOH activation process below 1000 K, with petroleum coke as an example, can be expressed by the following equations: [47]



In the initial stage, KOH is transformed into K₂O via the dehydration reaction under 700 K (Eq. 1) while the carbon sources are being consumed by the reaction between C and H₂O with the emission of CO₂ and H₂ (Eqs. 2 and 3). K₂CO₃ is formed via the reaction between K₂O and CO₂ (Eq. 4). When the temperature is increased to 900 K, KOH is consumed entirely by the reaction between KOH and C, leading to the formation of metallic potassium (Eq.5).



When the temperature is raised over 1000 K, the as-obtained K₂CO₃ starts to decompose to K₂O and CO₂ (Eq. 6) and completely disappears at ~1100 K. At higher temperature (over 1000 K), CO₂ is reduced to CO by consuming C (Eq. 7), while K₂CO₃ and K₂O also being reduced by C to form metallic potassium (Eqs. 8 and 9). The KOH activation appears to have three stages: (I) The

chemical reactions between potassium compounds and carbon (Eqs. 5, 8 and 9), which are also called chemical activation process, form carbon framework with porous network architecture; (II) H₂O and CO₂ are mixed up to form hot steam at high temperature (Eqs. 1, 3 and 6). This is a physical activation process, facilitating the porosity development of carbon (Eqs. 2 and 7); (III) As demonstrated in Figure 1.5b, the as-formed metallic potassium diffuses into the carbon matrix (Eqs. 5, 8 and 9), resulting in the expansion of carbon lattices.

To date, various raw materials, ranging from traditional coal, pitches, cokes, peat, lignite to renewable biomass precursors including different agricultural and forestry wastes (such as corncob, rice husks, rice straw, sawdust, nut shells, wood, and barks) have been widely used for the industrial production of activated carbons by chemical activation method. [48,49] Especially, as demonstrated in Figure 1.5c, KOH-activated porous carbons from abundant natural biomass sources, such as pig bone, fish scale, wheat flour, wheat straw, corncob, fungi, banana peel, pomelo peel gelatin, have been prepared for the energy conversion and storage application. [50-58]

1.4.3 Hydrothermal Carbonization

In nature, peat or coal are usually transformed from biological materials under a long natural chemical coaling process, which often takes place on the timescale of thousands to millions of years. Inspired by such natural “coaling process”, efforts have made to chemically imitate the carbon formation from natural biomass materials with faster chemical processes. Hydrothermal carbonization (HTC) is, in particular, a promising method for transforming cellulose into coal-like materials, which was firstly reported by Bergius in 1913 and further developed by Berl and Schmidt in 1932. [59] Recently, HTC was used to derive various carbonaceous materials from biomass materials under mild conditions at a relatively low temperature (< 500 K) with pure water solution and self-generated pressure. [60] Compared with conventional physical and chemical activation processes, hydrothermal carbonization has been recognized as an important alternative to obtain carbon materials because of its low cost, mild synthesis conditions, and environmental friendliness.

To gain a fundamental understanding of the HTC process, different carbohydrates, such as glucose, hydroxymethylfurfural (HMF), xylose, furfural, sucrose, and starch, were used to obtain carbonaceous materials under hydrothermal conditions at 180°C. [61] The chemical composition and structure of the hydrothermal carbons were analyzed by ¹³C solid-state NMR, elemental analysis and scanning electron microscopy (SEM). The gas chromatography-mass spectrometry

(GS-MS) experiments were also used to analyze the side-products and unreacted species in the residual liquid solution. It was demonstrated that all hexose sugars were finally condensed to carbonaceous materials with similar structure and same chemical composition. Further experiments showed that no matter what kind of starting materials (pure sugar or real-life biomass) used, the outcomes of the hydrothermal carbonization process turned out to be similar in terms of morphology and structure. Based on the aforementioned experiments, the basic reaction appears to have three main steps: (1) dehydration of the carbohydrate to (hydroxymethyl)furfural; (2) polymerization towards polyfurans; and (3) carbonization via further intermolecular dehydration. Finally, spherical hydrothermal carbons were obtained in the final solution when the solution color changed from brown to dark. The spherical carbons were decorated with numerous polar oxygenated functional groups, providing the possibility of further functionalization and making such materials more hydrophilic and easier dispersion in water.

HTC has been proven to be a low-cost process that derives porous carbonaceous materials directly from biomass materials. [60] However, as compared to activated carbons, the HTC derived carbonaceous materials exhibit fewer pores and low specific surface area, which is not desirable for the applications such as catalysis, adsorption or energy storage, in which controlled porosity at the nanometer-scale is preferred. Strives such as adding various templates (SPA-15) or additives (KOH) during the HTC process [62,63] have been made to improve the porosity and specific surface area of HTC-derived carbons.

1.5 Biomass-Derived Carbon Materials for Energy Storage Applications

Supercapacitors and batteries have been proven to be the most effective electrochemical energy storage devices. [64] However, as the key components in those devices, traditional electrode materials (e.g. graphite and inorganic compounds containing rare metals) are neither renewable nor sustainable. In this context, renewable biomass and their derivatives are regarded as promising alternatives to replace traditional non-sustainable electrode materials, because of their intrinsic properties and advantages, such as environment-friendliness, natural abundance, diverse structures, inherent mechanical strength, and flexibility, as well as their versatility to hybrid with other functional materials. Many efforts have been devoted to developing sustainable and high-performance electrode materials from biomass and their derivatives for energy conversion and storage devices, [19,65] especially for supercapacitors with high power density

and lithium-sulfur batteries with ultrahigh capacity. Renewable carbon materials derived from biomasses have demonstrated huge potential in improving the electrode performance for both supercapacitors and lithium-sulfur batteries. In fact, biomass-derived materials have been used as separators, binders, and electrodes for both electrochemical capacitors and lithium-ion batteries. [66] Below we present state of the art of biomass-derived carbon electrode materials for supercapacitors and lithium-sulfur batteries.

1.5.1 Biomass-Derived Carbon Materials for Supercapacitors

Supercapacitors, also called ultracapacitors or electrochemical capacitors, have emerged as promising energy storage devices for electronic devices and electric vehicles due to their excellent power density, outstanding pulse charge-discharge performance, superior lifespan, and low maintenance cost. [67] Based on charge-storage mechanisms, supercapacitors can be grouped into two main categories: (i) electrical double layer capacitors (EDLCs), where an electrostatic charge is accumulated at the electrode surface; (ii) pseudo-capacitors, where capacitance arises from the fast and reversible surface redox reactions at the characteristic potential. [68] Electrode material lies at the heart of developing high-performance supercapacitors. Carbon-based materials, transition metal oxides/hydroxides, and conducting polymers have been regarded as the most promising materials for supercapacitors. [69-72] It is noteworthy that carbon-based materials, ranging from traditionally activated carbons to advanced nanostructured carbons (such as graphene and CNTs) have been widely used for supercapacitor electrodes because of their desirable physicochemical properties, such as high specific surface area, excellent chemical stability, eminent electronic conductivity, and controllable porosity. [73] However, most of the commercial carbon electrodes are produced from fossil fuel-based precursors (e.g. petroleum coke and coal), which are expensive and nonrenewable. On the other hand, most of the nanostructured carbons are prepared under harsh and complicated conditions, such as high temperature and high vacuum, which are expensive and energy-consuming. From energy and environmental views, the development of facile and environmental benign techniques for producing carbon electrode materials is in urgent need. Efforts have been made to obtain renewable carbon materials from biomasses or their byproducts. Those biomass-derived electrode materials often show encouraging electrochemical properties, to a larger extent, comparable to activated carbons, carbon nanotubes, carbon fibers, and graphene.

Table 1.1 Summary of various biomass-derived carbon materials by different activation methods for supercapacitor application as well as their specific surface area, pore volume, and specific capacitance

<i>Ref.</i>	<i>Biomass Resources</i>	<i>Activation Method</i>	<i>Specific Surface Area (cm² g⁻¹)</i>	<i>Pore Volume (cm³ g⁻¹)</i>	<i>Electrolyte</i>	<i>High capacitance</i>
76	coffee endocarp	physical activation	1050	0.5	H ₂ SO ₄ (1 M)	176
77	rubber wood sawdust	physical activation	913	0.61	H ₂ SO ₄ (1 M)	138
78	oil palm	physical activation	1704	0.89	—	150
79	firwoods	physical activation	1016	0.747	NaNO ₃ (1 M)	105
79	pistachio shell	physical activation	1009	0.667	NaNO ₃ (1 M)	80
80	cherry stone	activation KOH a	1100-1300	—	H ₂ SO ₄ (2 M)	230
81	fish scale	KOH activation	2273	2.74	KOH (7 M)	168
82	waste paper	KOH activation	416	0.225	KOH (6 M)	160
83	water bamboo	KOH activation	2352	1.11	KOH (6 M)	268
84	yeast cell	KOH activation	—	—	KOH (1 M)	330
85	fallen leaves	KOH/K ₂ CO ₃ activation	2869	1.598	KOH (6 M)	242
86	pin-cone	KOH activation	3950	2.395	Organic	198
50	pig bone	KOH activation	2157	0.77	KOH (7 M)	185
87	willow catkins	KOH activation	1586	0.78	KOH (6 M)	253
88	celtuce leaves	KOH activation	3404	1.88	KOH (2 M)	421
89	waste tea-leaves	KOH activation	2841	1.366	KOH (2 M)	330
90	sunflower seed	KOH activation	2585	1.41	30wt.% KOH	311
91	ginkgo shells	KOH activation	1775	—	KOH (6 M)	178
92	cow dung	KOH activation	1984	0.91	Organic	124
93	silk	KOH activation	2494	2.28	Liquid ionic	242
94	human hair	KOH activation	1306	0.9	KOH (6 M)	340
95	sewage sludge	KOH activation	2839	2.65	Na ₂ SO ₄ (1 M)	379
96	wood saw dust	HTC/KOH activation	2967	1.35	TEABF ₄ (1 M)	236
97	hemicellulose	HTC/KOH activation	2200-2300	~1	H ₂ SO ₄ (0.5 M)	300
98	paper pulp	HTC/KOH activation	2980	1.75	Organic	166
99	D-glucosamine	HTC	598	0.34	H ₂ SO ₄ (1 M)	300
55	fungi	HTC	80.08	0.496	KOH (6 M)	196
100	fungus	HTC/KOH activation	1103	0.54	KOH (6 M)	360
101	bamboo waste	HTC/KOH activation	1472	—	KOH (6 M)	301
102	microalgae	HTC/KOH activation	2190	0.94	LiCl (6 M)	200
103	watermelon	HTC	—	—	KOH (6 M)	333.1
105	hemp	HTC/KOH activation	2287	1.45	liquid ionic	142
106	rice husk	Microwave/ZnCl ₂ activation	1442	0.71	KOH (6 M)	243
107	peanut shell	Microwave/ZnCl ₂ activation	1634	1.39	KOH (6 M)	245

To date, various biomass resources, including all kinds of wood and plant tissues, agricultural wastes, even industrial wastes, and municipal wastes have been used as precursor materials to prepare carbon electrodes for supercapacitors, and have gained increasing attention due to their abundant availability and low cost. [74-76] The specific surface area, pore size

distribution and final electrochemical performance of the obtained carbon materials are determined by their biomass precursors and the adopted activation techniques. Here, we summarize state of the art of the biomass-derived activated carbon materials and their applications in supercapacitors.

1.5.2 Biomass-Derived Carbon Materials for Lithium-Sulfur Battery

Lithium-sulfur battery, with an ultrahigh theoretical specific capacity of 1650 mAh g⁻¹ and an energy density up to 2600 Wh kg⁻¹, is very promising for next-generation high-energy batteries, especially for the application in fields that need higher energy deliver, such as electric vehicles, and grid-scale stationary storage. More encouragingly, sulfur, as the key component in the lithium-sulfur battery, is naturally abundant, low cost, and environmentally friendly. However, there are still some critical challenges hindering the commercialization of lithium-sulfur battery, such as low sulfur utilization, fast capacity decay, and poor cycling stability. All of the aforementioned drawbacks result from the insulating nature of sulfur, dissolution of reaction intermediates (lithium polysulfides) and large volume variation between sulfur and sulfides during the electrochemical reaction process. [108] To date, various approaches, such as developing new electrolytes, [109-111] modifying the separator, [112] protecting lithium anode, [113] as well as designing new configuration, [114,115] have been adopted to mitigate the “shuttle effect” of polysulfides and prolong cyclic life. Particularly, to improve the practical lithium-sulfur performance, many efforts have been devoted to developing advanced sulfur cathodes, including adding advanced binder or hybridizing sulfur with conductive host to improve conductivity, modifying surface chemistry or introducing metal oxides with strong adsorption to retard the dissolution of polysulfides, inserting interlayer to manipulate the “shuttle effects” of polysulfides, or designing nanostructure (yolk-shell or hollow) to accommodate the volume change during electrochemical reaction process. [116] Among various approaches, hybridizing sulfur with conductive carbon substrate to prepare C/S composite has been proven to be the most effective method. [117] To date, various carbon materials, such as microporous carbon, mesoporous carbon, hierarchical carbon with interconnected pores, graphene nanosheets, carbon nanotubes, and hollow carbon fibers, have been used to fabricate C/S composites because of their excellent conductivity, superior chemical stability, and eminent mechanical robustness. [118]. For example, L.F. Nazar *et al.* [10] used ordered mesoporous carbon (CMK-3) to encapsulate sulfur species within resident nanochannels by a melting-diffusion method, which enabled the assembled CMK-3/sulfur composite with highly improved electrochemical performance. Spherical ordered mesoporous carbon nanoparticles with

high porosity were also employed to hold sulfur for lithium-sulfur battery with high initial discharge capacity and good cyclic performance. [119] Unfortunately, the synthesis of these porous carbon materials is often expensive and difficult to scale up, which hinders their practical application. For example, ordered porous carbon materials are usually fabricated by elaborate procedures with the use of expensive templates, including energy-consuming high-temperature process and non-environmentally friendly corrosive acid treatment to remove the templates. Therefore, it is in urgent need to develop facile, low cost conductive porous carbons to host sulfur. Nature provides us with much inspiration. Since most of the biomass materials possess intriguing hierarchically porous structures, which can be used as precursors to produce porous conductive carbon materials through well-designed activation methods. These biomass-derived carbon materials with well-defined porous structures are ideal sulfur hosts. More importantly, most of the biomass precursors can be obtained from bio-wastes, which are often cheap, renewable, environmentally friendly and commercially available. Recently, many efforts have been made to design and produce hierarchically porous carbons from biomass precursors to prepare C/S composites. For lithium-sulfur battery applications, these carbon/sulfur (C/S) composites are able to manipulate “shuttle effects” for better stability, while larger pores to facilitate ion transportation for improving rate performance. To date, all kinds of biomass precursors, such as pig bone, [120] fish scales, [51] shrimp shell, [121] litchi shells, [122] olive stones, [123] cotton, [124] silk cocoon, [125] bamboo, [126] wheat straw, [127] mango stone, [128] pomelo peels, [129] banana peels, [130] gelatin, [131] cassava, [132] bark of plane trees, [133] starch, [134] have been widely explored to prepare hierarchical porous carbons by well-designed carbonization processes. All of these biomass-derived hierarchical carbons can be used as a conductive host of sulfur for lithium-sulfur battery with improved electrochemical performances. For instance, Shaochen Wei *et al.* [120] reported a unique hierarchical porous carbon derived from pig bone by KOH activation method, which demonstrated a large BET specific surface area of $2157 \text{ m}^2 \text{ g}^{-1}$ and a high pore volume of $4.18 \text{ cm}^3 \text{ g}^{-1}$. The obtained hierarchically porous C/S composite exhibited a high sulfur utilization, with a high initial capacity of 1265 mAh g^{-1} and a well-retained capacity of 643 mAh g^{-1} after 50 cycles, which was superior to that of the normal cathodes with compact structures. Table 2 presents a brief summary of various biomass-derived carbon materials via different activation methods for lithium-sulfur batteries together with their specific surface area, pore volume and cyclic performance.

Table 1.2 Summary of various biomass-derived carbon materials by different activation methods for lithium sulfur battery application as well as their specific surface area, pore volume and cyclic capacitance

Ref.	Biomass Resources	Activation Method	Specific Surface Area ($\text{cm}^2 \text{g}^{-1}$)	Pore Volume ($\text{cm}^3 \text{g}^{-1}$)	Electrolyte	Capacity
51	fish scales	KOH activation	2441	1.69	0.5 M LiTFSI (1:1 DOL:DME) 0.4 M LiNO_3	98% after
120	pig bone	KOH activation	2157	2.26	1 M LiClO_4 (2:1 DOL:DME)	50.8% after
121	shrimp shell	KOH activation	1917	0.882	1 M LiTFSI (1:1 DOL:DME) 10wt% LiNO_3	70% after
122	litchi shells	KOH activation	3164	1.88	1 M LiTFSI (1:1 DOL:DME)	51% after
123	olive stones	KOH activation	587	—	1 M LiCF_3SO_3 (1:1 DOL:DME) with LiNO_3	73% after
124	cotton	KOH activation	1286	1.15	1 M LiTFSI (1:1 DOL:DME)	74% after
125	silk cocoon	KOH activation	3243	2.1	0.5 M LiTFSI (1:1 DOL:DME) 0.1 M LiNO_3	55% after
126	bamboo	KOH/annealing	791.8	0.380	1 M LiTFSI (1:1 DOL:DME) 0.1 M LiNO_3	42% after
127	wheat straw	KOH activation	1066	0.62	1 M LiTFSI (1:1 DOL:DME) 0.1 M LiNO_3	76% after
128	mango stone	KOH activation	3334	2.17	1 M LiTFSI (1:1 DOL:DME) 1wt% LiNO_3	65% after
129	pomelo peels	KOH activation	1533	0.837	1 M LiTFSI (1:1 DOL:DME) 0.1 M LiNO_3	59% after
130	banana peels	KOH activation	2741	1.23	1 M LiTFSI (1:1 DOL:DME) 1wt% LiNO_3	66% after
131	gelatin	KOH activation	2892.6	2.80	2 M LiTFSI (1:1 DOL:DME) 0.1 M LiNO_3	47% after
132	cassava	carbonization	13.80	0.015	1 M LiTFSI (1:1 DOL:DME) 0.1 M LiNO_3	62% after
133	bark	carbonization	528	0.72	1 M LiTFSI (1:1 DOL:DME) 0.1 M LiNO_3	52% after
134	starch	carbonization	949.85	3.14	1 M LiTFSI (1:1 DOL:DME) 0.1 M LiNO_3	74% after
135	soybean	KOH activation	2690.3	1.34	1 M LiTFSI (1:1 DOL:DME) 0.1 M LiNO_3	62% after

1.6 Specific Research Objectives

In this dissertation, cotton textile, as the commonly overlooked everyday households, will be chosen as the starting precursor materials to prepare renewable flexible conductive substrates

for different energy storage systems. The primary objective is to derive flexible activated cotton textiles and use them for the design of flexible energy systems. Based on different applications and different emphases, the research objectives can be categorized into the following four aspects: (1) Design of cotton textile enabled flexible supercapacitors; (2) Design of cotton textile enabled flexible lithium-ion battery; (3) Design of cotton textile enabled flexible lithium-sulfur battery; (4) Exploration of new polysulfides trapping mechanism; (5) Development of cotton textile enabled self-sustaining solar/supercapacitor hybrid power pack.

Objective 1: Design of cotton textile enabled flexible supercapacitors

Supercapacitors (also known as ultracapacitors or electrochemical capacitors) have been regarded as one of the most promising energy storage devices due to their high-power performance, long lifespan, and low maintenance cost, which can fill the power/energy gap between the traditional capacitors (with high power density) and batteries/fuel cells (with high energy density). To date, however, textile-based energy devices are still lacking. Streamlined manufacturing processes for integrating flexible energy storage devices with wearable electronics have not been truly realized. Here, natural cotton textiles will be chosen as the precursor to prepare activated cotton textiles (ACTs) with excellent conductivity and ideal flexibility. The ACT can be used as the flexible electrode for the development of flexible supercapacitor. However, the pure ACT electrode has been suffered from its limited capacity. In order to improve the electrochemical performance of ACT-based flexible supercapacitors, high energy density metal oxide/hydroxide active materials with delicate nanostructures, including core/shell $\text{NiCo}_2\text{O}_4@ \text{NiCo}_2\text{O}_4$, and core/shell $\text{CoO}@ \text{NiO}$ will be *in-situ* decorated on the individual ACT fibers to construct high-performance flexible supercapacitors with high electrochemical performance. The relationship between microstructure and final electrochemical performance will be also explored.

Objective 2: Design of cotton textile enabled flexible lithium-ion battery

In addition to supercapacitors, lithium-ion battery is another important energy storage device, which almost revolutionized our modern society in all aspects, especially for consumer electronics and electric vehicles. In this thrust, the ACT will be explored as a flexible substrate to construct next-generation flexible lithium-ion battery. A two-step strategy will be used to deposit nanostructured NiS_2 with the bowl-like structure on ACT fibers. First, the cotton textile precursor will be soaked with $\text{Ni}(\text{NO}_3)_2$ solution. After drying and annealing, the cotton textile will be

converted to flexible conductive ACT with homogeneously distributed nickel nanoparticles (ACT/Ni). The flexible ACT/Ni will be further treated with sulfur to convert Ni nanoparticles to NiS₂ nanobowls. The whole conversion mechanism will be examined and explored. The electrochemical performances of the as-prepared flexible ACT/NiS₂ electrode will be carefully investigated. A flexible cell with ACT/NiS₂ as a flexible electrode will be assembled to demonstrate its potential for flexible lithium-ion battery application.

Objective 3: Design of cotton textile-enabled flexible lithium-sulfur battery

Lithium-sulfur (Li-S) battery is very promising for the development of next-generation high-energy battery because of its ultra-high theoretical capacity ($\sim 1650 \text{ mAh g}^{-1}$), outstanding specific energy ($\sim 2654 \text{ Wh Kg}^{-1}$), natural abundance, as well as environmental friendliness. However, Li-S battery encounters several roadblocks, including low sulfur utilization, severe capacity fading, limited lifespan and poor Coulombic efficiency, which can be ascribed to the insulating nature of sulfur and the dissolution of polysulfides. In this thrust, the flexible, conductive and porous ACT will be employed as sulfur host to fabricate ACT/S cathode for the flexible Li-S battery application. In order to mitigate the notorious “shuttle effect” of dissolvable polysulfides and improve the performance of Li-S battery, graphene oxide (GO) coating and KOH-treated porous ACT interlayer will be exploited to innovate the Li-S cell design. The flexible Li-S cell will also be assembled to expand the potential of the ACT for the design of next-generation flexible high-energy battery.

Objective 4: Exploration of new polysulfides trapping mechanism

The lithium-sulfur (Li-S) battery is a promising candidate for next-generation high-density energy storage devices because of its ultra-high theoretical energy density and the natural abundance of sulfur. However, the practical performance of sulfur cathode is plagued by fast capacity decay and poor cycle life, both of which can be attributed to the intrinsic dissolution/shuttling of lithium polysulfides. Cotton textile has been proven an excellent substrate for the design of flexible lithium-sulfur batteries. However, the 200 cycles' lifespan is not promising for practical applications. Lithium-sulfur battery is still bothered by its poor lifespan. Here, a new built-in magnetic field enhanced polysulfide trapping mechanism will be explored and validated by introducing ferromagnetic iron/iron carbide (Fe/Fe₃C) nanoparticles with a graphene shell (Fe/Fe₃C/graphene) onto a flexible activated cotton textile (ACT) fiber to prepare

the ACT@Fe/Fe₃C/graphene sulfur host. The novel trapping mechanism will be demonstrated by significant differences in the diffusion behavior of polysulfides in a custom-designed liquid cell compared to a ACT/S cathode. Furthermore, the electrochemical performances of the cell assembled using the ACT@Fe/Fe₃C/S cathode will be tested. The new magnetic field-enhanced trapping mechanism provides not only novel insight but unveils new possibilities for mitigating the “shuttle effect” of polysulfides, thereby promoting the practical applications of Li-S batteries.

Objective 5: Cotton textile-enabled self-sustaining solar/supercapacitor hybrid power pack

Solar cells hold huge promise as energy conversion devices for sustainable energy sourcing due to their utilization of readily accessible solar energy; however, the output of solar cells is non-continuous and unstable. Therefore, it is necessary to combine solar cells with compatible energy storage devices to realize a stable power output. To this end, supercapacitors, as highly efficient energy storage devices, can be integrated with solar cells to mitigate the power fluctuations. In this thrust, we will firstly focus on developing a high-performance, cotton-textile-enabled flexible supercapacitor. In order to simultaneously improve the energy density and power density of the supercapacitor, an asymmetric cell design strategy will be employed with ACT/Co-Al layered double hydroxide (ACT/Co-Al LDH) electrode as an energy source and ACT/reduced graphene oxide (ACT/rGO) electrode as a power source. A commercial flexible solar cell will be hybridized with the home-made flexible supercapacitor to construct a self-sustaining power pack via a roll-to-roll manufacturing process.

References:

- [1] Dell RM, Rand DAJ. Energy storage-A key technology for global energy sustainability. *J. Power Sources*. 2001;100:2–17.
- [2] Centi G, Perathoner S, Passalacqua R, Ampelli C. In: Muradov N Z, Veziroglu T N. Carbon-neutral fuels and energy carriers. Boca Raton: CRC Press, 2011. 291.
- [3] Grey CP, Tarascon JM. Sustainability and in situ monitoring in battery development, *Nat. Mater*. 2016;16:45–56.
- [4] Larcher D. Tarascon JM. Towards greener and more sustainable batteries for electrical energy storage, *Nat. Chem*. 2014;7:19–29.

- [5] Xu B, Qian D, Wang Z, Meng YS. Recent progress in cathode materials research for advanced lithium ion batteries, *Mater. Sci. Eng. R Reports*. 2012;73:51–65.
- [6] Zhang LL, Zhou R, Zhao XS. Graphene-based materials as supercapacitor electrodes, *J. Mater. Chem.* 2010;20:5983.
- [7] Conway BE. Electrochemical science and technology. Transition from “Supercapacitor” to “Battery” behavior in electrochemical energy storage. *J. Electrochem. Soc.* 1991;138:1539–1548.
- [5] Inagaki M, Kang FY. *Materials science and engineering of carbon: fundamentals*, Tinghua University Press, 2014.
- [6] Zhu J, Chen M, Wei H, Yerra N, Haldolarrachchige N, Luo Z, Yong D, Ho T, Wei S, Guo Z. Magnetocapacitance in magnetic microtubular carbon nanocomposites under external magnetic field. *Nano Energy*. 2014;6:180–132.
- [7] Yang C, Wei H, Guan L, Guo J, Wang Y, Yan X, Zhang X, Wei S, Guo Z. Polymer nanocomposites for energy storage, energy saving, and anticorrosion. *J. Mater. Chem. A*. 2015;3:14929–14941.
- [8] Qiu B, Wang Y, Sun D, Wang Q, Zhang X, Weeks B, O’connor R, Huang X, Wei S, Guo Z. Cr(VI) removal by magnetic carbon nanocomposites derived from cellulose at different carbonization temperatures. *J. Mater. Chem. A*. 2015;3:9817–9825.
- [9] Simon P, Gogotsi Y. Materials for electrochemical capacitors. *Nat. Mater.* 2008;7:845–854.
- [10] Nazar LF, Cuisinier M, Pang Q. Lithium-sulfur batteries. *MRS Bull.* 2014;39:436–442.
- [11] Ji X, Lee KT, Nazar LF. A highly ordered nanostructured carbon-sulphur cathode for lithium-sulphur batteries. *Nat. Mater.* 2009;8:500–506.
- [12] Song J, Gordin ML, Xu T, Chen S, Yu Z, Sohn H, Lu J, Ren Y, Duan Y, Wang D. Strong lithium polysulfide chemisorption on electroactive sites of nitrogen-doped carbon composites

- for high-performance lithium–sulfur battery cathodes. *Angew. Chemie Int. Ed.* 2015;54:4325–4329.
- [13] Wang H, Yang Y, Liang Y, Robinson JT, Li Y, Jackson A. Graphene-wrapped sulfur particles as a rechargeable lithium-sulfur battery cathode material with high capacity and cycling stability. *Nano Lett.* 2011; 11 (7): 2644–2647.
- [14] Yaman S. Pyrolysis of biomass to produce fuels and chemical feedstocks. *Energy Convers. Manag.* 2004;45:651–671.
- [15] Titirici MM, Antonietti M. Chemistry and materials options of sustainable carbon materials made by hydrothermal carbonization. *Chem. Soc. Rev.* 2010;39:103–116.
- [16] Wang J, Kaskel S. KOH activation of carbon-based materials for energy storage. *J. Mater. Chem.* 2012;22:23710.
- [17] Péan C, Merlet C, Rotenberg B, Madden PA, Taberna PL, Daffos B, Salanne M, Simon P. Hierarchically porous carbon derived from polymers and biomass: effect of interconnected pores on energy applications. *Energy Environ. Sci.* 2014;8:1576–1583.
- [18] Titirici MM, White RJ, Falco C, Sevilla M. Black perspectives for a green future: hydrothermal carbons for environment protection and energy storage. *Energy Environ. Sci.* 2012;5:6796.
- [19] Titirici MM, White RJ, Brun N, Budarin VL, Su DS, Del Monte F, Clark JH, MacLachlan MJ. Sustainable carbon materials. *Chem. Soc. Rev.* 2014;44:250–290.
- [20] Demirbaş A. Biomass resource facilities and biomass conversion processing for fuels and chemicals. *Energy Convers. Manag.* 2001;42:1357–1378.
- [21] Caputo AC, Palumbo M, Pelagagge PM, Scacchia F. Economics of biomass energy utilization in combustion and gasification plants: Effects of logistic variables. *Biomass and Bioenergy.* 2005;28:35–51. manganese acetate
- [22] Kim S, Dale BE. Life cycle assessment of various cropping systems utilized for producing biofuels: Bioethanol and biodiesel. *Biomass and Bioenergy.* 2005;29:426–439.

- [23] Sheldon RA. Green and sustainable manufacture of chemicals from biomass: state of the art. *Green Chem.* 2014;16:950–963.
- [24] Atkinson CJ, Fitzgerald JD, Hips NA. Potential mechanisms for achieving agricultural benefits from biochar application to temperate soils: A review. *Plant Soil.* 2010;337:1–18.
- [25] Ioannidou O, Zabaniotou A. Agricultural residues as precursors for activated carbon production-A review. *Renew. Sustain. Energy Rev.* 2007;11:1966–2005.
- [26] Zhou H, Fan T, Zhang D. Biotemplated materials for sustainable energy and environment: Current status and challenges. *ChemSusChem.* 2011;4:1344–1387.
- [27] Manocha S, Manocha LM, Joshi P, Patel B, Dangi G, Verma N. Activated carbon from biomass. *AIP Conf. Proc.* 2013;1538:120–123.
- [28] McKendry P. Energy production from biomass (part 2): conversion technologies. 2012;83:47–54.
- [29] Pütün AE, Özbay N, Önal EP, Pütün E. Fixed-bed pyrolysis of cotton stalk for liquid and solid products. *Fuel Process. Technol.* 2005;86:1207–1219.
- [30] Tay T, Ucar S, Karagoz S. Preparation and characterization of activated carbon from waste biomass. *J. Hazard. Mater.* 2009;165:481–485.
- [31] Marriott AS, Hunt AJ, Bergström E, Wilson K, Budarin VL, Thomas-Oates J, Clark JH, Brydson R. Investigating the structure of biomass-derived non-graphitizing mesoporous carbons by electron energy loss spectroscopy in the transmission electron microscope and X-ray photoelectron spectroscopy. *Carbon N. Y.* 2014;67:514–524.
- [32] Primo A, Atienzar P, Sanchez E, Delgado JM, García H. From biomass wastes to large-area, high-quality, N-doped graphene: catalyst-free carbonization of chitosan coatings on arbitrary substrates. *Chem. Commun.* 2012;48:9254.
- [33] Su DS. The use of natural materials in nanocarbon synthesis. *ChemSusChem.* 2009;2:1009–1020.
- [34] Su DS, Centi G. A perspective on carbon materials for future energy application. *J. Energy Chem.* 2013;22:151–173.

- [35] El-Hendawy ANA, Samra SE, Girgis BS. Adsorption characteristics of activated carbons obtained from corncobs. *Colloids Surfaces A Physicochem. Eng. Asp.* 2001;180:209–221.
- [36] Rodriguez-Reinoso F, Molina-Sabio M. Activated carbons from lignocellulosic materials by chemical and/or physical activation: an overview. *Carbon* 1992;30:1111–1118.
- [37] Zhang T, Walawender WP, Fan LT, Fan M, Daugaard D, Brown RC. Preparation of activated carbon from forest and agricultural residues through CO₂ activation. *Chem. Eng. J.* 2004;105:53–59.
- [38] Daifullah AAM, Yakout SM, Elreefy SA. Adsorption of fluoride in aqueous solutions using KMnO₄-modified activated carbon derived from steam pyrolysis of rice straw. *J. Hazard. Mater.* 2007;147:633–643.
- [39] Aworn A, Thiravetyan P, Nakbanpote W. Preparation and characteristics of agricultural waste activated carbon by physical activation having micro- and mesopores. *J. Anal. Appl. Pyrolysis.* 2008;82:279–285.
- [40] Balci S, Dogu T, Yucel H. Characterization of activated carbon produced from almond shell and hazelnut shell. *J. Chem. Technol. Biotechnol.* 1994(4);60:419–426.
- [41] Romanos J, Beckner M, Rash T, Firlej L, Kuchta B, Yu P, Suppes G, Wexler C, Pfeifer P. Nanospace engineering of KOH activated carbon. *Nanotechnology.* 2011;23:015401.
- [42] Inorganica Q, Quimica I. Preparation of activated carbon by chemical activation with ZnCl₂. *Carbon.* 1991;29(7):999–1007.
- [43] Lillo-Rodenas MA, Cazorla-Amoros D, Linares-Solano A. Understanding chemical reactions between carbons and NaOH and KOH: An insight into the chemical activation mechanism. *Carbon.* 2003;41(2):267–275.
- [44] Prahas D, Kartika Y, Indraswati N, Ismadji S. Activated carbon from jackfruit peel waste by H₃PO₄ chemical activation: Pore structure and surface chemistry characterization. *Chem. Eng. J.* 2008;140(1-3):32–42.
- [45] Hayashi J, Horikawa T, Takeda I, Muroyama K, Nasir Ani F. Preparing activated carbon from various nutshells by chemical activation with K₂CO₃. *Carbon.* 2002;40(13):2381–2386.

- [46] Wennerberg AN, O'Grady TM. U.S. Pat. 1978;4,082,694.
- [47] Otowa T, Nojima Y, Miyazaki T. Development of KOH activated high surface area carbon and its application to drinking water purification. *Carbon*. 1997;35(9):1315–1319.
- [48] Juan Y, Ke-qiang Q. Preparation of Activated Carbon by Chemical Activation under Vacuum. *Environ. Sci. Technol.* 2009;43(9):3385–3390.
- [49] Hayashi J, Kazehaya A, Muroyama K, Watkinson AP. Preparation of activated carbon from lignin by chemical activation. *Carbon*. 2000;38(13):1873–1878.
- [50] Huang W, Zhang H, Huang Y, Wang W, Wei S. Hierarchical porous carbon obtained from animal bone and evaluation in electric double-layer capacitors. *Carbon*. 2011;49(3):838–843.
- [51] Zhao S, Li C, Wang W, Zhang H, Gao M, Xiong X, Wang A, Yuan K, Huang Y, Wang F. A novel porous nanocomposite of sulfur/carbon obtained from fish scales for lithium–sulfur batteries. *J. Mater. Chem. A*. 2013;1:3334–3339.
- [52] Wu X, Jiang L, Long C, Fan Z. From flour to honeycomb-like carbon foam: Carbon makes room for high energy density supercapacitors. *Nano Energy*. 2015;13:527–536.
- [53] Li X, Han C, Chen X, Shi C. Preparation and performance of straw based activated carbon for supercapacitor in non-aqueous electrolytes. *Microporous Mesoporous Mater.* 2010;131(1-3):303–309.
- [54] Qu WH, Xu YY, Lu AH, Zhang XQ, Li WC. Converting biowaste corncob residue into high value added porous carbon for supercapacitor electrodes. *Bioresour. Technol.* 2015;189:285–291.
- [55] Zhu H, Wang X, Yang F, Yang X. Promising carbons for supercapacitors derived from fungi. *Adv. Mater.* 2011;23(24):2745–2748.
- [56] Wang H, Li Z, Mitlin D. Tailoring biomass-derived carbon nanoarchitectures for high-performance supercapacitors. *ChemElectroChem*. 2014;1(2):332–337.
- [57] Liang Q, Ye L, Huang Z-H, Xu Q, Bai Y, Kang F, Yang QH. A honeycomb-like porous carbon derived from pomelo peel for use in high-performance supercapacitors. *Nanoscale*. 2014;6:13831–13837.

- [58] Xu B, Hou S, Cao G, Wu F, Yang Y. Sustainable nitrogen-doped porous carbon with high surface areas prepared from gelatin for supercapacitors. *J. Mater. Chem.* 2012;22:19088–19093.
- [59] Berl E, and Schmidt A, Über die Entstehung der Kohlen. II. Die inkohlung von cellulose und lignin in neutralem medium. *Justus Liebigs Ann. Chem.* 1932; 493:97-123.
- [60] Hu B, Wang K, Wu L, Yu SH, Antonietti M, Titirici MM. Engineering carbon materials from the hydrothermal carbonization process of biomass. *Adv. Mater.* 2010;22(7):813–828.
- [61] Titirici MM, Antonietti M, Baccile N. Hydrothermal carbon from biomass: a comparison of the local structure from poly- to monosaccharides and pentoses/hexoses. *Green Chem.* 2008;10:1204–1212.
- [62] Titirici MM, Thomas A, Antonietti M. Replication and coating of silica templates by hydrothermal carbonization. *Adv. Funct. Mater.* 2007;17(6):1010–1018.
- [63] Sevilla M, Fuertes a. B, Mokaya R. High density hydrogen storage in superactivated carbons from hydrothermally carbonized renewable organic materials. *Energy Environ. Sci.* 2011;4:1400-1410.
- [64] Larcher D, Tarascon JM. Towards greener and more sustainable batteries for electrical energy storage. *Nat. Chem.* 2015;7:19-29.
- [65] Abioye AM, Ani FN, Nasir F. Recent development in the production of activated carbon electrodes from agricultural waste biomass for supercapacitors: A review. *Renew. Sustain. Energy Rev.* 2015;52:1282–1293.
- [66] Zhang L, Liu Z, Cui G, Chen L. Biomass-derived materials for electrochemical energy storages. *Prog. Polym. Sci.* [Internet]. Elsevier Ltd; 2014;43:136–164.
- [67] Gao Z, Wang J, Li Z, Yang W, Wang B, Hou M, He Y, Liu Q, Mann T, Yang P, Zhang M, Liu L. Graphene nanosheet/Ni²⁺/Al³⁺ layered double-hydroxide composite as a novel electrode for a supercapacitor. *Chem. Mater.* 2011;23(15):3509–3516.

- [68] Wang J, Gao Z, Li Z, Wang B, Yan Y, Liu Q, Mann T, Zhang M, Jiang Z. Green synthesis of graphene nanosheets/ZnO composites and electrochemical properties. *J. Solid State Chem.* 2011;184:1421–1427.
- [69] Wang G, Zhang L, Zhang J. A review of electrode materials for electrochemical supercapacitors. *Chem. Soc. Rev.* 2012;41:797-828.
- [70] Yang W, Gao Z, Ma J, Zhang X, Wang J. Controlled synthesis of Co_3O_4 and $\text{Co}_3\text{O}_4@\text{MnO}_2$ nanoarchitectures and their electrochemical capacitor application. *J. Alloys Compd.* 2014;611:171–178.
- [71] Gao Z, Yang W, Yan Y, Wang J, Ma J, Zhang X, Xing B, Liu L. Synthesis and exfoliation of layered $\alpha\text{-Co}(\text{OH})_2$ nanosheets and their electrochemical performance for supercapacitors. *Eur. J. Inorg. Chem.* 2013;4832–4838.
- [72] Yang W, Gao Z, Song N, Zhang Y, Yang Y. Synthesis of hollow polyaniline nano-capsules and their supercapacitor application. *J. Power Sources.* 2014;272:915–921.
- [73] Yang Z, Ren J, Zhang Z, Chen X, Guan G, Qiu L, Zhang Y, Peng H. Recent Advancement of Nanostructured Carbon for Energy Applications. *Chem. Rev.* 2015;115(11):5159-5223.
- [74] Zhi M, Yang F, Meng F, Li M, Manivannan A, Wu N. Effects of pore structure on performance of an activated-carbon supercapacitor electrode recycled from scrap waste tires. *ACS Sustain. Chem. Eng.* 2014;2(7):1592–1598.
- [75] Ab DA, Hegde G. Activated carbon nanospheres derived from bio- waste materials for supercapacitor applications – a review. *RSC Adv.* 2015;5:88339–88352.
- [76] Valente Nabais JM, Teixeira JG, Almeida I. Development of easy made low cost binderless monolithic electrodes from biomass with controlled properties to be used as electrochemical capacitors. *Bioresour. Technol.* 2011;102(3):2781–2787.
- [77] Taer E, Deraman M, Talib IA, Awitdrus A, Hashmi SA, Umar AA. Preparation of a highly porous binderless activated carbon monolith from rubber wood sawdust by a multi-step activation process for application in supercapacitors. *Int. J. Electrochem. Sci.* 2011;6:3301–3315.

- [78] Farma R, Deraman M, Awitdrus A, Talib IA, Taer E, Basri NH, Manjunatha JG, Ishak MM, Dollah BNM, Hashmi SA. Preparation of highly porous binderless activated carbon electrodes from fibres of oil palm empty fruit bunches for application in supercapacitors. *Bioresour. Technol.* 2013;132:254–261.
- [79] Wu FC, Tseng RL, Hu CC, Wang CC. Effects of pore structure and electrolyte on the capacitive characteristics of steam- and KOH-activated carbons for supercapacitors. *J. Power Sources.* 2005;144(1):302–309.
- [80] Olivares-Marin M, Fernandez JA, Lazaro MJ, Fernandez-Gonzalez C, Macias-Garcia A, Gomez-Serrano V, Stoeckli F, Centeno TA. Cherry stones as precursor of activated carbons for supercapacitors. *Mater. Chem. Phys.* 2009;114(1):323–327.
- [81] Chen W, Zhang H, Huang Y, Wang W. A fish scale based hierarchical lamellar porous carbon material obtained using a natural template for high performance electrochemical capacitors. *J. Mater. Chem.* 2010;20:4773-4775.
- [82] Kalpana D, Cho SH, Lee SB, Lee YS, Misra R, Renganathan NG. Recycled waste paper-A new source of raw material for electric double-layer capacitors. *J. Power Sources.* 2009;190(2):587–591.
- [83] Li J, Wu Q. Water bamboo-derived porous carbons as electrode materials for supercapacitors. *New J. Chem.* 2015;39:3859–3864.
- [84] Sun H, He W, Zong C, Lu L. Template-free synthesis of renewable macroporous carbon via yeast cells for high-performance supercapacitor electrode materials. *ACS Appl. Mater. Interfaces.* 2013;5(6):2261–2268.
- [85] Li YT, Pi YT, Lu LM, Xu SH, Ren TZ. Hierarchical porous active carbon from fallen leaves by synergy of K_2CO_3 and their supercapacitor performance. *J. Power Sources.* 2015;299(20):519–528.
- [86] Karthikeyan K, Amaresh S, Lee SN, Sun X, Aravindan V, Lee YG, Lee YS. Construction of high-energy-density supercapacitors from pine-cone-derived high-surface-area carbons. *ChemSusChem.* 2014;7(5):1435–1442.

- [87] Wang K, Zhao N, Lei S, Yan R, Tian X, Wang J, Song Y, Xu D, Guo Q, Liu L. Promising biomass-based activated carbons derived from willow catkins for high performance supercapacitors. *Electrochim. Acta.* 2015;166:1–11.
- [88] Wang R, Wang P, Yan X, Lang J, Peng C, Xue Q. Promising porous carbon derived from celtuce leaves with outstanding supercapacitance and CO₂ capture performance. *ACS Appl. Mater. Interfaces.* 2012;4(11):5800–5806.
- [89] Peng C, Yan X Bin, Wang RT, Lang JW, Ou YJ, Xue QJ. Promising activated carbons derived from waste tea-leaves and their application in high performance supercapacitors electrodes. *Electrochim. Acta.* 2013;87:401–408.
- [90] Li X, Xing W, Zhuo S, Zhou J, Li F, Qiao SZ, Lu GQ. Preparation of capacitor's electrode from sunflower seed shell. *Bioresour. Technol.* 2011;102(2):1118–1123.
- [91] Jiang L, Yan J, Hao L, Xue R, Sun G, Yi B. High rate performance activated carbons prepared from ginkgo shells for electrochemical supercapacitors. *Carbon.* 2013;56:146–154.
- [92] Bhattacharjya D, Yu JS. Activated carbon made from cow dung as electrode material for electrochemical double layer capacitor. *J. Power Sources.* 2014;262(15):224–231.
- [93] Hou J, Cao C, Idrees F, Ma X. Hierarchical porous nitrogen-doped carbon nanosheets derived from silk for ultrahigh-capacity battery anodes and supercapacitors. *ACS Nano.* 2015;9:2556–2564.
- [94] Qian W, Sun F, Xu Y, Qiu L, Liu C, Wang S, Yan F. Human hair-derived carbon flakes for electrochemical supercapacitors. *Energy Environ. Sci.* 2014;7:379–386.
- [95] Feng H, Zheng M, Dong H, Xiao Y, Hu H, Sun Z, Long C, Cai Y, Zhao X, Zhang H, Lei B, Liu Y. Three-dimensional honeycomb-like hierarchically structured carbon for high-performance supercapacitors derived from high-ash-content sewage sludge. *J. Mater. Chem. A.* 2015;3:15225–15234.
- [96] Wei L, Sevilla M, Fuertes AB, Mokaya R, Yushin G. Hydrothermal carbonization of abundant renewable natural organic chemicals for high-performance supercapacitor electrodes. *Adv. Energy Mater.* 2011;1:356–361.

- [97] Falco C, Sieben JM, Brun N, Sevilla M, Van Der Maelen T, Morallon E, Cazorla-Amoros D, Titirici MM. Hydrothermal carbons from hemicellulose-derived aqueous hydrolysis products as electrode materials for supercapacitors. *ChemSusChem*. 2013;6:374–382.
- [98] Wang H, Li Z, Tak JK, Holt CMB, Tan X, Xu Z, Amirkhiz BS, Harfield D, Anyia A, Stephenson T, Mitlin D. Supercapacitors based on carbons with tuned porosity derived from paper pulp mill sludge biowaste. *Carbon N. Y.* 2013;57:317–328.
- [99] Zhao L, Fan LZ, Zhou MQ, Guan H, Qiao S, Antonietti M, Titirici MM. Nitrogen-containing hydrothermal carbons with superior performance in supercapacitors. *Adv. Mater.* 2010;22:5202–5206.
- [100] Long C, Chen X, Jiang L, Zhi L, Fan Z. Porous layer-stacking carbon derived from in-built template in biomass for high volumetric performance supercapacitors. *Nano Energy*. 2015;12:141–151.
- [101] Tian W, Gao Q, Tan Y, Yang K, Zhu L, Yang C, Zhang H. Bio-inspired beehive-like hierarchical nanoporous carbon derived from bamboo-based industrial by-product as a high performance supercapacitor electrode material. *J. Mater. Chem. A*. 2015;3:5656–5664.
- [102] Sevilla M, Gu W, Falco C, Titirici MM, Fuertes AB, Yushin G. Hydrothermal synthesis of microalgae-derived microporous carbons for electrochemical capacitors. *J. Power Sources*. 2014;267:26–32.
- [103] Wu XL, Wen T, Guo HL, Yang S, Wang X, Xu AW. Biomass-derived sponge-like carbonaceous hydrogels and aerogels for supercapacitors. *ACS nano*. 2013;7(4):3589–97.
- [104] Wang H, Xu Z, Kohandehghan A, Li Z, Cui K, Tan X, Stephenson TJ, King’Ondu CK, Holt CMB, Olsen BC, Tak JK, Harfield D, Anyia AO, Mitlin D. Interconnected carbon nanosheets derived from hemp for ultrafast supercapacitors with high energy. *ACS Nano*. 2013;7:5131–5141.
- [105] Xin-hui D, Srinivasakannan C, Jin-hui P, Li-bo Z, Zheng-yong Z. Comparison of activated carbon prepared from *Jatropha* hull by conventional heating and microwave heating. *Biomass Bioenergy*. 2011;35:3920–3926.

- [106] He X, Ling P, Yu M, Wang X, Zhang X, Zheng M. Rice husk-derived porous carbons with high capacitance by ZnCl₂ activation for supercapacitors. *Electrochim. Acta.* 2013;105:635–641.
- [107] He X, Ling P, Qiu J, Yu M, Zhang X, Yu C, Zheng M. Efficient preparation of biomass-based mesoporous carbons for supercapacitors with both high energy density and high power density. *J. Power Sources.* 2013;240:109–113.
- [108] Manthiram A, Fu Y, Chung S, Zu C, Su Y. Rechargeable lithium – sulfur batteries. *Chem. Rev.* 2014;114(23):11751-11787.
- [109] Suo L, Hu Y-S, Li H, Armand M, Chen L. A new class of Solvent-in-Salt electrolyte for high-energy rechargeable metallic lithium batteries. *Nat. Commun.* 2013;4:1481.
- [110] Lin Z, Liu Z, Fu W, Dudney NJ, Liang C. Phosphorous pentasulfide as a novel additive for high-performance lithium-sulfur batteries. *Adv. Funct. Mater.* 2013;23:1064–1069.
- [111] Hassoun J, Scrosati B. Moving to a solid-state configuration: A valid approach to making lithium-sulfur batteries viable for practical applications. *Adv. Mater.* 2010;22:5198–5201.
- [112] Huang J-Q, Zhang Q, Peng H-J, Liu X-Y, Qian W-Z, Wei F. Ionic shield for polysulfides towards highly-stable lithium–sulfur batteries. *Energy Environ. Sci.* 2014;7:347.
- [113] Huang C, Xiao J, Shao Y, Zheng J, Bennett WD, Lu D, Laxmikant S V., Engelhard M, Ji L, Zhang J, Li X, Graff GL, Liu J. Manipulating surface reactions in lithium–sulphur batteries using hybrid anode structures. *Nat. Commun.* 2014;5:1–7.
- [114] Su Y-S, Manthiram A. Lithium–sulphur batteries with a microporous carbon paper as a bifunctional interlayer. *Nat. Commun.* 2012;3:1166.
- [115] Zhou G, Pei S, Li L, Wang D-W, Wang S, Huang K, Yin L-C, Li F, Cheng H-M. A graphene-pure-sulfur sandwich structure for ultrafast, long-life lithium-sulfur batteries. *Adv. Mater.* 2014;26:625–631.
- [116] Manthiram A, Chung S-H, Zu C. Lithium-sulfur batteries: progress and prospects. *Adv. Mater.* 2015; 27(12):1980-2006.

- [117] Li Z, Huang Y, Yuan L, Hao Z, Huang Y. Status and prospects in sulfur-carbon composites as cathode materials for rechargeable lithium-sulfur batteries. *Carbon N. Y.* 2015;92:41–63.
- [118] Wang D-W, Zeng Q, Zhou G, Yin L, Li F, Cheng H-M, Gentle IR, Lu GQM. Carbon-sulfur composites for Li-S batteries: status and prospects. *J. Mater. Chem. A.* 2013;1:9382.
- [119] Schuster J, He G, Mandlmeier B, Yim T, Lee KT, Bein T, Nazar LF. Spherical ordered mesoporous carbon nanoparticles with high porosity for lithium-sulfur batteries. *Angew. Chemie Int. Ed.* 2012;51:3591–3595.
- [120] Wei S, Zhang H, Huang Y, Wang W, Xia Y, Yu Z. Pig bone derived hierarchical porous carbon and its enhanced cycling performance of lithium-sulfur batteries. *Energy Environ. Sci.* 2011;4:736.
- [121] Qu J, Lv S, Peng X, Tian S, Wang J, Gao F. Nitrogen-doped porous “green carbon” derived from shrimp shell: Combined effects of pore sizes and nitrogen doping on the performance of lithium sulfur battery. *J. Alloys Compd.* 2016;671:17–23.
- [122] Zhang S, Zheng M, Lin Z, Li N, Liu Y, Zhao B, Pang H, Cao J, He P, Shi Y. Activated carbon with ultrahigh specific surface area synthesized from natural plant material for lithium-sulfur batteries. *J. Mater. Chem. A.* 2014;2:15889–15896.
- [123] Moreno N, Caballero A, Hernán L, Morales J. Lithium-sulfur batteries with activated carbons derived from olive stones. *Carbon N. Y.* 2014;70:241–248.
- [124] Wang H, Chen Z, Liu HK, Guo Z. A facile synthesis approach to micro-macroporous carbon from cotton and its application in the lithium-sulfur battery. *Rsc Adv.* 2014;4:65074–65080.
- [125] Zhang B, Xiao M, Wang S, Han D, Song S, Chen G, Meng Y. Novel hierarchically porous carbon materials obtained from natural biopolymer as host matrixes for lithium-sulfur battery applications. *ACS Appl. Mater. Interfaces.* 2014;6:13174–13182.
- [126] Gu X, Wang Y, Lai C, Qiu J, Li S, Hou Y, Martens W, Mahmood N, Zhang S. Microporous bamboo biochar for lithium-sulfur batteries. *Nano Res.* 2014;8:129–139.
- [127] Cheng Y, Ji S, Xu X, Liu J. Wheat straw carbon matrix wrapped sulfur composites as a superior cathode for Li-S batteries. *RSC Adv.* 2015;5:100089–100096.

- [128] Zhang S, Zheng M, Lin Z, Zang R, Huang Q, Xue H, Cao J, Pang H. Mango stone-derived activated carbon with high sulfur loading as a cathode material for lithium–sulfur batteries. *RSC Adv.* 2016;6:39918–39925.
- [129] Zhang J, Xiang J, Dong Z, Liu Y, Wu Y, Xu C, Du G. Biomass derived activated carbon with 3D connected architecture for rechargeable lithium - sulfur batteries. *Electrochim. Acta.* 2014;116:146–151.
- [130] Yang K, Gao Q, Tan Y, Tian W, Qian W, Zhu L, Yang C. Biomass-derived porous carbon with micropores and small mesopores for high-performance lithium-sulfur batteries. *Chem. - A Eur. J.* 2016;22:3239–3244.
- [131] Qu Y, Zhang Z, Zhang X, Ren G, Lai Y, Liu Y, Li J. Highly ordered nitrogen-rich mesoporous carbon derived from biomass waste for high-performance lithium-sulfur batteries. *Carbon N. Y.* 2015;84:399–408.
- [132] Qin F, Zhang K, Fang J, Lai Y, Li Q, Zhang Z, Li J. High performance lithium sulfur batteries with a cassava-derived carbon sheet as a polysulfides inhibitor. *New J. Chem.* 2014;38:4549–4554.
- [133] Xu J, Zhou K, Chen F, Chen W, Wei X, Liu X-W, Liu J. Natural integrated carbon architecture for rechargeable lithium–sulfur batteries. *ACS Sustain. Chem. Eng.* 2016;4:666–670.
- [134] Li J, Qin F, Zhang L, Zhang K, Li Q, Lai Y, Zhang Z, Fang J. Mesoporous carbon from biomass: one-pot synthesis and application for Li–S batteries. *J. Mater. Chem. A.* 2014;2:13916.
- [135] Li Q, Zhang Z, Guo Z, Lai Y, Zhang K, Li J. Improved cyclability of lithium-sulfur battery cathode using encapsulated sulfur in hollow carbon nanofiber@nitrogen-doped porous carbon core-shell composite. *Carbon N. Y.* 2014;78:1–9.

Chapter 2. Cotton Textile-Enabled Flexible Symmetric Supercapacitors

2.1 Introduction

In modern society, energy is the lifeblood. To solve the issues of global warming, environmental pollution, and the depletion of fossil-fuel, a worldwide imperative is to make the use of sustainable and renewable energy. Numerous energy storage solutions, for instance, mechanical, magnetic and chemical storage, are being intensively investigated to harvest renewable energies, such as solar, wind, geothermal and tidal energy. [1] Batteries, fuel cells, and electrochemical capacitors that can convert chemical energy directly into electrical energy are the most effective technologies for practical electrochemical energy storage and conversion. Recently, supercapacitors (also known as ultracapacitors or electrochemical capacitors) have been regarded as one of the most promising energy storage devices due to their high-power performance, long lifespan, and low maintenance cost. [2] Most importantly, supercapacitors fill the power/energy gap between the traditional capacitors (with higher power density) and batteries/fuel cells (with higher energy density), [3] and have shown a great potential in transportation, electrical power, electronics, and aviation. Much effort has been devoted to developing lightweight, flexible, and highly efficient power devices to meet the urgent need of flexible/wearable electronics, such as flexible cell phones, roll-up, and bendable displays, photovoltaic cells, artificial electronics skin, and distributed sensors. [4]

However, previous research was mainly focused on the aqueous solution, organic solution or ionic liquids, which usually brought serious package and safety problem. [5-8] The possible leakage of highly toxic or corrosive electrolyte impedes its practical application in portable/wearable electronics. [9] Solid-state supercapacitors, because of their combined advantages, such as small size, ease of handling, robust mechanical performance, excellent reliability and safety, wide operation temperature range and extended working potential, have attracted more and more attention. [4] Flexible solid-state supercapacitors usually consist of flexible electrodes, solid-state electrolyte, flexible separator, and packaging material. As the most crucial functional blocks, flexible electrodes

have attracted considerable attention. For instance, carbon materials, such as carbon nanotubes (CNTs), carbon cloth, graphene papers, and carbon fibers, have been intensively investigated as the flexible electrodes due to their higher power density, longer life cycle, outstanding mechanical robustness, and excellent electrical conductivity. [10-14] However, the use of expensive CNTs or graphene to construct flexible electrodes will increase the cost of the device. Another drawback of using CNTs or graphene is their relatively low energy density. These two factors more or less hinder its widespread commercialization.

It is imperative to develop wearable energy storage systems for future flexible electronics. To date, however, textile-based energy devices are still lacking. Streamlined manufacturing processes for integrating flexible energy storage devices with wearable electronics have not been truly realized. [15] Cotton textiles are the most widely used natural fibers for soft and breathable clothing. In our previous work, we have successfully converted a commercial cotton T-shirt into activated carbon textiles (ACTs) with high conductivity and flexibility for flexible energy storage application. [16] By integrating ACTs with MnO_2 , the textile-based flexible supercapacitors exhibited remarkably enhanced electrochemical performance. To further improve the electrochemical performance of carbon-based supercapacitors, pseudocapacitive materials (MnO_2 , [17,18] NiCo_2O_4 , [19] Co_3O_4 , [20] NiO , [21] LDH [22] and conducting polymer [23,24]) have been used to decorate the surfaces of carbon materials. However, due to the poor conductivity and short ion diffusion path of pseudo-capacitive materials, the electrochemical reaction process happens only on the very surface layer of the electrode, which limits the contribution of the inner active materials to the total capacitance. [25] To make full utilization of pseudocapacitive materials, an intelligent strategy is to compound two types of materials or nanostructures on one conductive substrate with integrated hierarchical architectures, which fully exploit the potential of individual materials and bring together many competitive advantages, such as rich electroactive sites, easy accessibility of electrolyte ions, short diffusion path, superior current collection efficiency and the fascinating synergetic effect of different components. [26-29] For example, Guan *et al.* [30] reported enhanced electrochemical performance (areal capacitance of 2.04 F/cm^2 at the scan rate of 5 mV/s) from hierarchical $\text{Co}_3\text{O}_4@ \text{NiCo}_2\text{O}_4$ nanoforest on Ni-foam. Daoping *et al.* [31] achieved a specific capacitance of 14.67 F/cm^2 from

NiCo₂O₄@CoMoO₄ core/shell nanowire arrays. Yu *et al.* [32] demonstrated that NiCo₂O₄@MnO₂ core/shell pseudocapacitors achieved a specific capacitance of 1.66 F/cm². Recently we fabricated Zn₂SnO₄/MnO₂ core/shell nanocables on carbon microfibers and NiCo₂O₄@NiO core/shell nanostructure on carbon cloth for high-performance flexible electrodes. [33,34] The drawback of the aforementioned core/shell structure is the high contact resistance between the core and shell which are dissimilar materials. It remains a great challenge to synthesize core/shell nanostructures of the same material due to the difficulties in controlling the assembly and fusion of the core and the shell with pre-designed morphologies. [35] Recently, ternary nickel cobaltite (NiCo₂O₄) has been intensively studied as a high-performance electrode material for supercapacitors due to the exceptional combination of its high electrical conductivity and electrochemical activity. Several types of NiCo₂O₄ nanostructures including 1D nanowire, [36] 2D nanosheet [37] and 3D urchin-like microsphere [38] have shown great promise for supercapacitor applications. Although the capacitive performance of various nanostructures has been intensively investigated, there are rare reports about the integration of hierarchical nanostructures comprised of the same material with different morphologies.

In this study, we synthesized hierarchical NiCo₂O₄@NiCo₂O₄ core/shell nanostructure on highly flexible and conductive activated carbon textiles (ACTs) which were converted directly from cotton textiles. The conductive NiCo₂O₄ nanowires, radially anchored on the ACT fibers, served as cores (backbones) to support the NiCo₂O₄ nanoflake shells to form a hierarchical 3D porous nanostructure of the same material. Such scaffold-like porous architecture served as a reservoir for electrolyte ions, providing a highly electrolytic accessible surface area, robust electrical connection to substrate and short ion diffusion path. The nanowire core and nanoflake shell are of the same material, thereby eliminating the contact resistance between the core and the shell, enabling a fast-reversible Faradaic reaction and full utilization of active materials during the charge-discharge process. After dipped in polyvinyl alcohol (PVA)/KOH solid-state electrolyte, the interspace of the NiCo₂O₄@NiCo₂O₄ core/shell scaffold-like architecture was completely filled with gel electrolyte which concurrently served as a separator, not only improving the accessibility of electrolyte ions but also intensifying the mechanical strength of the flexible electrode. The fabricated flexible NiCo₂O₄@NiCo₂O₄/ACT hybrid electrode achieved an exceptional combination of electrochemical and mechanical properties in terms of specific capacitance (1929

F/g), energy density (83.6 Wh/kg), power density (8.4 KW/kg), cycling stability, and mechanical robustness (the tensile strength is 6.4 times higher than that of pure ACT). Such hierarchical core/shell nanostructure of the same material on the cotton-enabled flexible substrate should inspire us to develop flexible solid-state textile energy storage devices for future wearable electronics.

2.2 Experimental Section

2.2.1 Preparation of Flexible NiCo₂O₄@NiCo₂O₄/ACT Electrode Activation of cotton textile

All the chemicals were of analytical grade (purchased from Sigma) and used without further purification. A commercial cotton T-shirt was cleaned in distilled water prior to activation. Activation of cotton T-shirt textile was performed following the previous report. [16] Briefly, a piece of the pure cotton T-shirt was firstly dipped into 1 M NaF solution and kept for 1 h. The dipped textile was then dried at 120 °C for 3 h. Finally, the dried, NaF-treated cotton textile was inserted into a horizontal tube furnace and heated at 1000 °C for 1 h with a continuous argon gas flow. After cooling down to room temperature, the as-obtained activated cotton textiles were washed with distilled water to remove the residual NaF and then dried at 80 °C for 6 h.

2.2.2 Fabrication of NiCo₂O₄ nanowires on activated cotton textiles

NiCo₂O₄ nanowires were radically grown on the ACT fibers via a simple hydrothermal process. Typically, 1.45 g of Ni(NO₃)₂·6H₂O, 2.91 g of Co(NO₃)₂·6H₂O, and 0.9 g of urea were dissolved in 70 mL of distilled water to form a pink-color solution. Then, the solution was transferred into a 100 mL Teflon-lined stainless autoclave with a piece of ACT (1 cm × 2 cm) vertically suspended in the solution. After that, the autoclave was kept at 120 °C in an electric oven for 12 h. Finally, the as-synthesized products were taken out, washed with ethanol and distilled water for several times, dried at 80 °C overnight, and annealed at 400 °C in argon atmosphere for 2 h to produce NiCo₂O₄ nanowire/ACT. The mass loading of NiCo₂O₄ nanowires on activated carbon textiles was measured to be 2.12 mg/cm².

2.2.3 Coating NiCo₂O₄ nanoflakes onto NiCo₂O₄ nanowires

The shell layer of NiCo₂O₄ nanoflakes was prepared by a simple chemical bath deposition process. [39] Typically, 2 mL of aqueous ammonia (25-28%) was added to the mixture of 5 mL of 1 M nickel sulfate, 5 mL of 2 M cobalt nitrate, and 8 mL of 0.25 M potassium persulfate to form chemical bath deposition solution. After that, the obtained NiCo₂O₄ nanowire/ACT was vertically placed in the fresh, chemical bath deposition solution and kept for 10 min at room temperature for coating the Ni-Co hydroxide precursor shell. After the deposition, the sample was rinsed with distilled water and then dried at 80 °C for 12 h in an electric oven. Finally, the obtained hybrid was further annealed at 400 °C under argon protection for 2 h to obtain the flexible NiCo₂O₄@NiCo₂O₄/ACT electrode. The mass loading of NiCo₂O₄@NiCo₂O₄ on activated carbon textiles was measured to be 2.63 mg/cm².

2.2.4 Characterization Methods

The crystallographic structure of the synthesized materials was determined by a PANalytical X'Pert Pro Multi-Purpose Diffractometer (MPD) equipped with Cu K_α radiation ($\lambda = 0.15406$ nm). The microstructure of the samples was characterized by scanning electron microscopy (SEM; FEI Quanta 650) and transmission electron microscopy (TEM; Philips CM 200 FEG, 160 kV). X-ray photoelectron spectroscopy (XPS) measurements were performed using a PHI 5700 ESCA spectrometer with monochromated Al KR radiation ($h\nu = 1486.6$ eV). All the XPS spectra were corrected by the C1s line at 284.5 eV.

2.2.5 Fabrication and Electrochemical Characterization of Flexible All-Solid-State Supercapacitors

The flexible supercapacitors were assembled with two pieces of flexible electrodes (2 cm × 1 cm) face-to-face separated by the solid-state polymer electrolyte. The PVA/KOH gel was prepared by mixing 3 g KOH and 6 g PVA in 60 mL deionized water and heated to 80 °C under stirring until the solution became clear. A flat Petridish was used to prepare a thin KOH/PVA film by a natural solidification process. Prior to assembly, the fabricated flexible electrodes were first dipped into the gel electrolyte for 3 min to ensure that the internal interspace of active materials was completely filled with the electrolyte. After

solidified at room temperature, the solid-state flexible supercapacitor was fabricated with a KOH/PVA film by mechanical pressing. The KOH/PVA film served as both the separator and electrolyte.

The electrochemical characterization was carried out using a CHI 660E electrochemical workstation. The comprehensive electrochemical properties of the as-obtained products and assembled flexible supercapacitors were investigated by both three-electrode and two-electrode electrochemical systems. For the three-electrode system, ACT, NiCo₂O₄ nanowire/ACT, and NiCo₂O₄@NiCo₂O₄/ACT electrodes were directly used as the working electrode, a platinum foil (1 cm × 1 cm) and a saturated calomel electrode (SCE) were used as the counter and reference electrodes, respectively. The three-electrode tests were carried out in 6 M KOH aqueous electrolyte at room temperature. Cyclic voltammograms (CV), galvanostatic charge/discharge curves, and electrochemical impedance spectroscopy (EIS) in the frequency range from 100 kHz to 0.05 Hz with an AC perturbation of 5 mV were used to evaluate the electrochemical performance of the flexible electrode. Asymmetric and symmetric flexible cells were also assembled by using ACT, NiCo₂O₄ nanowire/ACT, and NiCo₂O₄@NiCo₂O₄/ACT as the flexible electrodes, conductive copper tape attached on the PET film as current collectors, and the as-made solid-state polymer PVA/KOH gel film served as both the separator and electrolyte sandwiched between the two electrodes. The total electrode masses (including ACT) are 11.12 mg and 10.71 mg for the symmetric and asymmetric supercapacitors, respectively.

2.3 Results and Discussion

2.3.1 Structural and Morphological Characterization

Figure 2.1 shows the design wisdom and fabrication procedure of hierarchical NiCo₂O₄@NiCo₂O₄ core/shell nanostructure on ACTs. In a typical experiment, NiCo₂O₄ nanowire arrays were first radially grown on ACT fibers using a facile hydrothermal method, followed by a calcination process under argon protection (Step i). The hydrothermally synthesized NiCo₂O₄ nanowire arrays then served as the backbone for the deposition of NiCo₂O₄ nanoflakes by a chemical bath deposition method (Step ii). Such a hierarchical nanostructure (NiCo₂O₄ nanowire core/NiCo₂O₄ nanoflake shell) on conductive ACTs provides plenty of interspaces, which not only increase electrolyte ion

accessibility but also short the transport path, jointly improving the electrochemical performance.

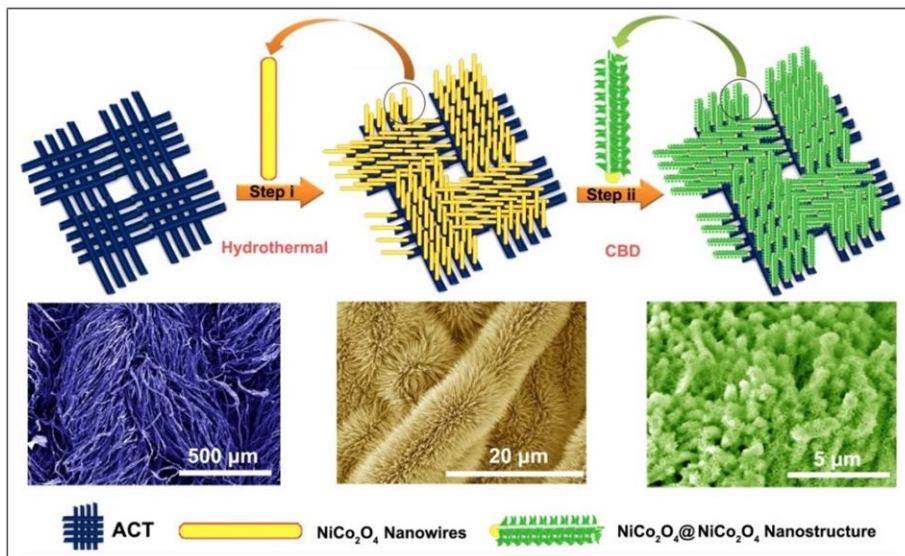


Figure 2.1 Illustration of the fabrication process of hierarchical $\text{NiCo}_2\text{O}_4@/\text{NiCo}_2\text{O}_4$ core/shell nanostructure on activated carbon textiles (ACTs).

The highly conductive and flexible ACTs were fabricated by direct conversion of a commercial cotton T-shirt through a dipping, drying and curing process as described in our previous report. Figure 2.2 Aa shows the digital photograph of a commercial cotton T-shirt, which was used to prepare ACTs. Figure 2.2 Ab shows the digital photograph of a piece of ACT, which is mechanically flexible even under folding state (Fig. 2.2 Ac) and highly conductive (resistance $\sim 10\text{-}20 \Omega \text{sq}^{-1}$). SEM image of ACT shows that the interwoven fibers of activated textile have the diameters ranging from 5 to 10 μm , which inherit the cellulose fiber architecture of cotton textile (Fig. 2.2 Ad). Fig. 2.2 Ae-f shows the morphology of NiCo_2O_4 nanowires hydrothermally grown on the surface of ACT. High-density of NiCo_2O_4 nanowires, with the length of several micrometers and diameter of around 70 nm, were radially aligned on individual ACT fibers, forming uniform nano-arrays with highly open and porous structure. After the coupled chemical bath deposition and following-up heat treatment, the surfaces of individual NiCo_2O_4 nanowires were uniformly decorated with NiCo_2O_4 nanoflakes (Fig. 2.2 Ag-h). The cross-sectional and side-view images of the $\text{NiCo}_2\text{O}_4@/\text{NiCo}_2\text{O}_4$ core/shell nanoarchitecture (Figure 2.2 Ag and h) jointly reveal that the tiny flaky NiCo_2O_4 nanosheets ($< 10 \text{nm}$) were densely anchored on individual NiCo_2O_4 nanowires. Of importance, the nanowire core and nanoflake shell are of the same material

NiCo₂O₄, thereby eliminating the contact resistance between the core and shell and ultimately enhancing both energy and power densities. The tiny NiCo₂O₄ nanoflakes render a highly porous hierarchical architecture, which serves as a reservoir for electrolyte ions, providing dense diffusion channels for energy storage.

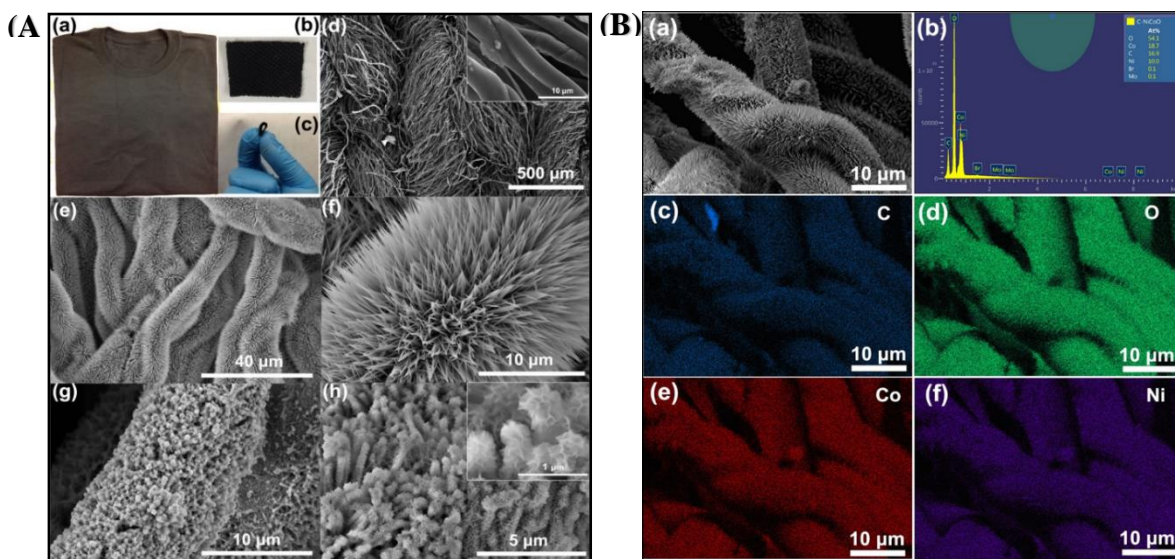


Figure 2.2 (A) Optical photographs of (a) a commercial cotton T-shirt, (b) a piece of ACT and (c) a piece of ACT under folding condition, showing its super flexibility; (d) SEM image of ACT, inset is the amplified SEM image; (e-f) SEM images of NiCo₂O₄ nanowires grown on the ACT microfibers by a hydrothermal method; (g) and (h) SEM images of NiCo₂O₄@NiCo₂O₄ core/shell nanostructure on the ACT fibers, inset is the SEM image of NiCo₂O₄@NiCo₂O₄ nanoflake at high magnification. (B) EDS spectrum and element mapping images of C, O, Co and Ni elements of NiCo₂O₄ nanowire/ACT.

The chemical compositions of the NiCo₂O₄ nanowire/ACT were further analyzed by energy-dispersive X-ray spectrometry (EDS) (Fig. 2.2 B). The Ni/Co atomic ratio is 10:19, which is close to the theoretical atomic ratio (1:2) of NiCo₂O₄, indicating that the Ni-Co hydroxide precursors were entirely transformed into the NiCo₂O₄ after the heat treatment, which agrees well with the XRD result (Fig. 2.4 b), confirming the ACT microfibers were uniformly covered by the NiCo₂O₄ nanowire arrays. The structure and morphology of Ni-Co hydroxide precursors, NiCo₂O₄ nanowire/ACT and NiCo₂O₄@NiCo₂O₄/ACT hybrids were further investigated by TEM. As illustrated in Figure 2.3a, the Ni-Co hydroxide precursor nanowires have a smooth surface with a diameter of about 50 nm and plenty of mesopores with the size of 2-4 nm inside individual NiCo₂O₄ nanowires (Fig. 2.3b). Such internal active surface areas further enhance the pseudocapacitance. The mesoporous NiCo₂O₄ nanowires are anticipated to exhibit unusually high electrochemical properties because of the high density of active sites and

short electron transport path. [40] Clearly, such NiCo_2O_4 nanowires provide a unique backbone for the design of hierarchical nanoarchitecture with the goal to further push up the electrochemical properties. After the chemical bath deposition, the NiCo_2O_4 nanowires were elegantly wrapped with leaf-like NiCo_2O_4 nanoflakes, forming a core/shell hierarchical nanoarchitecture of the same material- NiCo_2O_4 , with high porosity (Figs. 3c-d). Figs. 2.3e and f show the HRTEM image and SAED pattern of the $\text{NiCo}_2\text{O}_4@ \text{NiCo}_2\text{O}_4$ nanostructure. A grain boundary was observed between the core and shell, with the d-spacing of 0.47 nm for the core and 0.28 nm for the shell, indicating different growth direction. The different lattice direction and typical amorphous diffraction pattern (Fig. 2.3f) suggest that the $\text{NiCo}_2\text{O}_4@ \text{NiCo}_2\text{O}_4$ nanostructure is a mixture of crystal and amorphous phases, indicating poor crystalline in good agreement with the XRD results.

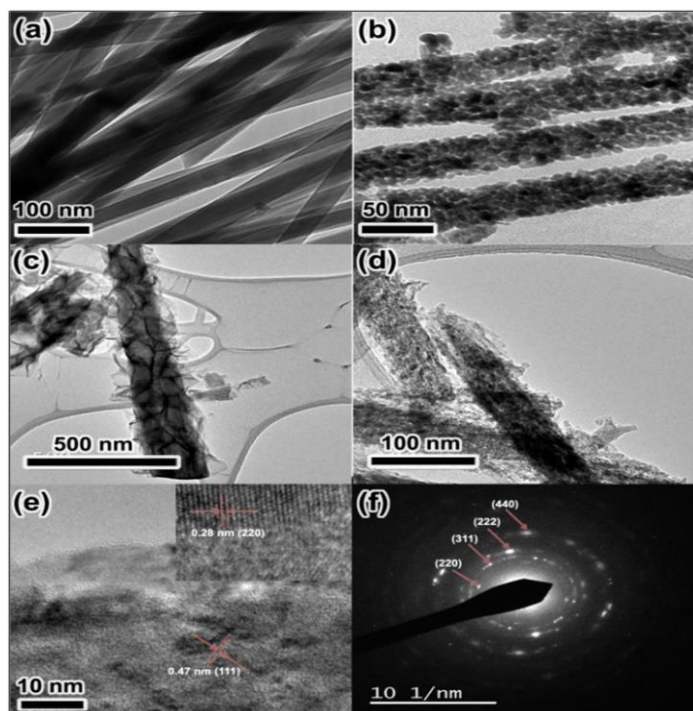


Figure 2.3 (a) TEM image of Ni-Co hydroxide precursor nanowires; (b) TEM image of NiCo_2O_4 nanowires grown on ACTs after the annealing process; (c) TEM image of $\text{NiCo}_2\text{O}_4@ \text{NiCo}_2\text{O}_4$ core/shell nanostructure precursor; (d) TEM image of $\text{NiCo}_2\text{O}_4@ \text{NiCo}_2\text{O}_4$ core/shell nanostructure after the annealing process; (e) HRTEM image of $\text{NiCo}_2\text{O}_4@ \text{NiCo}_2\text{O}_4$ nanostructure, inset is the amplified region; (f) Selected area electron diffraction (SAED) pattern of $\text{NiCo}_2\text{O}_4@ \text{NiCo}_2\text{O}_4$ nanostructure.

The XRD patterns of the obtained ACT, NiCo_2O_4 nanowire/ACT, and $\text{NiCo}_2\text{O}_4@ \text{NiCo}_2\text{O}_4/ \text{ACT}$ are respectively shown in Figure 2.4b. The peak at about 21° was identified to be the amorphous carbon from ACTs. The diffraction peaks in the XRD patterns of $\text{NiCo}_2\text{O}_4/ \text{ACT}$ and $\text{NiCo}_2\text{O}_4@ \text{NiCo}_2\text{O}_4/ \text{ACT}$ can be indexed to the (111), (220),

(311), (511) and (440) planes of the cubic NiCo_2O_4 phase (JCPDS card no. 20-0781). [41] No foreign peaks were detected, indicating that both of the core and shell are pure NiCo_2O_4 . The diffraction peak of ACT at 21° is hidden in the relative intense diffraction peak (111) of NiCo_2O_4 at 19° of the XRD patterns of the $\text{NiCo}_2\text{O}_4/\text{ACT}$ and $\text{NiCo}_2\text{O}_4@\text{NiCo}_2\text{O}_4/\text{ACT}$. The relatively weaker intensity of the NiCo_2O_4 peaks in the hybrid $\text{NiCo}_2\text{O}_4/\text{ACT}$ and $\text{NiCo}_2\text{O}_4@\text{NiCo}_2\text{O}_4/\text{ACT}$ indicates low crystallinity, which is beneficial for the improvement of specific capacitance. [42] XPS measurements were performed to explore the chemical states and compositions of the as-prepared $\text{NiCo}_2\text{O}_4@\text{NiCo}_2\text{O}_4/\text{ACT}$ hybrid (Figs. 2.4c and d). The cobalt 2p XPS spectra consist of two spin-orbit doublets at 781.9 eV and 797.8 eV, respectively, pointing towards Co^{2+} and Co^{3+} , and two shakeup satellites at 786.9 eV and 803.8 eV (identified as “Sat.”) (Fig. 2.4c). Similarly, the nickel 2p XPS spectra consist of two spin-orbit doublets at 872.8 eV and 855.7 eV, resulting from Ni^{2+} and Ni^{3+} , and two shakeup satellite peaks at 879.8 and 861.3 eV (Fig. 2.4d). [43,44]

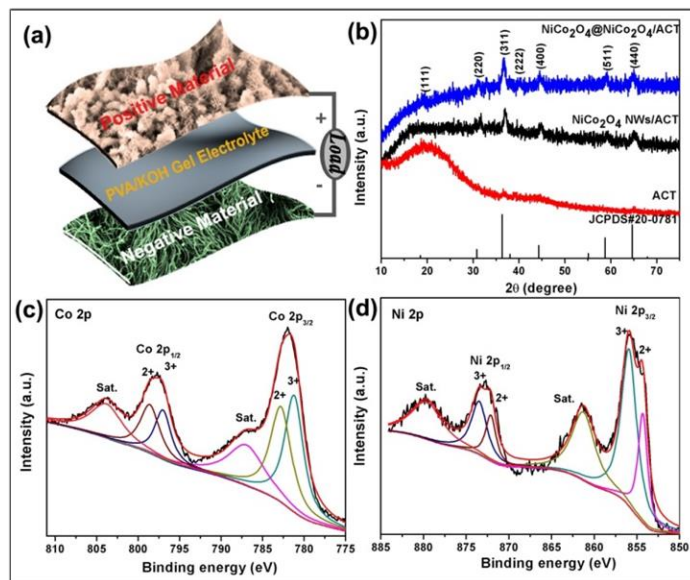


Figure 2.4 (a) Illustration of the assembled flexible all-solid-state asymmetric supercapacitor; (b) XRD patterns of the as-obtained ACT, NiCo_2O_4 nanowire/ACT, and $\text{NiCo}_2\text{O}_4@\text{NiCo}_2\text{O}_4/\text{ACT}$; (c) Co 2p and (d) Ni 2p XPS spectra of $\text{NiCo}_2\text{O}_4@\text{NiCo}_2\text{O}_4/\text{ACT}$.

2.3.2 Electrochemical Performance

The CV curves of the ACT and NiCo_2O_4 nanowire/ACT hybrid at the scan rates of 5, 10, 25, 50, 75, 100 mV/s with the potential windows ranging from -0.2 to 0.5 V versus SCE in 6 M KOH aqueous solution can be found in Figs. 2.5a and c in the Supporting Information. The quasi-rectangular shape of CV curves for ACT (Fig. 2.5a) indicates ideal

electrical double layer capacitive behavior. The CV curve of the NiCo₂O₄/ACT hybrid shows a more complicated shape with two pairs of redox peaks, which correspond to Faradaic redox reactions of NiCo₂O₄ that can be expressed in the following equations. [45]

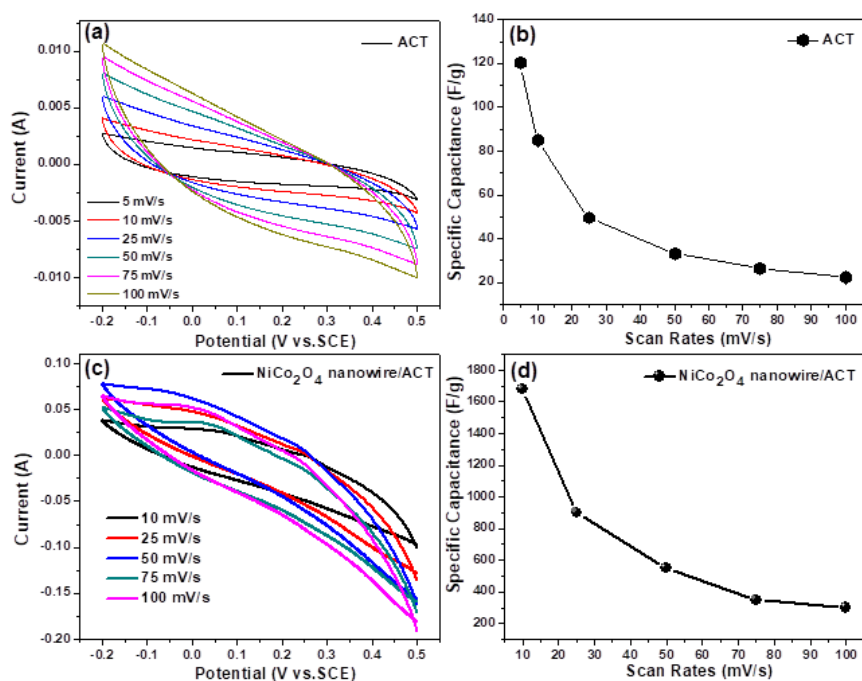


Figure 2.5 (a) Cyclic voltammetry (CV) curves of ACT at different scan rates in 6 M KOH aqueous solution; (b) Specific capacitances of ACT at different scan rates derived from the CV curves; (c) CV curves of NiCo₂O₄ nanowire/ACT at different scan rates in 6 M KOH aqueous solution. (d) Specific capacitances of NiCo₂O₄ nanowire/ACT derived from the CV curves.

The calculated specific capacitances from the CV curves can be found in Figs. 2.5b and d in the Supporting Information. The specific capacitances of ACT electrode are 120, 85, 49.4, 33.1, 26.3, 22.3 F/g at the scan rates of 5, 10, 25, 50, 75, 100 mV/s, respectively, while the specific capacitances of the NiCo₂O₄ nanowire/ACT are respectively 1679, 902, 550, 348, 301 F/g (based on the mass of NiCo₂O₄) at the scan rates of 10, 25, 50, 75, 100 mV/s. The remarkably improved capacitance of the NiCo₂O₄/ACT results from the high pseudocapacitance of NiCo₂O₄ nanowires. [46] The decay of specific capacitance with increasing scan rate is due to the slow current accumulating process at low scan rates, which enables full access of active pores/sites, corresponding to its pseudocapacitive feature. Overall, the ACT electrode shows better rate performance while the NiCo₂O₄ nanowires

possess high specific capacitance. The coupling of the ACT and NiCo₂O₄ nanowires renders the NiCo₂O₄ nanowire/ACT electrode higher electrochemical performance.

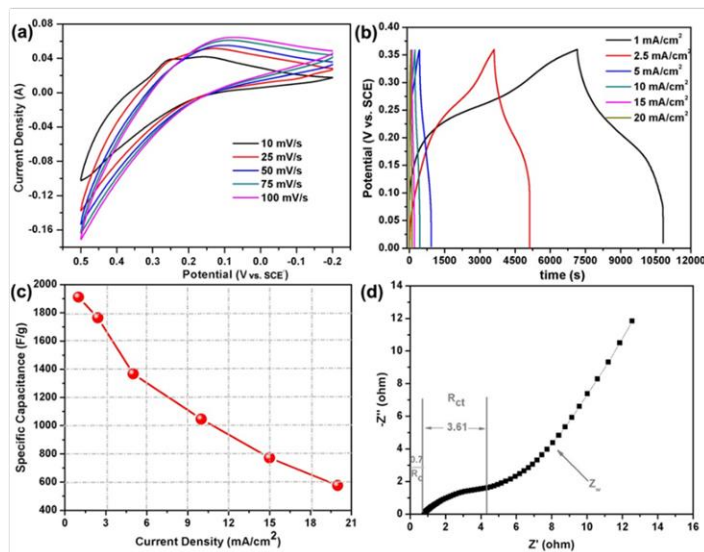


Figure 2.6 (a) CV curves of NiCo₂O₄@NiCo₂O₄/ACT at different scan rates in 6 M KOH aqueous solution; (b) Galvanostatic (GV) constant-current charge/discharge curves of NiCo₂O₄@NiCo₂O₄/ACT in 6 M KOH aqueous solution at different current densities; (c) Specific capacitances of NiCo₂O₄@NiCo₂O₄/ACT in 6 M KOH aqueous solution at different current densities; (d) Nyquist plots of electrochemical impedance spectra of NiCo₂O₄@NiCo₂O₄/ACT in 6 M KOH aqueous solution in the frequency range of 100 kHz to 0.05Hz.

Figure 2.6a shows the CV curves obtained from the NiCo₂O₄@NiCo₂O₄/ACT electrode in 6 M KOH aqueous solution within the potential range of -0.2-0.5 V (vs SCE) at different scan rates. Two pairs of peaks were found in each individual CV curve, indicating that the capacitance is mainly based on the Faradaic redox reaction. The well-retained shape of the CV curve with an increase in scan rate suggests that the porous nanostructure of the NiCo₂O₄@NiCo₂O₄/ACT hybrid electrode is indeed beneficial to the fast redox reaction. Furthermore, it is evident that each curve at different scan rates keeps similar redox couples, indicating the quasi-reversible and continuous faradic redox during the charge/discharge processes. The galvanostatic charge/discharge curve (Fig. 2.6b) of the NiCo₂O₄@NiCo₂O₄/ACT electrode at a low current density (1 mA/cm²) exhibits two voltage stages which result from the pseudocapacitive feature of the electrode, agreeing well with the aforementioned CV study. The specific capacitances of the NiCo₂O₄@NiCo₂O₄/ACT hybrid electrode were calculated to be 1929, 1764, 1367, 1046, 771 and 576 F/g from the discharge curves at the current densities of 1, 2.5, 5, 10, 15 and 20 mA/cm², respectively (Fig. 2.6c). The well-defined hierarchical NiCo₂O₄@NiCo₂O₄

core/shell nanostructure increases the exposed active surface area for electrolyte and provides an express-path for the diffusion of electrolyte ions, leading to the high mass-specific capacitance. The small equivalent series resistance (ESR) (0.27Ω) and charge-transfer resistance (R_{ct}) (3.61Ω) obtained from the Nyquist plots of electrochemical impedance spectra (EIS) (calculated by the method given in Ref 44) [47] of the $\text{NiCo}_2\text{O}_4@/\text{NiCo}_2\text{O}_4/\text{ACT}$ electrode are supportive of the remarkable electrochemical performance.

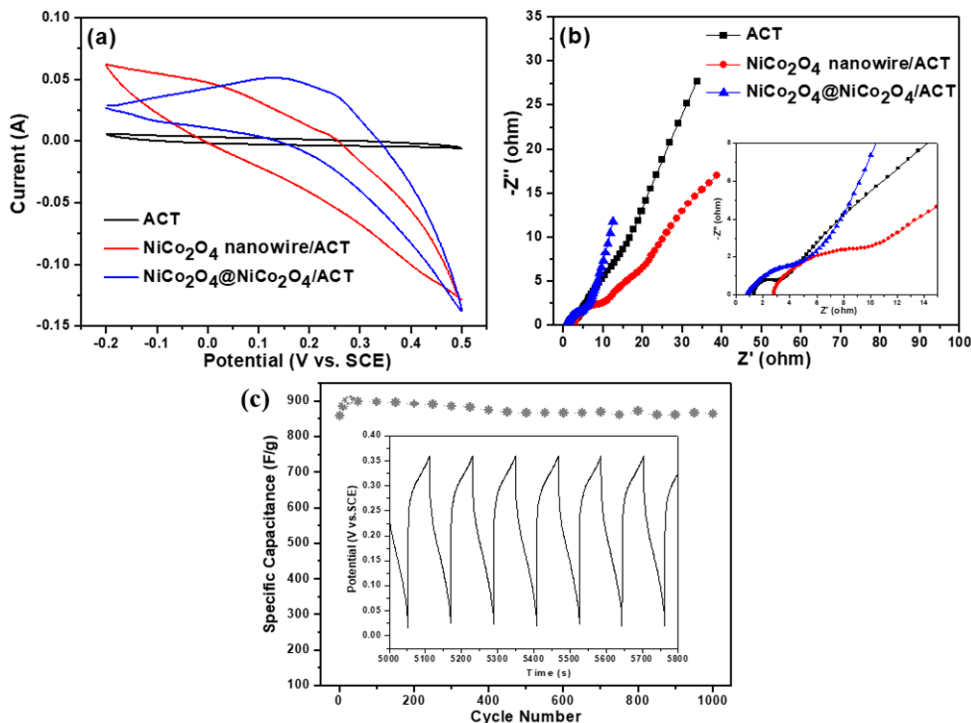


Figure 2.7 (a) Comparative CV curves of ACT, NiCo_2O_4 nanowire/ACT and $\text{NiCo}_2\text{O}_4@/\text{NiCo}_2\text{O}_4/\text{ACT}$ at a scan rate of 25 mV/s in 6 M KOH aqueous solution; (b) Comparative Nyquist plots of electrochemical impedance spectra of ACT, NiCo_2O_4 nanowire/ACT and $\text{NiCo}_2\text{O}_4@/\text{NiCo}_2\text{O}_4/\text{ACT}$ in 6 M KOH aqueous solution within the frequency range from 100 kHz to 0.05 Hz; (c) Cycling performance of $\text{NiCo}_2\text{O}_4@/\text{NiCo}_2\text{O}_4/\text{ACT}$ in 6 M KOH aqueous solution at a current density of 20 mA/cm², inset is a part of the charge/discharge curve of $\text{NiCo}_2\text{O}_4@/\text{NiCo}_2\text{O}_4/\text{ACT}$ during the GV constant-current test.

The CV curves and Nyquist plots of the ACT, NiCo_2O_4 nanowire/ACT and $\text{NiCo}_2\text{O}_4@/\text{NiCo}_2\text{O}_4/\text{ACT}$ electrodes are comparatively shown in Figure 2.7. The CV curve of the ACT shows electrical double layer characteristics with a rectangular shape, while the CV curves of the NiCo_2O_4 nanowire/ACT and $\text{NiCo}_2\text{O}_4@/\text{NiCo}_2\text{O}_4/\text{ACT}$ electrodes exhibit typical pseudocapacitive features with two pairs of redox peaks (Fig. 2.7a). Compared with the ACT and NiCo_2O_4 nanowire/ACT electrodes, the larger integrated area of the current-potential curves (Fig. 2.7a) and reduced charge-transfer resistance (Fig. 2.7b) of the

NiCo₂O₄@NiCo₂O₄/ACT hybrid electrode indicate improved electrochemical performance, which is attributed to the intriguing hierarchical core/shell architecture with a plethora of internal mesopores, facilitating both mass and ions transport during the charging/discharging process. Long lifespan is a key factor for evaluating the practical application of supercapacitor electrode. Fig 2.7c shows the cyclic performance of the NiCo₂O₄@NiCo₂O₄/ACT hybrid electrode conducted by the galvanostatic charge/discharge tests at a current density of 20 mA/cm² for up to 1000 cycles. The NiCo₂O₄@NiCo₂O₄/ACT hybrid electrode exhibits a high specific capacitance and eminent cyclic stability with an increase of capacitance for the initial 50 cycles and 3.98 % increase after 1000 cycle tests, which are ascribed to the full exposure of active Ni and Co sites to the electrolyte after the repetitive charge/discharge. The results obtained from the three electrode test system jointly show that the NiCo₂O₄@NiCo₂O₄/ACT is an exceptional supercapacitor electrode material in terms of high specific capacitance, excellent rate performance, long lifespan, and low charge transfer resistance.

However, the three-electrode configuration could not fully reflect the real electrochemical performance of an electrode in real-world applications, because only one electrode contains the test material and the applied voltage and charge transfer across the single electrode are markedly different from the two-electrode configuration. [48] To examine the practical performance of the NiCo₂O₄@NiCo₂O₄/ACT in a packaged cell, we assembled both symmetric and asymmetric flexible supercapacitors. Here ACT was chosen as the negative electrode to assemble a NiCo₂O₄@NiCo₂O₄/ACT//ACT asymmetric supercapacitor, as illustrated in the inset of Figure 2.4a. The CV curves of the NiCo₂O₄@NiCo₂O₄/ACT symmetric and asymmetric supercapacitors were collected at different scan rates, as demonstrated in Figures 2.8a and b. The CV curves of both symmetric and asymmetric supercapacitors exhibit nearly rectangular shape at slow scan rates, corresponding to the excellent synergistic effect of the double-layer capacitive ACT and pseudocapacitive NiCo₂O₄. However, with the scan rate increases, the obvious deviation from rectangularity of the symmetric supercapacitor suggests higher charge transfer resistance and poor rate performance.

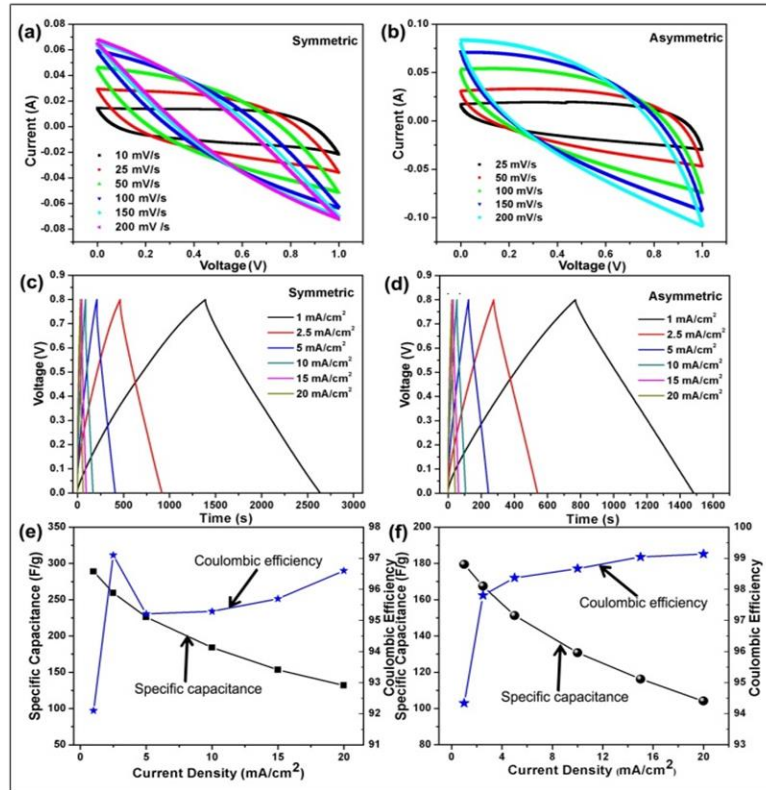


Figure. 2.8 (a) CV curves of the symmetric supercapacitor with NiCo₂O₄@NiCo₂O₄/ACT as both the positive electrode and negative electrode, PVA/KOH as polymer gel electrolyte; (b) CV curves of the asymmetric supercapacitor with NiCo₂O₄@NiCo₂O₄/ACT hybrid as the positive electrode, ACT as the negative electrode, and PVA/KOH as polymer gel electrolyte, respectively; (c) Charge/discharge curves of the symmetric supercapacitor with NiCo₂O₄@NiCo₂O₄/ACT as both the positive electrode and negative electrode, PVA/KOH as polymer gel electrolyte; (d) Charge/discharge curves of the asymmetric supercapacitor with NiCo₂O₄@NiCo₂O₄/ACT hybrid as the positive electrode, ACT as the negative electrode, and PVA/KOH as polymer gel electrolyte, respectively; (e) Specific capacitances and coulombic efficiency of the symmetric supercapacitor with NiCo₂O₄@NiCo₂O₄/ACT as both the positive electrode and negative electrode, PVA/KOH as polymer gel electrolyte at different current densities; (f) Specific capacitances and coulombic efficiency of the asymmetric supercapacitor with NiCo₂O₄@NiCo₂O₄/ACT hybrid as the positive electrode, ACT as the negative electrode, and PVA/KOH as polymer gel electrolyte, respectively.

The constant current charge/discharge curves of the symmetric and asymmetric at different current densities (1, 2.5, 5, 10, 15 and 20 mA/cm²) are shown in Figs. 2.8c and d. The charge/discharge curves for both the symmetric and asymmetric supercapacitors are almost symmetric with a small internal resistance (IR) drop, indicating a good electrochemical capacitive characteristic and superior reversible redox reaction. Rate capability and Coulombic efficiency are two important factors for evaluating the power applications of supercapacitors. The corresponding specific capacitances for the symmetric supercapacitor are 288 F/g at 1 mA/cm² and 131 F/g at 20 mA/cm², showing 45.48% of capacitance retention after the current density was increased 20 times (Fig. 2.8e). The specific capacitances for the asymmetric supercapacitor are 179 F/g at 1 mA /cm² and 104

F/g at 20 mA/cm², respectively, and 58.1% of the capacitance is retained (Fig. 2.8f), suggest better rate performance of the asymmetric supercapacitor, agreeing well with the CV results. Compared with the symmetric supercapacitor, the asymmetric supercapacitor exhibited relatively “poor” capacitance performance, probably due to the practical capacitance mismatch of positive and negative electrodes. The initial Coulombic efficiency values of the symmetric and asymmetric cells were calculated to be 92.01% and 94.3% at 1 mA/cm², respectively. The Coulombic efficiency of the symmetric cell quickly increased to the peak value of 97.16%, immediately followed by a decrease and then a slow increase with the increase of current density. For the asymmetric cell, the Coulombic efficiency exhibited a fast increase at the initial stage and then a gradual increase up to 99.16%. The high Coulombic efficiency helps enhance energy utilization efficiency and promote electrochemical reversibility.

To further explore the potential of the asymmetric supercapacitor, the applied voltage was extended to 1.6 V (Fig. 2.9a). The asymmetric cell exhibited a stable potential window even at the high voltage window, which is essential for practical applications. Fig. 2.9c shows the GV curves of the asymmetric supercapacitor at different current densities. The asymmetric cell exhibited a high capacitance retention 60 F/g At the current density 100 mA/cm², indicating excellent rate performance. The EIS tests were carried out for an in-depth understanding of the electrochemical behavior of the assembled symmetric and asymmetric flexible cells. The Nyquist plots of the ACT//ACT cell, NiCo₂O₄@NiCo₂O₄/ACT//NiCo₂O₄@NiCo₂O₄/ACT symmetric cell, and NiCo₂O₄@NiCo₂O₄/ACT//ACT asymmetric cell are compared in Fig. 2.9b. In the high-frequency range, the intercept of the semicircle with the real axis represents the equivalent series resistance (ESR), which includes the ionic resistance, the intrinsic resistance, and the contact resistance at the electrode/current collector interface. [49] Clearly, the smaller ESR of the NiCo₂O₄@NiCo₂O₄/ACT//ACT asymmetric cell results from the hierarchical porous nanostructure of the NiCo₂O₄@NiCo₂O₄/ACT electrode, which facilitates the access of electrolyte ions to the active surface and shortens the ion diffusion path. A straight line close to 90° was found for the asymmetric cell in the low-frequency range, indicating a pure capacitive behavior and low diffusion resistance of electrolyte ions in the core of the electrode. [50]

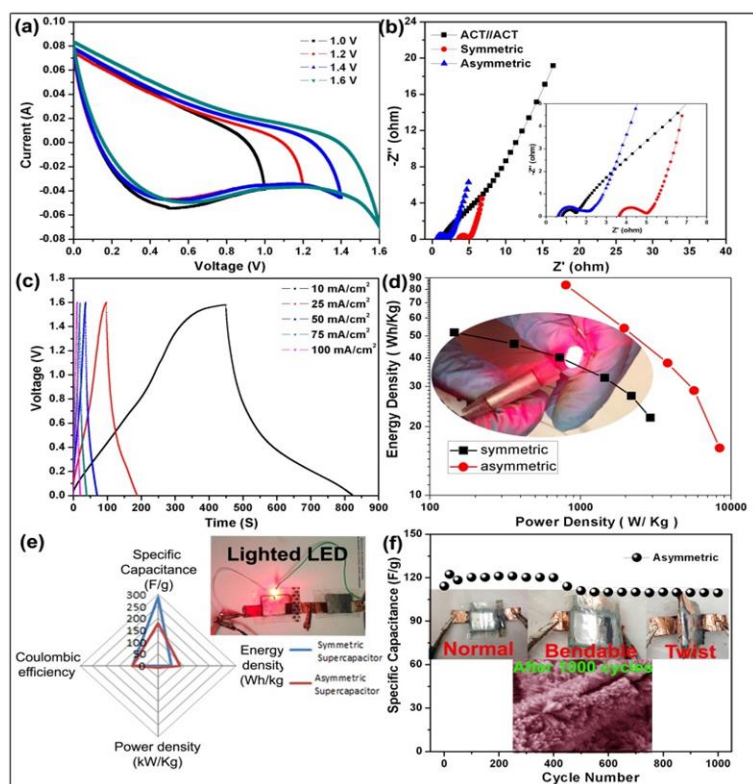


Figure 2.9 (a) CV curves of NiCo₂O₄@NiCo₂O₄/ACT//ACT asymmetric supercapacitor with PVA/KOH polymer gel electrolyte under the voltage windows of 1, 1.2, 1.4 and 1.6 V at the scan rate of 50 mV/s; (b) Nyquist plots of the ACT//ACT symmetric supercapacitor with PVA/KOH polymer gel electrolyte, NiCo₂O₄@NiCo₂O₄/ACT//ACT asymmetric supercapacitor with PVA/KOH polymer gel electrolyte and NiCo₂O₄@NiCo₂O₄/ACT//NiCo₂O₄@NiCo₂O₄/ACT symmetric supercapacitor with PVA/KOH polymer gel electrolyte; (c) charging/discharging curves of asymmetric supercapacitor with PVA/KOH polymer gel electrolyte at different current densities; (d) Ragone plots of the as-assembled NiCo₂O₄@NiCo₂O₄/ACT//ACT asymmetric supercapacitor with PVA/KOH polymer gel electrolyte, and NiCo₂O₄@NiCo₂O₄/ACT//NiCo₂O₄@NiCo₂O₄/ACT symmetric supercapacitor with PVA/KOH polymer gel electrolyte (inset is a red light-emitting diode (LED) lighted by two asymmetric supercapacitors under folded state); (e) Radar plot of the symmetric supercapacitor and asymmetric supercapacitor, inset is a lighted LED by two asymmetric supercapacitors connected in series; (f) Cycling performance of NiCo₂O₄@NiCo₂O₄//ACT asymmetric supercapacitor with PVA/KOH polymer gel electrolyte under normal, bent and twisted state at a current density of 15 mA/cm² (inset is the SEM image of NiCo₂O₄@NiCo₂O₄/ACT obtained after 1000 cycles).

Energy density and power density are crucial factors for evaluating the practical application of supercapacitors. A good supercapacitor is expected to provide both high energy density and high capacitance at high charge/discharge rates. The Ragone plots of the all-solid-state flexible NiCo₂O₄@NiCo₂O₄/ACT//NiCo₂O₄@NiCo₂O₄/ACT symmetric cell and NiCo₂O₄@NiCo₂O₄/ACT//ACT asymmetric cell are shown in Fig. 2.9d. As the plots show, the values and trends of energy and power densities for both symmetric and asymmetric cells are similar. For the symmetric cell, the energy density decreases from 51.6 down to 23.3 Wh/kg, while the power density increases from 144 up to 2943 W/kg. Compared with the symmetric cell, the asymmetric cell shows higher energy density of

83.6 Wh/kg at a high-power density of 800 W/kg and remains 21.16 Wh/Kg at the power density of 8.4 kW/kg. Clearly, the asymmetric supercapacitor exhibits much higher power density than that of the symmetric cell. The comprehensive performances for both symmetric and asymmetric cells were compared in the radar plots in Fig. 2.9e, indicating the synergistic effects of the ACT and hierarchical NiCo₂O₄ nanostructure.

A long cycling lifespan is another important requirement for supercapacitor applications. The cycling stability of NiCo₂O₄@NiCo₂O₄/ACT//ACT asymmetric cell was evaluated by repeating the constant current charge/discharge test under different states (normal, bent and twisted states) at a current density of 15 mA/cm² for 1000 cycles (Fig. 2.9f). The asymmetric cell showed an increase in specific capacitance at the initial normal state, which is ascribed to the incomplete exposure of Ni and Co active sites to the gel electrolyte. There is almost no specific capacitance loss after 1000 charge-discharge even at the bent and twisted states, indicating excellent robustness and flexibility. The insets of Fig. 2.9d and Fig. 2.9f show the digital photographs of the as-assembled flexible supercapacitor packed with PET tape. To demonstrate its practical application, two pieces of the as-assembled flexible all-solid-state cells in series were used to light a commercial red LED (inset of Fig. 2.9e). Even in harsh conditions such as folded state (inset of Fig. 2.9d), the brightness of the lightened LED did not change, showing its robust functionality and excellent flexibility. The inset of Fig. 2.9f is the SEM image of the NiCo₂O₄@NiCo₂O₄/ACT electrode after 1000 cycles (without dipping polymer electrolyte during the test). It can be seen that the morphology of the NiCo₂O₄@NiCo₂O₄ core/shell architecture well remained in the entire charge/discharge process, ensuring the excellent electrochemical performance of the flexible electrode.

In real-world applications, flexible supercapacitors should be able to provide power under harsh environments, such as wearable, bendable, stretchable or twisted states, requiring that both the current collector and electrode have both flexibility and stability. To enhance the mechanical robustness of a supercapacitor without sacrificing its flexibility, a 200 μm thick transparent solid-state polymer electrolyte film was fabricated to serve as both separator and electrolyte. Furthermore, the NiCo₂O₄@NiCo₂O₄/ACT hybrid electrode was coated with polymer electrolyte to further improve its mechanical performance. Fig. 2.10a shows the digital photograph of such prepared solid-state electrolyte film and

polymer gel electrolyte. After dipped in the polymer electrolyte, the interspace of the $\text{NiCo}_2\text{O}_4@\text{NiCo}_2\text{O}_4$ core/shell was filled with gel electrolyte (Figs. 2.10b and c), which not only improves the accessibility of electrolyte ions but also intensifies the mechanical strength of the flexible electrode. Fig. 2.10 d shows the tensile stress-strain curves of the pure ACT and $\text{NiCo}_2\text{O}_4@\text{NiCo}_2\text{O}_4/\text{ACT}$ hybrid electrode dipped with the polymer gel electrolyte. Compared with the pure ACT, the tensile strength of the $\text{NiCo}_2\text{O}_4@\text{NiCo}_2\text{O}_4/\text{ACT}$ electrode dipped with polymer gel electrolyte increases to 0.97 MPa, which is 6.5 times higher than that of the pure ACT (0.15 MPa).

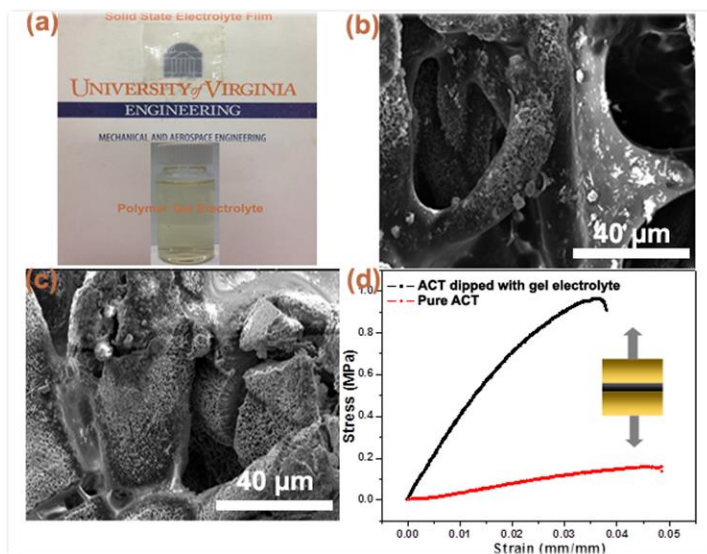


Figure 2.10 (a) Digital photograph of the as-prepared solid-state electrolyte film and polymer gel electrolyte; (b) and (c) SEM images of the $\text{NiCo}_2\text{O}_4@\text{NiCo}_2\text{O}_4/\text{ACT}$ dipped with the polymer gel electrolyte; (d) Tensile stress-strain curves of the $\text{NiCo}_2\text{O}_4@\text{NiCo}_2\text{O}_4/\text{ACT}$ dipped with the polymer gel electrolyte and pure ACT, respectively.

Clearly, the design of the hierarchical $\text{NiCo}_2\text{O}_4@\text{NiCo}_2\text{O}_4/\text{ACT}$ core/shell nanostructure with the mesoporous NiCo_2O_4 nanowires as “core” and upright grown flaky NiCo_2O_4 nano-sheets as “shell” on high conductive ACTs advances the development of flexible textile supercapacitors. The high electrochemical performance of the $\text{NiCo}_2\text{O}_4@\text{NiCo}_2\text{O}_4/\text{ACT}$ hybrid electrode is attributed to the following unique features of the design. First, the activated carbon fibers serve as highly conductive backbones, allowing for efficient current collection and rapid access of electrolyte ions to the surfaces of the active materials. Second, the mesoporous NiCo_2O_4 nanowires with high conductivity directly grew on the conductive substrates, reducing the contact resistance between electrode materials and charge collectors. Third, the ultrathin NiCo_2O_4 nanoflakes well wrapped around the NiCo_2O_4 nanowires to form a porous nanostructure, which shortens

the electrolyte ion diffusion path, and enables faster kinetics and higher utilization of active material. More importantly, both core and shell are of the same material-NiCo₂O₄, eliminating the contact resistance of dissimilar materials. Finally, the polymer gel electrolyte fully penetrated into the interspace of the core/shell nanostructure, which not only highly increases accessibility of electrolytic ions, but also improves the mechanical property of the NiCo₂O₄@NiCo₂O₄/ACT hybrid, making it more suitable for practical applications.

2.4 Conclusions

We have synthesized hierarchical NiCo₂O₄@NiCo₂O₄ core/shell nanostructure on flexible, cotton activated carbon textiles (ACTs) for supercapacitor electrodes using coupled hydrothermal synthesis and chemical bath deposition process. The hierarchical NiCo₂O₄ nanowire/NiCo₂O₄ nanoflake core/shell facilitated the access of electrolyte ions to the active surface and shortened the ion diffusion path, concurrently enhancing charge efficiency and pushing up redox capacitance. On the other hand, the activation of cotton textiles into porous, highly conductive ACTs with high accessible surface area endowed the asymmetric flexible supercapacitor with high rate performance. After dipped the flexible hybrid electrode with PVA-KOH solid-state gel which served as both the electrolyte and separator, the assembled NiCo₂O₄@NiCo₂O₄/ACT//ACT asymmetric supercapacitor exhibited not only high electrochemical performance in terms of high specific capacitance, excellent cycling stability, remarkable energy density, and power density, but also an exceptional mechanical robustness. The coupling of outstanding electrochemical performance, superior flexibility, and excellent mechanical performance promises that such solid-state textile-based supercapacitors should boost the practical application of the flexible power source in the future portable/wearable electronics.

Reference

- [1] J. M. Tarascon, *Phil. Trans. R. Soc. A*, 2010, **368**, 3227.
- [2] A. Burke, *J. Power Sources*, 2000, **91**, 37.
- [3] B. E. Conway, *Electrochemical Supercapacitors: Scientific Fundamentals and Technological Applications*, Kluwer Academic Publishers/Plenum Press, New York, **1999**.

- [4] X. H. Lu, M. H. Yu, G. M. Wang, Y. X. Tong and Y. Li, *Energy Environ. Sci.*, 2014, **7**, 2160
- [5] A. E. Fischer, K. A. Pettigrew, D. R. Rolison, R. M. Stroud and J. W. Long, *Nano Lett.*, 2007, **7**, 281.
- [6] K. Fic , G. Lota , M. Meller and E. Frackowiak, *Energy Environ. Sci.*, 2012, **5**, 5842.
- [7] M. Deschamps, E. Gilbert, P. Azais, E. Raymundo-Piñero, M. R. Ammar, P. Simon, D. Massiot and F. Béguin, *Nat. Mater.*, 2013, **12**, 351.
- [8] V. Ruiz, T. Huynh, S. R. Sivakkumara and A. G. Pandolfo, *RSC Adv.*, 2012, **2**, 5591.
- [9] M. Koo, K. Park, S. H. Lee, M. Suh, D. Y. Jeon, J. W. Choi, K. Kang and K.. J. Lee, *Nano Lett.*, 2012, **12**, 4810.
- [10] H. Pan, J. Li and Y. P. Feng, *Nanoscale Res Lett.* 2010, **5**, 654.
- [11] G. H. Yu, L. B. Hu, M. Vosgueritchian, H. L. Wang, X. Xie, J. R. McDonough, X. Cui, Y. Cui and Z. N. Bao, *Nano Lett.* 2011, **11**, 2905.
- [12] L. B. Hu, M. Pasta, F. La Mantia, L. F. Cui, S. Jeong, H. D. Deshazer, J. W. Choi, S. M. Han and Y. Cui, *Nano Lett.* 2010, **10**, 708.
- [13] G. Zhang and X. W. Lou, *Sci. Rep.* 2013, **3**, 170.
- [14] H. Wang and X. Wang, *ACS Appl. Mater. Interfaces*, 2013, **5**, 6255.
- [15] K. Jost, G. Dion and Y. Gogotsi, *J. Mater. Chem. A*, 2014, **2**, 10776.
- [16] L. H. Bao and X. D. Li, *Adv. Mater.*, 2012, **24**, 3246.
- [17] G. Yu, L. Hu, N. Liu, H. Wang, M. Vosgueritchian, Y. Yang, Y. Cui, and Z. N. Bao, *Nano Lett.*, 2011, **11**, 4438.
- [18] G. Xiong, K. Hembram, R. G. Reifenberger, and T. S. Fisher, *J. Power Sources*, 2013, **227**, 254.
- [19] L. Shen, Q. Che, H. Li and X. Zhang, *Adv. Funct. Mater.*, 2014, **24**, 2630.
- [20] W.W. Zhou, J. Liu, T. Chen, K. S. Tan, X. Jia, Z. Luo, C. Cong, H. Yang, C. M. Li and T. Yu, *Phys. Chem. Chem. Phys.*, 2011, **13**, 14462.
- [21] C. Yuan, X. Zhang, L. Su, B. Gao and L. Shen, *J. Mater. Chem.*, 2009, **19**, 5772.
- [22] Z. Gao, J. Wang, Z. Li, W. Yang, B. Wang, M. Hou, Y. He, Q. Liu, T. Mann, P. Yang, M. Zhang, and L. Liu, *Chem. Mater.* 2011, **23**, 3509.
- [23] C. Meng, C. Liu, L. Chen, C. Hu, and S. Fan, *Nano Lett.*, 2010, **10**, 4025.

- [24] G. Xiong, C. Meng, R. G. Reifenger, P. P. Irazoqui and T. S. Fisher, *Adv. Energy Mater.* 2014, **4**, 1300515.
- [25] Z. Lu, Q. Yang, W. Zhu, Z. Chang, J. Liu, X. Sun, D. Evans and X. Duan, *Nano Research*, 2012, **5**, 369.
- [26] Z. Chen, V. Augustyn, J. Wen, Y. Zhang, M. Shen, B. Dunn and Y. Lu, *Adv. Mater.*, 2011, **23**, 791.
- [27] H. Jiang, J. Ma and C. Z. Li, *Chem. Commun.*, 2012, **48**, 4465.
- [28] L. Huang, D. Chen, Y. Ding, S. Feng, Z. L. Wang and M. L. Liu, *Nano Lett.*, 2013, **13**, 3135.
- [29] Y. Dai, S. Tang, S. Vongehr, and X. Meng, *ACS Sustainable Chem. Eng.*, 2014, **2**, 692.
- [30] G. Zhang, T. Wang, X. Yu, H. Zhang, H. Duan and B. Lu, *Nano Energy*, 2013, **2**, 586.
- [31] D. P. Cai, B. Liu, D. D. Wang, L. L. Wang, Y. Liu, H. Li, Y. R. Wang, Q. H. Lia and T. H. Wang, *J. Mater. Chem. A*, 2014, **2**, 4954.
- [32] L. Yu, G. Zhang, C. Yuan and X. W. Lou, *Chem. Commun.*, 2013, **49**, 137.
- [33] L. H. Bao, J. Zang and X. D. Li, *Nano Lett.*, 2011, **11**, 1215.
- [34] W. Yang, Z. Gao, J. Ma, X. Zhang, J. Wang and J. Liu, *J. Mater. Chem. A*, 2014, **2**, 1448.
- [35] C. Yilmaz, A. E. Cetin, G. Goutzamanidis, J. Huang, S. Somu, H. Altug, D. Wei, and A. Busnaina, *ACS Nano*, 2014, **8**, 4547.
- [36] Q. Wang, X. Wang, B. Liu, Gang Yu, X. Hou, D. Chen and G. Shen, *J. Mater. Chem. A*, 2013, **1**, 2468.
- [37] J. Du, G. Zhou, H. Zhang, C. Cheng, J. Ma, W. Wei, L. Chen and T. Wang, *ACS Appl. Mater. Interfaces*, 2013, **5**, 7405.
- [38] X. Y. Yu, X. Z. Yao, T. Luo, Y. Jia, J. H. Liu and X. J. Huang, *ACS Appl. Mater. Interfaces*, 2014, **6**, 3689.
- [39] X. Liu, S. Shi, Q. Xiong, L. Li, Y. Zhang, H. Tang, C. Gu, X. Wang and J. Tu, *ACS Appl. Mater. Interfaces*, 2013, **5**, 8790.
- [40] M. R. Tarasevich and B. N. Efremov, *Electrodes of Conductive Metallic Oxides, Part A*, Elsevier, USA, **1982**, 227.
- [41] S. Verma, H. M. Joshi and T. Jagadale, *J. Phys. Chem. C*, 2008, **112**, 15106.

- [42] R. R. Salunkhe, K. Jang, H. Yu, S. Yu, T. Ganesh, S. H. Han and H. Ahn, *J. Alloys Compd.* 2011, **509**, 6677.
- [43] R. Ding, L. Qi, M. J. Ji and H. Y. Wang, *Nanoscale*, 2014, **6**, 1369.
- [44] J. G. Kim, D. L. Pugmire, D. Battaglia and M. A. Langell, *Appl. Surf. Sci.*, 2000, **165**, 70.
- [45] C. C. Hu and C. Y. Cheng, *Electrochem. Solid-State Lett.* 2002, **5**, A43.
- [46] T. Y. Wei, C. H. Chen, H. C. Chien, S. Y. Lu and C. C. Hu, *Adv. Mater.*, 2010, **22**, 347.
- [47] J. Wang, Z. Gao, Z. Li, B. Wang, Y. Yan, Q. Liu, T. Mann, M. Zhang and Z. Jiang, *J. Solid State Chem.* 2011, **184**, 1421.
- [48] M. D. Stoller and R. S. Ruoff, *Energy Environ. Sci.*, 2010, **3**, 1294.
- [49] Z. Gao, W. Yang, J. Wang, B. Wang, Z. Li, Q. Liu, M. Zhang, and L. Liu, *Energy Fuels*, 2013, **27**, 568.
- [50] G. J. Brug, A. V. Eeden, M. Sluyters-Rehbach and J. H. Sluyters *J. Electroanal. Chem.*, 1984, **176**, 275.

Chapter 3. Cotton Textile-Enabled Flexible Asymmetric Supercapacitors

3.1 Introduction

To solve the energy crisis in the 21st century, tremendous efforts have been devoted to developing energy storage and conversion devices to meet the increasing demand for energy. [1,2] Batteries, fuel cells, and electrochemical capacitors, which directly convert chemical energy into electrical energy, have been proven effective for practical energy storage and conversion. Recently, electrochemical capacitors (ECs) (also known as supercapacitors or ultracapacitors) are emerging as very promising energy storage devices for flexible electronics and electric vehicles due to the excellent combination of their electrochemical properties such as high-power density, good pulse charge-discharge performance, long lifespan, and low maintenance cost. [3,4] However, compared with lithium-ion batteries, supercapacitors often suffer from relatively low energy density, which limits their practical applications. [5] Progress has been made in developing new electrode materials with high surface area architectures for enhancing the electrochemical performance of supercapacitors. [6-8] To date, various electrode materials including carbon materials, [9-12] transition-metal oxides and hydroxides, [13-17] conducting polymers [18-21] have been explored for supercapacitor applications.

It has been challenging to achieve joint improvements in all aspects of electrochemical properties and performance. For example, carbon materials have higher power density and longer lifespan, but lower capacitance and energy density. In contrast, transition metal oxides possess higher energy density but relatively lower power density and poorer cyclic life due to their intrinsic poor electrical conductivity and short diffusion distance (~20 nm), which limit the contribution of the inner active materials to the total capacitance. [22] The electrochemical performance of an electrode material depends strongly on the morphology and microstructure of the material. [23] An intelligent approach to push up the electrode material's performance is to create architectures with the high specific surface area, which is anticipated to achieve a joint improvement in electrical conductivity, specific capacitance, energy density and power density, and cyclic stability. [24] The future of electronics will be flexible and wearable. Many attempts have been devoted to developing safe, lightweight and flexible power sources to meet the urgent needs of flexible and wearable

electronics. [25] However, to date, a streamlined manufacturing process for integrating flexible energy storage devices with wearable electronics has not realized. Most of the reported flexible electrodes were fabricated by depositing active materials on conductive carbon cloth, carbonized or paper-like polymers. [26-28] Textile-based energy devices with outstanding mechanical robustness and superior electrochemical performance are still lacking. It is challenging to fabricate nano-architectures with pre-designed morphologies and tunable functions on flexible textile substrates.

Recently, transition metal oxides have been widely investigated as pseudocapacitive or “battery-type” Faradic electrode materials due to their good electroactivity, high theoretical capacitance, low cost, and natural abundance. [29,30] However, the reported values are often much lower than theoretically predicted capacities. To enhance the specific capacitance, cycle life and rate performance of transition metal oxide electrodes, many efforts have been devoted to rationally design of hetero-/homo-nanostructures. Fan *et al.* reported that core/shell $\text{Co}_3\text{O}_4@\text{NiO}$ hetero-nanostructure deposited on nickel foam showed a specific capacitance of 853 F g^{-1} at the current density of 2 A g^{-1} . [31] Zhang *et al.* demonstrated that the enhanced electrochemical performance of hierarchical $\text{Co}_3\text{O}_4@\text{NiCo}_2\text{O}_4$ nanoforest on Ni-foam (areal capacitance is 2.04 F cm^{-2} at the scan rate of 5 mV s^{-1}). [32] Recently, the fabricated $\text{NiCo}_2\text{O}_4@\text{NiCo}_2\text{O}_4$ homo-nanostructure on flexible activated carbon textile also exhibited exceptional electrochemical performance. [33] In those studies, the integrated hierarchical 3D porous structure, coupling two types of materials and/or nanostructures on conductive substrates, brings together many competitive advantages such as easy accessibility of electrolyte ions, rich electroactive sites, short ion diffusion path, superior current collection efficiency and the fascinating synergetic effects of different components. Among various transition metal oxides, Co_3O_4 and NiO have aroused great interests because of their high theoretical capacity (3560 F g^{-1} and 2584 F g^{-1} , respectively), good electronic conductivity, favorable capacitive characteristics, and controllable size and morphology. [34] In fact, CoO possesses a higher theoretical capacitance of 4292 F g^{-1} , which can be a better candidate for supercapacitor applications.³⁵ But until now, there are only fewer reports about the nanostructured CoO and its nanocomposites for supercapacitor applications. [36,37]

Energy density and power density of supercapacitor are always contradictory each other. Energy density can be enhanced at the sacrifice of power density by using pseudocapacitive

transition metal oxides. To resolve such contradiction between energy density and power density, an intelligent approach is to develop an asymmetric supercapacitor, which consists of a battery-type Faradic electrode (as energy source) and a capacitor-type electrode (as power source). [38] Carbon is the most widely used capacitor-type electrode material with high power density and excellent rate performance due to its good electrical conductivity and often a high surface area in its electrode architecture. [39] Among various carbon materials, two-dimensional (2D) single-layered graphene has been recognized as an ideal candidate because of its high specific surface area, superior electrical conductivity, high flexibility, outstanding mechanical properties, and relative wide operation windows. [40] Graphene-based films and papers with three dimensional (3D) porous structures have also been intensively explored for flexible supercapacitor applications. [41-44]

Cotton is flexible, green and renewable and is the most widely used natural fibers for soft and breathable clothing and textiles. [45] Our previous studies have shown that the activated carbon textile (ACT) converted from a cotton T-shirt can be an excellent wearable platform for flexible energy storage devices because of its lightweight, eminent flexibility, and excellent conductivity. [46] In this paper, we report a new route for fabricating hybrid CoO@NiO nano-architectures on the ACT with high surface area. Battery-type Faradic CoO nanostructures with different morphologies (sheet-like, petal-like and urchin-like) were controllably synthesized on ACTs by simply changing the reactant concentration during the hydrothermal process. We unveiled that the electrochemical properties of CoO nanostructures are morphology-dependent. The specific capacitance increased exponentially with the surface/volume ratio of nanostructures. The architecture with higher surface area exhibits better electrochemical performance. Due to its higher surface/volume ratio and better electrochemical performance, urchin-like CoO was further chosen as a backbone to deposit NiO nanoflakes to construct a hierarchical core/shell CoO@NiO hybrid nanostructure. The hybrid CoO@NiO nanostructured electrode with high surface area enables fast charge accumulation and ion transport. For the negative electrode, we coated ACT fibers with corrugated, high conductive graphene coating by a simple dipping, drying and reducing process. The graphene coating, serving as a current “expressway”, bridged the electrolyte and current substrate, ensuring higher current collection efficiency and faster ion transition. Finally, the nanostructured core/shell CoO@NiO/ACT (serving as the positive electrode), ACT/graphene (serving as the negative electrode), and PVA-KOH gel (serving as both the solid-state electrolyte

and separator) were assembled into a flexible all-solid-state (CoO@NiO/ACT//ACT/graphene) asymmetric supercapacitor, which synergically worked together to achieve an exceptional combination of electrochemical properties in terms of working potential (1.6 V), energy density (52.26 Wh kg⁻¹), power density (9.53 KW kg⁻¹), and cycling stability (capacitance retention ratio of 97.53% after 2000 cycles).

3.2 Experiment Section

3.2.1 Preparation of Flexible CoO@NiO/ACT Positive Electrode

Fabrication of CoO nano-architectures on ACT with different morphologies

All chemicals were used after purchasing without further purification. A commercial cotton T-shirt was cleaned by distilled water in ultrasonic bath prior to activation. Activation of cotton T-shirt into ACT was performed following our previously established method. [33] CoO nano-architectures of different morphologies were grown on ACT fibers via a simple hydrothermal process. Typically, 0.01086 g of Co(NO₃)₂·6H₂O, 0.0269 g NH₄F, and 0.1051 g of urea (the concentration of reactants is named as 1 C) were dissolved in 70 mL distilled water. The resulting solution was transferred into a 100 mL Teflon-lined stainless autoclave with a piece of the vertically suspended ACT (1 cm × 2 cm) in the solution. Then, the autoclave was placed in an electric oven at 120 °C for 5 h. Finally, the as-prepared products were washed with ethanol and distilled water for several times, dried at 80 °C overnight, and annealed at 450 °C in argon atmosphere for 2 h to produce CoO/ACT. To achieve different morphologies the reactant concentration was varied from 1 C to 10 C. Sheet-like, petal-like, and urchin-like CoO nanostructures were uniformly deposited on ACT fibers at the reactant concentration of 1 C, 5 C, and 10 C, respectively.

Coating NiO nanoflakes onto urchin-like CoO nanowires

The screening on the as-synthesized CoO nanostructures showed that the urchin-like CoO nanostructure exhibited superior electrochemical performance. To further enhance its electrochemical properties NiO nanoflakes were deposited onto the urchin-like CoO nanostructure by a simple chemical bath deposition process, forming hierarchical core/shell CoO@NiO precursor. [47] Typically, 2 mL of aqueous ammonia (25-28%) was added to the mixture of 5 mL of 1 M nickel sulfate, and 8 mL of 0.25 M potassium persulfate to form a deposition solution. The

obtained urchin-like CoO/ACT was vertically dipped in the above solution and kept for 10 min at room temperature. The obtained sample was rinsed with distilled water and then dried at 80 °C for 12 h. The as-prepared hybrid CoO@NiO precursor was further annealed at 450 °C under argon gas protection for 2 h to realize a flexible hierarchical core/shell CoO@NiO/ACT electrode.

3.2.2 Preparation of Flexible ACT/Graphene Negative Electrode

Graphite oxide was synthesized from natural graphite flakes by a modified Hummers method. [48] The obtained graphite oxide was further exfoliated by ultrasonication in an ultrasonic bath for 1 h to prepare graphene oxide. Then, the above graphene oxide solution was centrifuged at 3000 rpm for 5 min to remove aggregates, forming a brown graphene oxide aqueous colloid with a concentration of 4 mg mL⁻¹. A piece of ACT (1 cm × 2 cm) was then soaked with the clean graphene oxide aqueous colloid. After drying at 60 °C for 6 h, the as-prepared ACT with graphene oxide coating was carried out at 450 °C 1 h with argon/hydrogen mixture gas (v/v 90/10) for the thermal reduction of ACT/graphene oxide to prepare a flexible ACT/graphene negative electrode.

2.3 Characterization Methods

The microstructure of the as-prepared samples was characterized by scanning electron microscopy (SEM; FEI Quanta 650) and transmission electron microscopy (TEM; JEOL 2000FX), high-resolution transmission electron microscopy (HRTEM, FEI Titan) and atomic force microscopy (AFM; Nanoscope IIIa). The crystallographic structure of the synthesized materials was determined by a PANalytical X'Pert Pro Multi-Purpose Diffractometer (MPD) equipped with Cu K_α radiation ($\lambda = 0.15406$ nm). Raman measurements were carried out by a Renishaw InVia Raman microscope at 785 nm (with 5% Laser Power).

3.2.4 Fabrication and Electrochemical Characterization of Flexible, All-Solid-State Asymmetric Supercapacitors

The asymmetric supercapacitors presented in this paper were assembled with two pieces of flexible electrodes (positive and negative) face-to-face separated by the solid-state polymer gel electrolyte. The polymer gel electrolyte was prepared by mixing 3 g KOH and 6 g PVA in 60 mL deionized water at 80 °C while being stirred magnetically until the solution became clear. Both the positive and negative electrodes were firstly dipped into the gel electrolyte solution for 3 min to soak gel electrolyte. After solidified at room temperature, two pieces of flexible electrodes

separated by the PVA/KOH gel film were used to assemble a flexible asymmetric supercapacitor. The as-obtained solid-state polymer PVA/KOH gel film served as both the separator and electrolyte. The electrochemical properties of the assembled flexible asymmetric supercapacitors were measured by using a CHI 660E electrochemical workstation. Cyclic voltammograms (CV), galvanostatic charge/discharge curves, and electrochemical impedance spectroscopy (EIS) in the frequency range from 100 kHz to 0.05 Hz with an AC perturbation of 5 mV were used to evaluate the electrochemical performance of the flexible solid-state asymmetric supercapacitors.

3.3 Results and Discussion

3.3.1 Positive Electrode Materials



Figure 3.1 Schematic illustration of the formation processes of CoO nanostructures of different morphologies and the core/shell CoO@NiO nanocomposite on the ACT.

The specific capacitances of transition metal oxides are usually sensitive to the thickness and mass of the active materials because of their poor conductivity. [49] An intelligent strategy to enhance electrochemical performance of transition metal oxides is to tune their microstructure to achieve large specific surface area. Figure 3.1 schematically illustrates the design and fabrication procedure of CoO nano-architectures of different morphologies on ACT fibers. The morphologies of CoO were found to be dependent strongly on the reactant concentration. Sheet-like, petal-like and urchin-like CoO nano-architectures were uniformly anchored on individual ACT fibers at the reactant concentration of 1 C, 5 C, and 10 C, respectively. Microporous transition metal oxide nanowires often possess higher conductivity and more active for energy storage applications. Therefore, the hydrothermally synthesized urchin-like CoO nanoarrays were chosen as the

backbone (core) for the deposition of NiO nanoflakes (shell) by a simple chemical bath deposition method. Finally, a hierarchical core/shell CoO@NiO

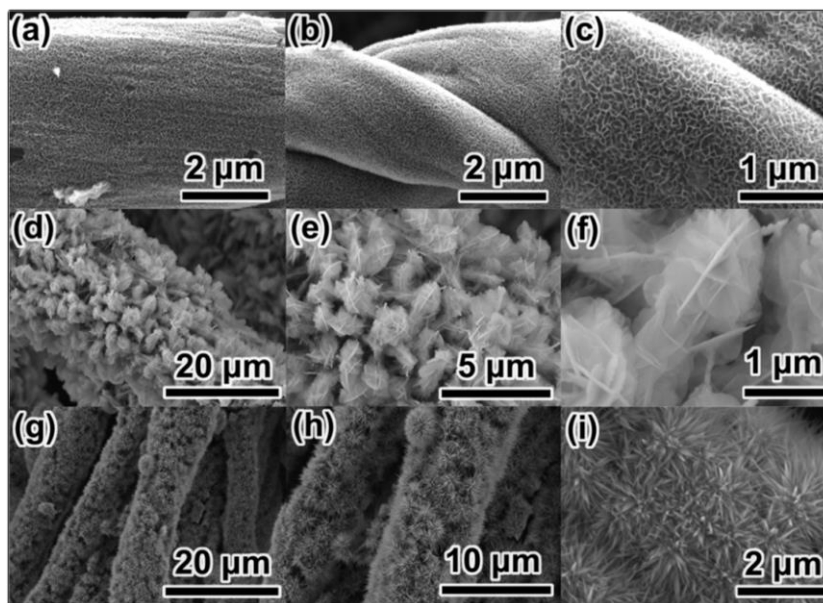
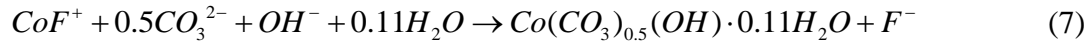
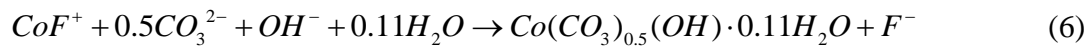


Figure 3.2 (a-c) SEM images of sheet-like CoO on ACT fibers at different magnifications; (d-f) SEM images of petal-like CoO on ACT fibers at different magnifications; (g-h) SEM images of urchin-like CoO on ACT fibers at different magnifications.

heterogeneous nanostructure with plenty of interspaces was closely anchored on the ACT fibers, which can be directly used as the binder-free flexible electrode. Importantly, the absence of conductive agent and polymer binders could effectively avoid the “dead volume” of active materials during the energy storage procedure. Such unique 3D hierarchical nanostructure not only enhances the contact between active material and substrate but also shorts the ion transport path and facilitates the continuous charge transfer, jointly improving the electrochemical performance.

Three different types of CoO nanostructures grown on ACT fibers were prepared by coupled hydrothermal and annealing processes. The morphologies and microstructure of CoO nano-architectures on ACT fibers are shown in Figure 3.2. As shown in Figures 3.2a-c, at the relatively low reactant concentration of 1 C, ACT fibers were uniformly covered by vertically grown CoO nanoarrays with cross-linked porous structure. Upon increasing reactant concentration up to 5 C, petal-like CoO nanosheets were assembled together to form flower-like nanotrees, closely anchored on the surfaces of ACT (Figures 3.2d-f). Those hierarchical nanotrees were uniformly distributed on individual ACT fibers to form a thick nanoforest, which provides larger surface areas for ion attachment, improving electrochemical performance. Interestingly, when the

reactant concentration was increased up to 10 C, urchin-like CoO nanospheres with interconnected CoO nanowires were jointly grown on ACT fibers to form open porous nano jungles with plenty of interspaces (Figures 3.2g-i). Such special nano-architecture possesses a higher surface/volume ratio and reaction activity, thereby enhancing its electrochemical performance. The chemical reactions involved in the hydrothermal synthesis and post-annealing process can be expressed with the following equations: [50,51]



The morphological change with the reactant concentration can be explained by the interplays of the nucleation rate, the growth rate of the nucleus and Ostwald-Ripening mechanism. [52] From the viewpoint of nucleation rate, the larger reactant concentration should result in a higher nucleation rate. Thus, much more nuclei formed in the solution at high reactant concentration. At the relatively low reactant concentration, a small number of CoO precursor nuclei first formed on the surface of the ACT, and grew slowly, leading to CoO precursor nanosheets vertically grown on the ACT. With further increasing reactant concentration, a large number of nuclei formed at the initial stage, the growth of nuclei and the aggregation of particles were both promoted. According to the Ostwald-Ripening mechanism, [53] small particles were absorbed by the relatively large ones, therefore a higher density of urchin-like CoO precursor nanospheres was synthesized at the high reactant concentration during the hydrothermal process.

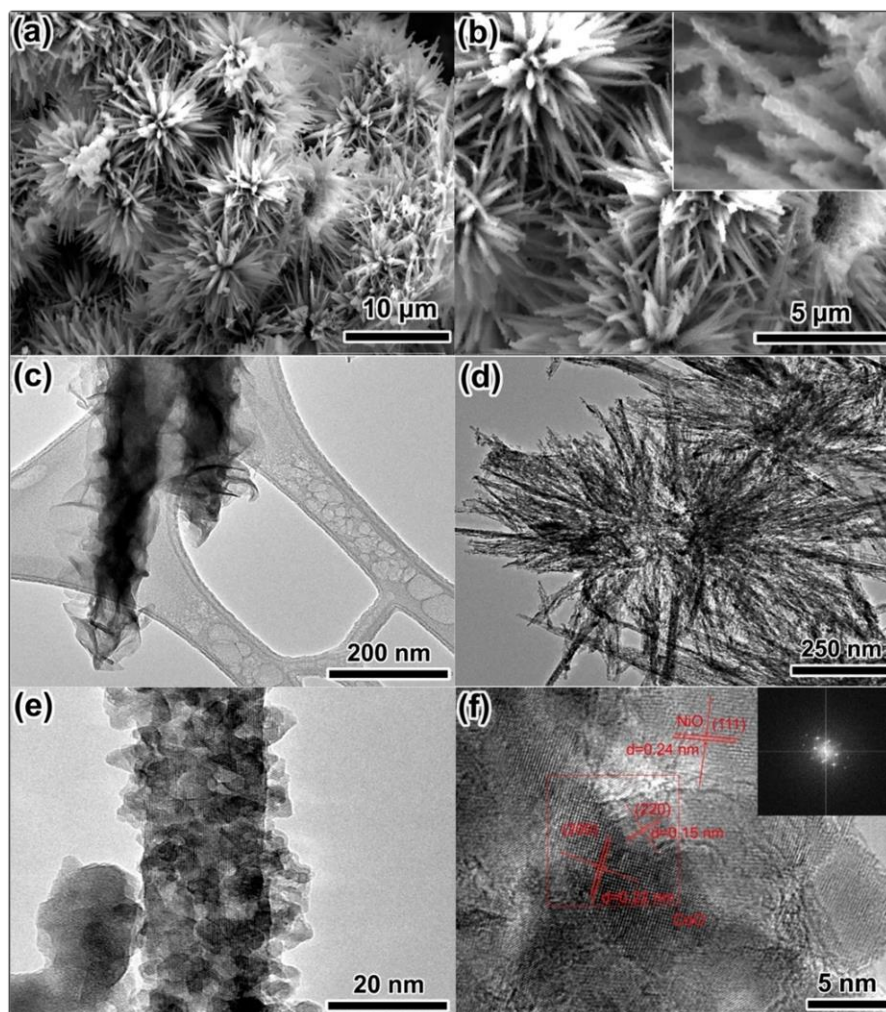


Figure 3.3 (a-b) SEM images of core/shell CoO@NiO nanostructure on ACT fibers at different magnifications; (c) TEM image of core/shell CoO@NiO precursor; (d-f) TEM and HRTEM images of core/shell CoO@NiO nanostructure, inset of (f) is the corresponding FFT pattern.

Ordered 1D CoO nanowires are thought to possess good electrochemical properties because they have easier electron transport paths and larger active interfacial sites. Therefore, urchin-like CoO nanosphere architecture was chosen as a backbone (core) to deposit a layer of NiO nanoflakes (shell). Figures 3.3a-b show the morphology of the as-prepared urchin-like CoO@NiO core/shell nanostructure on ACT fibers. The CoO nanowires have an average diameter of ~ 70 nm and the length up to ~ 5 μm . After the chemical bath deposition, uniform NiO nanoflakes were grown on the entire framework, forming a conformal NiO coating on the surface of CoO nanowires. The interconnected NiO nanoflake shells with a thickness of ~ 30 nm were uniformly decorated on the CoO backbone. The TEM images (Figures 3.3c-d) clearly reveal the details of such core/shell CoO@NiO nanostructure. After the heat treatment, mesopores with the size of 2-

4 nm appeared on the CoO nanowires (Figure 3.3e), which are anticipated to exhibit high electrochemical properties due to the high density of active sites and short electron transport path. The tiny NiO nano-flakes decorated on CoO nanowires render highly porous hierarchical nanostructure, which serves as a reservoir for electrolyte ions, providing dense diffusion channels for ion transport. Figure 3.3f shows the HRTEM image and corresponding FFT pattern of the core/shell CoO@NiO nanostructure. A clear grain boundary between the core and shell is apparent, with the interplanar spacings of 0.22 nm and 0.15 nm for the cubic phase CoO core, and 0.28 nm for the NiO shell, respectively.

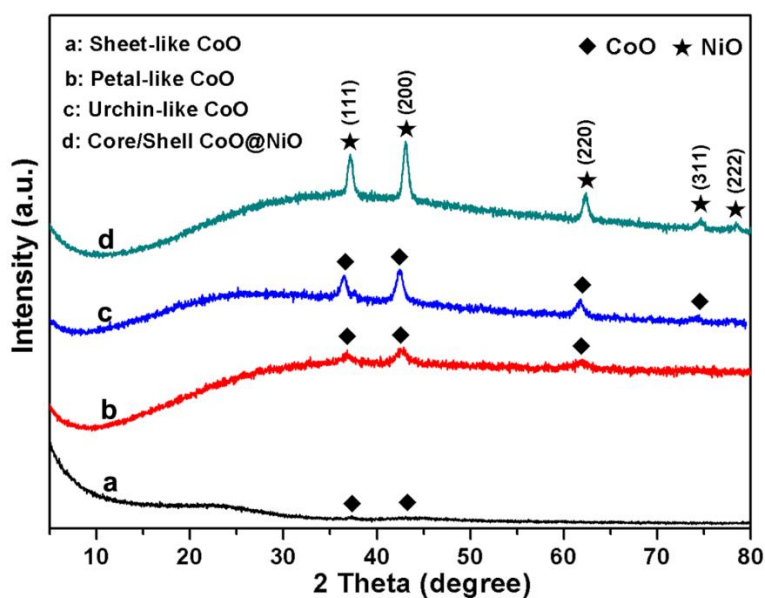


Figure 3.4 Typical XRD patterns of sheet-like CoO (a), petal-like CoO (b), urchin-like CoO (c) and the as-prepared hierarchical core/shell CoO@NiO nanocomposite (d).

Figure 3.4 shows the typical XRD patterns of the obtained sheet-like, petal-like, urchin-like CoO/ACT and the hierarchical core/shell CoO@NiO/ACT composite. The diffraction peaks of sheet-like CoO/ACT, petal-like CoO/ACT, urchin-like CoO/ACT can be indexed to the (111), (200), and (220) planes of the cubic CoO phase (JCPDS card no. 44-0962). Interestingly, not only the morphologies of the obtained CoO nano-architectures changed but also the crystallinity increased with increasing reactant concentration. The deposition of NiO shell on the urchin-like CoO/ACT significantly enhanced the diffraction intensity. However, it is difficult to differentiate the feature diffraction peaks among CoO and NiO (JCPDS card no. 65-2901), due to the similarity of their cubic crystal structures.

3.3.2 Negative Electrode Materials

Graphene has been regarded as a promising electrode material for energy storage and conversion due to its high surface area and superior conductivity. To further exploit its potential for a flexible electrode, graphene-based films/papers and 3D porous graphene structures have been widely used to overcome the re-stacking and aggregation of graphene nanosheets. In this study, a flexible ACT coated with graphene nanosheets was used as the negative electrode to construct asymmetric supercapacitors.

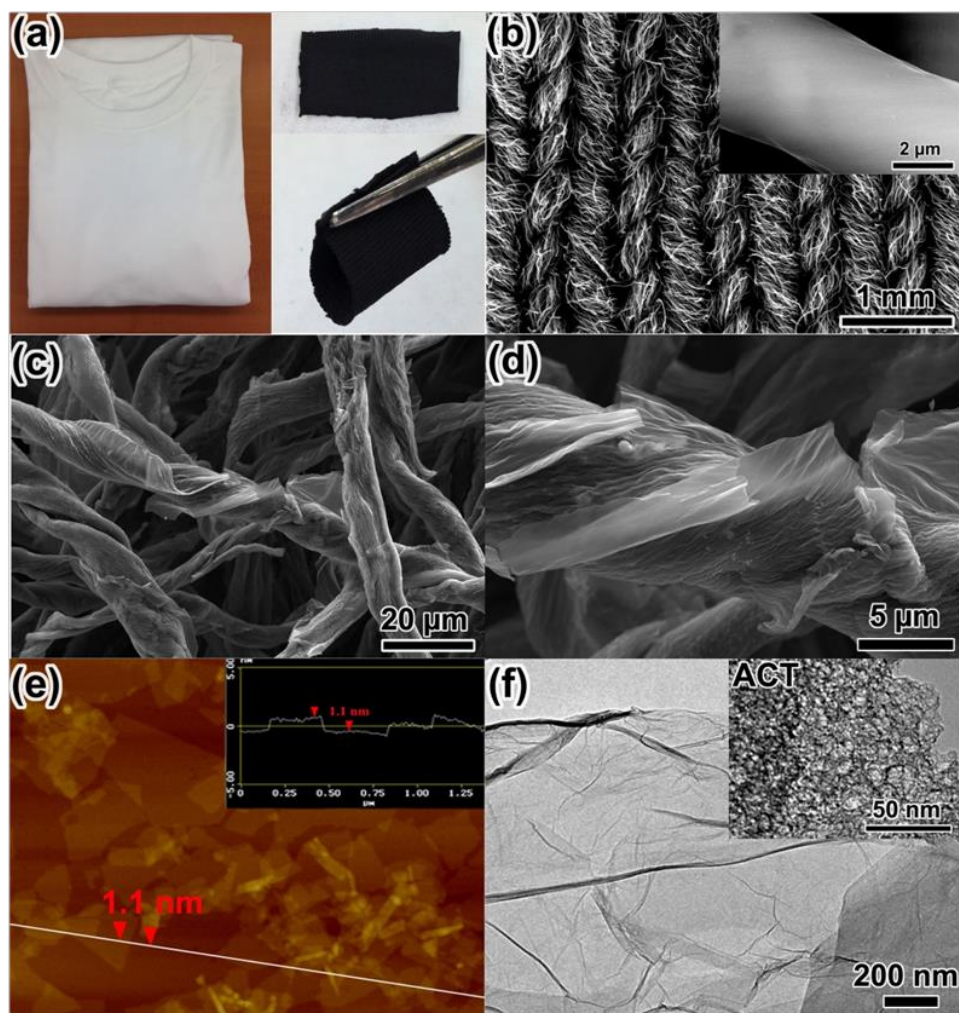


Figure 3.5 (a) Optical photographs of a cotton T-shirt, insets are a piece of ACT and a piece of ACT under folding state, showing its high flexibility; (b) SEM image of ACT, inset is the amplified SEM image; (c and d) SEM images of ACT coated with graphene sheets; (e) AFM image of graphene oxide with highlighted profile; (f) TEM image of graphene oxide nanosheet, inset is the TEM image of ACT.

Negative ACT/graphene electrode material was obtained by dipping ACT in a graphene oxide solution. ACT was prepared by direct conversion of a cotton T-shirt, as shown in Figure

3.5a. After activation, ACT was mechanically flexible even under folding state (inset of Figure 3.5a) and highly conductive (surface resistance: $\sim 10\text{-}20$ ohm/sq). Figure 3.5b is the SEM image of a piece of activated cotton textile, showing that the interwoven fibers of ACT inherit the cellulose fiber structure of cotton textile with the diameters ranging from 5 to 10 μm (inset of Figure 3.5b). After dipping ACT in the graphene oxide solution, individual ACT fibers were wrapped with single layered, curled and entangled graphene oxide sheet with a thickness of ~ 1.1 nm (Figures 3.5e and f). In the reduction process, reduced graphene oxide sheets were restored and conjugated, inducing partial overlapping or coalescing via π - π stacking or hydrogen bonding and consequently resulting in an interconnected 3D network (Figures 3.5c and d). [54,55] Interestingly, the ACT fibers also showed porous structure, as revealed by TEM image (the inset of Figure 3.5f). The coalesced and twisted graphene nanosheets randomly wrapped porous ACT fibers, forming a porous conductive ACT/graphene composite which serves as electron “highway” and collector. Such well-defined 3D porous structure is anticipated to facilitate electrolyte ion diffusion and electron transport in the rapid charge/discharge process, which in turn will improve the overall energy density of the cell.

Figure 3.6a shows the XRD patterns of cotton textile, ACT, ACT/graphene oxide and ACT/graphene. After activation, cotton’s (101), (002) and (040) peaks [56] disappeared, instead ACT exhibited a broader diffraction peak around 21° , pointing toward amorphous carbon. The ACT/graphene oxide exhibited a peak at 8.8° , corresponding to the (001) lattice plane of graphene oxide with a d-spacing of 0.78 nm. This indicates that graphite was completely exfoliated to single layered graphite oxide. [57] The peak at 8.8° disappeared for the ACT/graphene, indicating the complete reduction of graphene oxide to graphene. [58,59] Raman spectroscopy is an important nondestructive tool for characterizing graphitic materials, especially the ordered and disordered crystal structures of graphene. [60] The Raman spectrum of graphene usually can be characterized by two main feature bands: the G band arising from the first order scattering of the E_{1g} phonon of sp^2 C atoms at about 1575 cm^{-1} and the D band arising from a breathing mode of point photons of A_{1g} symmetry at about 1350 cm^{-1} . [61] Compared with ACT/graphite oxide, an increased I_D/I_G ratio of the ACT/graphene was observed (Figure 3.6b), indicating that the oxygen functional groups in graphene oxide sheets were removed and the conjugated graphene network (sp^2 carbon) was also reestablished during the heat reduction process. [62] The increase in the intensity ratio (I_D/I_G) is believed to result from the reestablishment of graphene network during the annealing

process, suggesting a relatively smaller average size and more defects and disordered structures than that of the original graphite oxide. [63,64] The results jointly demonstrate that most of the oxygen-containing groups have been successfully removed during the heat reduction process, which is consistent with the XRD data.

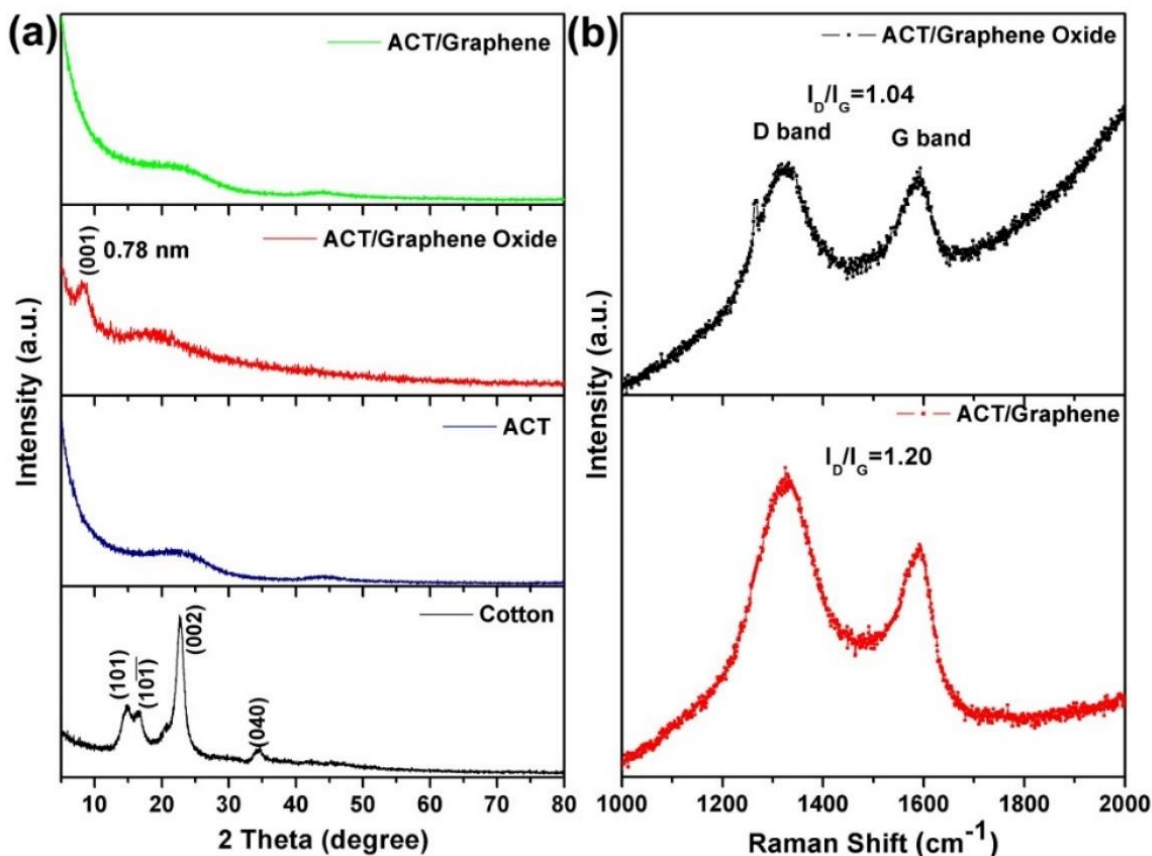


Figure 3.6 (a) Typical XRD patterns of cotton textile, ACT, ACT/graphene oxide and ACT/graphene; (b) Raman spectra of ACT/graphene oxide, and ACT/graphene.

3.3 Electrochemical Performance

A flexible asymmetric supercapacitor was constructed by two electrodes ($1 \times 2 \text{ cm}^2$) cemented with the PVA-KOH gel serving as both the solid electrolyte and separator, as schematically illustrated in Figure 3.7a. The as-prepared CoO/ACT with different morphologies and the hierarchical core/shell CoO@NiO/ACT were used as positive electrodes, whereas ACT/graphene was used as the negative electrode. The electrochemical performances of the asymmetric supercapacitors were investigated by cyclic voltammetry (CV) and galvanostatic charge/discharge and electrochemical impedance spectra (EIS) measurements under a two-electrode system.

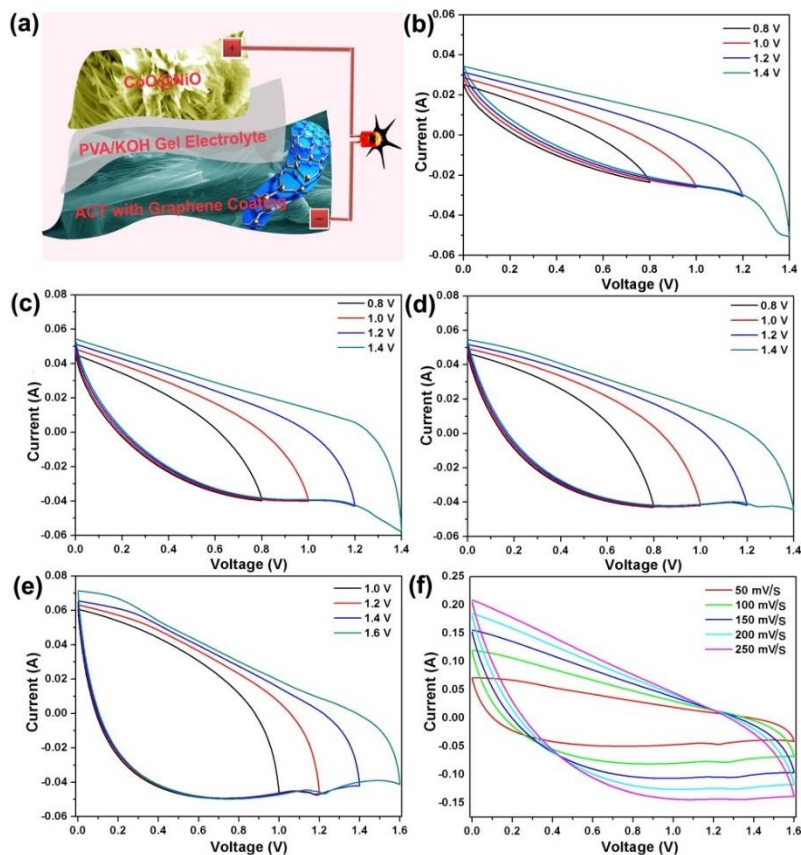
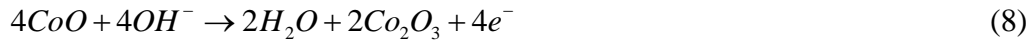


Figure 3.7 (a) Illustration of the assembled flexible all-solid-state asymmetric supercapacitor; (b) CV curves of sheet-like CoO/ACT//ACT/graphene asymmetric supercapacitor with PVA/KOH polymer gel electrolyte under the voltage windows of 0.8, 1.0, 1.2 and 1.4 V at the scan rate of 50 mV s^{-1} ; (c) CV curves of petal-like CoO//ACT/graphene asymmetric supercapacitor with PVA/KOH polymer gel electrolyte under the voltage windows of 0.8, 1.0, 1.2 and 1.4 V at the scan rate of 50 mV s^{-1} ; (d) CV curves of urchin-like CoO//ACT/graphene asymmetric supercapacitor with PVA/KOH polymer gel electrolyte under the voltage windows of 0.8, 1.0, 1.2 and 1.4 V at the scan rate of 50 mV s^{-1} ; (e) CV curves of core/shell CoO@NiO//ACT/graphene asymmetric supercapacitor with PVA/KOH polymer gel electrolyte under the voltage windows of 1, 1.2, 1.4 and 1.6 V at the scan rate of 50 mV s^{-1} ; (f) CV curves of core/shell CoO@NiO//ACT/graphene asymmetric supercapacitor with PVA/KOH polymer gel electrolyte under the voltage windows of 1.6 V at different scan rates.

Figures 3.7b-d show the CV curves of CoO/ACT//ACT/graphene asymmetric supercapacitors with the PVA/KOH polymer gel electrolyte under the voltage windows of 0.8, 1.0, 1.2 and 1.4 V at the scan rate of 50 mV s^{-1} . It can be seen that the working voltage for those CoO/ACT//ACT/graphene asymmetric supercapacitors can be extended to 1.4 V, which is essential for practical application. Compared with the sheet-like CoO/ACT cell, the CV curves for the petal-like and urchin-like CoO/ACT cells showed better rectangularity, suggesting lower charge transfer resistance and better rate performance. Although the shape of CV curves for the petal-like CoO/ACT cell and urchin-like CoO/ACT cell are similar, the integrated area based on the CV curve of the urchin-like petal-like CoO/ACT cell is larger than that of the petal-like

CoO/ACT cell at different potential windows, indicating a higher capacitance for the urchin-like CoO/ACT cell. Therefore, the urchin-like CoO/ACT nanowire was further selected for the fabrication of hierarchical porous core/shell CoO@NiO/ACT composite electrode for high-performance flexible supercapacitors. Figure 3.7e shows the CV curves of the flexible all-solid-state core/shell CoO@NiO/ACT//ACT/graphene asymmetric supercapacitor at the different voltage windows, performed at the scan rate of 50 mV s⁻¹. Compared with the CoO/ACT cells with different CoO nanostructures, the fabricated core/shell CoO@NiO/ACT//ACT/graphene asymmetric cell showed combined pseudo-capacitive and electric double-layer capacitive behaviors, even at a high working potential up to 1.6 V. Therefore, the operation potential window was chosen as 1.6 V for the core/shell CoO@NiO/ACT to further evaluate its supercapacitor performance. Figure 3.7f shows the CV curves of the CoO@NiO/ACT//ACT/graphene asymmetric cell at different scan rates ranging from 50 to 250 mV s⁻¹ at the operation window of 1.6 V. Apparently, all the curves exhibit a similar shape, and the current density increases with increasing scan rate, indicating stable reversibility and excellent rate performance. The charge storage is ascribed to the Faradaic redox reactions of CoO and NiO in the PVA-KOH electrolyte as follows: [65,66]



However, unlike traditional pseudo-capacitive electrode, the CoO@NiO/ACT//ACT/graphene asymmetric cell displayed a quasi-rectangular CV geometry, indicating an electrochemical double layer capacitor behavior.

Figure 3.8 shows the typical galvanostatic charging/discharging curves of the different morphological CoO/ACT//ACT/graphene and core/shell CoO@NiO/ACT//ACT/graphene asymmetric supercapacitors at different current densities. The cell voltage of the as-fabricated CoO/ACT is 1.4 V, while the cell voltage can be expanded to 1.6 V (from 0 to 1.6 V) for the core/shell CoO@NiO/ACT//ACT/graphene asymmetric cell without showing obvious IR drop, which could be attributed to the small internal resistance. The specific capacitances for the sheet-like CoO@NiO/ACT, petal-like CoO@NiO/ACT, urchin-like CoO@NiO/ACT and core/shell CoO@NiO/ACT asymmetric cells at the current density of 10 mA cm⁻² are 106, 135, 138, and

147.6 F g⁻¹, respectively. The large specific capacitance, symmetric charging/discharging curves and the good linear relationship could be ascribed to the synergistic effects of the hierarchical CoO@NiO nanostructure and the electrochemical double layer capacitance of ACT/graphene, indicating excellent electrochemical capacitive characteristic and superior reversible redox reaction.

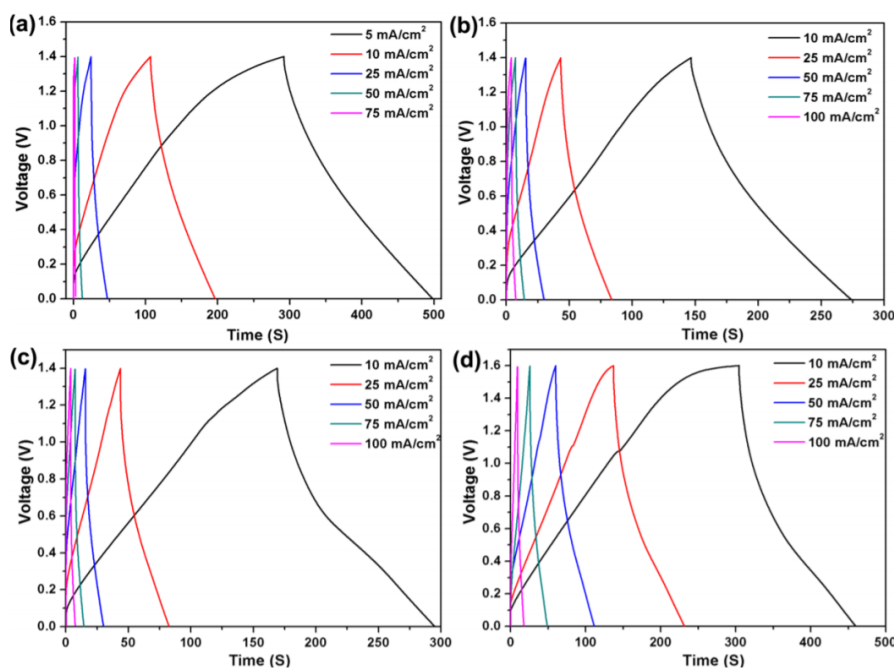


Figure 3.8 (a) Charging/discharging curves of sheet-like CoO/ACT//ACT/graphene asymmetric supercapacitor with PVA/KOH polymer gel electrolyte at different current densities; (b) Charging/discharging curves of petal-like CoO/ACT//ACT/graphene asymmetric supercapacitor with PVA/KOH polymer gel electrolyte at different current densities; (c) Charging/discharging curves of urchin-like CoO/ACT//ACT/graphene asymmetric supercapacitor with PVA/KOH polymer gel electrolyte at different current densities; (d) Charging/discharging curves of core/shell CoO@NiO/ACT//ACT/graphene asymmetric supercapacitor with PVA/KOH polymer gel electrolyte at different current densities.

Rate performance and Coulombic efficiency are also important factors for real power application. To further evaluate the potential of the core/shell CoO@NiO/ACT//ACT/graphene asymmetric cell for practical application, the galvanostatic charge/discharge tests were carried out at different current densities ranging from 10 to 100 mA cm⁻² (Figure 3.9a). The corresponding specific capacitances for the asymmetric supercapacitor are respectively 147.6 F g⁻¹ at 10 mA cm⁻² and 86.7 F g⁻¹ at 100 mA cm⁻² with a capacitance retention of 58.7% while the current density was increased by 10 times, suggesting great rate performance for the asymmetric CoO@NiO/ACT//ACT/graphene supercapacitor. The Coulombic efficiency exhibited a fast

increase at the initial stage from 53.3% at 10 mA cm⁻² to 91.52 at 25 mA cm⁻² and then a gradual increase up to 98.8%. The high Coulombic efficiency is very important for enhancing the energy utilization efficiency and promoting electrochemical reversibility, which can be ascribed to the hierarchal structure with the higher activated surface, improved mass transportation, and good conductivity.

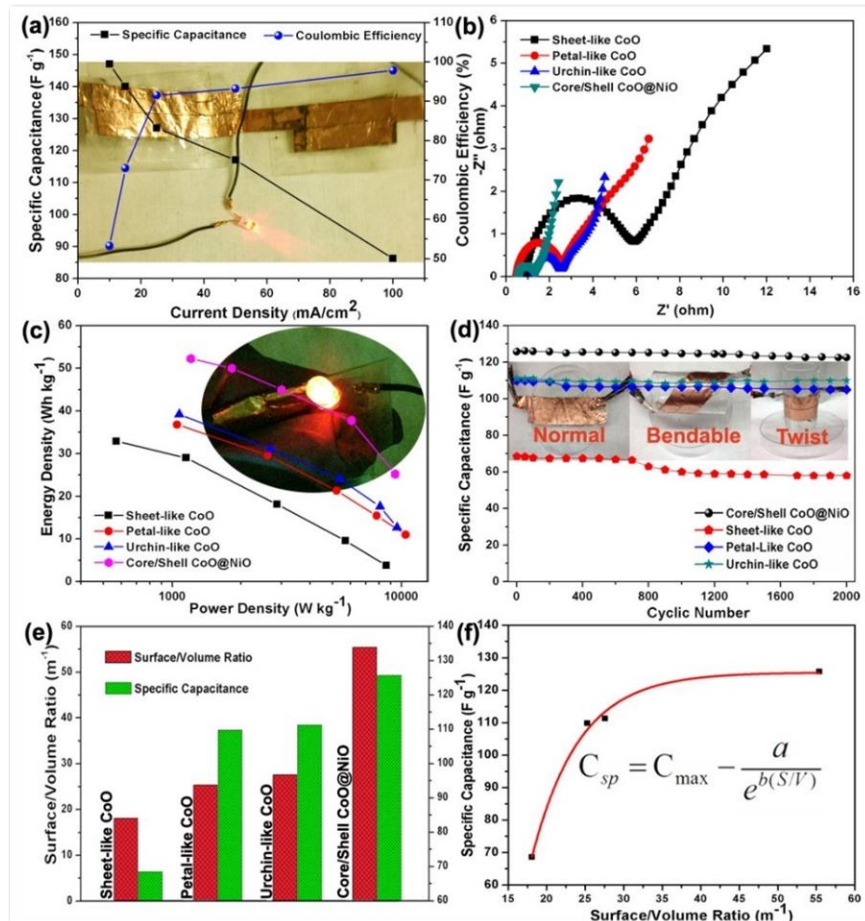


Figure 3.9 (a) Specific capacitances and Coulombic efficiency of the core/shell CoO@NiO/ACT//ACT/graphene asymmetric supercapacitor with PVA/KOH as polymer gel electrolyte, inset shows a lighted LED by two asymmetric supercapacitors connected in series; (b) Nyquist plots of the sheet-like CoO/ACT//ACT/graphene supercapacitor, petal-like CoO/ACT//ACT/graphene, urchin-like CoO/ACT//ACT/graphene and core/shell CoO@NiO/ACT//ACT/graphene asymmetric supercapacitors with PVA/KOH polymer gel electrolyte; (c) Ragone plots of the as-assembled sheet-like CoO/ACT//ACT/graphene supercapacitor, petal-like CoO/ACT//ACT/graphene, urchin-like CoO/ACT//ACT/graphene and core/shell CoO@NiO/ACT//ACT/graphene asymmetric supercapacitors with PVA/KOH polymer gel electrolyte, inset shows the lighted LED by the asymmetric supercapacitor even under totally folded state; (d) Cyclic performance of the sheet-like CoO/ACT//ACT/graphene supercapacitor, petal-like CoO/ACT//ACT/graphene, urchin-like CoO/ACT//ACT/graphene and core/shell CoO@NiO/ACT//ACT/graphene asymmetric supercapacitors with PVA/KOH polymer gel electrolyte under different working condition; (e) Surface/volume ratios and specific capacitances of sheet-like CoO, petal-like CoO, urchin-like CoO and the as-prepared hierarchical core/shell CoO@NiO nanocomposite; (f) Fitting result and corresponding mathematical expression of the relationship between surface/volume ratio and specific capacitance.

Electrochemical impedance spectroscopy (EIS) is one of the principal methods for studying the fundamental electrochemical behavior of supercapacitors. For an in-depth understanding of the electrochemical mechanism in the all-solid-state asymmetric supercapacitors, the impedance spectra of CoO@NiO/ACT//ACT/graphene with different morphologies and core/shell CoO@NiO/ACT//ACT/graphene asymmetric supercapacitors were measured in the frequencies ranging from 100 kHz to 0.05 Hz at the open circuit potential with an AC perturbation of 5 mV. All the impedance spectra exhibit a similar shape, with an arc at high frequency and a straight line at low frequency (Figure 3.9b). The high-frequency arc corresponds to the charge transfer limiting process, which is ascribed to the double-layer capacitance (C_{dl}) and the charge transfer resistance (R_{ct}) at the interface between electrode and electrolyte solution. [67] The charge-transfer resistance R_{ct} was directly measured from the diameter of the semicircle arc. Compared with the R_{ct} of CoO/ACT//ACT/graphene cells with different morphologies (sheet-like CoO/ACT (4.91 Ω), petal-like CoO/ACT (2.05 Ω), urchin-like CoO/ACT (1.37 Ω)), the core/shell CoO@NiO/ACT//ACT/graphene displays the smallest R_{ct} (0.81 Ω), indicating the good electron transport path and easy ions accessibility for the core/shell CoO@NiO/ACT//ACT/graphene cell. In addition, the straight line at low frequency exhibits a slope closer to 90°, indicating the improved conductivity and low ions diffusion resistance for core/shell CoO@NiO/ACT//ACT/graphene cell. [68]

Energy density and power density are also important factors for evaluating the practical application potentials of supercapacitors. It is expected that the good supercapacitor could provide both high energy density and high power density at high charge/discharge rates. Figure 3.9c shows the Ragone plots of all-solid-state flexible CoO/ACT//ACT/graphene and core/shell CoO@NiO/ACT//ACT/graphene asymmetric cells. All the asymmetric cells showed a similar trend of energy density and power density. Compared with the CoO/ACT//ACT/graphene cells, encouragingly, the core/shell CoO@NiO/ACT//ACT/graphene asymmetric cell achieved a higher energy density of 52.26 Wh kg⁻¹ at the power density of 1206 W kg⁻¹, and remained 25.2 Wh kg⁻¹ at the power density of 9.53 KW kg⁻¹. The superior performances for the core/shell CoO@NiO/ACT//ACT/graphene asymmetric cell are ascribed to the synergistic effects of ACT/graphene and hierarchical core/shell CoO@NiO nanostructure. A long cycling performance is another crucial requirement for the practical application of supercapacitors. Figure 3.9d shows the cyclic performances of the flexible all-solid-state CoO/ACT//ACT/graphene and core/shell

CoO@NiO/ACT//ACT/graphene asymmetric cells, examined by galvanostatic charge/discharge tests at the constant current density of 25 mA cm⁻² under different mechanical states (normal, bent and twisted states) for up to 2000 cycles. All the asymmetric cells exhibit small capacitance decay during the cyclic tests. Encouragingly, the core/shell CoO@NiO/ACT//ACT/graphene asymmetric cell showed an increase in specific capacitance at the initial 50 cycles under normal state, which is ascribed to the complete exposure and full use of Ni and Co active sites. It is remarkable that 97.53% of its pristine specific capacitance was maintained after 2000 cycles, even at the bent and twisted states (inset of Figure 3.9d), indicating excellent mechanical flexibility, electrochemical robustness and cycle stability. The digital photographs of the as-assembled flexible supercapacitors packed with PET tape are shown in the inset of Figure 3.9a to demonstrate its practical application. Two as-assembled flexible all-solid-state cells were then connected in series to light a commercial red LED (inset of Figure 3.9a). Even in a folded state (inset of Figure 3.9c), the brightness of the lightened LED did not change, showing its excellent coupled mechanical and electrochemical robustness. All in all, the core/shell CoO@NiO/ACT//ACT/graphene asymmetric cell exhibited superior electrochemical stability, which is believed to result from the unique structure of the CoO@NiO nanostructure and graphene, the intimate interfacial contact between hierarchical core/shell CoO@NiO and ACT substrate, high electrical conductivity of the wrapped graphene, and the excellent mechanical robustness of both electrodes and gel electrolyte film.

Based on the above electrochemical analysis, it can be seen that the electrochemical properties of CoO nanostructures are strongly morphology-dependent. To unveil the relationship between the morphology and electrochemical performance, 3D morphology models were established by using Autodesk 3ds Max for individual nano-architectures to estimate their surface/volume ratios, according to their size from the SEM images (Figures 3.2 and 3.3). Figure 3.9e shows the surface/volume ratios and specific capacitances of the prepared CoO nanostructures with different morphologies and the core/shell CoO@NiO composite. It can be seen that the architecture with a larger surface area exhibits higher specific capacitance. The relationship between the specific capacitance and surface/volume ratio can be well fitted by a negative exponential function:

$$C_{sp} = C_{max} - \frac{a}{e^{b(S/V)}} \quad (10)$$

where C_{sp} is the specific capacitance, C_{max} is the theoretical specific value for the system with the specific positive electrode, negative electrode, and electrolyte, S/V is the surface/volume ratio, a and b are constants which are system dependent. Here, the theoretical maximum specific capacitance (C_{max}) of the assembled cell at the current density of 25 mA cm^{-2} is $125.47756 \text{ F g}^{-1}$, the constants a and b are 1084.2981 and 0.1829, respectively. Clearly, the hierarchical core/shell CoO@NiO composite possesses higher surface/volume ratio and higher specific capacitance than other CoO nano-architectures. Thus, the specific surface area plays an important role in specific capacitance. However, there exists an upper limit (C_{max}), which cannot be exceeded. When approaching to the upper limit, further increasing specific surface area cannot push up specific capacitance much. This finding provides an important guideline for electrode materials design, microstructure control, and system construction.

3.4 Conclusion

Battery-type faradic CoO nano-architectures with different morphologies (sheet-like, petal-like and urchin-like) were controllably synthesized on ACTs by simply changing the reactant concentration during the hydrothermal process. The electrochemical properties of CoO nanostructures were found to be strongly morphology-dependent. The specific capacitance increased exponentially with the surface/volume ratio of nanostructures. Due to its higher surface/volume ratio and better electrochemical performance, the urchin-like CoO nanowire was further chosen as the backbones (core) for depositing a layer of pseudocapacitive NiO nano-flakes (shell) to construct a hierarchical 3D porous core/shell CoO@NiO/ACT nanostructure with super surface, which is beneficial for the charge accumulation and ion transport, enabling the high performance for flexible supercapacitor application. In addition, the activation of cotton textiles into porous, highly conductive ACTs with high accessible surface area, and the good electrical conductivity rendered by wrapped graphene endowed the flexible asymmetric supercapacitor with higher rate performance. PVA-KOH solid-state gel was used as both the electrolyte and separator. Finally, the assembled CoO@NiO/ACT//ACT/graphene asymmetric supercapacitor exhibited an exceptional combination of mechanical and electrochemical performances, including high specific capacitance, remarkable energy density and power density, exceptional high operating potential (1.6 V), excellent cycling stability and eminent mechanical robustness. This work opens up

unprecedented opportunities for designing hybrid transition metal oxides and graphene on flexible ACTs nanoarchitectures for next generation flexible/wearable energy storage devices.

References

- [1] J. M. Tarascon, *Philos. Trans. A. Math. Phys. Eng. Sci.* 2010, **368**, 3227.
- [2] P. Simon and Y. Gogotsi, *Nat. Mater.* 2008, **7**, 845.
- [3] B. E. Conway, *Electrochemical Supercapacitors: Scientific Fundamentals and Technological Applications*, Kluwer Academic Publishers/Plenum Press, New York, 1999.
- [4] A. Burke, *J. Power Sources* 2000, **91**, 37.
- [5] M. S. Halper and J. C. Ellenbogen, *Supercapacitors: a Brief Overview*, MITRE Nanosystems Group, Virginia, 2006
- [6] G. Yu, L. Hu, N. Liu, H. Wang, M. Vosgueritchian, Y. Yang, Y. Cui and Z. Bao, *Nano Lett.* 2011, **11**, 4438.
- [7] L. Bao, J. Zang and X. Li, *Nano Lett.* 2011, **11**, 1215.
- [8] J. W. Jeon, R. Sharma, P. Meduri, B. W. Arey, H. T. Schaefer, J. L. Lutkenhaus, J. P. Lemmon, P. K. Thallapally, M. I. Nandasiri, B. P. McGrail and S. K. Nune, *ACS Appl. Mater. Interfaces* 2014, **6**, 7214.
- [9] E. Frackowiak, Carbon Materials for Supercapacitor Application. *Phys. Chem. Chem. Phys.* 2007, **9**, 1774.
- [10] Y. B. Tan and J. M. Lee, *J. Mater. Chem. A* 2013, **1**, 14814.
- [11] H. Pan, J. Li and Y. P. Feng, *Nanoscale Res. Lett.*, 2010, **5**, 654.
- [12] Q. Liang, L. Ye, Z. H. Huang, Q. Xu, Y. Bai, F. Kang and Q. H. Yang, *Nanoscale* 2014, **6**, 13831.
- [13] C. C. Hu, K. H. Chang, M. C. Lin and Y. T. Wu, *Nano Lett.* 2006, **6**, 2690.
- [14] P. Yu, X. Zhang, D. Wang, L. Wang and Y. Ma, *Cryst. Growth Des.* 2009, **9**, 528.

- [15] W. Yang, Z. Gao, J. Ma, J. Wang, B. Wang and L. Liu, *Electrochim. Acta* 2013, **112**, 378.
- [16] J. Li, W. Zhao, F. Huang, A. Manivannan and N. Wu, *Nanoscale* 2011, **3**, 5103.
- [17] Z. Gao, W. Yang, Y. Yan, J. Wang, J. Ma, X. Zhang, B. Xing and L. Liu, *Eur. J. Inorg. Chem.* 2013, **27**, 4832.
- [18] G. A. Snook, P. Kao and A. S. Best, *J. Power Sources* 2011, **196**, 1.
- [19] K. Jurewicz, S. Delpoux, V. Bertagna, F. Béguin and E. Frackowiak, *Chem. Phys. Lett.* 2001, **347**, 36.
- [20] W. Yang, Z. Gao, N. Song, Y. Zhang, Y. Yang and J. Wang, *J. Power Sources* 2014, **272**, 915.
- [21] H. Wei, Y. Wang, J. Guo, X. Yan, R. O'Connor, X. Zhang, N. Z. Shen, B. L. Weeks, X. Huang, S. Wei and Z. Guo, *ChemElectroChem*, 2015, **2**, 119-126.
- [22] C. Liu, F. Li, L. P. Ma and H. M. Cheng, *Adv. Mater.* 2010, **22**, E28.
- [23] R. B. Rakhi, W. Chen, D. Cha and H. N. Alshareef, *Mater. Renew. Sustain. Energy* 2013, **2**, 17.
- [24] H. Wang, Z. Xu, H. Yi, H. Wei, Z. Guo and X. Wang, *Nano Energy*, 2014, **7**, 86-96.
- [25] K. Jost, G. Dion and Y. Gogotsi, *J. Mater. Chem. A* 2014, **2**, 10776.
- [26] W. Yang, Z. Gao, J. Ma, X. Zhang, J. Wang and J. Liu, *J. Mater. Chem. A* 2014, **2**, 1448.
- [27] L. Yuan, X. Lu, X. Xiao, T. Zhai, J. Dai, F. Zhang, B. Hu, X. Wang, L. Gong, J. Chen, C. Hu, Y. Tong, J. Zhou and Z. L. Wang, *ACS Nano*, 2012, **6**, 656.
- [28] C. Meng, C. Liu, L. Chen, C. Hu and S. Fan, *Nano Lett.* 2010, **10**, 4025.
- [29] C. D. Lokhande, D. P. Dubal and O. S. Joo, *Curr. Appl. Phys.* 2011, **11**, 255.
- [30] P. Simon, Y. Gogotsi and B. Dunn, *Science*, 2014, **343**, 1210.
- [31] X. Xia, J. Tu, Y. Zhang, X. Wang, C. Gu, X. B. Zhao and H. J. Fan, *ACS Nano* 2012, **6**, 5531.

- [32] G. Zhang, T. Wang, X. Yu, H. Zhang, H. Duan and B. Lu, *Nano Energy* 2013, **2**, 586.
- [33] Z. Gao, N. N. Song, Y. Y. Zhang and X. D. Li, *RSC Adv.* 2015, **5**, 15438.
- [34] P. Liu, Z. Hu, Y. Liu, M. Yao, Q. Zhang and Z. Xu, *Int. J. Electrochem. Sci.* 2014, **9**, 7986.
- [35] D. Lan, Y. Chen, P. Chen, X. Chen, X. Wu, X. Pu, Y. Zeng and Z. Zhu, *ACS Appl. Mater. Interfaces* 2014, **6**, 11839.
- [36] C. Zhou, Y. Zhang, Y. Li, J. Liu, C. Zhou, Y. Zhang, Y. Li. And J. Liu, *Nano Lett.* 2013, **13**, 2078.
- [37] C. Guan, X. Li, Z. Wang, X. Cao, C. Soci, H. Zhang and H. J. Fan, *Adv. Mater.* 2012, **24**, 4186.
- [38] Z. Fan, J. Yan, T. Wei, L. Zhi, G. Ning, T. Li and F. Wei, *Adv. Funct. Mater.* 2011, **21**, 2366.
- [39] Y. G. Wang, Z. D. Wang and Y. Y. Xia, *Electrochim. Acta* 2005, **50**, 5641.
- [40] Y. B. Tan and J. M. Lee, *J. Mater. Chem. A* 2013, **1**, 14814.
- [41] J. Liu, L. Zhang, H. B. Wu, J. Lin, Z. Shen and X. W. (David), Lou, *Energy Environ. Sci.* 2014, **7**, 3709.
- [42] H. Gao, F. Xiao, C. B. Ching and H. Duan, *ACS Appl. Mater. Interfaces* 2012, **4**, 2801.
- [43] A. Sumboja, C. Y. Foo, X. Wang and P. S. Lee, *Adv. Mater.* 2013, **25**, 2809.
- [44] Z. Gao, W. Yang, J. Wang, N. Song and X. Li, *Nano Energy* 2015, **13**, 306.
- [45] A. G. Avila and J. P. Hinstroza, *Nat. Nanotechnol.* 2008, **3**, 458-459.
- [46] L. Bao, and X. Li, *Adv. Mater.* 2012, **24**, 3246.
- [47] X. H. Xia, J. P. Tu, J. Zhang, X. L. Wang, W. K. Zhang and H. Huang, *Sol. Energy Mater. Sol. Cells* 2008, **92**, 628.
- [48] W. S. Hummers and R. E. Offeman, *J. Am. Chem. Soc.* 1958, **80**, 1339-1339.
- [49] G. Li, W. Li, K. Xu, R. Zou, Z. Chen and J. Hu, *J. Mater. Chem. A* 2014, **2**, 7738.

- [50] Y. G. Zhu, Y. Wang, Y. Shi, J. I. Wong and H. Y. Yang, *Nano Energy* 2014, **3**, 46.
- [51] K. Cao, L. Jiao, Y. Liu, H. Liu, Y. Wang and H. Yuan, *Adv. Funct. Mater.* 2015, **25**, 1082.
- [52] W. P. Zhang, B. G. Zhao, C. D. Zou, Q. J. Zhai and Y. L. Gao, *Trans. Nonferrous Met. Soc. China English Ed.* 2013, **23**, 1668.
- [53] P. W. Voorhees, *J. Statist. Phys* 1985, **38**, 231..
- [54] H. Bai, C. Li, X. Wang and G. Shi, *J. Phys. Chem. C* 2011, **115**, 5545.
- [55] W. Chen and L. Yan, *Nanoscale* 2011, **3**, 3132.
- [56] E. N. J. Ford, S. K. Mendon, S. F. Thames and J. W. Rawlins, *J. Eng. Fiber. Fabr.* 2010, **5**, 10.
- [57] Z. H. Liu, Z. M. Wang, X. Yang and K. Ooi, *Langmuir* 2002, **18**, 4926.
- [58] H. M. A. Hassan, V. Abdelsayed, A. E. R. S. Khder, K. M. AbouZeid, J. Turner, M. S. El-Shall, S. I. Al-Resayes and A. A. El-Azhary, *J. Mater. Chem.* 2009, **19**, 3832.
- [59] M. J. McAllister, J. L. Li, D. H. Adamson, H. C. Schniepp, A. A. Abdala, J. Liu, M. Herrera-Alonso, D. L. Milius, R. Car, R. K. Prud'homme and I. A. Aksay, *Chem. Mater.* 2007, **19**, 4396.
- [60] G. Bronoel, A. Millot and N. Tassin, *J. Power Sources* 1991, **34**, 243.
- [61] A. Ferrari and J. Robertson, *Phys. Rev. B* 2000, **61**, 14095.
- [62] Z. Ji, X. Shen, M. Li, H. Zhou, G. Zhu and K. Chen, *Nanotechnology* 2013, **24**, 115603.
- [63] C. Xu, X. Wang and J. Zhu, *J. Phys. Chem. C* 2008, **112**, 19841.
- [64] Y. Wang, Q. He, H. Qu, X. Zhang, J. Guo, J. Zhu, G. Zhao, H. A. Colorado, J. Yu, L. Sun, S. Bhana, M. A. Khan, X. Huang, D. P. Young, H. Wang, X. Wang, S. Wei and Z. Guo, *J. Mater. Chem. C*, 2014, **2**, 9478-9488.
- [65] C. Zheng, C. Cao, Z. Ali and J. Hou, *J. Mater. Chem. A* 2014, **2**, 16467.
- [66] K. Liang, X. Tang and W. Hu, *J. Mater. Chem.* 2012, **22**, 11062.

- [67] A. D. Fabio, A. Giorgi, M. Mastragostino and F. Soavi, *J. Electrochem. Soc.* 2001,**148**, A845.
- [68] G. J. Brug, A. V. Eeden, M. Sluyters-Rehbach and J. H. Sluyters, *J. Electroanal. Chem.* 1984, **176**, 275.

Chapter 4. Cotton Textile Enabled Flexible Lithium-ion Batteries

4.1 Introduction

With the impending energy crisis and increasing environmental concerns, a worldwide imperative is to develop greener and more efficient energy conversion and storage devices with the goal of utilizing renewable and sustainable energy sources, such as solar, wind, geothermal and tidal energy. [1] Lithium-ion batteries, as one of the most important energy storage devices, have revolutionized the modern society in all aspects, especially for consumer electronics and electric vehicles, because of their high energy density, lightweight and long lifespan. [2-6] To date, graphite is frequently used as an anode material, however, its low theoretical capacity (372 mAh g^{-1}) and unresolved safety issue hinder its practical application, especially for large-scale grid energy storage and sustainable transport. [7] Many efforts have been made to develop electrode materials with superior capacity and longer lifespan to replace graphite. In this context, numerous anode materials including silicon, [8] germanium, [9] tin, [10] transition metal oxides (*i.e.* Co_3O_4 , SnO_2 , NiO) [11-13] and sulfides (*i.e.* NiS , Ni_3S_4 , SnS_2 , CoS_2 , Co_9S_8 , FeS_2) [14-19] have been extensively explored as alternative anode materials, due to their remarkable theoretical capacities, high lithium activity, low cost and natural abundance. However, metal oxides and sulfides usually suffer from huge volume change and pulverization during Li^+ insertion-extraction process, which often leads to cracking, poor electronic conductivity or even fracture of the anode. [20]

Compared with metal oxides, metal sulfides possess combinatory physical and chemical properties, such as higher electrical conductivity, better thermal stability, and richer redox chemistry, making them more promising for lithium-ion batteries. [21-22] Among various metal sulfides, nickel sulfides have been well explored in a wide range of technical fields, including solar cell, hydrogen production, catalysis, optoelectronics, energy conversion, and storage. [23-27] For instance, NiS , NiS_2 , Ni_3S_2 , and Ni_3S_4 have gained special attention as electrode materials for lithium-ion batteries and supercapacitors. [21,27-31] Unfortunately, a bulk electrode usually exhibits sluggish lithium ion diffusivity because of its low active surface area, which limits the inner capacitive contribution from active materials, thereby leading to poor power and energy density. A smart strategy to address the aforementioned issues is to develop new advanced

electrode materials with three-dimensional (3D) nano-architectures with open pores to shorten lithium ion diffusion paths, alleviate electrode internal stresses, increase the contact between active materials and current collectors, and enhance surface conductivity, which should jointly warrant larger specific capacity, longer lifespan, and better rate performance. [32] It has proven that a judiciously nano-architected electrode is a prerequisite for high-performance lithium-ion batteries. [33-34] Many efforts have been made to enhance the capacity and extend the lifespan of lithium-ion batteries by either constructing nanostructures of metal sulfides on conductive porous carbon matrix or coating carbon onto metal sulfide nano-architectures. Recent studies have shown that the design wisdom of nanostructured active materials on the conductive porous backbone (usually carbon) indeed pushes up energy and power outputs. [35-37]

It has been predicted that next-generation electronics will be flexible and wearable. Many efforts have been made to develop safe, lightweight and flexible power sources to meet the urgent need for flexible/wearable electronics. [38-40] For instances, Cheng *et al.* developed a folding paper-based flexible lithium-ion battery with high areal energy density. [41] Lee reported a wearable textile battery, which could work even under severe folding-unfolding processes. [42] Cotton textiles, as the most widely used natural fibers for soft and breathable clothing, have been proven to be an exceptional platform for fabricating flexible energy storage devices. [43-46] On the other hand, 2D graphene has been recognized as an ideal substrate to hybridize active materials for high-performance energy storage devices because of its large surface area, ultra-high electrical conductivity, high flexibility, outstanding mechanical properties, and eminent chemical stability. [47] To date, advances have been made in the synthesis of graphene-based, hybrid active materials for energy storage. [48-50] The graphene in those hybrid electrodes serves as both conductive matrix and building blocks, forming a superstructure with interconnected conductive networks, which in turn facilitates Li^+ ion transportation.

Our previous study has shown that the activated cotton textiles (ACTs) converted from a cotton T-shirt can be an excellent wearable platform for fabricating flexible supercapacitors due to their magnificent flexibility, lightweight, and conductivity. [51] However, ACTs have not been explored to construct flexible lithium-ion batteries. Herein we converted cotton textiles into ACTs by annealing a $\text{Ni}(\text{NO}_3)_2$ solution treated cotton T-shirt. Interestingly, such ACTs were porous tubular fibers embedded with Ni nanoparticles and wrapped with multilayered graphene sheets which formed spontaneously during the activation process. After thermally treating the ACT/Ni-

graphene with sulfur, the Ni nanoparticles in ACT fibers transformed into NiS₂ nanobowls with ultra-large surface area whereas the ACT fibers and graphene remained as they were. Such nanobowl architectures alleviated structure collapse, maintaining the structural stability during the charge/discharge process. When used as a binder-free anode, the ACT/NiS₂-graphene electrode delivered an exceptionally high initial discharge capacity (~1710 mAh g⁻¹ at 0.01 C), impressive rate performance (the discharge capacitance retained at ~645.3 mAh g⁻¹ at 1 C after 100 cycles) and outstanding cyclic stability (the discharge capacitance recovered up to ~1016 mAh g⁻¹ at 0.1 C after 400 cycles). A thin, lightweight, and flexible lithium-ion battery was assembled to demonstrate its practical use as a flexible power source. This flexible battery retained its high capacity and excellent mechanical stability without structural failure after repeated bending process, opening up unprecedented opportunities for constructing high performance flexible lithium-ion batteries.

4.2 Experimental Section

4.2.1 Preparation of Flexible ACT/NiS₂-graphene Hybrid Anode Electrode

Fabrication of ACT/Ni-graphene: All chemicals were used after purchasing without further purification. Prior to the activation, a commercial cotton T-shirt was cleaned by distilled water in an ultrasonic bath. Activation of cotton T-shirt into ACTs was performed according to our previously established method.⁴⁵ Typically, a piece of cotton T-shirt made of woven cotton fibers was firstly dipped into Ni(NO₃)₂ solution and kept for 10 min. Then the wet textile soaked with Ni(NO₃)₂ was dried in a pre-heated electronic oven at 80 °C for 6 h to remove the residual water. The Ni(NO₃)₂-treated cotton textiles were put into a horizontal tube furnace and heated at 1000 °C (heating rate 5°C/min) for 1 h with 300 sccm (standard cubic centimeter) gas flow of argon. Finally, the as-prepared ACT/Ni-graphene composite was washed with distilled water several times to remove the residual Ni(NO₃)₂, and dried at 80 °C overnight for further usage. To study the effect of concentration of Ni(NO₃)₂ on Ni particle size and distribution, the concentration of Ni(NO₃)₂ solution was varied from 0.01 M to 2 M. ACT/Ni-0.01, ACT/Ni-0.5, ACT/Ni-1 and ACT/Ni-2 were used to name the composites obtained at the reactant concentration of 0.01 M, 0.5 M, 1 M and 2 M, respectively. The mass of Ni on ACT can be calculated by the difference of ACT/Ni-graphene composite and pure ACT.

Transformation of Ni Nanoparticles into NiS₂ Nanobowls: The flexible ACT/NiS₂-graphene composite was obtained by thermally treating ACT/Ni-graphene with sulphur. A piece of ACT/Ni-graphene composite was first cut into small rectangular pieces with a size of 1.5 cm × 2 cm, and coated with a thin layer of sulfur. To homogeneously coat ACT/Ni-graphene fibers with sulfur, sulfur was first placed into distilled water and dispersed by shear stirring at 3000 r/min for 30 min. Such sulfur solution was then dropped onto the surface of ACT/Ni-graphene pieces and dried at 80°C for 6 h, and transferred into a sealed autoclave at 156 °C for 10 h to facilitate sulfur diffusion and reaction with Ni nanoparticles. After such thermal treatment, NiS₂ nanobowls were homogeneously coated on and embedded inside the ACT fibers to form ACT/NiS₂-graphene composite. To remove the residual sulfur, the ACT/NiS₂-graphene composite was heated at 200°C for 2 h. In our study, we thermally treated ACT/Ni-graphene-0.5 with sulfur to obtain ACT/NiS₂-graphene composite (for simplicity we name ACT/NiS₂-graphene-0.5 as ACT/NiS₂-graphene) for electrochemical characterization and battery assembly. Finally, the ACT/NiS₂-graphene composite was punched into a circular electrode with a diameter of 14 mm. The loading of NiS₂-graphene on the final ACT/NiS₂-graphene electrode was calculated by weighing the ACT/NiS₂-graphene and ACT circular electrode with the same size. The mass of ACT per area is 4.9 mg cm⁻². The mass loading of ACT/NiS₂-graphene is 1.5 mg cm⁻².

4.2.2 Characterization Methods

A PANalytical X'Pert Pro Multi-Purpose Diffractometer (MPD) equipped with Cu K_α radiation ($\lambda = 0.15406$ nm) was used to determine the crystallographic structure of the synthesized materials. Raman measurements were carried out using a Renishaw InVia Raman microscope at 514 nm (with 5% Laser Power). The microstructure of the as-prepared samples was characterized by scanning electron microscopy (SEM; FEI Quanta 650) and transmission electron microscopy (TEM; JEOL 2000FX), high-resolution transmission electron microscopy (HRTEM, FEI Titan), atomic force microscopy (AFM; Dimension Icon with ScanAsyst, Bruker) and X-ray computed tomography (XCT, Xradia MicroXCT-200).

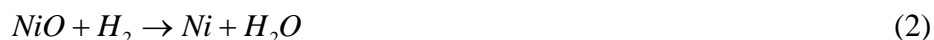
4.2.3 Fabrication and Electrochemical Characterization of Flexible ACT/NiS₂ Composite Electrode

The electrochemical properties of the ACT/NiS₂-graphene composite were measured using CR2032 coin cells with lithium metal as an anode and Celgard 2400 film as a separator. The

flexible ACT/NiS₂-graphene was used directly as the cathode material without using any conductive agent and binder. The electrode was first punched into circular disks with a diameter of 14 mm, and dried at 60°C for 24 h in a vacuum electronic oven. To further demonstrate its potential for constructing flexible energy storage devices, a piece of nanostructured ACT/NiS₂-graphene (1 cm × 2 cm) was used as the flexible cathode to assemble flexible lithium-ion battery, together with a piece of lithium film as the anode and Celgard 2400 as a separator, respectively. The electrolyte solution was 1 M LiPF₆ in EC+DMC+DEC organic solvent (1:1:1 in volume, from MTI corporation). Both the CR2032 coin cell and flexible lithium ion cell were assembled with MTI MSK-110 crimping machine in an argon-filled glove box (Mbraun, Germany) with oxygen and water contents below 1 and 0.1 ppm, respectively. A LAND CT2003A battery test instrument was used to perform galvanostatic charge/discharge measurements between 1.0-3.0 V. The specific capacities and charge/discharge rates were calculated based on the active NiS₂-graphene on the ACT. A CHI 660E electrochemical workstation was used to do the cyclic voltammograms (CV) and electrochemical impedance spectroscopy (EIS) in the frequency range from 100 kHz to 0.05 Hz with an AC perturbation of 5 mV.

4.3 Results and Discussion

Figure 4.1a schematically illustrates the design and fabrication procedures of NiS₂ nanobowl-graphene hybrid architectures on porous ACT tubular fibers. Typically, a piece of cotton textile was first dipped into a Ni(NO₃)₂ solution and then dried in the oven to obtain Ni(NO₃)₂ loaded cotton textile (Step I). The Ni(NO₃)₂ loaded cotton textile was transferred into a tube furnace and heated at 1000°C with argon protection for 1 h (Step II). During the activation process, many gaseous products including CH₄, H₂, CO, CO₂ formed by the thermal pyrolysis of cotton cellulose. [52] The Ni(NO₃)₂ first decomposed into NiO, then reduced to Ni nanoparticles which embedded in the ACT fibers. Interestingly, such ACT fibers exhibited porous tubular structure embedded Ni nanoparticles and wrapped with multilayered graphene sheets which formed spontaneously during the activation process. The chemical reactions involved in such thermal decomposition process can be expressed with the following equations: [53]



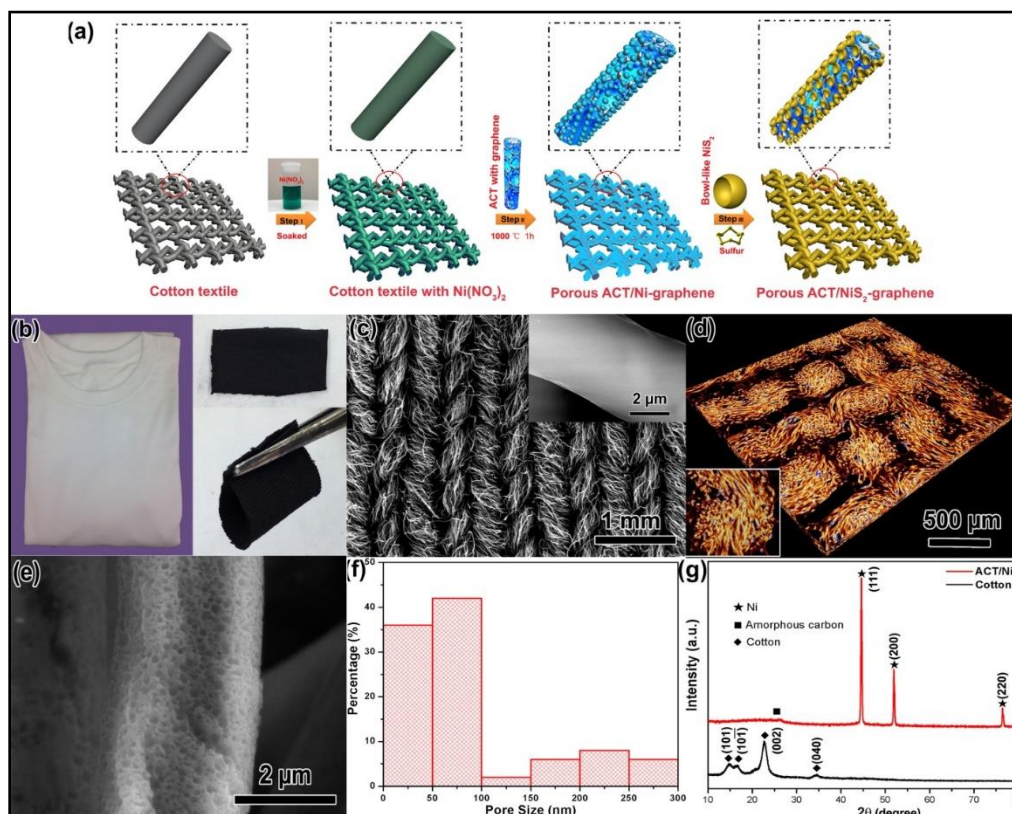


Figure 4.1 (a) Schematically Illustration of the fabrication process of porous ACT/NiS₂-graphene composite; (b) Optical photograph of a commercial cotton T-shirt, a piece of ACT/Ni-graphene under normal and folded state, showing its high flexibility; (c) SEM image of cotton textile, inset is the amplified SEM image of a cotton fiber; (d) XCT images of ACT/Ni-graphene composite after removing the Ni nanoparticles by using 2 M HNO₃, inset is the amplified region; (e) SEM image and (f) corresponding size distribution of porous ACT fibers after removing the Ni nanoparticles; (g) XRD patterns of cotton T-shirt textile and ACT/Ni-graphene composite.

The formed corrosive nitric acid will etch the cotton fiber into the porous structure during the thermal activation process. The formation of graphene originated from the dissolution of C atoms (obtained from the methane thermal decomposition) into the nickel at high temperature. During the cooling process, those carbon atoms precipitated out and segregated at the nickel surface to form graphene. [54] Those graphene sheets, serving as current “expressways”, bridged the electrolyte and active electrode material, enabling higher current collection efficiency and faster Li⁺ ion transport. The obtained ACT/Ni-graphene composite was then thermally treated with

sulfur at 156 °C for 10 h to synthesize ACT/NiS₂-graphene composite (Step III). In order to obtain NiS₂, the amount of the added sulfur needed to be two times of the Ni on ACT. The following-up annealing process at 200 °C was used to remove residual sulfur in the ACT/NiS₂-graphene composite. Finally, open-arc-shaped NiS₂ nanobowls anchored on the ACT surface and embedded inside ACT fibers. The formation of bowl-like NiS₂ can be explained by the Kirkendall effect, caused by the different diffusion rates of two components (nickel and sulfur) in a diffusion couple during the thermal reaction process. [55] Such ACT/NiS₂-graphene composite can be directly used as a binder-free flexible electrode for lithium-ion batteries. Most importantly, the “dead volume” of electrode materials due to the degradation of conductive agents and binders during charge/discharge processes could be overcome. Such open NiS₂ nanostructures together with graphene sheets on porous ACT tubular fibers shortened Li⁺ ion diffusion path, facilitated charge transfer and effectively accommodated the volume change of NiS₂ during the Li⁺ ion insertion-desertion process, jointly improving the rate performance and cyclic stability of lithium-ion batteries.

The cotton textile was comprised of cotton fibers with diameters ranging from 5 to 10 μm (Figure 4.1c). The ACT/Ni-graphene composite, converted from the cotton textile, was mechanical flexible (Figure 4.1b). X-ray computed tomography (XCT) is a nondestructive technique to visualize the interior features within solid objects by 3D reconstructing the inner structure mathematically from the measured data. [56] Figure 4.1d shows the reconstructed 3D images of ACT/Ni-graphene, revealing ACT's tubular fibers. To investigate the distribution of Ni nanoparticles in the ACT/Ni-graphene composite, the Ni nanoparticles were removed by using 2 M HNO₃ under 120 °C for 2 h. Figure 4.1e shows the SEM image of the ACT fibers after removing the Ni nanoparticles, revealing small pores on the ACT surface and inside ACT fibers. Most of the pores had diameters less than 100 nm (Figure 4.1f). The tiny mesopores together with the tubular ACT fibers served as a reservoir for electrolyte ions, providing channels for Li⁺ ion diffusion and space for accommodating volume change of active materials during the charging/discharging processes. Figure 4.1g shows the XRD patterns of the cotton textile and ACT/Ni-graphene composite. After activation, cotton's characteristic (101), (002) and (040) peaks [57] disappeared, instead of a broader diffraction peak at around 21° pointing toward amorphous carbon and nickel's (111), (200) and (220) peaks presented in the XRD spectrum. The density and distribution of Ni nanoparticles on ACT have a significant influence on the electrochemical performance of the

ACT/NiS₂ composite. It is well known that the concentration of chemical reactants plays an important role in the size and morphology of the final products.

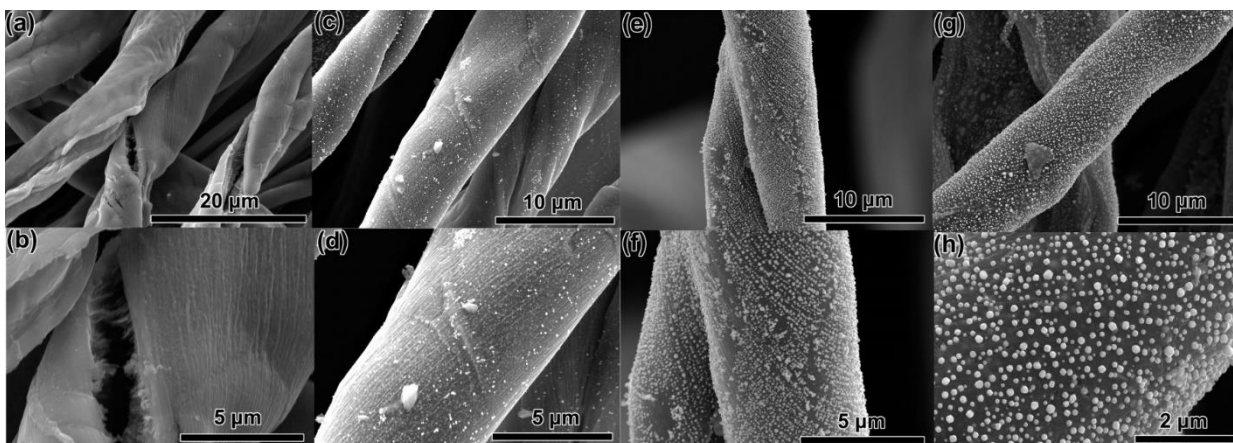


Figure 4.2 SEM images of ACT/Ni-graphene composites obtained at various Ni(NO₃)₂ concentrations: (a) and (b) 0.01 M, (c) and (d) 0.5 M, (e) and (f) 1 M, (g) and (h) 2 M.

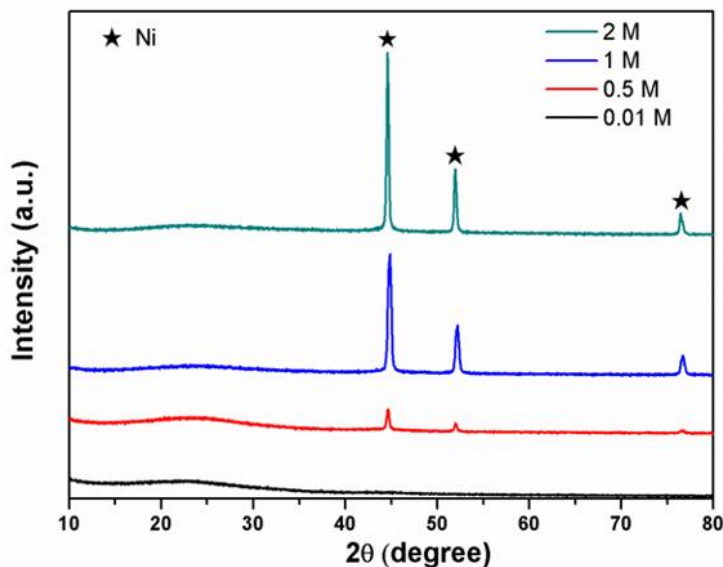


Figure 4.3 XRD patterns of ACT/Ni-graphene composites obtained at the Ni(NO₃)₂ concentration of 0.01 M, 0.5 M, 1 M, and 2 M, respectively.

Figure 4.2 shows the SEM images of the ACT/Ni composites obtained at the Ni(NO₃)₂ concentration of 0.01 M, 0.5 M, 1 M, and 2 M, respectively. The density and size of Ni nanoparticles increased with increasing Ni(NO₃)₂ concentration, which was evident in the XRD pattern where the intensities of Ni diffraction peaks increased as the Ni(NO₃)₂ solution was more concentrated (Figure 4.3). However, when the Ni(NO₃)₂ solution was diluted down to 0.01 M, no

Ni particles were found (Figures 4.2a,b), which was further verified by XRD (Figure 4.3). On the other hand, 2 M $\text{Ni}(\text{NO}_3)_2$ concentration produced large sized Ni particles (Figure 4.2g,h), which is not desirable. 1 M $\text{Ni}(\text{NO}_3)_2$ concentration led to the formation of pearl necklace-like Ni particles (Figures 4.2e,f). Much smaller and more homogeneously distributed Ni nanoparticles formed on ACTs when the concentration was reduced down to 0.5 M (Figure 4.2c,d). More importantly, multilayered graphene sheets formed spontaneously with Ni particles on the ACTs (Figures 4.4a,b), which was confirmed by Raman spectroscopy (Figure 4.4).

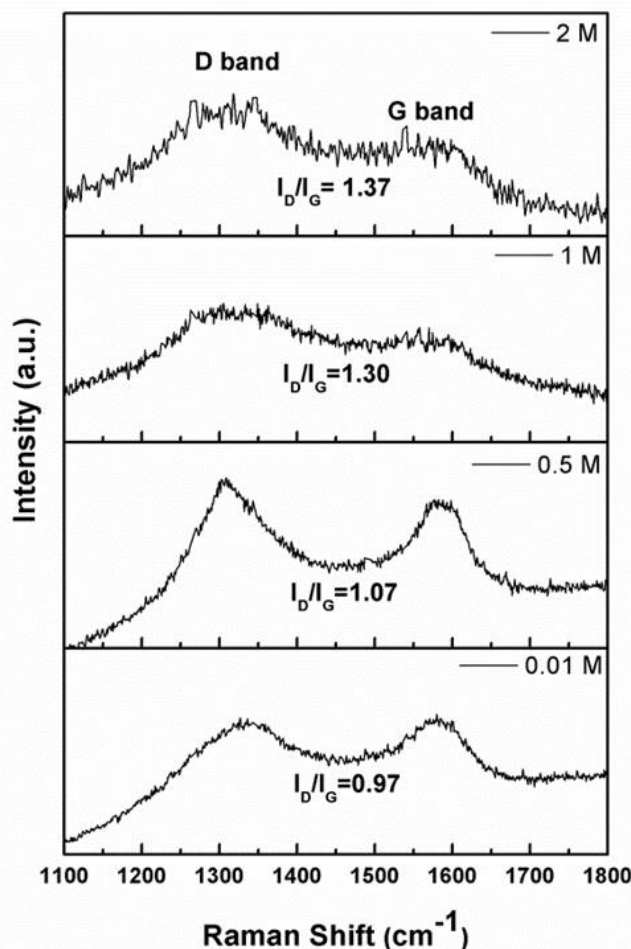


Figure 4.4 Raman spectra of ACT/Ni-graphene composites obtained at the $\text{Ni}(\text{NO}_3)_2$ concentration of 0.01 M, 0.5 M, 1 M, and 2 M, respectively.

Raman spectroscopy is an important nondestructive technique to characterize graphitic materials, especially for the ordered/disordered crystal structures of graphene. [58] Usually, graphene can be characterized by two main feature bands in a Raman spectrum: the G band arising from the first order scattering of the E_{2g} phonon mode of in-plane sp^2 C atoms at about 1575 cm^{-1}

and the D band arising from a breathing mode of point photons of A_{1g} symmetry at about 1350 cm^{-1} . [59] The increased I_D/I_G ratio in the ACT/Ni composite (Figure 4.4) resulted from the construction of the graphene network during the annealing process. The higher I_D/I_G ratio indicates the formation of smaller sized graphene with more defects and disordered structure. [60,61] Compared with other ACT/Ni composites, ACT/Ni-graphene-0.5 (here -0.5 indicates that the ACT/Ni-graphene obtained at the $\text{Ni}(\text{NO}_3)_2$ concentration of 0.5 M) showed sharper D band and G band and relatively lower I_D/I_G , suggesting that larger and more ordered graphene formed on the ACT fibers. The graphene is anticipated to facilitate electron transportation along the ACT surface, thus promoting the current collection. Based on our preliminary screening results, ACT/Ni-graphene-0.5 composite was chosen as a representative to synthesize ACT/ NiS_2 -graphene composite and was further investigated in detail as a potential electrode for flexible lithium-ion batteries.

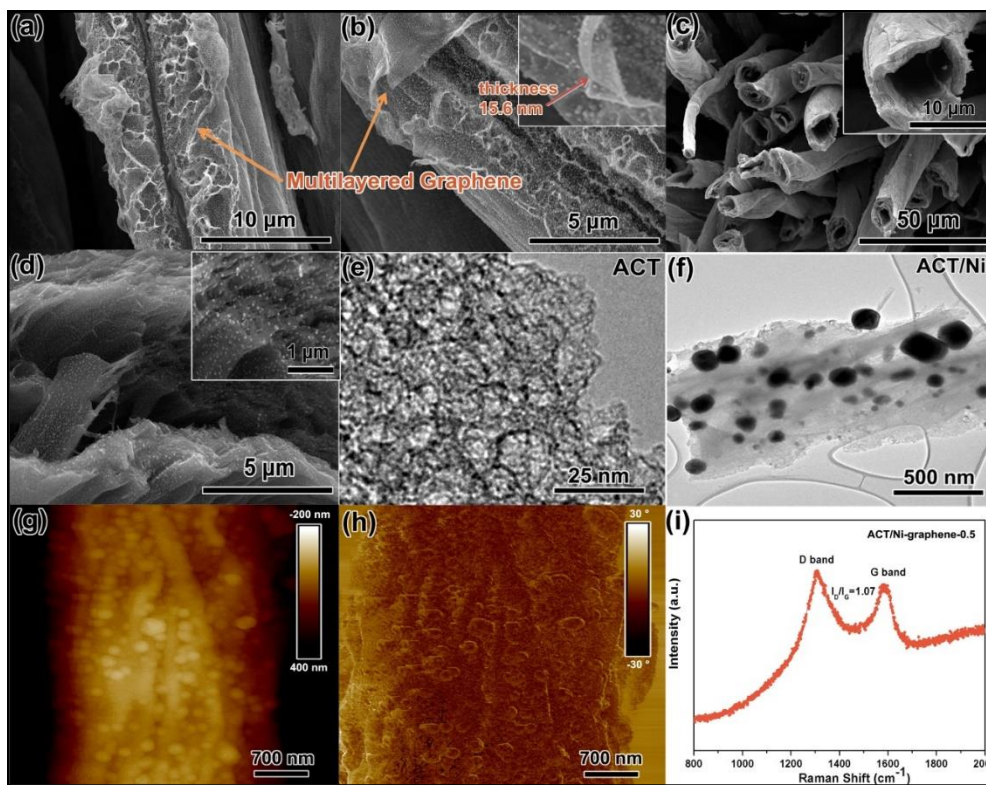


Figure 4.5 (a) and (b) SEM images of ACT/Ni-graphene-0.5 composite at different magnifications; (c) and (d) Cross-sectional SEM images of ACT/Ni-graphene-0.5 composite at different magnifications, insets are the corresponding amplified regions; (e) TEM image of ACT alone; (f) TEM image of ACT/Ni-graphene-0.5; (g) AFM height and (h) corresponding phase images of ACT/Ni-graphene-0.5 composite; (i) Raman spectrum of ACT/Ni-graphene-0.5.

The close-up observation of ACT/Ni-graphene-0.5 is shown in Figure 4.5a-d. After

annealing, Ni nanoparticles with a diameter of ~ 20 nm were closely anchored on the surface of corrugated and scrolled multilayered graphene sheets with a thickness of ~ 15.6 nm (about 50 mono-graphene layers). Those curled and entangled graphene sheets, wrapping along the ACT fibers, served as a conductive coat for fast electron transportation (Figures 4.5a,b). The cross-sectional SEM images of ACT/Ni-graphene-0.5 (Figure 4.5c and inset of the amplified region) showed that the ACT fibers exhibited an intriguing tubular structure with a layered tube wall. The Ni nanoparticles not only decorated the outer surface of the ACT fibers but also embedded inside the tube walls (Figure 4.5d). In addition, plenty of micro-channels were found in the walls of ACT fibers, which inherited from the cellulose structure of cotton (inset of Figure 4.5d). Such tubular structure with micro-channels is expected to facilitate electrolyte ion diffusion and buffer volume change during the electrochemical reaction process. Figures 4.5e and f show the TEM images of ACT and ACT/Ni-graphene-0.5, revealing the porous structure of ACT fibers and Ni nanoparticles in the ACT. The AFM height and phase images (Figure 4.5g,h) show crumpled silk veil waves (from graphene) with Ni nanoparticles on the ACT fibers. Figures 4.6a and b show the representative SEM images of ACT/NiS₂-graphene composite (transformed from the ACT/Ni-graphene-0.5). The NiS₂ nanobowls with an average size of ~ 200 nm were coated on or embedded inside the hollow ACT fibers. It is known that the bowl-like structure with interior and exterior arc surfaces could stand more contractile force induced by volume change during the insertion/deinsertion of Li⁺ ions. [15]

The shell thickness of a typical NiS₂ nanobowl was about ~ 10 nm, as shown in the TEM images (Figure 4.6c,d), from which the surround porous carbon substrate can be clearly unveiled. The TEM and HRTEM images of the NiS₂ nanobowls (Figure 4.6d,e) reveal the lattice spacing of 0.283 nm in accordance with the (200) lattice plane of NiS₂. The selected area electron diffraction (SAED) pattern of the NiS₂ nanobowl shows spotty diffraction rings with a messy character (Figure 4.6f), indicating that the NiS₂ bowl is a mixture of polycrystalline and amorphous phase, which is in good agreement with the XRD results (Figure 4.7f). Figures 4.6g and h show the AFM images of ACT/NiS₂-graphene. The mesoscale porous structure of ACT/NiS₂-graphene composite is anticipated to facilitate Li⁺ ion diffusion and electron transport in the electrochemical reaction process, which in turn improve the overall energy density and rate performance of the cell. The chemical compositions of the ACT/NiS₂-graphene were further analyzed by energy-dispersive X-ray spectrometry (EDS) (Figure 4.7). The Ni-S atomic ratio is about 11:25, which is close to the

theoretical atomic ratio (1:2) of NiS₂, indicating that the Ni nanoparticles were transformed into the NiS₂ during the heat treatment process. The EDS C and S element maps further revealed that the ACT fibers were uniformly covered by the NiS₂ nanoparticles. The Raman spectrum of ACT/NiS₂-graphene (Figure 4.6i) exhibited a similar I_D/I_G ratio compared with ACT/Ni (Figure 4.5i), indicating that the multilayered graphene sheets on the ACT remained after the annealing process.

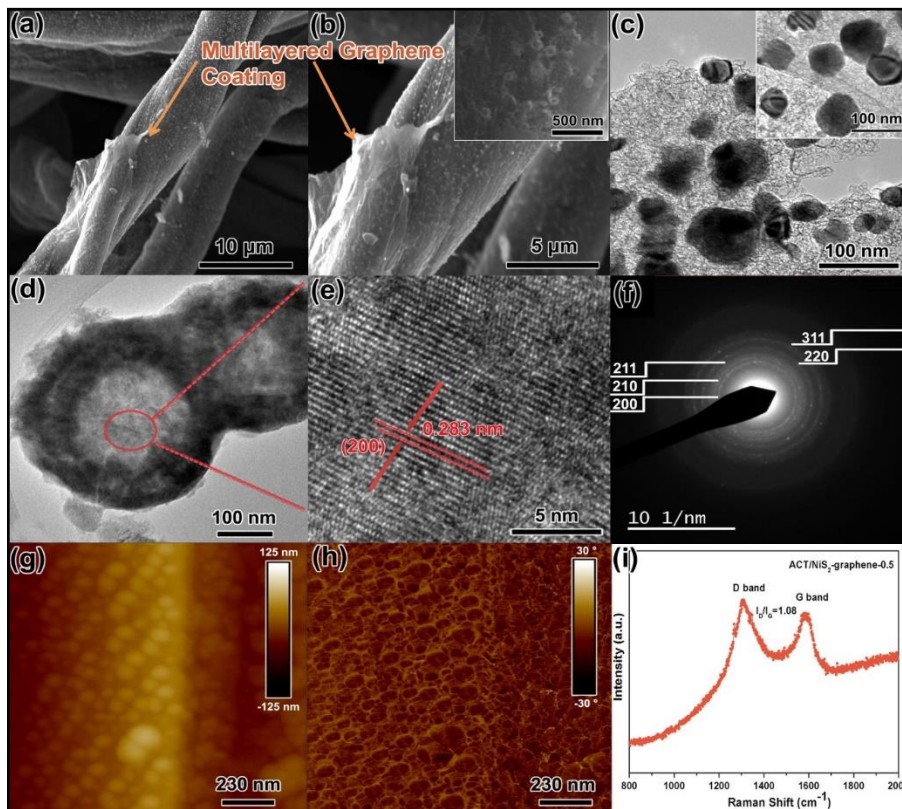


Figure 4.6 (a) and (b) SEM images of ACT/NiS₂-graphene composite at different magnifications, inset of b is the corresponding amplified region; (c) TEM images of ACT/NiS₂-graphene, inset of c is amplified region; (d) and (e) TEM images of NiS₂ nanobowls on ACT; (f) Selected area electron diffraction (SAED) pattern of the NiS₂ nanobowl; (g) AFM height and corresponding phase (h) images of ACT/NiS₂-graphene; (i) Raman spectrum of porous ACT/NiS₂-graphene.

Lithium-ion electrode materials with high specific surface areas are expected to render a large number of active sites to participate in the Faradaic redox reaction and these active sites in turn serve as pre-reserved spaces for the volume expansion during the lithiation-delithiation process. A suitable pore size distribution is critical to shorten the electrolyte ion transport path and improve the rate performance in fast Faradaic redox reactions. The pore characteristics of ACT/NiS₂-graphene composite were investigated by the N₂-adsorption/desorption measurement,

as shown in Figure 4.8. The adsorption/desorption isotherm curve exhibited a typical type IV profile with a clear hysteresis loop, indicating the mesoporosity nature of the ACT/NiS₂-graphene composite. A large Brunauer–Emmet–Teller (BET) surface area of 528.63 m² g⁻¹ was revealed for the ACT/NiS₂-graphene composite, which is ascribed to the joint contributions from the porous ACT tubes, NiS₂ nanobowls and graphene sheets. The pores exhibit a relatively wide size distribution ranging from 10 to 160 nm, with the average pore radius of ~15 nm, which is desirable for lithium-ion battery applications. [62]

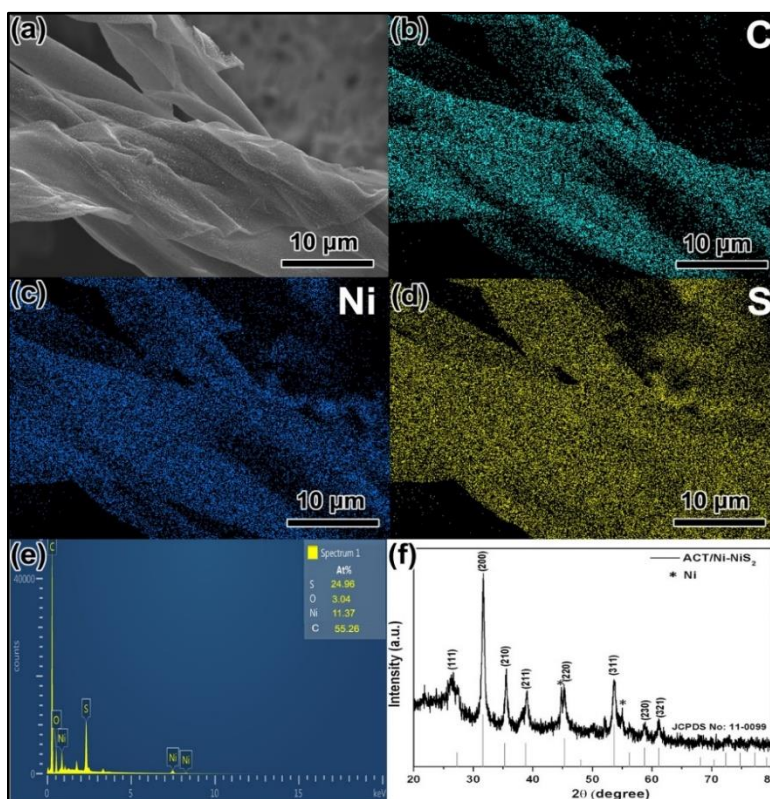


Figure 4.7 (a)-(d) SEM image and the corresponding EDS maps of the obtained ACT/NiS₂-graphene-0.5 composite; (e) Relative element ratio of C, O, S, Ni in the ACT/NiS₂-graphene composite; (f) XRD pattern of ACT/NiS₂-graphene composite.

To evaluate the battery performance of the as-prepared ACT/NS₂-graphene composite, both coin and flexible cells were assembled with the ACT/NS₂-graphene composite as cathode, lithium foil as anode, and a piece of Celgard 2400 as separator, as schematically illustrated in Figure 4.9a. The electrochemical performance of the as-assembled cells was investigated by cyclic voltammetry (CV) and galvanostatic charge/discharge tests and electrochemical impedance spectroscopy (EIS). Figure 4.9b shows the 1st and 2nd CV curves of the ACT/NS₂-graphene

composite at a constant scan rate of 0.5 mV s^{-1} from 3 to 1 V. Two reduction peaks appear at about 1.2 V and 1.6 V in the first cycle, which was ascribed to the insertion of the Li^+ ions into the composite. However, in the following cycles, the reduction peak at 1.2 V disappeared, replaced by a new reduction peak at around 1.5 V. This suggests that the solid electrolyte interphase (SEI) layers formed mainly in the first cycle. [10] The broad reduction peak at 1.2 V in the first cycling was ascribed to the insertion of Li^+ ions into NiS_2 , forming LiNiS_2 . The electrochemical reaction processes in the first cycle can be expressed using the following equations: [63]

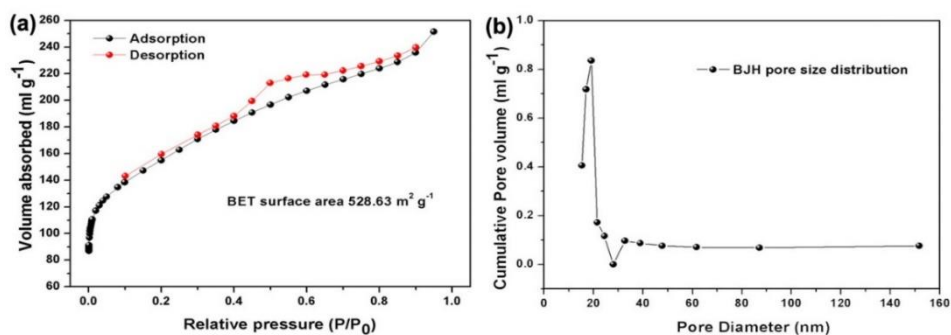
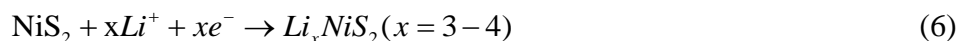


Figure 4.8 (a) BET measurement-isothermal curve of ACT/ NiS_2 -graphene composite; (b) BJH pore size distribution of ACT/ NiS_2 -graphene composite.

In contrast, the two oxidation peaks, which appeared at 1.96 and 2.3 V in the first cycle resulting from the extraction of Li^+ ions, did not change much in subsequent cycles. The anodic peak at 2.3 V corresponds to the oxidation of Li_2S into sulfur. [64] Thus, after the first cycle, the electrode could be regarded as a mixture of S and Ni instead of the pristine NiS_2 compound. This was validated by the constant current discharge/charge profile (Figure 4.9c) in which the discharge and charge potential plateaus match well with the CV curve in the corresponding electrochemical process.

The typical discharge capacities for the 1st and 2nd cycles at the current density of 0.01 C were about 1710 and 1515 mAh g^{-1} , respectively. The large irreversible capacities could be ascribed to the irreversible reactions during the cyclic process, such as the trapping of lithium inside the active materials, the formation of SEI films, and the electrolyte decomposition. [65-67] The ultrahigh initial discharge capacity probably resulted from the residual sulfur in ACT fibers.

After 10 charge/discharge cycles, the reduction peak shifted from 1.5 V to 1.6 V. At the same time, the oxidation peak at 1.96 V becomes smaller and shifted to 1.9 V, and the oxidation peak at 2.3 V shifted to 2.2 V (Figure 4d), corresponding respectively to the formation of NiS₂ and the decomposition of Li₂S ($Ni / Li_x + 2Li_2S \rightarrow Li_x NiS_2 + 4Li^+ + 4e^-$). The CV results agree well with the potential plateaus in the charge/discharge profiles (Figure 4.9e). After 10 charge/discharge cycles, the capacity reduced down to ~1100 mAh g⁻¹, which may be caused by the dissolution of polysulfide in the electrolyte.

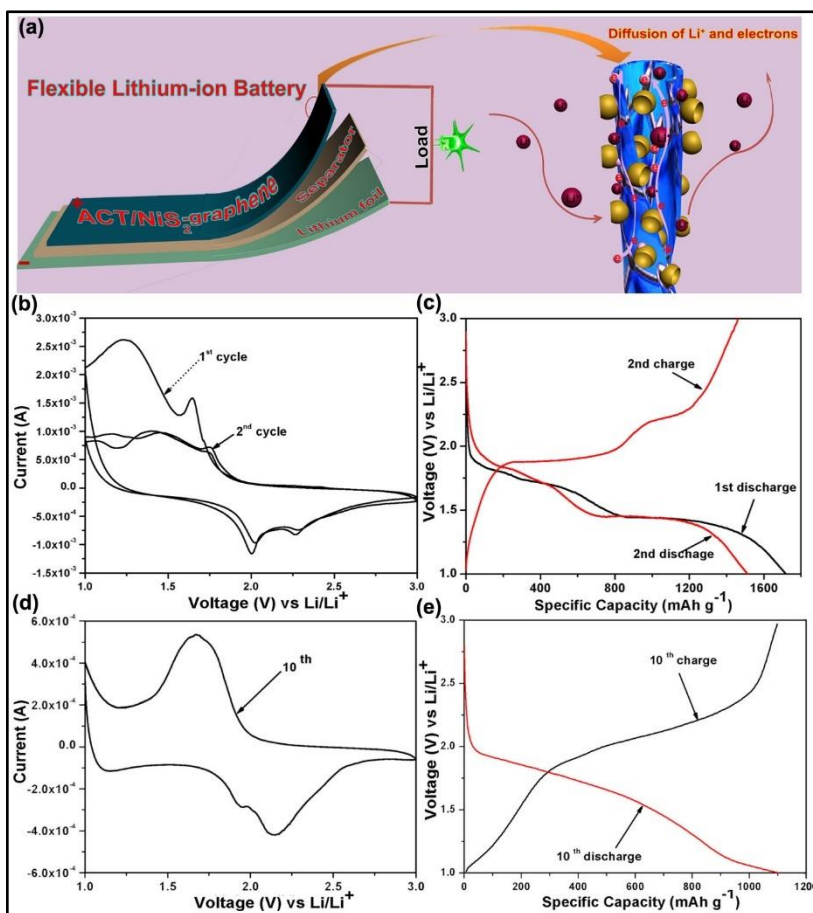


Figure 4.9 (a) Schematically illustration of the assembled flexible lithium-ion battery; (b) Initial cyclic voltammogram profiles of ACT/NiS₂-graphene; (c) Initial charge/discharge voltage-specific capacity curves of porous ACT/NiS₂-graphene at 0.01 C; (d) Cyclic voltammogram profiles of ACT/NiS₂-graphene after 10 charge/discharge processes; (e) 10th charge/discharge voltage-specific capacity curves of ACT/NiS₂-graphene at 0.01 C.

Rate capability is an important factor for evaluating the performance of a battery. In this study, the current densities were varied from 0.01 C to 1 C to investigate the rate performance of the ACT/NiS₂-graphene composite electrode. Figure 4.10a shows the representative charge/discharge profiles. With increasing charge/discharge rate, the charge potential plateau

increased whereas the discharge potential plateau decreased, which might be ascribed to the kinetic effects of the electrode material, leading to higher overpotential and lower capacity at the high rate regime.

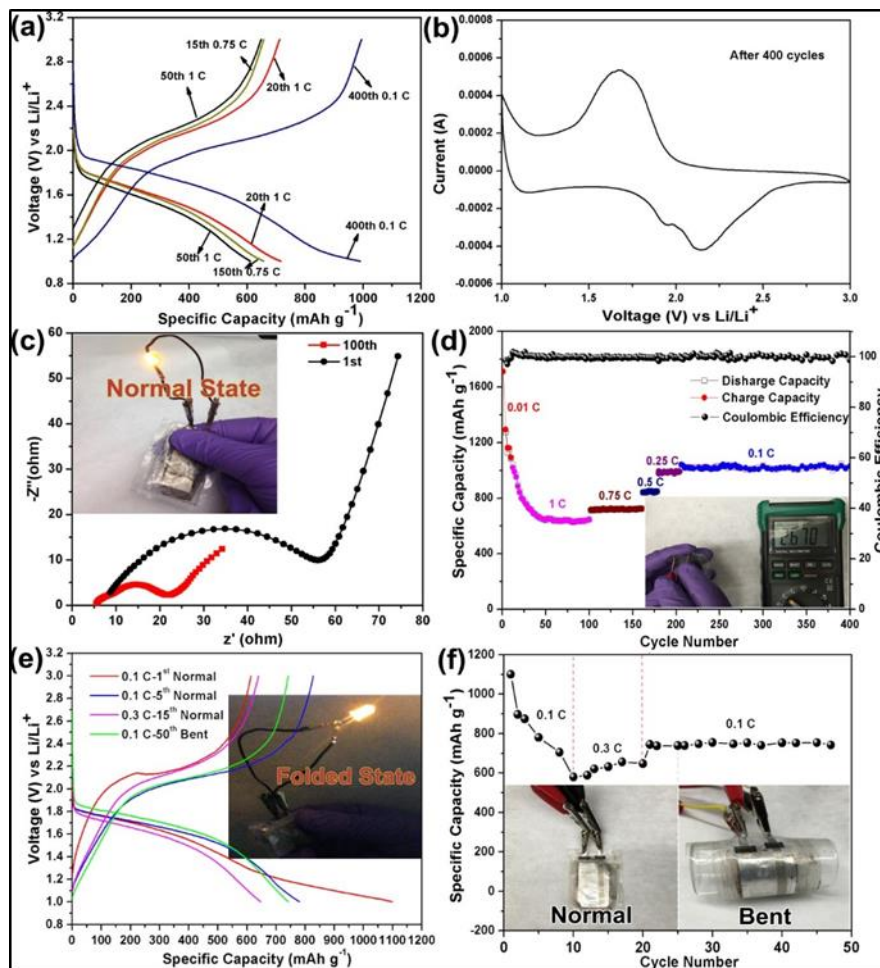


Figure 4.10 (a) 20th, 50th, 150th and 400th charge/discharge voltage-specific capacity curves of ACT/NiS₂-graphene at different charge/discharge rates; (b) Cyclic voltammogram profiles of ACT/NiS₂-graphene after 400 charge/discharge processes; (c) Nyquist plots of ACT/NiS₂-graphene at the 1st and 100th charge/discharge processes; (d) Cycling and rate performance of porous ACT/NiS₂-graphene, inset is the open circuit potential of the assembled flexible battery cell under bent state; (e) 1st (0.1 C), 5th (0.1 C), and 15th (0.3 C) charge/discharge voltage-specific capacity curves at normal state and the 50th charge/discharge voltage-specific capacity curve at the bent state of the flexible cell; (f) the cyclic performance of the flexible cell at normal and bent states; Insets of (c) and (e) are optical photograph of a yellow light-emitting diode (LED) lighted by the assembled flexible cell under normal and folded states, respectively.

The reversible capacities at the 20th (1 C), 50th (1 C), 150th (0.75 C) and 400th (0.1 C) cycles are ~710, ~608, ~680, and ~1030 mAh g⁻¹, respectively. It can be seen that the capacity retained at ~608 mAh g⁻¹ even when the charge/discharge rate increased 100 times from 0.01 C to 1 C. More importantly, after 400 cycles the capacity of ~1030 mAh g⁻¹ was reversibly restored when the charge/discharge rate was reduced down to 0.1 C. In particular, compared with the CV curve

of the 10th cycle (Figure 4.10d), the redox peaks of the CV curves after 400 cycles (Figure 4.10b) kept almost unchanged, demonstrating robust reversibility of the ACT/NiS₂-graphene hybrid electrode.

To further demonstrate the advantages of the ACT/NiS₂-graphene electrode, electrochemical impedance spectroscopy (EIS) measurements were carried out before and after 100 cycling times. As shown in Figure 4.10c, both profiles exhibit characteristically a semicircle in the high-frequency regime and a straight line in the low-frequency region, indicating that the electrochemical process was controlled by charge transfer and lithium ion transport. The semicircle arc at the high-frequency range can be assigned to the charge transfer resistance (R_{ct}), and the straight line at the low-frequency regime corresponds to the lithium ion diffusion. [29] The charge-transfer resistance was measured from the diameter of the semicircle arc. [68] Clearly, the ACT/NiS₂-graphene electrode displayed a larger R_{ct} (50 Ω) before cycling than that of the cell after 100 cycles (10 Ω) because of the inactivation of the electrode before cycling, which was also used to measure the resistance of SEI layer on the electrode surface. The small semicircle for the ACT/NiS₂-graphene electrode after 100 cycles indicates its good conductivity and fast electrolyte ion diffusion, which can be ascribed to the multiscale porous hierarchical structure of active materials - NiS₂ nanobowls, graphene and hollow ACT fibers, good adhesion and excellent electrical contact between the active material and conductive substrate.

Cycling life and Coulombic efficiency are two important parameters for evaluating the practical applications of a battery. The cyclic performance and corresponding Coulombic efficiency of the ACT/NiS₂-graphene cell were characterized by the charge/discharge tests at different charge/discharge rates for up to 400 cycles, as shown in Figure 4.10d. It can be seen that the capacity decreased sharply for the first 10 cycles at 0.01 C. The fast capacity decay at the initial stage may be ascribed to the formation of the SEI film, decomposition of the electrolyte, and the further lithium insertion at the Ni/LiS₂ interface. [14, 69] For the following-up cycles at 1 C, the capacity decreased gradually and then maintained at about 610 mAh g⁻¹ after 50 cycles, which could be caused by the fast-kinetic effect at the high charge/discharge rate regime, the dissolution of the polysulfide intermediates and the volume expansion during the electrochemical reaction. However, after 50 cycles, the structure and the composition of the electrode became more stable, leading to an excellent reversible capacity. Furthermore, the ACT/NiS₂-graphene hybrid material

showed better cyclic performance at stepwise charge/discharge rates, with a recovery of the capacity of $\sim 1032 \text{ mAh g}^{-1}$ at 0.1 C even after 400 cycles. Most importantly, except for the initial several cycles, the Coulombic efficiency of the ACT/NiS₂-graphene electrode maintained almost 100% upon cycling (Figure 4.10d). To further demonstrate the practical applications of the as-prepared ACT/NiS₂ composite for flexible energy storage devices, the flexible cell was used to light a commercial LED (Inset of Figure 4.10c). The open circuit potential maintained at 2.67 V even in a bent state (inset of Figure 4.10d). The brightness of the lightened LED did not change even at severely folded state (Inset of Figure 4.10e). Figure 4.10e shows the voltage-specific capacity curves at different charge/discharge rates under normal or bent states. All of the voltage-specific capacity curves of the flexible cell had similar charge/discharge plateaus at both normal and bent states as the coin cell, indicating its excellent flexibility and robustness. The cyclic performance of the flexible cell at normal and bent states is shown in Figure 4.10f. Compared with the coin cell, the flexible cell showed a relatively lower specific capacity, which might be led by the loose contact between positive and negative electrodes. However, the capacity can be well maintained at $\sim 740 \text{ mAh g}^{-1}$ at 0.1 C even after 50 cycles, which is still very promising for the practical application as flexible power source.

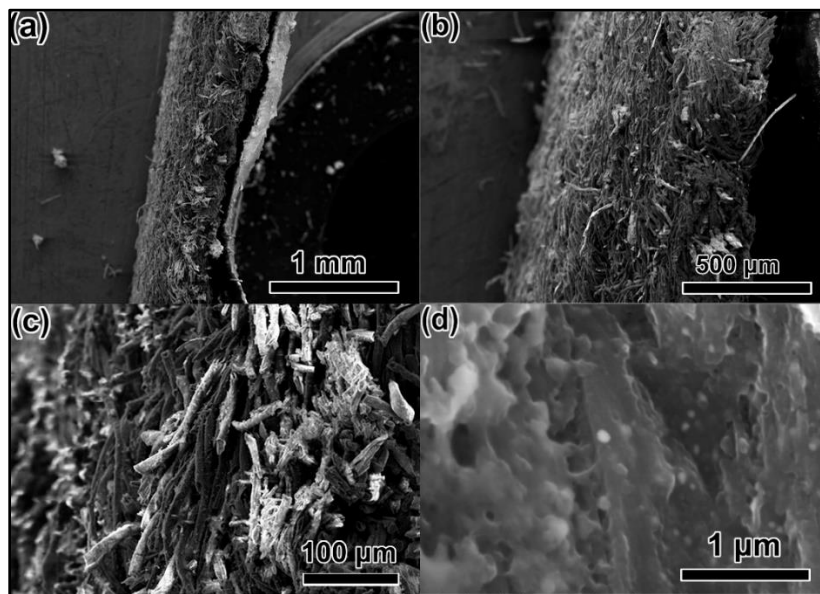


Figure 4.11 SEM images of ACT/Ni-graphene composite electrode after repeated charge/discharge processes at normal and bent states, cross-section (a,b) and surface with the amplified region (c,d).

Figure 4.11 shows the SEM images of ACT/NiS₂-graphene composite electrode washed with alcohol solution after repeated charge/discharge processes at normal or bent states. Interesting,

except residual solid electrolyte particles, there are no cracks found on the surface of ACT, which might result from the hollow structure of ACT fiber, releasing the internal stresses during the bending process, and maintaining the excellent mechanical stability of ACT/NiS₂-graphene composite (Figure 4.11a,b). At the same time, the bowl structure was also well maintained after the charging/discharging processes (Figure 4.11c,d).

The superior cyclic performance, excellent rate capacity and exceptional flexibility of the as-prepared ACT/NiS₂-graphene electrode can be ascribed to the following merits: (1) porous ACT fibers effectively buffered the stress induced by the volume change and maintained the structure stability during the electrochemical reaction; (2) the tubular structure of ACT fibers served as an electrolyte reservoir, shortening the transportation/diffusion path for lithium ions and enabling faster kinetics and high-rate capability; (3) the NiS₂ nanobowls with interior and exterior arc surfaces not only increased the specific surface areas to facilitate the penetration of electrolyte ions, but also stood for more stresses to enable the structural integrity during the charge/discharge process. In a word, the synergistic effects of individual components in the ACT/NiS₂-graphene composite enable the fast ion/electron transfer, leading to exceptional electrochemical performances.

4.4 Conclusion

In summary, porous ACT tubular fibers embedded with NiS₂ nanobowls and wrapped with graphene sheets have been successfully fabricated using a simple two-step heat treatment method. As a self-supported electrode material, the assembled ACT/NiS₂-graphene cell exhibited an exceptional electrochemical performance in terms of ultra-high capacity, impressive cyclic stability and excellent rate capability. The cell achieved an ultrahigh initial capacity of ~1710 mAh g⁻¹ at a rate of 0.01 C, and maintained a high reversible capacity of ~1016 mAh g⁻¹ after 400 cycles at the rate of 0.1 C. A thin, lightweight, and flexible ACT/NiS₂ lithium-ion battery was also assembled to demonstrate its practical application for flexible energy storage devices. This cotton textile enabled lithium-ion battery system presents a new promise for the design and fabrication of high performance flexible/wearable energy storage devices for applications in an extensive range of fields.

Reference

- [1] Tarascon, J.-M. *Philos. Trans. A. Math. Phys. Eng. Sci.* **2010**, *368*, 3227-3241.
- [2] Armand, M.; Tarascon, J.-M. *Nature* **2008**, *451*, 652-657.
- [3] Bruce, P. G.; Freunberger, S. A.; Hardwick, L. J.; Tarascon, J.-M. *Nat. Mater.* **2011**, *11*, 172.
- [4] Chiang, Y. M. *Science* **2010**, *330*, 1486-1487.
- [5] Seh, Z. W.; Yu, J. H.; Li, W.; Hsu, P.-C.; Wang, H.; Sun, Y.; Yao, H.; Zhang, Q.; Cui, Y. *Nat. Commun.* **2014**, *5*, 5017.
- [6] Goodenough, J. B.; Park, K. S. *J. Am. Chem. Soc.* **2013**, *135*, 1167-1176.
- [7] Liang, M.; Zhi, L. *J. Mater. Chem.* **2009**, *19*, 5871-5878.
- [8] Ge, M.; Rong, J.; Fang, X.; Zhou, C. *Nano Lett.* **2012**, *12*, 2318-2323.
- [9] Li, X.; Yang, Z.; Fu, Y.; Qiao, L.; Li, D.; Yue, H.; He, D. *ACS Nano* **2015**, *9*, 1858-1867.
- [10] Xiao, J.; Wang, X.; Yang, X. Q.; Xun, S.; Liu, G.; Koech, P. K.; Liu, J.; Lemmon, J. P. *Adv. Funct. Mater.* **2011**, *21*, 2840-2846.
- [11] Li, Y.; Tan, B.; Wu, Y. *Nano Lett.* **2008**, *8*, 265-270.
- [12] Zhou, X.; Wan, L. J.; Guo, Y. G. *Adv. Mater.* **2013**, *25*, 2152-2157.
- [13] Wang, X.; Li, X.; Sun, X.; Li, F.; Liu, Q.; Wang, Q.; He, D. *J. Mater. Chem.* **2011**, *21*, 3571-3573.
- [14] Mahmood, N.; Zhang, C.; Hou, Y. *Small* **2013**, *9*, 1321-1328.
- [15] Zhou, W.; Zheng, J. L.; Yue, Y. H.; Guo, L. *Nano Energy* **2015**, *11*, 428-435.
- [16] Wang, Q.; Nie, Y. X.; He, B.; Xing, L. L.; Xue, X. Y. *Solid State Sci.* **2014**, *31*, 81-84.
- [17] Yan, J. M.; Huang, H. Z.; Zhang, J.; Liu, Z. J.; Yang, Y. *J. Power Sources* **2005**, *146*, 264-269.

- [18] Zhou, Y.; Yan, D.; Xu, H.; Feng, J.; Jiang, X.; Yue, J.; Yang, J.; Qian, Y. *Nano Energy* **2015**, *12*, 528-537.
- [19] Evans, T.; Piper, D. M.; Kim, S. C.; Han, S. S.; Bhat, V.; Oh, K. H.; Lee, S. H. *Adv. Mater.* **2014**, *26*, 7386-7392.
- [20] Son, M. Y.; Choi, J. H.; Kang, Y. C. *J. Power Sources* **2014**, *251*, 480-487.
- [21] Rui, X.; Tan, H.; Yan, Q.; *Nanoscale* **2014**, *6*, 9889-9924.
- [22] Goriparti, S.; Miele, E.; De Angelis, F.; Di Fabrizio, E.; Proietti Zaccaria, R.; Capiglia, C. *J. Power Sources* **2014**, *257*, 421-443.
- [23] Sun, H.; Qin, D.; Huang, S.; Guo, X.; Li, D.; Luo, Y.; Meng, Q. *Energy Environ. Sci.* **2011**, *4*, 2630-2637.
- [24] Zhang, B.; Ye, X.; Dai, W.; Hou, W.; Xie, Y. *Chem.- A Eur. J.* **2006**, *12*, 2337-2342.
- [25] Cao, F.; Liu, R.; Zhou, L.; Song, S.; Lei, Y.; Shi, W.; Zhao, F.; Zhang, H. *J. Mater. Chem.* **2010**, *20*, 1078-1085.
- [26] Wang, Q. H.; Kalantar-Zadeh, K.; Kis, A.; Coleman, J. N.; Strano, M. S. *Nat. Nanotechnol.* **2012**, *7*, 699-712.
- [27] Geng, H.; Kong, S. F.; Wang, Y. *J. Mater. Chem. A* **2014**, *2*, 15152-15158.
- [28] Takeuchi, T.; Sakaebe, H.; Kageyama, H.; Sakai, T.; Tatsumi, K. *J. Electrochem. Soc.* **2008**, *155*, A679-A684.
- [29] Duan, W.; Yan, W.; Yan, X.; Munakata, H.; Jin, Y.; Kanamura, K. *J. Power Sources* **2015**, *293*, 706-711.
- [30] Wang, Q.; Gao, R.; Li, J. *Appl. Phys. Lett.* **2007**, *90*, 28-31.
- [31] Wang, L.; Liu, J.; Zhang, L. L.; Dai, B.; Xu, M.; Ji, M.; Zhao, X. S.; Cao, C.; Zhang, J.; Zhu, H.; *RSC Adv.* **2015**, *5*, 8422-8426.

- [32] Liu, C.; Li, F.; Ma, L.-P.; Cheng, H. M. *Adv. Mater.* **2010**, *22*, E28-E62.
- [33] Wang, N.; Chen, L.; Ma, X.; Yue, J.; Niu, F.; Xu, H.; Yang, J.; Qian, Y. *J. Mater. Chem. A* **2014**, *2*, 16847-16850.
- [34] Su, Y.; Li, S.; Wu, D.; Zhang, F.; Liang, H.; Gao, P.; Cheng, C.; Feng, X. *ACS Nano* **2012**, *6*, 8349-8356.
- [35] Sun, Y.; Hu, X.; Luo, W.; Xia, F.; Huang, Y. *Adv. Funct. Mater.* **2013**, *23*, 2436-2444.
- [36] Zhou, X.; Liu, W.; Yu, X.; Liu, Y.; Fang, Y.; Klankowski, S.; Yang, Y.; Brown, J. E.; Li, J. *ACS Appl. Mater. Interfaces* **2014**, *6*, 7434-7443.
- [37] Hu, Y. S.; Liu, X.; Müller, J. O.; Schlögl, R.; Maier, J.; Su, D. S. *Angew. Chemie - Int. Ed.* **2009**, *48*, 210-214.
- [38] Gwon, H.; Hong, J.; Kim, H.; Seo, D.-H.; Jeon, S.; Kang, K. *Energy Environ. Sci.* **2014**, *7*, 538-551.
- [39] Zhou, G.; Li, F.; Cheng, H. M. *Energy Environ. Sci.* **2014**, *7*, 1307-1338.
- [40] Wang, X.; Lu, X.; Liu, B.; Chen, D.; Tong, Y.; Shen, G.; *Adv Mater* **2014**, *26*, 4763-4782.
- [41] Lee, Y. H.; Kim, J. S.; Noh, J.; Lee, I.; Kim, H. J.; Choi, S.; Cheng, Q.; Song, Z.; Ma, T.; Smith, B. B.; Tang, R.; Yu, H.; Jiang, H.; Chan, C. K. *Nano Lett.* **2013**, *13*, 4969-4974.
- [42] Seo, J.; Jeon, S.; Kim, T.; Lee, J.; Choi, J. W. *Nano Lett.* **2013**, *13*, 5753-5761.
- [43] Hu, L.; Pasta, M.; La Mantia, F.; Cui, L.; Jeong, S.; Deshazer, H. D.; Choi, J. W.; Han, S. M.; Cui, Y. *Nano Lett.* **2010**, *10*, 708-714.
- [44] Gorgutsa, S.; Gu, J. F.; Skorobogatiy, M. *Smart Mater. Struct.* **2011**, *21*, 015010.
- [45] Bao, L.; Li, X. *Adv. Mater.* **2012**, *24*, 3246-3252.
- [46] Gao, Z.; Song, N.; Zhang, Y.; Li, X. *RSC Adv.* **2015**, *5*, 15438-15447.
- [47] Raccichini, R.; Varzi, A.; Passerini, S.; Scrosati, B. *Nat. Publ. Gr.* **2014**, *14*, 271-279.

- [48] Srivastava, M.; Singh, J.; Kuil, T.; Layek, R. K.; Kime, N. H.; Lee, J. H. *Nanoscale* **2015**, 7, 4820-4868.
- [49] Wang, X.; Shi, G.; *Energy Environ. Sci.* **2015**, 8, 790-823.
- [50] Kim, M.; Kim, D. Y.; Kang, Y.; Park, O. O. *RSC Adv.* **2015**, 5, 3299-3305.
- [51] Gao, Z.; Song, N.; Li, X. *J. Mater. Chem. A* **2015**, 3, 14833-14844.
- [52] Lin, Y.; Cho, J.; Tompsett, G. A.; Westmoreland, P. R.; Huber, G. W. *Cellulose* **2009**, 20097-20107.
- [53] Zhang, Y.; Zhang, L.; Zhou, C. *Acc. Chem. Res.* **2013**, 46, 2329.
- [52] Kim, K. S.; Zhao, Y.; Jang, H.; Lee, S. Y.; Kim, J. M.; Kim, K. S.; Ahn, J.-H.; Kim, P.; Choi, J.-Y.; Hong, B. H. *Nature* **2009**, 457, 706.
- [55] Yin, Y.; Rioux, R. M.; Erdonmez, C. K.; Hughes, S.; Somorjai, G. A.; Alivisatos, A. P. *Science* **2004**, 304 (5671), 711-714.
- [56] Kalender, W. A. *Phys. Med. Biol.* **2006**, 51, R29-R43.
- [57] Ford, E. N. J.; Mendon, S. K.; Thames, S. F.; Ph, D.; Rawlins, J. W. *J. Eng. Fiber. Fabr.* **2010**, 5, 10-20.
- [58] Ferrari, A.; Robertson, J. *Phys. Rev. B* **2000**, 61, 14095-14107.
- [59] Ji, Z.; Shen, X.; Li, M.; Zhou, H.; Zhu, G.; Chen, K. *Nanotechnology* **2013**, 24, 115603.
- [60] Xu, C.; Wang, X.; Zhu, J. *J. Phys. Chem. C* **2008**, 112, 19841-19845.
- [61] Wang, Y.; He, Q.; Qu, H.; Zhang, X.; Guo, J.; Zhu, J.; Zhao, G.; Colorado, H. A.; Yu, J.; Sun, L.; Bhana, S.; Khan, M. A.; Huang, X.; Young, D. P.; Wang, H.; Wang, X.; Wei, S.; Guo, Z. *J. Mater. Chem. C* **2014**, 2, 9478-9488.
- [62] Ma, X. M.; Gan, L. H.; Liu, M. X.; Tripathi, P. K.; Zhao, Y. H.; Xu, Z. J.; Zhu, D. Z.; Chen, L. W. *J. Mater. Chem. A* **2014**, 2, 8407-8415.

- [63] Poizot, P.; Laruelle, S.; Grugeon, S.; Tarascon, J. M. *J. Electrochem. Soc.* **2002**, *149*, A1212-A1217.
- [64] Wang, J.; Yang, J.; Wan, C.; Du, K.; Xie, J.; Xu, N. *Adv. Funct. Mater.* **2003**, *13*, 487-492.
- [65] Su, L.; Zhong, Y.; Zhou, Z. *J. Mater. Chem. A* **2013**, *1*, 15158-15166.
- [66] Ponrouch, A.; Taberna, P. L.; Simon, P.; Palacín, M. R. *Electrochim. Acta* **2012**, *61*, 13-18.
- [67] Lee, S. H.; Kim, Y. H.; Deshpande, R.; Parilla, P. A.; Whitney, E.; Gillaspie, D. T.; Jones, K. M.; Mahan, A. H.; Zhang, S.; Dillon, A. C. *Adv. Mater.* **2008**, *20*, 3627-3632.
- [68] Wang, J.; Gao, Z.; Li, Z.; Wang, B.; Yan, Y.; Liu, Q.; Mann, T.; Zhang, M.; Jiang, Z. *J. Solid State Chem.* **2011**, *184*, 1421-1427.
- [69] Mai, Y. J.; Tu, J. P.; Gu, C. D.; Wang, X. L. *J. Power Sources* **2012**, *209*, 1-6.

Chapter 5. Cotton Textile-Enabled Flexible Lithium-Sulfur Battery

5.1 Introduction

Rechargeable lithium-ion batteries have largely revolutionized modern portable and mobile electronics devices and are still the most important energy storage systems, because of their high energy efficiency and long lifespan [1,2]. However, traditional electrode materials (such as LiCoO_2 and LiFePO_4) have almost reached their theoretical limit, which cannot meet the increasing needs for fields that demand higher energy storage, such as electric vehicles and grid storage [3,4]. Therefore, it is necessary to explore new electrode materials or new redox chemistry for the development of next-generation batteries [5,6]. Lithium-sulfur (Li-S) battery is very promising for the development of next-generation high-energy battery because of its ultra-high theoretical capacity ($\sim 1650 \text{ mAh g}^{-1}$), outstanding specific energy ($\sim 2654 \text{ Wh Kg}^{-1}$), natural abundance, as well as environmental friendliness [7,8]. More encouragingly, some reported Li-S batteries have demonstrated superior practical capacity ($\sim 550 \text{ mAh g}^{-1}$), more than twice of the state-of-the-art lithium-ion batteries ($\sim 180 \text{ mAh g}^{-1}$) [9,10].

However, despite the aforementioned advantages, Li-S battery manufacturing still encounters several roadblocks, including low sulfur utilization, severe capacity fading, poor cycling life and bad Coulombic efficiency [11-14], which can be ascribed to the fundamentally different chemistry of Li-S batteries. For instances, in the Li-S system, sulfur usually undergoes a series of compositional and structural changes, including the formation of soluble lithium polysulfides (Li_2S_8 , Li_2S_6 , Li_2S_4 , and Li_2S_3) and insoluble lithium sulfides ($\text{Li}_2\text{S}_2/\text{Li}_2\text{S}$) [15]. Specifically, the dissolution of polysulfides often leads to the low utilization of sulfur, fast capacity fading, and serious “shuttle effect”, resulting in poor Coulombic efficiency [16]. Additionally, the poor conductivity of both sulfur and the formed insoluble lithium sulfides jointly increase the reaction resistance, leading to poor utilization of active sulfur and bad cycling reversibility [17]. Furthermore, a large volume expansion up to 80% usually occurs during the conversion reaction from sulfur to lithium sulfide [18].

To date, various strategies have been explored to push up the potential of Li-S systems. For instances, numerous efforts have been devoted to hybridizing sulfur particles with various carbon materials (such as activated carbons [19,20], micro-/mesoporous carbon [21-24], CNTs [25], graphene [26,27], carbon fibers [28]) or conducting polymer (polyaniline [29]) to mitigate the poor conductivity of sulfur, or endowing the sulfur host materials with high porosity to retard the dissolution of polysulfides and buffer the volume change. In addition, some other attempts, such as designing nanostructured cathode, adding additives (LiNO_3) into the electrolyte, and optimizing cell configuration, have also been performed to suppress the “shuttle effect”, improve Coulombic efficiency and extend the lifespan of lithium-sulfur systems [30-34]. Recently, graphene oxides (GO) were also employed as a sulfur immobilizer in GO/S composite cathode to prevent the dissolution of polysulfides through the strong chemical bonding between sulfur and the rich functional groups of GO [35-37]. Furthermore, the future portable/wearable electronic devices will be flexible and more functional, which definitely require the corresponding flexible power supplies with larger energy storage capacities. Recently, many efforts have been devoted to developing flexible Li-S batteries by incooperation sulfur with flexible substrates (such as carbon paper [38], mesoporous graphene paper [39], three-dimensional (3D) carbonaceous aerogel [40] or porous polymer sheets [41], which hold great promise for next-generation flexible power sources because of their superior energy density than that of lithium-ion batteries [42]. Our previous studies have demonstrated that the activated cotton textile (ACT) converted from cotton textile could be an excellent platform for constructing flexible energy systems (e.g. flexible supercapacitors and flexible lithium-ion batteries) due to their excellent conductivity and eminent flexibility [43,44]. Recently, the fabrication of carbon materials from cotton have been reported for both supercapacitor and Li-S battery applications [45-48]. However, to the best of our knowledge, ACTs have not been explored for flexible Li-S batteries. High energy flexible Li-S battery could be combined with a solar cell to fabricate self-sustained power sources, which hold great promise for future outdoor sensors and unmanned devices [49-51].

Herein, porous ACT fibers with tubular hollow structure were firstly prepared by a simple dipping, drying, and annealing process [52]. Sulfur nanoparticles were further infiltrated into ACT fibers via a simple heat treatment process in a sealed autoclave at the temperature of 156°C , where sulfur has the lowest viscosity, ensuring the full penetration of sulfur into the pores and inner cavities of ACT fibers. The unique porous tubular structure of ACT fiber helped the infiltration of

sulfur, finally enabling a high sulfur loading of $\sim 5.5 \text{ mg cm}^{-2}$. The porous hollow structure of ACTs also helped to trap the formed polysulfides and facilitated fast lithium-ion transport during the electrochemical reaction processes. To effectively suppress the dissolution of polysulfides, the prepared ACT/S fibers were further wrapped with graphene oxide sheets, and then thermally treated at $200 \text{ }^\circ\text{C}$ for 2 h to partially reduce GO to form ACT/S-reduced graphene oxide (ACT/S-rGO) composite, which demonstrated a strong capability to retard the dissolution of polysulfides through strong chemical bonding between polysulfides and the surface functional groups of rGO. Furthermore, a piece of KOH-activated ACT with hierarchical porous structure and micropore size distribution was cemented between the ACT/S-rGO cathode and the separator to serve as an interlayer with the purpose to trap polysulfides and mitigate the “shuttle effect” of polysulfides between cathode and anode. Finally, the ACT/S-rGO cell with porous ACT interlayer exhibited an exceptional capacity increasing (from 3th cycle $\sim 852 \text{ mAh g}^{-1}$ to 150th cycle $\sim 1037 \text{ mAh g}^{-1}$), impressive rate performance (the discharge capacity retained well even with current density increasing from 0.3 to 2.4 mA cm^{-2}) and doubled cyclic stability (compared with the 100 cycles of ACT/S cell). A flexible Li-S cell was also assembled to demonstrate its practical use as a flexible power source, which kept its high capacity and excellent mechanical stability even after repeated bending processes, holding great promise for fabricating next-generation flexible power supply for portable/wearable electronics.

5.2 Experimental Section

5.2.1 Preparation of Flexible ACT/S-rGO Hybrid Cathode Electrode

All chemicals are analytical grade and were used after purchasing without further purification. Activation of cotton T-shirt into ACTs followed our previously established method [53]. Typically, a piece of cotton textile was soaked in 1 M NaF solution and then dried overnight in the oven. The NaF treated cotton textile was thermally treated at $1000 \text{ }^\circ\text{C}$ for 1 h in a horizontal tube furnace under a continuous argon gas flow (300 sccm). After cooling, the as-obtained ACTs were washed with distilled water to remove residual NaF and then dried at $80 \text{ }^\circ\text{C}$ for 12 h. A piece of ACT ($1.5 \text{ cm} \times 2 \text{ cm}$) was first loaded with sulfur powders and then thermally treated at $156 \text{ }^\circ\text{C}$ for 10 h in a sealed autoclave to infiltrate sulfur into the inner pores and cavities of the ACT. After such thermal treatment, sulfur nanoparticles were homogeneously anchored on or penetrated into the ACT fibers to form an ACT/S nanocomposite. The mass of ACT is $\sim 2 \text{ mg cm}^{-2}$. The sulfur

loading of ACT/S composite was measured to be $\sim 5.5 \text{ mg cm}^{-2}$.

To prepare ACT/S-rGO nanocomposites, graphene oxide solution with a concentration of $\sim 4 \text{ mg mL}^{-1}$ was prepared using a modified Hummers method [54]. The ACT/S nanocomposite was dipped in the graphene oxide solution. A piece of ACT was also soaked in the same graphene oxide solution to serve as a reference for calculating the loading of graphene oxide in ACT/S-rGO. After drying for 6 h at $80 \text{ }^\circ\text{C}$, the as-prepared ACT/S-rGO was heated at $200 \text{ }^\circ\text{C}$ for 2 h to facilitate the reaction between sulfur and graphene oxide. Such thermal treatment process partially reduced the graphene oxide to conductive reduced graphene oxide. The loading of sulfur was calculated by weighing the ACT/S-rGO and ACT/rGO electrode with the same size. The mass of the ACT/rGO is $\sim 3 \text{ mg cm}^{-2}$. The sulfur loading of the as-prepared ACT/S-rGO electrode was measured to be $\sim 4.5 \text{ mg cm}^{-2}$. The mass ratio of sulfur in the ACT/S-rGO composite is $\sim 60\%$.

5.2.2 Preparation of Flexible Porous ACT Interlayer

A piece of cotton textile was first soaked with 1 M KOH solution. The KOH loaded textile was then dried at $80 \text{ }^\circ\text{C}$ for 6 h. The KOH treated textile was thermally treated at $1000 \text{ }^\circ\text{C}$ for 1 h with an argon flow of 300 sccm. The obtained KOH-activated ACT was further washed using distilled water and then dried in a vacuum oven at $105 \text{ }^\circ\text{C}$ for 24 h. The mass of the porous ACT is $\sim 1 \text{ mg cm}^{-2}$.

5.2.3 Characterization Methods

Scanning electron microscopy (SEM; FEI Quanta 650) and transmission electron microscopy (TEM; JEOL 2000FX), high resolution transmission electron microscopy (HRTEM, FEI Titan), X-ray diffraction (XRD; PANalytical X'Pert Pro Multi-Purpose Diffractometer (MPD)) equipped with Cu K_α radiation with $\lambda = 0.15406 \text{ nm}$, Raman spectroscopy (Renishaw InVia Raman microscope at 514 nm with 5% laser power), atomic force microscopy (AFM; Dimension Icon with ScanAsyst, Bruker) were used to characterize the structure of the as-prepared samples at different length scales.

5.2.4 Electrochemical Characterization of Flexible ACT/S-rGO Hybrid Cathode

The electrochemical properties of the ACT/S-rGO cathode were measured by using CR2032 type coin cells. The flexible ACT/S-rGO nanocomposite was directly used as the binder-free cathode material without adding any conductive agent. The ACT/S-rGO hybrid textile was punched into circular disks and dried at $60 \text{ }^\circ\text{C}$ for 24 h in a vacuum oven. The Li-S coin cell was

assembled with ACT/S-rGO as a cathode, KOH treated the porous ACT as the interlayer, lithium metal as an anode and Celgard 2400 film as a separator, respectively. The mass ratio of sulfur in the ACT/S-rGO with porous ACT cell system is ~13%, which will lower the energy density of the whole cell. To demonstrate its potential in constructing a flexible energy storage device, a piece of ACT/S-rGO (1 cm × 2 cm) was used as the flexible cathode to assemble flexible lithium-sulfur battery, together with a piece of lithium film of the same size as an anode and Celgard 2400 as a separator, respectively. For comparison, the ACT/S nanocomposite alone (without coating graphene oxide and using porous ACT interlayer) was also assembled into a Li-S cell. The electrolyte solution was freshly prepared with 1 M lithium bis(trifluoromethanesulfonyl)imide and 0.4 M LiNO₃ dissolved in 1:1 v/v 1,2-dimethoxyethane (DME) and 1,3-DOL solution. The CR2032 coin cells were assembled with MTI MSK-110 crimping machine in an argon-filled glove box (Mbraun, Germany) with oxygen and water contents below 1 and 0.1 ppm. The flexible Li-S cell was assembled using a handmade fixture and heat sealer. Galvanostatic charge/discharge measurements were carried out using a LAND CT2003A battery tester at the voltage window of 1.5 and 3.0 V vs Li/Li⁺. The capacities and charge/discharge rates were calculated based on the active sulfur. A CHI 660E electrochemical workstation was used to measure the cyclic voltammograms (CV) and electrochemical impedance spectroscopy (EIS) properties in the frequency range from 100 kHz to 0.05 Hz with an AC perturbation of 5 mV.

5.3 Results and Discussion

5.3.1 Structural and Morphological Characterization

The design and fabrication procedures of hollow ACT/S-rGO nanocomposite are schematically illustrated in Figure 5.1. Typically, a piece of cotton textile was first soaked with 1 M NaF solution and then dried in an oven to obtain NaF-treated cotton textile. After the heat treatment at 1000 °C, the NaF-treated cotton textile was transformed into a hollow activated cotton textile (ACT) (Step I). Nitrogen adsorption/desorption results showed that such hollow ACT had a large Brunauer–Emmet–Teller (BET) surface area of ~422.96 m² g⁻¹ with a pore size distribution ranging from 3 to 30 nm (Figure 5.2), which is desirable for impregnating sulfur into such conductive carbon substrate. During thermal impregnation at 156 °C (Step II), molten sulfur infiltrated into the inner pores and cavities of hollow ACT fibers to form ACT/S composite with a

high sulfur loading of $\sim 5.5 \text{ mg cm}^{-2}$. After the sulfur infiltration, the BET surface area of ACT/S composite was reduced down to $98 \text{ m}^2 \text{ g}^{-1}$.

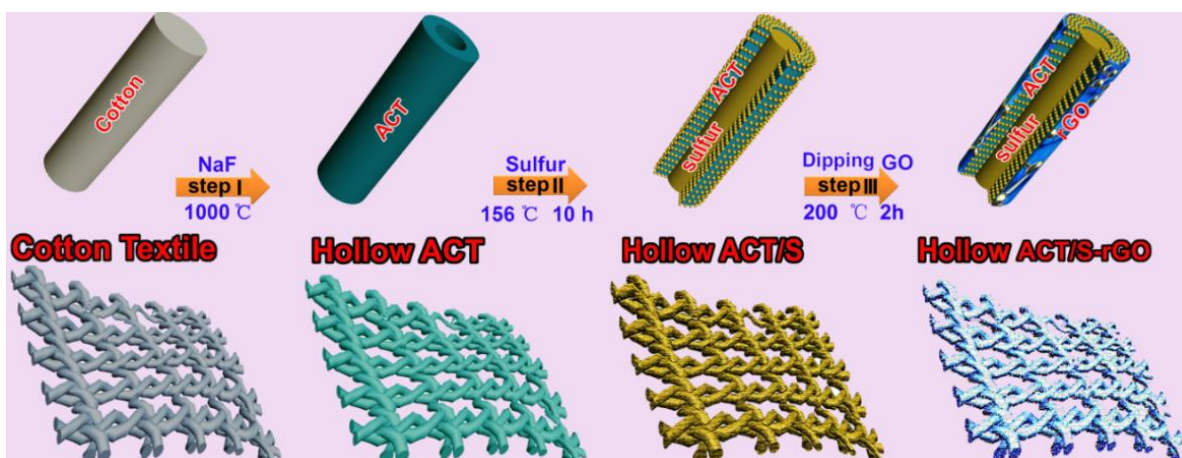


Figure 5.1 Schematic illustration of the fabrication process of hollow ACT/S-rGO composite.

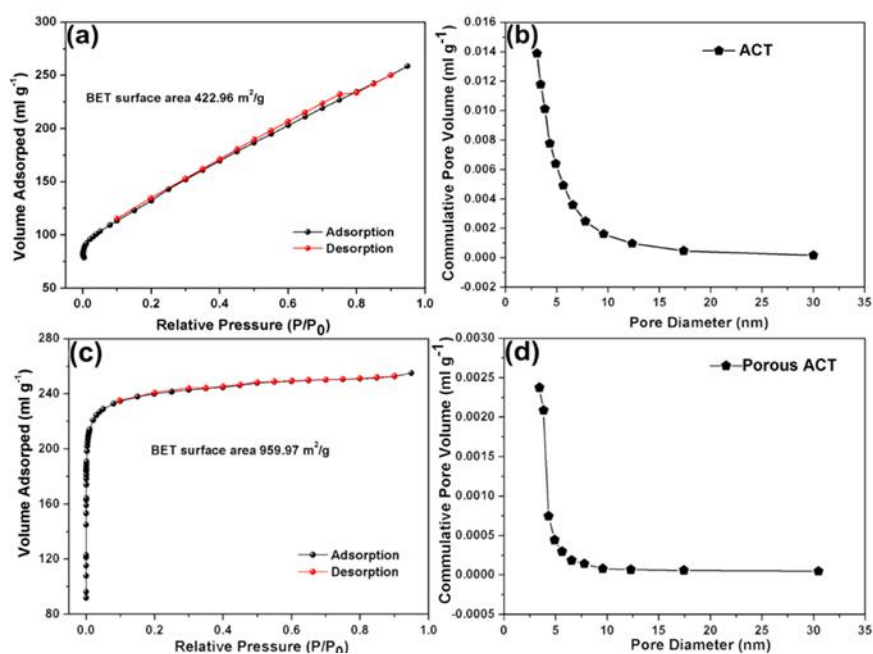


Figure 5.2 Nitrogen adsorption/desorption isotherms (a) and pore size distribution (b) curves of the prepared ACT. Nitrogen adsorption/desorption isotherms (c) and pore size distribution (d) curves of the prepared porous ACT treated by KOH.

It has been proven that the functional groups (epoxy and hydroxyl groups) on the surfaces of graphene oxide sheets could prevent lithium polysulfide from dissolution [37]. Herein, we dipped the ACT/S into a graphene oxide solution to wrap ACT fibers with scrolled graphene oxide sheets. Under the thermal treatment at 200 °C (Step III), on one hand, sulfur further penetrated into

the pores of ACT, on the other hand, the sulfur on ACT also attached to the graphene oxide sheets, additionally, the GO nanosheets were partially reduced to recover their conductivity, jointly retarding the loss of sulfur during the charge/discharge processes, improving the conductivity of ACT/S-rGO composite cathode and enabling fast electron transfer along ACT fibers. The as-prepared ACT/S-rGO composite could be directly used as a binder-free flexible cathode to construct Li-S batteries. The hollow ACT fiber together with the reduced graphene oxide sheets enhanced the sulfur loading, suppressed the dissolution of polysulfide, buffered the volume change, shortened Li^+ ion diffusion path, and facilitated fast charge transfer, synergistically leading to significantly improved electrochemical performances.

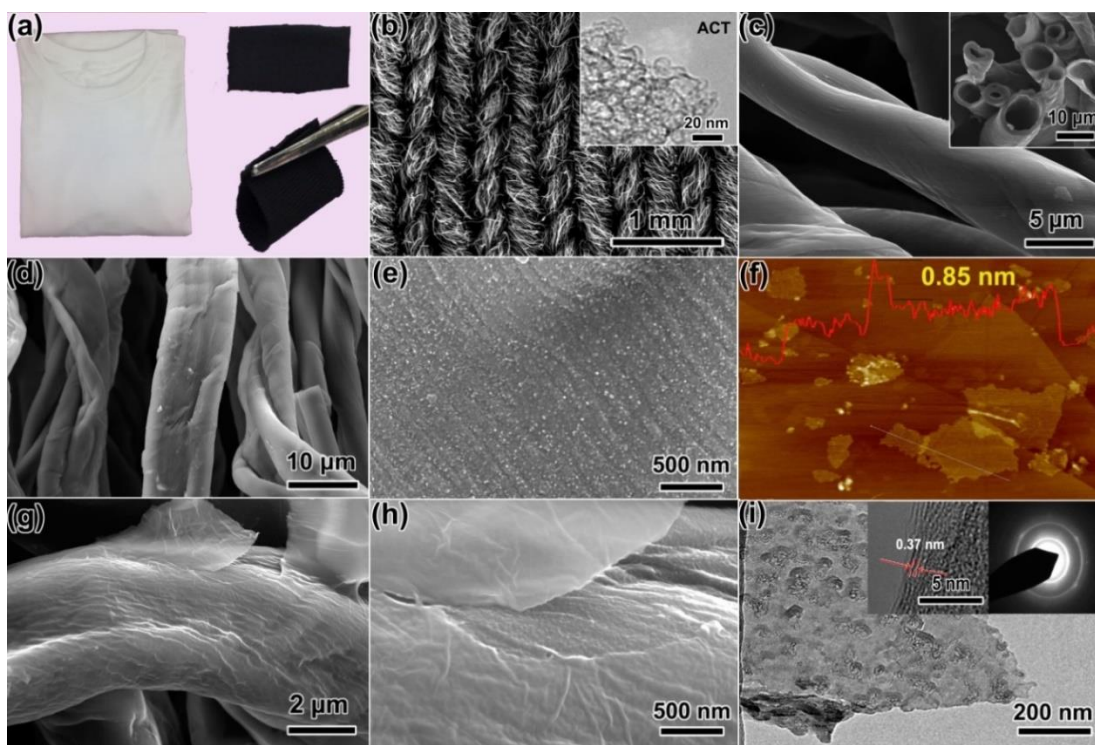


Figure 5.3 (a) Digital photograph of a commercial cotton T-shirt, and a piece of ACT under normal and folded state, showing its excellent flexibility; (b) SEM image of ACT, inset is the TEM image of ACT; (c) SEM image of ACT fiber, inset is the amplified cross-section of ACT fiber. (d) SEM image of ACT/S composite; (e) the amplified SEM image ACT/S composite; (f) AFM height image of graphene oxide nanosheet; g,h) SEM images of ACT/S-rGO composite at different magnifications; (i) TEM image of graphene oxide (GO) nanosheet, inset is the HRTEM image and SAED of rGO nanosheet.

Figure 5.3 shows the synthesis and morphology of ACT/S-rGO nanocomposite from a commercial cotton T-shirt. As demonstrated in Figure 5.3a, after activation, a piece of cotton T-shirt was transformed into ACT with excellent mechanical flexibility and outstanding conductivity (sheet resistance: $\sim 10\text{-}20$ ohm/sq.). Meanwhile, the ACT retained the interwoven pattern (Figure

5.3b). After activation, the ACT fibers were closely compacted together to form a highly conductive network. More impressively, the ACT fibers (diameters: ranging from 5 to 10 μm) not only inherited the cellulose fiber structure of the cotton textile but also exhibited porous tubular microstructure (Figure 5.3c and inset of Figure 5.3b). Such porous hollow tubular fibers helped sulfur infiltration, achieving high sulfur loading, facilitating ion diffusion, slowing down cathode polarization, and mitigating polysulfide dissolution.

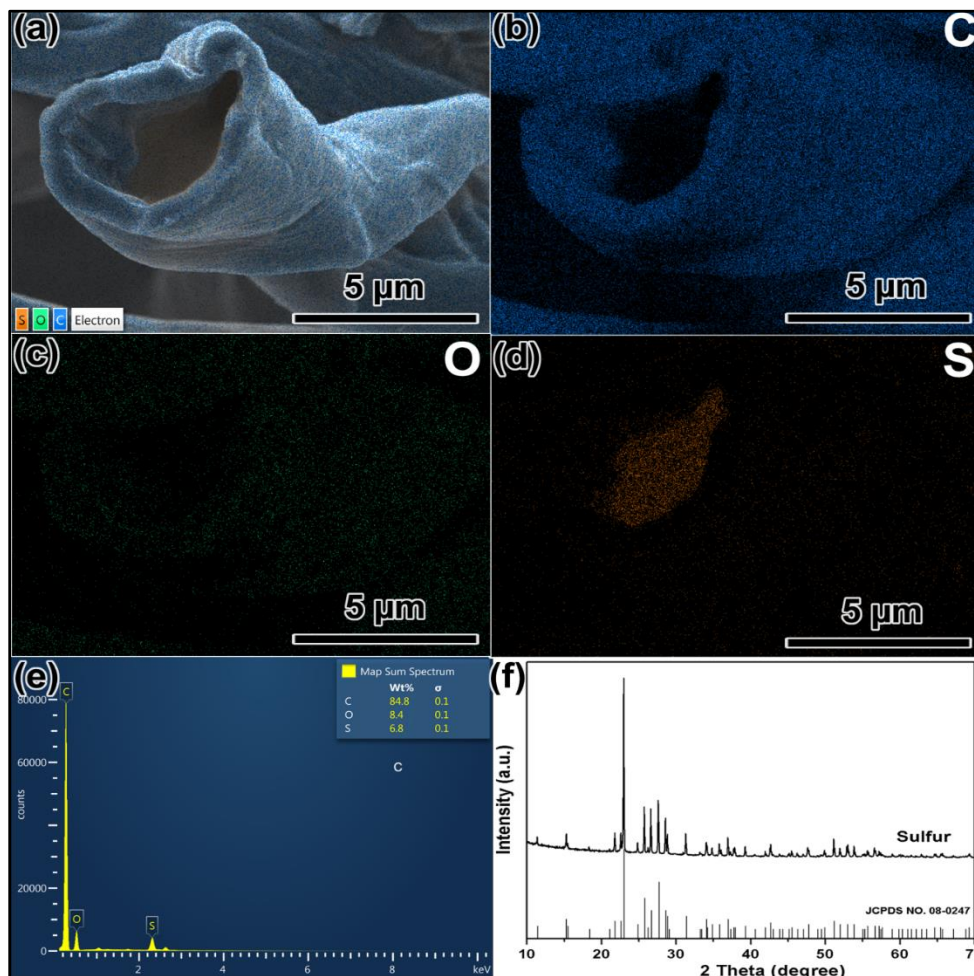


Figure 5.4 (a-d) EDS maps of the obtained ACT/S composite; (e) Relative element ratio of C, O, S in the ACT/S composite; (f) XRD pattern of the used S and its corresponding standard peaks.

Figure 5.3d shows the SEM images of the ACT/S composite. The close-up observation (Fig. 5.3e) showed that sulfur nanoparticles were homogeneously anchored on the corrugated surface of ACT with a sulfur/carbon mass ratio up to 3:1. Energy dispersive X-ray spectroscopy (EDX) was used to map the distribution of sulfur and carbon in ACT/S composite. As shown in Fig. 5.4a-d, in addition to the homogeneously deposited sulfur on the outer surface of ACT fibers,

sulfur mainly stored in the inner tubes of ACT fibers (Fig. 5.4d), which enabled higher sulfur loading than most of the reported carbon/sulfur composites. The tubular interwoven ACT not only increased the sulfur loading but also constructed a 3D conductive host for sulfur, enabling fast electrolyte ion diffusion and electron transfer. More importantly, such sulfur infiltrated porous tubular fibers were able to accommodate the volume change of sulfur during electrochemical reaction processes, ultimately maintaining the structural integrity of the electrode, minimizing polysulfide dissolution and improving sulfur utilization.

High sulfur loading and efficient sulfur utilization are essential to realizing high specific energy of the Li-S battery. Although, porous tubular ACT fibers showed potential as sulfur host and indeed improved the sulfur loading and electrical conductivity of the whole composite. The relatively wide range pore size distribution was not able to completely prevent sulfur dissolution during the electrochemical reaction processes, thereby leading to low sulfur utilization and fast capacity fading. To solve the aforementioned issues, graphene oxide was used as the immobilizer to wrap the ACT/S fiber to further prevent the sulfur losing by retarding the dissolution of polysulfides. The thickness of the as-synthesized graphene oxide sheets was measured to be 0.85 nm (Fig. 5.3f), indicating that the coated graphene oxide is almost monolayered sheet [55]. The functional groups (hydroxyl, epoxide, carbonyl, and carboxyl groups) on the surfaces of the graphene oxide sheets made the prepared graphene oxide sheets rough and thicker than single-layered graphene (0.78 nm). The graphene oxide sheets also showed rippled surface and etched pits resulting from oxygen-containing functional groups (Fig. 5.3i), which helped to anchor sulfur particles and prevented the dissolution of polysulfides. After soaking in GO solution, individual ACT/S fibers were wrapped with curved and entangled GO sheets (Figs. 5.3g,h). During sulfur infiltration at high temperature (200°C), sulfur interacted with the GO functional groups, which could prevent the loss of polysulfides by strong chemical bonding in the electrochemical reaction process. Meanwhile, the GO was partially reduced to rGO with recovered conductivity, forming a graphene-enabled conductive coating along the ACT fiber. Inset Fig. 5.3i is the typical HRTEM and SAED pattern of the rGO sheet. Although the discontinued crystal fringes in the HRTEM image of rGO indicated the existed defects, the well-defined diffraction spots in SAED pattern suggested re-established crystalline state in rGO nanosheets. The recovered crystal structure of rGO in ACT/S-rGO composite mitigated the poor conductivity of sulfur and facilitated fast electron transportation during the electrochemical reaction processes.

The reaction between sulfur and GO was further validated by Raman spectroscopy (Fig. 5.5a), which was often used to characterize the ordered/disordered structure of graphitic materials, especially for graphene [56]. In general, two feature bands in a typical Raman spectrum were used to identify graphene, one is the D band at $\sim 1350\text{ cm}^{-1}$ arising from the breathing mode of point photons of A_{1g} symmetry, the other is the G band at $\sim 1575\text{ cm}^{-1}$ resulting from the first order scattering of the E_{2g} phonon mode of in-plane sp^2 C atoms [57]. Compared with the ACT and GO, the new peaks ranging from 100 to 400 cm^{-1} and the shifted D band in the Raman spectrum of ACT/S-rGO can be assigned to the vibration modes of sulfur, suggesting the appearance of sulfur and the formation of chemical bonds between sulfur and rGO in the composite [58]. The increased I_D/I_G ratio in the ACT/S-rGO composite indicates more defects and disordered structure of the rGO sheets formed on the outside of the ACT fibers [57]. Figure 5.5b shows the XRD patterns of cotton textile, ACT, and ACT/S. After activation, the feature diffraction peaks of cotton textile disappeared, whereas a broad peak at $\sim 21^\circ$ for ACT appeared, indicating the formation of amorphous carbon. The XRD patterns of ACT/S and ACT/S-rGO (Fig. 5.5c) agreed well with the standard diffraction peaks of sublimed sulfur (JCPDS no. 08-0247), as shown in Fig. 5.5f.

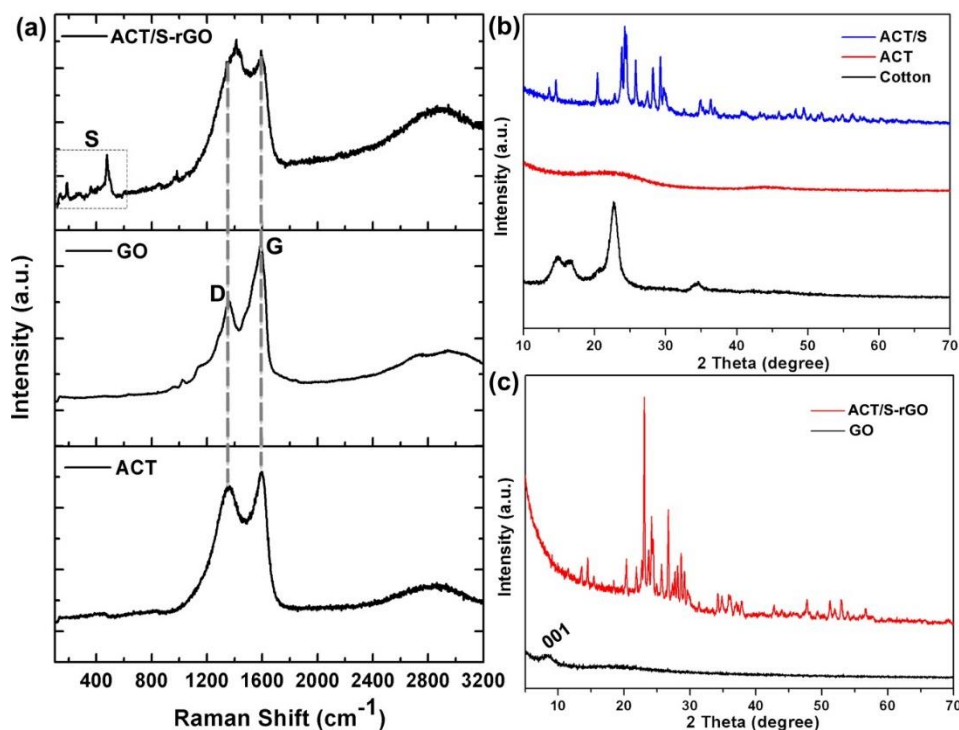


Figure 5.5 (a) Raman spectra of ACT, GO, and ACT/S-rGO; (b) XRD patterns of the cotton textile, ACT, ACT/S composite; (c) XRD patterns of GO and ACT/S-rGO composite.

Although the micropores were filled with sulfur, there were still numerous of open mesopores in the ACT/S-rGO composite (Fig. 5.6a). These open mesopores were able to accumulate the volume change of sulfur during the electrochemical reaction processes. HRTEM images showed that chain-like sulfur was closely anchored onto the porous ACT substrate (Figs. 5.6b,c) after the co-heating process. The d-space of the anchored sulfur is ~ 0.36 nm, which is in accordance with the (133) lattice plane of monoclinic sulfur. The messy diffraction pattern (Fig. 5.6d) suggests that the sulfur in the ACT/S composite is a mixture of polycrystalline and amorphous phases, in good agreement with the XRD results (Fig. 5.5c).

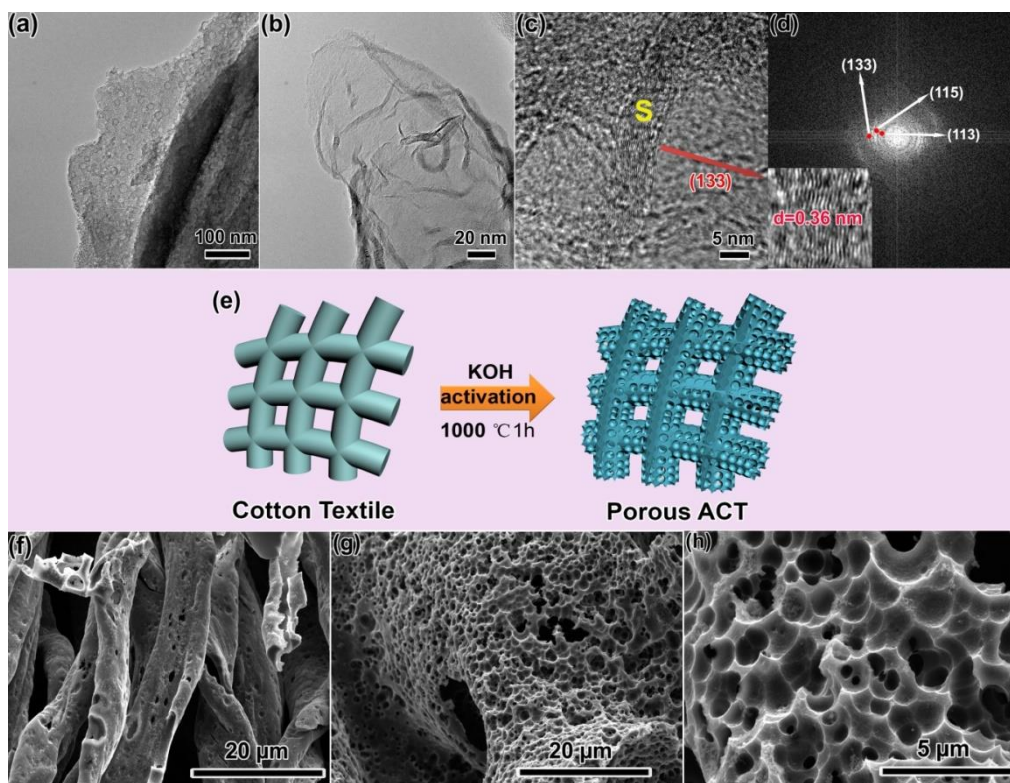


Figure 5.6 (a,b) TEM images of ACT/S at different magnifications; (c) HRTEM image of ACT/S, inset of d is the amplified region; (d) the corresponding FFT pattern of ACT/S; (e) Illustration of the conversion of cotton textile to porous ACT; (f-h) SEM images of porous ACT treated with KOH during the activation process.

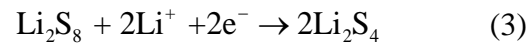
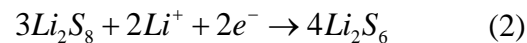
To push up the utilization of active materials and slow down the dissolution of polysulfide, a porous ACT was used as a bi-functional interlayer to enhance the cell configuration. As illustrated in Fig. 5.6e, the porous ACT was prepared by a simple one-step KOH activation method. The KOH activation process created micropores in the ACT fibers (Figs. 5.6f and g). The close-up observation showed that micropores were densely anchored on the surface of macropores (Fig. 5.6h). N_2 adsorption/desorption isotherms were used to further characterize the KOH-activated

porous ACT (Figs. 5.2c and d). The adsorption/desorption isotherm curve exhibited a typical type I profile, indicating the existence of microsized pores in the KOH-activated porous ACT. The KOH-activated porous ACT exhibited a larger BET surface area of $\sim 959.97 \text{ m}^2 \text{ g}^{-1}$ and a relatively wide size distribution ranging from 1 to 32 nm, with the average pore size of $\sim 2 \text{ nm}$. Such KOH-activated porous ACT, serving as the interlayer between the cathode and separator, not only facilitated fast charge transfer but also absorbed the dissoluble polysulfides, synergistically increasing the utilization of active materials and pushing up the cyclic performance.

5.3.2 Electrochemical Performance of Lithium-Sulfur Batteries with the KOH-activated Porous ACT Interlayer

To evaluate the electrochemical performance of the as-assembled lithium-sulfur batteries, CR2032-type coin cells were assembled with the ACT/S-rGO composite as cathode, lithium foil as anode, Celgard 2400 as separator, respectively. The electrochemical behaviors of the lithium-sulfur cells were investigated by cyclic voltammetry (CV), galvanostatic charge/discharge tests and electrochemical impedance spectroscopy (EIS). Figure 5.9a schematically illustrates the design wisdom of manipulating the “shuttle effect” of polysulfides by using a KOH-activated porous ACT as interlayer in the lithium-sulfur cell. Compared with the traditional lithium-sulfur cell configuration, the inserted flexible and conductive porous ACT simultaneously served as traps for the dissolved polysulfides and reservoir for the electrolyte, provided additional pathways for electrons and lithium ions, and accommodated large volumetric variation of sulfur during the electrochemical reaction processes. Theoretically, the CV curve of a typically lithium-sulfur cell is characterized by two reduction peaks (at $\sim 2.35 \text{ V}$ and $\sim 2.1 \text{ V}$ vs. Li^+/Li) and one oxidation peak ($\sim 2.5 \text{ V}$ vs. Li^+/Li), corresponding to the two-step reaction of sulfur with lithium, as described in the following equations: [59,60]

Step I: formation of dissoluble long chain lithium polysulfides (Li_2S_x , $4 \leq x$);



Step II: formation of insoluble Li_2S_2 and Li_2S ;

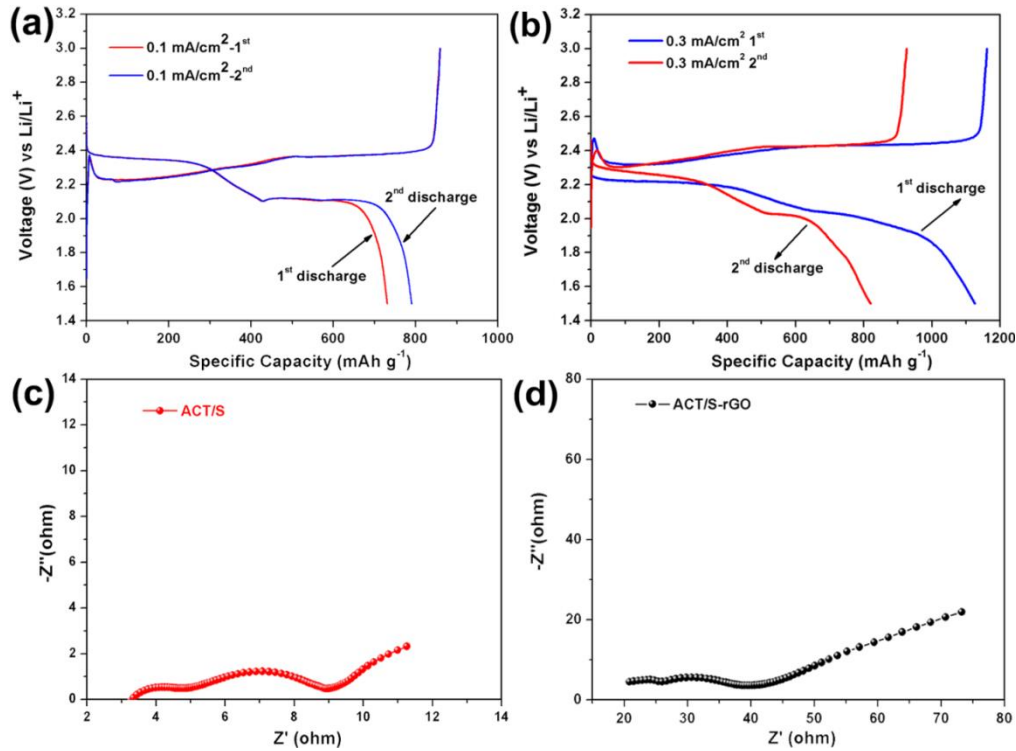
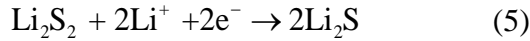
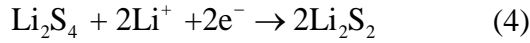


Figure 5.7 (a) Initial charge/discharge voltage-capacity profiles of porous ACT/S graphene at the current density of 0.1 mA cm^{-2} ; (b) Initial charge/discharge voltage-capacity profiles of ACT/S-rGO cathode with porous ACT interlayer at the current density of 0.3 mA cm^{-2} ; (c) Nyquist plot of ACT/S cathode; (d) Nyquist plots of ACT/S-rGO cathode with porous ACT interlayer.

To analyze the synergistic effects of the rGO coating and porous ACT interlayer in the ACT/S-rGO cell, the ACT/S and ACT/S-rGO cells without using porous ACT interlayer were also assembled and compared (Figure 5.7 and Figure 5.8). Figure 5.7a shows the first and second cycle charging/discharging voltage-capacity profiles of the ACT/S cell without porous ACT interlayer at the current density of 0.1 mA cm^{-2} . Both of the discharge curves displayed a typical two-plateau behavior of the sulfur cathode, indicating the formation of lithium polysulfides and $\text{Li}_2\text{S}_2/\text{Li}_2\text{S}$. Figure 5.7b shows the initial two cycles of charging/discharging voltage-capacity curves of the ACT/S-rGO cell with porous ACT interlayer at the current density of 0.3 mA cm^{-2} . Compared with ACT/S and ACT/S-rGO cells without porous ACT interlayer, the initial charging/discharging curves of ACT/S-rGO cathode with porous ACT interlayer showed a potential hysteresis phenomenon, leading to a low potential reduction, which could be due to the extra electrode

polarization required to overcome the nanoconfinement barrier of strong adsorption energy because of the introduction of the porous ACT interlayer. In fact, the porous ACT has demonstrated a strong micropore size distribution, as evidenced by the BET test (Figure 5.2c). On the other hand, the porous ACT will make more low-molecular (S_{2-4}) forms of elemental sulfur in a high dispersion state and a short chain configuration confined inside the narrow micropores of ACT, which are usually unstable due to their high energy state (low potential difference versus metallic lithium) as compared to large molecules of elemental sulfur with crown rings, finally leading to the electrochemical reduction process starting from S_{2-4} to S^{2-} . The similar phenomena have been reported for most of the Li-S system with micropore confinement [17, 61-64].

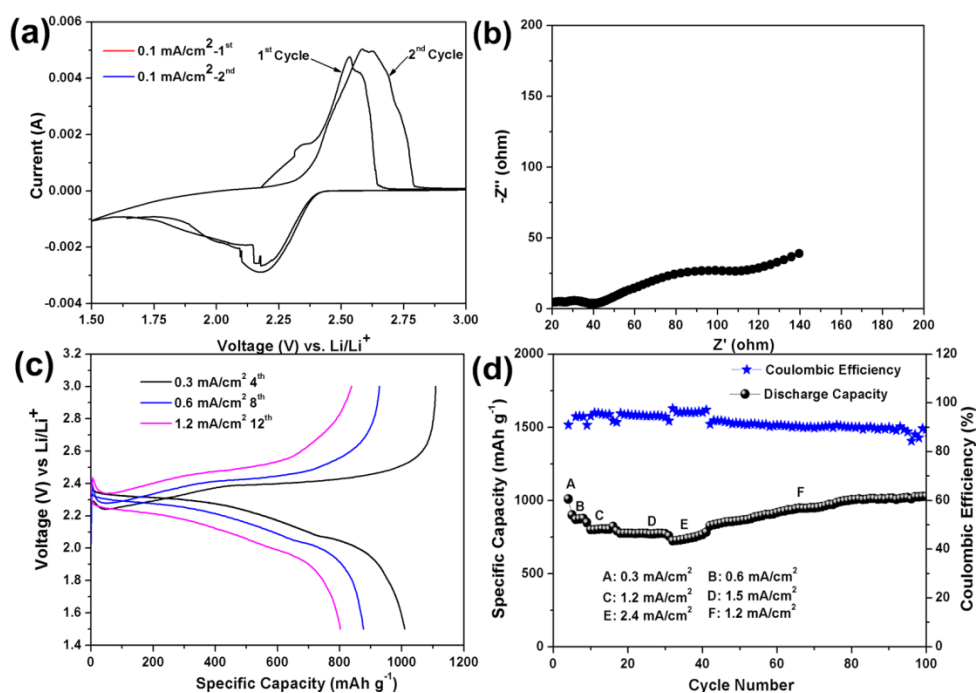


Figure 5.8 (a) Initial cyclic voltammogram profile of ACT/S-rGO cathode without porous ACT interlayer; (b) Nyquist plots of ACT/S-rGO cathode without porous ACT interlayer; (c) 4th, 8th, and 12th charge/discharge voltage-capacity profiles of ACT/S-rGO without porous ACT interlayer at different current densities; (d) Stepwise cycling performance of ACT/S-rGO cathode without porous ACT interlayer and its Coulombic efficiency.

Figures 5.8a and c show the initial cyclic voltammogram profiles and representative charging/discharging voltage-capacity curves of ACT/S-rGO cathode without porous ACT interlayer, respectively. Compared with the two discharging plateaus of ACT/S cell (at ~ 2.37 V and ~ 2.1 V), the ACT/S-rGO cell without porous ACT interlayer exhibited a single pair of redox peaks (Figure 5.8a), which also corresponds to the representative charging/discharging curves (Figure 5.8c), indicating the special functions of rGO to retard the dissolution of polysulfides. On

the other hand, the ACT/S-rGO cell with porous ACT interlayer demonstrated two lower discharging plateaus (at ~ 2.2 V and ~ 2.0 V) with a high initial capacity of 1126 mAh g^{-1} .

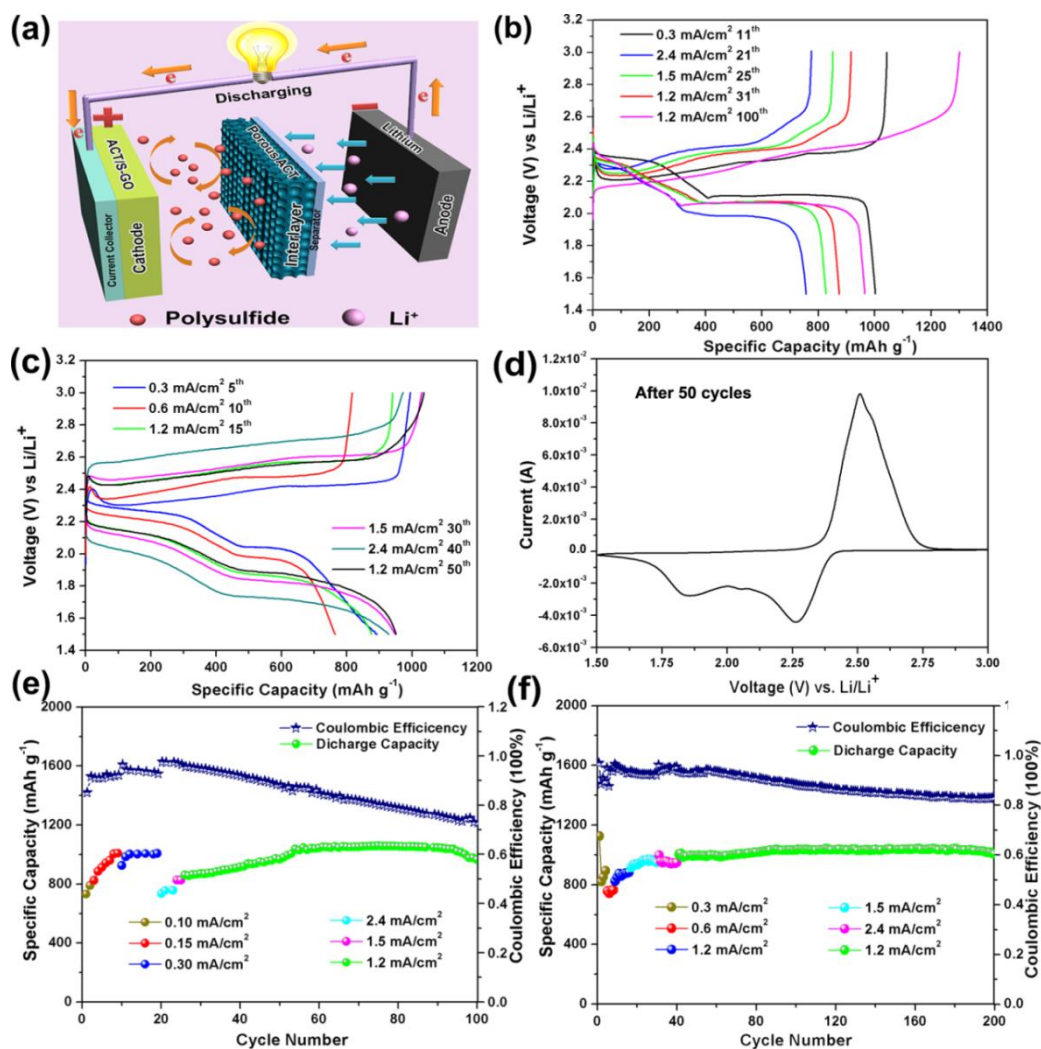


Figure 5.9 (a) Schematic illustration of the systematic effects of a Li-S battery with ACT/S-rGO as a cathode and porous ACT as an interlayer to manipulate the “shuttle effect”; (b) 11th, 21th, 25th, 31th and 100th charge/discharge voltage-capacity profiles of ACT/S cathode at different current densities; (c) 5th, 10th, 15th, 30th, 40th and 50th charge/discharge voltage-capacity profiles of ACT/S-GO with porous ACT interlayer at different current densities; (d) Cyclic voltammogram profile of ACT/S-rGO cathode with porous ACT interlayer after 50 charge/discharge cycles; (e) Stepwise cycling performance of ACT/S cathode and its Coulombic efficiency; (f) Stepwise cycling performance of ACT/S-rGO cathode with KOH-activated porous ACT as an interlayer and its Coulombic efficiency.

Unusually, the ACT/S-rGO cell with porous ACT interlayer exhibited a shorter second discharging plateau at ~ 2.0 V corresponding to a fast drop discharge capacity of 820 mAh g^{-1} . The high initial capacity could be ascribed to the irreversible reactions during the first cyclic process, such as the trapping of lithium inside the active materials, the adsorption of polysulfides in the porous interlayer, the formation of SEI films, and the electrolyte decomposition [65,66]. While,

the shorter discharge plateau at ~ 2.0 V in the second cycle could be attributed to the porous ACT interlayer suppressed the dissolution of long-chain polysulfides (Step I) and retarded the further reaction with lithium to form insoluble $\text{LiS}_2/\text{Li}_2\text{S}$ (Step II). With the increasing of cyclic number, the second discharge voltage plateau became longer and more clear, along with the increase of capacity (Fig. 5.9c), which could be ascribed to the gradually weakened trapping capability of porous ACT interlayer. With the saturation of long-chain polysulfides in the porous ACT interlayer, some of them were released to react under the second discharge plateau, contributing to the increasing capacity. After 50 charge/discharge cycles, the anodic oxidation peak remained at ~ 2.5 V, while two cathodic reduction peaks appeared with the main peak at ~ 1.8 V and the other peak at ~ 2.1 V (Fig. 5.9d). The new appeared low potential CV peaks (at ~ 1.8 V) agreed well with the low discharge plateau (at ~ 1.8 V) at 50th charge/discharge voltage-capacity profile at the current density of 1.2 mA/cm^2 (Fig. 5.9c). Most importantly, in contrast with the fast capacity decay in traditional sulfur or carbon/sulfur composite cathodes, ACT/S cell exhibited an increased capacity in the initial cycles (Fig. 5.9e). However, besides a fast capacity decay in the second discharge cycle, ACT/S-rGO cell also demonstrated a similar increasing trend of capacity as that of ACT/S cell (Fig. 5.9f) since the third cycle, which could be ascribed to the unique tubular structure of ACT fibers with open channels and interconnected pores. The hollow cavities in ACT fibers enabled high sulfur loading, meanwhile, the porous structure provided access of electrolyte ions to the inner sulfur in ACT fiber, ensuring the contribution of the inner active sulfur to the total capacity.

To evaluate the rate performance for the practical application, the charging/discharging voltage-capacity profiles of the ACT/S and ACT/S-rGO cells were compared at the current densities ranging from 0.3 mA cm^{-2} to 2.4 mA cm^{-2} (Fig. 5.9b,c). As the current density raised up, the ACT/S cell showed a remarkable kinetic effect, i.e., the charge plateau increased whereas the discharge plateau decreased, leading to higher overpotential and lower capacity at the high current density regime. The reversible discharge capacities of ACT/S cell at 11th (0.3 mA cm^{-2}), 21th (2.4 mA cm^{-2}), 15th (1.5 mA cm^{-2}), 31th (1.2 mA cm^{-2}), 100th (1.2 mA cm^{-2}) cycles are ~ 1002 , ~ 754 , ~ 825 , ~ 871 , and $\sim 965 \text{ mAh g}^{-1}$, respectively. For the ACT/S-rGO cell with porous ACT interlayer, the reversible discharge capacities at 5th (0.3 mA cm^{-2}), 10th (0.6 mA cm^{-2}), 15th (1.2 mA cm^{-2}), 30th (1.5 mA cm^{-2}), 40th (2.4 mA cm^{-2}) and 50th (1.2 mA cm^{-2}) cycles are ~ 892 , ~ 762 , ~ 875 , ~ 941 , ~ 929 , and $\sim 1036 \text{ mAh g}^{-1}$, respectively. In addition to the increased capacity, the

capacity remained well with the current densities increasing from 0.3 to 2.4 mA cm⁻², pointing towards excellent rate performance. The new discharge plateau at about 1.8 V, in good agreement with the CV results resulted from the gradually blocked micropores in the porous ACT interlayer, which disabled the trapping ability of the ACT interlayer.

To further demonstrate the advantages of the ACT/S-rGO cathode with porous ACT interlayer, electrochemical impedance spectroscopy (EIS) measurements were performed for the ACT/S and ACT/S-rGO cells without interlayer, as well as the ACT/S-rGO cell with an interlayer (Figs. 5.7c,d and Figure 5.8b). Both profiles consist of two semicircles in the high-frequency regime and a straight line in the low-frequency regime. The first semicircle in high-frequency range corresponds to the formation of the passivation layer (Li₂S₂/Li₂S) on the surface of lithium anode. The second semi-circle in the medium-to-low frequency can be assigned to the charge transfer resistance (R_{ct}), and the straight line in the low-frequency regime should be ascribed to the lithium ions diffusion [35]. Although the recovered conductivity of reduced graphene oxide coating could increase the conductivity of ACT/S cathode and ensure fast electron transfer, compared with the pure ACT/S cathode and ACT/S-rGO cathode with the ACT interlayer, the pure ACT/S-rGO cathode without the ACT interlayer showed increased diameter of the second semicircle arc, indicating relative larger charge transfer resistance, which could be ascribed to the residual oxygen-functional groups and defects on the surface of rGO, increasing the charge transfer resistance. However, the added porous ACT interlayer not only help trap the dissolution of the polysulfides but also increase the conductivity of the whole electrode.

Cycling life and Coulombic efficiency are also important parameters in evaluating the practical application of lithium-sulfur battery. Figure 5.9e, Figure 5.8d and Figure 4.9f show the cyclic performance and corresponding Coulombic efficiency of the ACT/S and ACT/S-rGO cells without interlayer, and the ACT/S-rGO cell with the ACT interlayer. Except for the fast second discharge capacity decay for ACT/S-rGO cell, all of them demonstrated increased capacities in the initial several cycles, indicating that the sulfur in the inner cores of the hollow ACT fibers was progressively consumed. The ACT/S-rGO did not show capacity decay but an increase from ~900 mAh g⁻¹ to ~1000 mAh g⁻¹ when it was cycled from 0.3 up to 2.4 mA cm⁻², indicating excellent rate performance. For the ACT/S cell, however, an obvious capacity decay was observed after 95 charge/discharge cycles (Fig. 5.9e), while the ACT/S-rGO cell without porous ACT interlayer

demonstrated an increased capacitance. One phenomenon is that the ACT/S cell will suddenly become unchargeable after ~ 100 cycles, which could be ascribed to the growth of lithium dendrites, leading to the partial internal short circuit. While, with the help of rGO coating and porous ACT interlayer, the ACT/S-rGO cell doubled its cycling life up to 200 cycles (Fig. 5.9f). It can be seen that all of the assembled Li-S cells demonstrated a similar decreasing trend during the cyclic process, which could be ascribed to the dissolution of the polysulfides, leading to the loss of the active sulfur. However, compared with the continually decreased Coulombic efficiency for the ACT/S cell ($\sim 72\%$ at 100^{th} cycle) and ACT/S-rGO cell ($\sim 84\%$ at 100^{th} cycle), the ACT/S-rGO cell with porous ACT interlayer exhibited remarkably improved performance with an effective Coulombic efficiency of $\sim 83\%$ even after 200 cycles, demonstrating the synergistic effects of rGO coating and porous ACT interlayer.

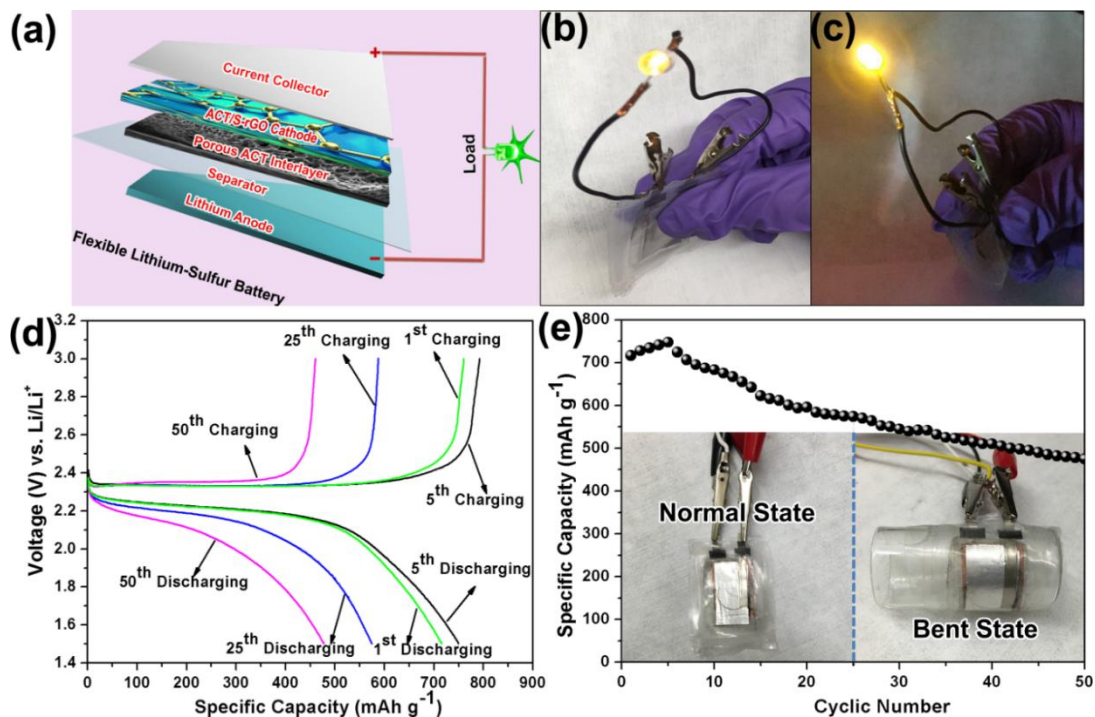


Figure 5.10 (a) Schematic illustration of the assembled flexible lithium-sulfur battery; (b,c) Digital photographs of a yellow light-emitting diode (LED) lighted by the assembled flexible Li-S cell under normal and bent states, respectively; (d) The 1st, 5th and 25th charge/discharge voltage-capacity profiles under the normal state and the 50th charge/discharge voltage-capacity profile under a bent state of the flexible Li-S cell at the current density of 1.2 mA cm^{-2} ; (e) Cyclic performance of the flexible lithium cell under normal and bent states at the current density of 1.2 mA cm^{-2} .

As illustrated in Fig. 5.10a, a flexible lithium cell with ACT/S-rGO as a cathode, porous ACT as an interlayer, and lithium foil as an anode was assembled to demonstrate its practical

application as a flexible energy storage device. The assembled flexible lithium-sulfur battery could be used to light a commercial LED (Fig. 5.10b). The brightness of the LED remained same even under a severely folded state (Fig. 5.10c). Figure 5.10d shows the representative charging/discharging voltage-capacity profiles of the assembled flexible cells under normal (1st, 5th and 25th cycles) and bent states (50th cycle). All voltage-capacity curves of the flexible cell exhibited similar charge/discharge plateaus whether at normal or bent states as that of the coin cell, indicating the excellent mechanical robustness and electrochemical stability. Figure 5.10e shows the cyclic performance of the flexible cell at normal and bent states for the initial 50 cycles. Compared with the coin cell, the flexible cell did not exhibit very high capacity, probably due to the package issues, which usually lead to the relatively loose contact between cathode and anode. More encouragingly, the capacity of the flexible cell retained more than 400 mAh g⁻¹ even after 50 cycles under the bent state, which is still very promising for practical application.

The exceptional capacity performance, excellent rate capacity, and improved Coulombic efficiency together with the remarkable flexibility of the as-prepared ACT/S-rGO cathode can be ascribed to the following merits: (1) the porous tubular structure of ACT with inner cavities not only remarkably increased sulfur loading, but also effectively accommodated the volumetric variation of sulfur and maintained the structure integrity of electrode during the electrochemical reaction process; (2) The hollow ACT fibers (served as an electrolyte reservoir) together with the partially reduced rGO (served as a polysulfide immobilizer and conductive coating), shortened the transportation/diffusion path, effectively trapped the dissolved polysulfides and facilitated the electron transfer, thereby enabling high sulfur utilization and faster kinetics; (3) the KOH-activated porous ACT with hierarchical porous structure, serving as the bi-functional interlayer, adsorbed the dissolved polysulfides, manipulated the “shuttle effect”, and promoted the penetration of electrolyte ions, enabling the exceptional capacity retention and outstanding rate capability. The individual components in the ACT/S-rGO cell were teamed up to achieve high sulfur loading and utilization, exceptional capacity performance, excellent reversibility and high rate discharge capability.

5.4 Conclusion

In summary, activated cotton textile (ACT) with porous tubular fibers was used to load sulfur to form ACT/S composite, which was further wrapped with partially reduced graphene

oxide (ACT/S-rGO) to immobilize polysulfides for Li-S battery application. In addition, the KOH-activated ACT with hierarchical porous structure was inserted between cathode and separator to innovate the cell configuration. The unique porous tubular structure promoted sulfur infiltration, enabling a high sulfur loading of $\sim 5.5 \text{ mg cm}^{-2}$. The wrapped rGO sheets together with the KOH-activated ACT interlayer not only suppressed the polysulfides dissolution but also modified the conductivity and facilitated fast electron transition along ACT fiber, jointly enabling high sulfur utilization and excellent rate performance. When used as a binder-free cathode, the ACT/S-rGO cell with porous ACT interlayer exhibited an exceptional capacity increasing (from 3th cycle 852 mAh g^{-1} to 150th cycle $\sim 1037 \text{ mAh g}^{-1}$) in the first 150 cycles, impressive rate performance (the discharge capacitance retained well with increasing current density from 0.3 to 2.4 mA cm^{-2}) and doubled cyclic stability (compared with the 100 cycles for ACT/S cell). A flexible ACT/S-rGO lithium-sulfur cell was also assembled to demonstrate its potential as a flexible energy storage device, which retained its high capacity and excellent mechanical stability after repeated mechanical bending processes. Such cotton textile enabled flexible Li-S system with porous interlayer opens the door for constructing next-generation flexible power sources for future flexible/wearable electronics application, including flexible cell phones, wearable electronics, electronic skins, and implantable biomedical devices.

References

- [1] P.G. Bruce, B. Scrosati, J.-M. Tarascon, Nanomaterials for rechargeable lithium batteries, *Angew. Chemie Int. Ed.* 47 (2008) 2930–2946.
- [2] H. Wei, D. Cui, J. Ma, L. Chu, X. Zhao, H. Song, H. Liu, T. Liu, N. Wang, Z. Guo, Energy conversion technologies towards self-powered electrochemical energy storage systems: the state of the art and perspectives, *J. Mater. Chem. A.* 5 (2017) 1873–1894.
- [3] J.B. Goodenough, Y. Kim, Challenges for Rechargeable Li Batteries [†], *Chem. Mater.* 22 (2010) 587–603.
- [4] A.S. Aricò, P. Bruce, B. Scrosati, J.-M. Tarascon, W. van Schalkwijk, Nanostructured materials for advanced energy conversion and storage devices., *Nat. Mater.* 4 (2005) 366–377.

- [5] S. Guo, J. Liu, S. Qiu, Y. Wang, X. Yan, N. Wu, S. Wang, Z. Guo, Enhancing Electrochemical Performances of TiO₂ Porous Microspheres through Hybridizing with FeTiO₃ and Nanocarbon, *Electrochim. Acta.* 190 (2016) 556–565.
- [6] S. Guo, G. Lu, S. Qiu, J. Liu, X. Wang, C. He, H. Wei, X. Yan, Z. Guo, Carbon-coated MnO microparticulate porous nanocomposites serving as anode materials with enhanced electrochemical performances, *Nano Energy.* 9 (2014) 41–49.
- [7] X. Ji, K.T. Lee, L.F. Nazar, A highly ordered nanostructured carbon-sulphur cathode for lithium-sulphur batteries., *Nat. Mater.* 8 (2009) 500–506.
- [8] P.G. Bruce, S. a. Freunberger, L.J. Hardwick, J.-M. Tarascon, Li–O₂ and Li–S batteries with high energy storage, *Nat. Mater.* 11 (2011) 172–172.
- [9] J. Xiao, Understanding the lithium sulfur battery system at relevant scales, *Adv. Energy Mater.* 5 (2015) 1501102.
- [10] Y.-S. Su, A. Manthiram, Lithium–sulphur batteries with a microporous carbon paper as a bifunctional interlayer, *Nat. Commun.* 3 (2012) 1166..
- [11] L. Suo, Y.-S. Hu, H. Li, M. Armand, L. Chen, A new class of Solvent-in-Salt electrolyte for high-energy rechargeable metallic lithium batteries., *Nat. Commun.* 4 (2013) 1481.
- [12] X. Ji, S. Evers, R. Black, L.F. Nazar, Stabilizing lithium–sulphur cathodes using polysulphide reservoirs, *Nat. Commun.* 2 (2011) 325.
- [13] J. Zheng, J. Tian, D. Wu, M. Gu, W. Xu, C. Wang, F. Gao, M.H. Engelhard, J.G. Zhang, J. Liu, J. Xiao, Lewis acid-base interactions between polysulfides and metal organic framework in lithium sulfur batteries, *Nano Lett.* 14 (2014) 2345–2352.
- [14] J. Ma, Z. Fang, Y. Yan, Z. Yang, L. Gu, Y.-S. Hu, H. Li, Z. Wang, X. Huang, Novel large-Scale Synthesis of a C/S Nanocomposite with Mixed Conducting Networks through a Spray Drying Approach for Li-S Batteries, *Adv. Energy Mater.* 5 (2015) 1500046.
- [15] A. Manthiram, Y. Fu, Y.S. Su, Challenges and prospects of lithium-sulfur batteries, *Acc. Chem. Res.* 46 (2013) 1125–1134.

- [16] S. Chen, F. Dai, M.L. Gordin, D. Wang, Exceptional electrochemical performance of rechargeable Li–S batteries with a polysulfide-containing electrolyte, *RSC Adv.* 3 (2013) 3540.
- [17] D. Aurbach, E. Pollak, R. Elazari, G. Salitra, C.S. Kelley, J. Affinito, On the surface chemical aspects of very high energy density, rechargeable Li-sulfur batteries, *J. Electrochem. Soc.* 156 (2009) A694–A702.
- [18] D.-W. Wang, Q. Zeng, G. Zhou, L. Yin, F. Li, H.-M. Cheng, I.R. Gentle, G.Q.M. Lu, Carbon–sulfur composites for Li–S batteries: status and prospects, *J. Mater. Chem. A.* 1 (2013) 9382.
- [19] H. OGAWA, A. UNEMOTO, I. HONMA, Quasi-Solid-State Lithium-sulfur battery using room temperature ionic liquid-Li-salt-fumed silica nanoparticle composites as electrolytes, *Electrochemistry.* 80 (2012) 765–767.
- [20] A. Unemoto, H. Ogawa, Y. Gambe, I. Honma, Development of lithium-sulfur batteries using room temperature ionic liquid-based quasi-solid-state electrolytes, *Electrochim. Acta.* 125 (2014) 386–394.
- [21] S. Urbonaite, T. Poux, P. Novák, Progress towards commercially viable Li-S battery cells, *Adv. Energy Mater.* 5 (2015) 1500118.
- [22] B. Zhang, X. Qin, G.R. Li, X.P. Gao, Enhancement of long stability of sulfur cathode by encapsulating sulfur into micropores of carbon spheres, *Energy Environ. Sci.* 3 (2010) 1531.
- [23] X. Li, Y. Cao, W. Qi, L. V. Saraf, J. Xiao, Z. Nie, J. Mietek, J.-G. Zhang, B. Schwenzer, J. Liu, Optimization of mesoporous carbon structures for lithium–sulfur battery applications, *J. Mater. Chem.* 21 (2011) 16603.
- [24] J. Schuster, G. He, B. Mandlmeier, T. Yim, K.T. Lee, T. Bein, L.F. Nazar, Spherical ordered mesoporous carbon nanoparticles with high porosity for Lithium-Sulfur batteries, *Angew. Chemie Int. Ed.* 51 (2012) 3591–3595.
- [25] J. Guo, Y. Xu, C. Wang, Sulfur-impregnated disordered carbon nanotubes cathode for lithium-sulfur batteries, *Nano Lett.* 11 (2011) 4288–4294.

- [26] H. Wang, Y. Yang, Y. Liang, J.T. Robinson, Y. Li, A. Jackson, Graphene-Wrapped Sulfur Particles as a Rechargeable Lithium Sulfur Battery Cathode Material with High Capacity and Cycling Stability, (2011) 2644–2647.
- [27] R. Chen, T. Zhao, J. Lu, F. Wu, L. Li, J. Chen, G. Tan, Y. Ye, K. Amine, Graphene-based three-dimensional hierarchical sandwich-type architecture for high-performance Li/S batteries, *Nano Lett.* 13 (2013) 4642–4649.
- [28] G. Zheng, Y. Yang, J.J. Cha, S.S. Hong, Y. Cui, Hollow carbon nanofiber-encapsulated sulfur cathodes for high specific capacity rechargeable lithium batteries, *Nano Lett.* 11 (2011) 4462–4467.
- [29] W. Zhou, Y. Yu, H. Chen, F.J. Disalvo, H.D. Abruña, Yolk-shell structure of polyaniline-coated sulfur for lithium-sulfur batteries, *J. Am. Chem. Soc.* 135 (2013) 16736–16743.
- [30] S.S. Zhang, Effect of Discharge Cutoff Voltage on Reversibility of Lithium/Sulfur Batteries with LiNO₃-Contained Electrolyte, *J. Electrochem. Soc.* 159 (2012) A920–A923..
- [31] A. Manthiram, S.-H. Chung, C. Zu, Lithium-sulfur batteries: progress and prospects, *Adv. Mater.* 27 (2015) 1980-2006.
- [32] Z. Wei Seh, W. Li, J.J. Cha, G. Zheng, Y. Yang, M.T. McDowell, P.-C. Hsu, Y. Cui, Sulphur–TiO₂ yolk–shell nanoarchitecture with internal void space for long-cycle lithium–sulphur batteries, *Nat. Commun.* 4 (2013) 1331.
- [33] Y.-S. Su, A. Manthiram, A new approach to improve cycle performance of rechargeable lithium–sulfur batteries by inserting a free-standing MWCNT interlayer, *Chem. Commun.* 48 (2012) 8817. doi:10.1039/c2cc33945e.
- [34] X. Wang, Z. Wang, L. Chen, Reduced graphene oxide film as a shuttle-inhibiting interlayer in a lithium–sulfur battery, *J. Power Sources.* 242 (2013) 65–69.
- [35] G. Zhou, S. Pei, L. Li, D.-W. Wang, S. Wang, K. Huang, L.-C. Yin, F. Li, H.-M. Cheng, A graphene-pure-sulfur sandwich structure for ultrafast, long-life lithium-sulfur batteries, *Adv. Mater.* 26 (2014) 625–631.

- [36] A. Manthiram, Y. Fu, S. Chung, C. Zu, Y. Su, Rechargeable lithium-sulfur batteries, *Chem. Rev.* 114 (2014) 11751–11787.
- [37] L.S. Cells, L. Ji, M. Rao, H. Zheng, L. Zhang, O.Y. Li, W. Duan, Graphene oxide as a sulfur immobilizer in high performance lithium/sulfur cells, *J. Am. Chem. Soc.* 133 (2011) 18522–18525.
- [38] N. Li, M. Zheng, H. Lu, Z. Hu, C. Shen, X. Chang, G. Ji, J. Cao, Y. Shi, High-rate lithium-sulfur batteries promoted by reduced graphene oxide coating, *Chem. Commun.* 48 (2012) 4106.
- [39] G. Zhou, F. Li, H.-M. Cheng, Progress in flexible lithium batteries and future prospects, *Energy Environ. Sci.* 7 (2014) 1307.
- [40] Z. Gao, W. Yang, J. Wang, N. Song, X. Li, Flexible all-solid-state hierarchical NiCo₂O₄/porous graphene paper asymmetric supercapacitors with an exceptional combination of electrochemical properties, *Nano Energy.* 13 (2015) 306–317.
- [41] Z. Song, T. Ma, R. Tang, Q. Cheng, X. Wang, D. Krishnaraju, R. Panat, C.K. Chan, H. Yu, H. Jiang, Origami lithium-ion batteries, *Nat. Commun.* 5 (2014) 1–6.
- [42] L. Li, Z.P. Wu, H. Sun, D. Chen, J. Gao, S. Suresh, P. Chow, C.V. Singh, N. Koratkar, A foldable lithium-sulfur battery, *ACS Nano* 9 (2015) 11342–11350.
- [43] Z. Gao, N. Song, X. Li, Microstructural design of hybrid CoO@NiO and graphene nano-architectures for flexible high performance supercapacitors, *J. Mater. Chem. A.* 3 (2015) 14833–14844.
- [44] Z. Gao, N. Song, Y. Zhang, X. Li, Cotton-textile-enabled, flexible lithium-ion batteries with enhanced capacity and extended lifespan, *Nano Lett.* 15 (2015) 8194–8203.
- [45] J. Zhu, M. Chen, H. Wei, N. Yerra, N. Haldolaarachchige, Z. Luo, D.P. Young, T.C. Ho, S. Wei, Z. Guo, Magnetocapacitance in magnetic microtubular carbon nanocomposites under external magnetic field, *Nano Energy.* 6 (2014) 180–132.
- [46] J. Zhu, M. Chen, N. Yerra, N. Haldolaarachchige, S. Pallavkar, Z. Luo, T.C. Ho, J. Hopper, D.P. Young, S. Wei, Z. Guo, Microwave synthesized magnetic tubular carbon

- nanocomposite fabrics toward electrochemical energy storage., *Nanoscale*. 5 (2013) 1825–30.
- [47] S.H. Chung, C.H. Chang, A. Manthiram, A Carbon-Cotton Cathode with Ultrahigh-Loading Capability for Statically and Dynamically Stable Lithium-Sulfur Batteries, *ACS Nano*. 10 (2016) 10462–10470.
- [48] H. Wang, Z. Chen, H.K. Liu, Z. Guo, A facile synthesis approach to micro–macroporous carbon from cotton and its application in the lithium–sulfur battery, *RSC Adv*. 4 (2014) 65074–65080.
- [49] Z. Gao, C. Bumgardner, N. Song, Y. Zhang, J. Li, X. Li, Cotton-textile-enabled flexible self-sustaining power packs via roll-to-roll fabrication, *Nat. Commun*. 7 (2016) 11586.
- [50] C. Alippi, A unique timely moment for embedding intelligence in applications, *CAAI Trans. Intell. Technol*. 1 (2016) 1–3.
- [51] H. Jin, Q. Chen, Z. Chen, Y. Hu, J. Zhang, Multi-LeapMotion sensor based demonstration for robotic refine tabletop object manipulation task, *CAAI Trans. Intell. Technol*. 1 (2016) 104–113.
- [52] Z. Gao, N. Song, Y. Zhang, X. Li, Cotton textile enabled, all-solid-state flexible supercapacitors, *RSC Adv*. 5 (2015) 15438–15447.
- [53] L. Bao, X. Li, Towards textile energy storage from cotton T-shirts., *Adv. Mater*. 24 (2012) 3246–52.
- [54] J. William S. Hummers, R.E. Offeman, Preparation of graphitic oxide, *J. Am. Chem. Soc*. 80 (1958) 1339.
- [55] D.R. Dreyer, S. Park, C.W. Bielawski, R.S. Ruoff, The chemistry of graphene oxide, *Chem. Soc. Rev*. 39 (2010) 228–240.
- [56] A. Ferrari, J. Robertson, Interpretation of Raman spectra of disordered and amorphous carbon, *Phys. Rev. B*. 61 (2000) 14095–14107.
- [57] Y. Wang, Q. He, H. Qu, X. Zhang, J. Guo, J. Zhu, G. Zhao, H. a. Colorado, J. Yu, L. Sun, S. Bhana, M. a. Khan, X. Huang, D.P. Young, H. Wang, X. Wang, S. Wei, Z. Guo,

- Magnetic graphene oxide nanocomposites: nanoparticles growth mechanism and property analysis, *J. Mater. Chem. C*. 2 (2014) 9478–9488.
- [58] S. Dzsaber, M. Negyedi, B. Bernath, B. Gyure, T. Feher, C. Kramberger, T. Pichler, F. Simon, A fourier transform Raman spectrometer with visible laser excitation, *J. Raman Spectrosc.* 46 (2015) 327–332.
- [59] Y. V. Mikhaylik, J.R. Akridge, Polysulfide shuttle study in the Li/S battery system, *J. Electrochem. Soc.* 151 (2004) A1969–A1976. doi:Doi 10.1149/1.1806394.
- [60] Z. Lin, C. Liang, Lithium–sulfur batteries: from liquid to solid cells, *J. Mater. Chem. A*. 3 (2015) 936–958. doi:10.1039/C4TA04727C.
- [61] S. Xin, L. Gu, N.-H. Zhao, Y.-X. Yin, L.-J. Zhou, Y.-G. Guo, L.-J. Wan, Smaller sulfur molecules promise better lithium-sulfur batteries., *J. Am. Chem. Soc.* 134 (2012) 18510–3.
- [62] K. Xi, P.R. Kidambi, R. Chen, C. Gao, X. Peng, C. Ducati, S. Hofmann, R.V. Kumar, Binder free three-dimensional sulphur/few-layer graphene foam cathode with enhanced high-rate capability for rechargeable lithium sulphur batteries, *Nanoscale*. 6 (2014) 5746.
- [63] K. Xi, S. Cao, X. Peng, C. Ducati, R. Vasant Kumar, A.K. Cheetham, Carbon with hierarchical pores from carbonized metal–organic frameworks for lithium sulphur batteries, *Chem. Commun.* 49 (2013) 2192.
- [64] R. Chen, T. Zhao, T. Tian, S. Cao, P.R. Coxon, K. Xi, D. Fairen-Jimenez, R. Vasant Kumar, A.K. Cheetham, Graphene-wrapped sulfur/metal organic framework-derived microporous carbon composite for lithium sulfur batteries, *APL Mater.* 2 (2014).
- [65] L. Su, Y. Zhong, Z. Zhou, Role of transition metal nanoparticles in the extra lithium storage capacity of transition metal oxides: a case study of hierarchical core–shell Fe₃O₄@C and Fe@C microspheres, *J. Mater. Chem. A*. 1 (2013) 15158.
- [66] Y. Zhou, D. Yan, H. Xu, S. Liu, J. Yang, Y. Qian, Multiwalled carbon nanotube@a-C@Co₉S₈ nanocomposites: a high-capacity and long-life anode material for advanced lithium ion batteries, *Nanoscale*. 7 (2015) 3520–3525

Chapter 6. Cotton-Textile-Enabled, Ferromagnetic Nanoparticle-Assisted Polysulfide New Trapping Mechanism

6.1 Introduction

With increasing environmental concerns and growing demand for renewable energy, a worldwide imperative is to develop efficient energy conversion and storage devices, aiming to utilize renewable and sustainable energy sources, such as solar, wind, geothermal, and tidal energy. [1-2] Lithium-ion (Li-ion) batteries have proven to be the most effective energy storage devices to date, due to their high energy density, long lifespan, lack of adverse memory effects and excellent safety; they have been widely used in portable electronics and electric vehicles (EVs), both of which substantially impacted our lifestyles. [3-5] However, the Li-ion battery chemistry is approaching its theoretical limit, and will not be able to satisfy the next generation of devices requiring higher storage capacities and longer lifespans. Therefore, new battery chemistries and new electrode materials with higher energy storage capacity are eagerly needed. [6-9] Currently, the lithium-sulfur (Li-S) battery is regarded as the most promising candidate for the next-generation high-energy battery due to its ultra-high theoretical capacity ($\sim 1650 \text{ mAh g}^{-1}$) and energy density ($\sim 2654 \text{ Wh kg}^{-1}$), low cost and environmental friendliness. [10,11] However, Li-S batteries continue to be plagued by a variety of challenges such as fast capacity decay, poor utilization of the active material, short lifespans and poor Coulombic efficiency due to the insulating nature of sulfur, the “shuttle effect” of polysulfides, as well as a large volume fluctuation during cycling. [12,13]

To overcome the abovementioned challenges, various strategies have been explored and remarkable progress has been achieved in trapping polysulfides through the design of new materials, modification of electrolyte composition and optimization of cell configuration. [14-16] Following the pioneering work of confining polysulfides in porous and conductive carbon reported by Nazar, [17] various carbon materials, such as graphene, [18,19] graphene oxide, [20,21] carbon nanotubes, [22,23] micro/meso-carbon, [24,25] and biomass-derived activated carbons [26,27] have been widely explored as sulfur hosts to trap polysulfides. Recently, novel conductive polymers, [28,29] porous metal-organic frameworks (MOF), [30,31] and metal-based compounds [32,33] have shown to be promising in the on-site chemical trapping of polysulfides to improve

Coulombic efficiency and cyclic stability of Li-S batteries. In addition to innovative cathode materials, modifications of the separator, [34] introduction of a carbonaceous interlayer, [35,36] protection of the lithium anode [37,38] as well as the optimization of electrolyte composition [39,40] have also been previously explored in attempts to mitigate the dissolution of polysulfides and improve Li-S battery performance. However, the persistence of the “shuttle effect” of polysulfides is hindering the advancement of the Li-S cell to practical applications. Recently, the use of superparamagnetic iron oxide nanoparticles to control the “shuttle effect” of polysulfides by introducing an external magnetic field was reported. [41] Adding ferroelectric BaTiO₃ (BTO) into the cathode to effectively trap the polysulfide by the “spontaneous polarization” of BTO has also been explored. [42] Simultaneously, magnetic field effects have been applied to improve the performance of capacitors. [43,44] Inspired by such preliminary steps, in this work the polysulfide trapping capability of ferromagnetic materials is demonstrated and its mechanism of action is explored.

Ferromagnetic materials elements such as iron, nickel, and cobalt all demonstrate strong magnetism under an applied magnetic field and have been widely used for magnetic memory storage and various electromechanical devices. Recently, ultrafine magnetic nanoparticles have been synthesized and used in a variety of applications, such as recording media, catalysts, medical diagnostics, drug delivery, and ferrofluids. [45,46] Here, we hypothesize that a built-in magnetic field can be formed during cycling when ferromagnetic nanoparticles are introduced into the sulfur cathode of the Li-S battery. Via the Lorentz force, the path of the dissolved negative polysulfide ions will be altered and thereby promote the trapping of polysulfides. This unique mechanism can be named the “shielding effect” via ferromagnetic nanoparticles. Beyond polysulfide trapping, the ACT@Fe/Fe₃C composite also offers broader applications in electromagnetic wave absorption. [47,48]

To verify our hypothesis, an activated cotton textile (ACT)-based flexible electrode was enriched with iron nanoparticles to demonstrate this novel magnetic field-assisted polysulfide trapping strategy. In our previous work, ACT has been demonstrated to be an excellent flexible substrate due to its flexibility, conductivity and favorable porosity, which was easily enriched with nanoparticles. [49,50] In this work, ferromagnetic iron/iron carbide (Fe/Fe₃C) nanoparticles with a graphene shell (Fe/Fe₃C/graphene) were successfully *in-situ* embedded into the ACT fibers to

prepare the ACT@Fe/Fe₃C/graphene sulfur host. After an annealing process of the mixture, sulfur nanoparticles infiltrated into the inner pores of the ACT and randomly distributed around the Fe/Fe₃C nanoparticles to form ACT@Fe/Fe₃C/S composite. When used as a cathode, the ACT@Fe/Fe₃C/S electrode demonstrated a unique single discharge plateau with a high initial discharge capacity of ~764 mAh g⁻¹, an exceptional capacity recovery after the initial drop during the first 120 cycles, excellent rate performance, as well as a remarkably extended lifespan (600 cycles for the ACT@Fe/Fe₃C/S cathode compared with only 100 cycles for pure ACT/S cathode). A custom-designed liquid electrolyte cell with ACT@Fe/Fe₃C/S as the cathode and lithium metal as the anode demonstrated a concentrated polysulfide diffusion layer near the ACT surface, which is substantially different from the homogeneous diffusion of the pure ACT/S cathode. The difference indicates a mechanistically new polysulfide trapping phenomenon. The modified reduction-oxidation chemistry and enhanced lifespan of the ACT@Fe/Fe₃C/S composite demonstrates a new trapping mechanism attributed to the built-in magnetic field facilitated by Fe/Fe₃C nanoparticles.

6.2 Experimental Sections

6.2.1 Synthesis of ACT@Fe/Fe₃C nanoparticles with a graphene shell

Chemicals used were as-supplied from vendors without further purification. Commercial cotton textile was first washed using distilled water in an ultrasonic bath. A simple one-step activation of cotton textile loaded with Fe(NO₃)₃ was performed to prepare ACT@Fe/Fe₃C nanoparticles with a graphene shell (ACT@Fe/Fe₃C/graphene). Specifically, the cotton textile was first soaked for 10 min in 1 M Fe(NO₃)₃ solution and dried at 80 °C for 6 h to remove any residual water. The material was then heated to 1000 °C with a heating rate 5 °C/min in a tube furnace and maintained at this temperature for 1 h with 300 sccm (standard cubic centimeters) gas flow of argon. A washing process of the ACT@Fe/Fe₃C/graphene composite using ethanol followed, with a final drying at 80 °C for 12 h.

6.2.2 Preparation of ACT@Fe/Fe₃C/S cathode

The ACT@Fe/Fe₃C/S composite was obtained by thermally treating ACT@Fe/Fe₃C/graphene with sulfur. First, a piece of ACT@Fe/Fe₃C/graphene was punched into discs 14 mm in diameter. The discs were coated with sulfur particles and thermally treated at

156 °C for 10 h in a sealed autoclave to make sulfur fully penetrate into the inner pores and cavities of the ACT. A heating process at 200 °C for 2 h was used to ensure the homogenous distribution of sulfur around Fe/Fe₃C nanoparticles. The areal weight of ACT@Fe/Fe₃C was measured to be ~2.5 mg cm⁻². The final sulfur loaded ACT@Fe/Fe₃C/S composite was ~5.0 mg cm⁻².

6.2.3 Characterization

The morphology and the microstructure of the prepared materials were characterized by scanning electron microscopy (SEM; FEI Quanta 650 with EDS detector) and transmission electron microscopy (TEM), high-resolution transmission electron microscopy (HRTEM, FEI Titan), and atomic force microscopy (AFM; Dimension Icon with ScanAsyst, Bruker). The crystallographic structure of the obtained materials was characterized by X-ray diffraction (XRD; PANalytical X'Pert Pro Multi-Purpose Diffractometer (MPD) equipped with Cu K_α radiation with $\lambda = 0.15406$ nm. Raman spectrum was collected by Renishaw InVia Raman microscope at 514 nm with 5% laser power.

6.2.4 Electrochemical Characterization of the ACT@Fe/Fe₃C/S Cathode

The electrochemical performance of the ACT@Fe/Fe₃C/S cathode was measured by assembling CR2032 type coin cells. The ACT@Fe/Fe₃C/S composite was directly used as a binder-free cathode for the coin cell. The ACT@Fe/Fe₃C/S composite was first dried at 80 °C for 24 h in a vacuum oven and Li-S coin cells were assembled with ACT@Fe/Fe₃C/S as a cathode, lithium metal as an anode and Celgard 2400 film as a separator, respectively. For comparison, cells with an ACT/S cathode were also assembled. Electrolyte solution consisting of 1 M lithium bis(trifluoromethanesulfonyl)imid and 0.4 M LiNO₃ dissolved in 1:1 v/v 1,2-dimethoxyethane (DME) and 1,3-DOL solution was used. The CR2032 coin cells were assembled with an MTI MSK-110 crimping machine in an argon-filled glove box (Mbraun, Germany) with oxygen and water contents below 2 ppm. A custom glass cell was used to directly observe the macroscopic polysulfide trapping behavior of the ACT@Fe/Fe₃C/S cathode during cycling. Galvanostatic charge/discharge measurements were carried out using a LAND CT2003A battery tester between 1.5 and 3.0 V vs Li/Li⁺. The capacities and charge/discharge rates were calculated based on the areal weight of active sulfur. A CHI 660E Electrochemical Workstation was used to measure the cyclic voltammograms (CV) and electrochemical impedance spectra (EIS) between 0.05Hz and 100 kHz with 5 mV of AC perturbation.

6.3 Results and Discussion

6.3.1 Microstructure Characterization

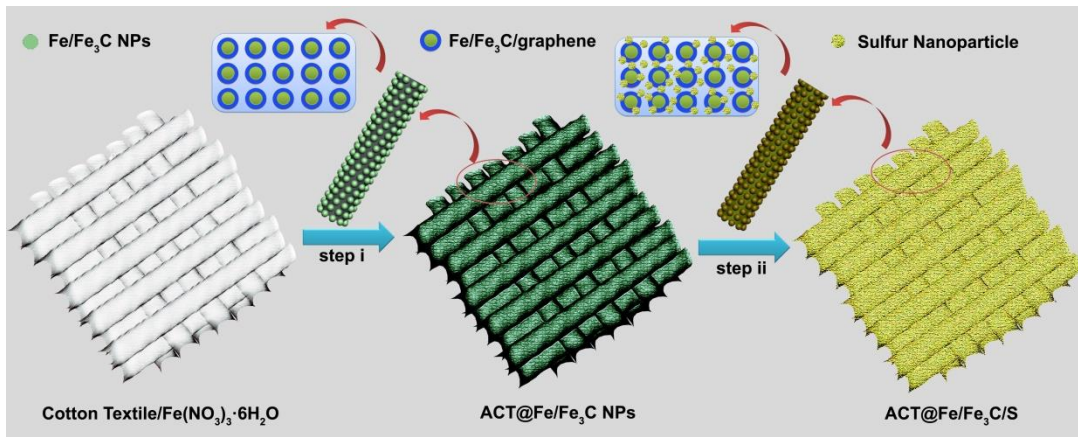
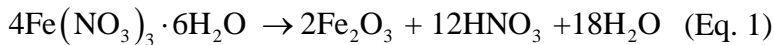


Figure 6.1 Schematic illustration of the synthesis of ACT@Fe/Fe₃C nanoparticles (ACT@Fe/Fe₃C NPs) composite and its hybridization with sulfur to prepare ACT@Fe/Fe₃C/S composite.

Synthesis of ACT@Fe/Fe₃C nanoparticles (NPs) with a graphene shell followed by a hybridization with sulfur to prepare the ACT@Fe/Fe₃C/S composite involved in a two-step process (Figure 6.1), which resulted in Fe/Fe₃C NPs anchored on both the inner and outer surfaces of the ACT fibers (step i). Interestingly, each Fe/Fe₃C NP was coated with a multilayered graphene shell. During the high-temperature annealing process, the cotton textile was first activated into conductive ACT accompanied by the release of gaseous byproducts such as CH₄, H₂, CO and CO₂. Simultaneously, the Fe(NO₃)₃ was decomposed into α-Fe₂O₃ and then reduced into pure iron nanoparticles. Finally, the dissolution of C atoms into the Fe-rich matrix led to the formation of Fe₃C and Fe/Fe₃C eutectoid, and the precipitation of C atoms resulted in the growth of graphene around Fe/Fe₃C nanoparticles. The reaction processes can be described using (Eq. 1-4): [51-53]



From the above reactions, the activation process yields a corrosive nitric acid, which can etch the cotton fibers and facilitate the formation of the porous structure of the ACT. Inside each

ACT fiber, the graphene shell coagulates around the conductive Fe/Fe₃C NPs forming a conductive network, which contributes to the favorable current collection efficiency and fast electron transport. Most importantly, the embedded Fe/Fe₃C NPs induced a magnetic field near the surface of the cathode, which alters the motion of the polysulfides via the Lorentz force. This intrinsic force enabled the dissolved polysulfides to diffuse back towards the cathode, thereby mitigating the polysulfide shuttle effect. Such a unique design strategy allows the ACT@Fe/Fe₃C NPs with a graphene shell to behave as an ideal sulfur host for high-performance Li-S batteries.

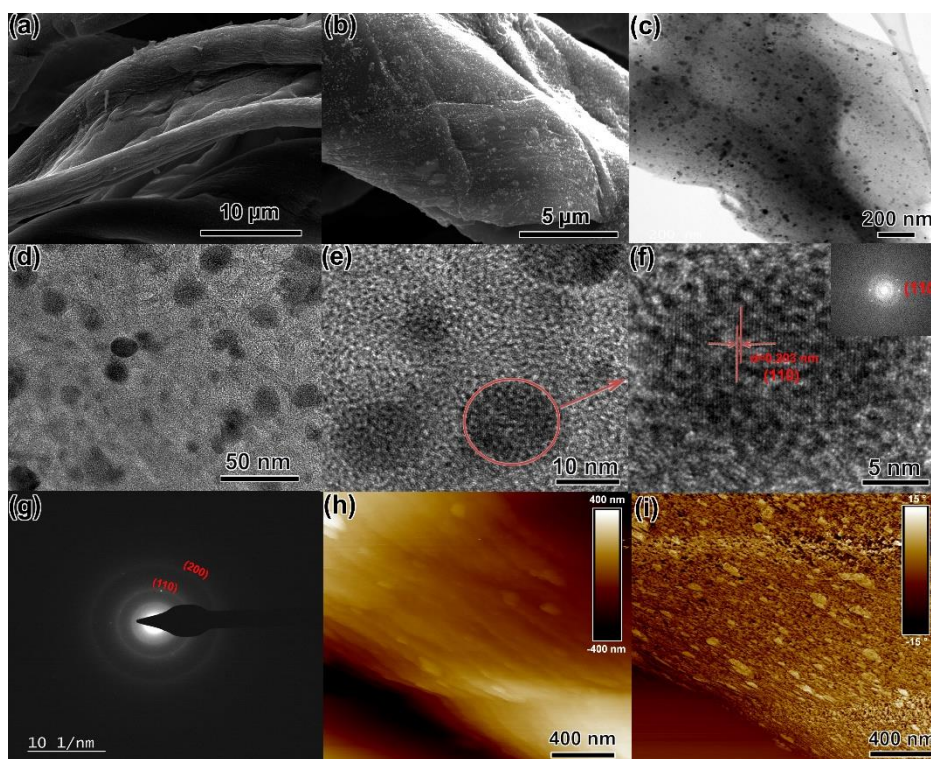


Figure 6.2 (a,b) Scanning electron microscopy (SEM) images of the ACT@Fe/Fe₃C NPs at different magnifications; (c,d) Transmission electron microscopy (TEM) images of the ACT@Fe/Fe₃C NPs at different magnifications; (e,f) High resolution transmission electron microscopy (HRTEM) images of the ACT@Fe/Fe₃C NPs at different magnifications, inset of f is the corresponding fast Fourier transform (FFT) pattern; (g) Selected area electron diffraction (SAED) pattern of the ACT@Fe/Fe₃C NPs; (h) Atomic force microscopy (AFM) height and corresponding phase (i) images of ACT@Fe/Fe₃C NPs.

The microstructure of the ACT@Fe/Fe₃C NPs was characterized using SEM, TEM, HRTEM and AFM, as shown in Figure 6.2. Dense Fe/Fe₃C NPs anchored on the surface of the ACT fibers were observed on the ACT@Fe/Fe₃C composite from SEM analysis (Figures 6.2a-b). Furthermore, the Fe/Fe₃C NPs were distributed not only on the exterior surfaces of the ACT fibers, but also homogeneously embedded inside the carbon matrix of each fiber. The average diameter of the Fe/Fe₃C NPs is ~10 nm, and HRTEM with corresponding FFT analysis of the particles

(Figure 6.2f) reveal a lattice spacing of 0.203 nm, in accordance with the (110) lattice plane of body-centered cubic α -Fe. The SAED pattern of the ACT/Fe/Fe₃C (Figure 6.2g) shows concentric diffraction rings together with strong diffraction spots indicating the presence of a mixture of poly/single crystalline Fe/Fe₃C (indexed as (110) and (200) plan of cubic α -Fe) and amorphous phase carbon, in good agreement with the X-Ray Diffraction (XRD) results in Figure 6.3b. The XRD pattern of the pure cotton and ACT compared in Figure S1a indicates an amorphous structure of ACT after activation. The crumpled morphology of the ACT surface is patterned with dense Fe/Fe₃C NPs as shown by AFM height analysis (Figure 2h-i), with the phase profile corresponding to a loosely porous ACT fiber structure.

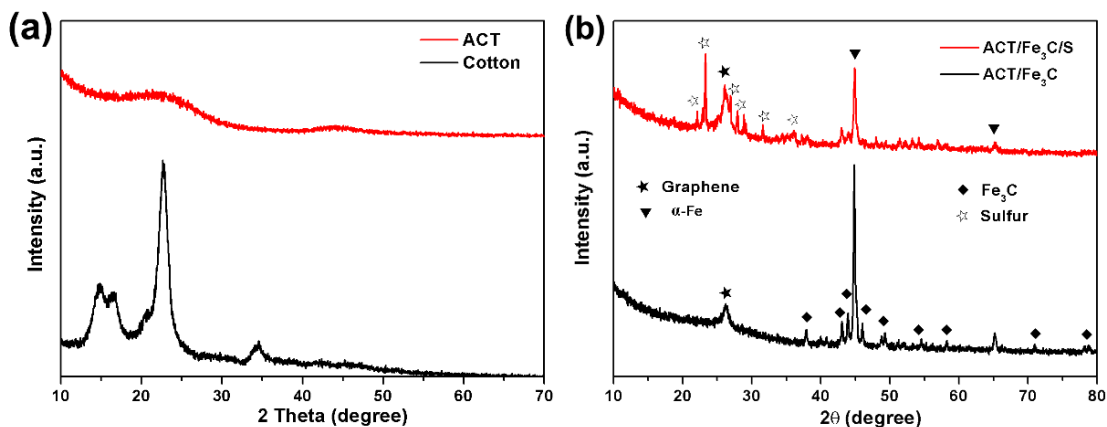


Figure 6.3 XRD patterns of the as-prepared (a) cotton textile and activated cotton textile (ACT); (b) ACT@Fe/Fe₃C NPs and ACT@Fe/Fe₃C/S composite.

Following the second step of sulfur impregnation and heating, the resulting ACT@Fe/Fe₃C/S composite exhibited a similar morphology (Figure 3a-c) to the ACT@Fe/Fe₃C NPs discussed above. Dense Fe/Fe₃C NPs anchored on the surface of ACT, and HRTEM images of ACT@Fe/Fe₃C/S confirmed a core/shell structure with an inner Fe/Fe₃C core and a multilayer outer graphene shell (Figure 3d). The amplified region (Figure 3e) exhibited non-homogenous crystal structures corresponding to different compositions that could be ascribed to the multi-layered graphene (I), monoclinic sulfur (II), α -Fe (III), and single crystal Fe₃C (IV). FFT pattern of region IV demonstrates the single-crystal nature of the Fe₃C/Fe NPs (inset of Fig. 3f), while SAED measurements (Figure 3g) suggest a mixture of the polycrystalline sulfur, crystal Fe₃C, and amorphous carbon, in good agreement with XRD results (Figure S1b). Compared with

ACT@Fe/Fe₃C, a different phase image of ACT@Fe/Fe₃C/S (Figure 3h-i) can be ascribed to the homogeneous distribution of sulfur throughout the Fe/Fe₃C NPs.

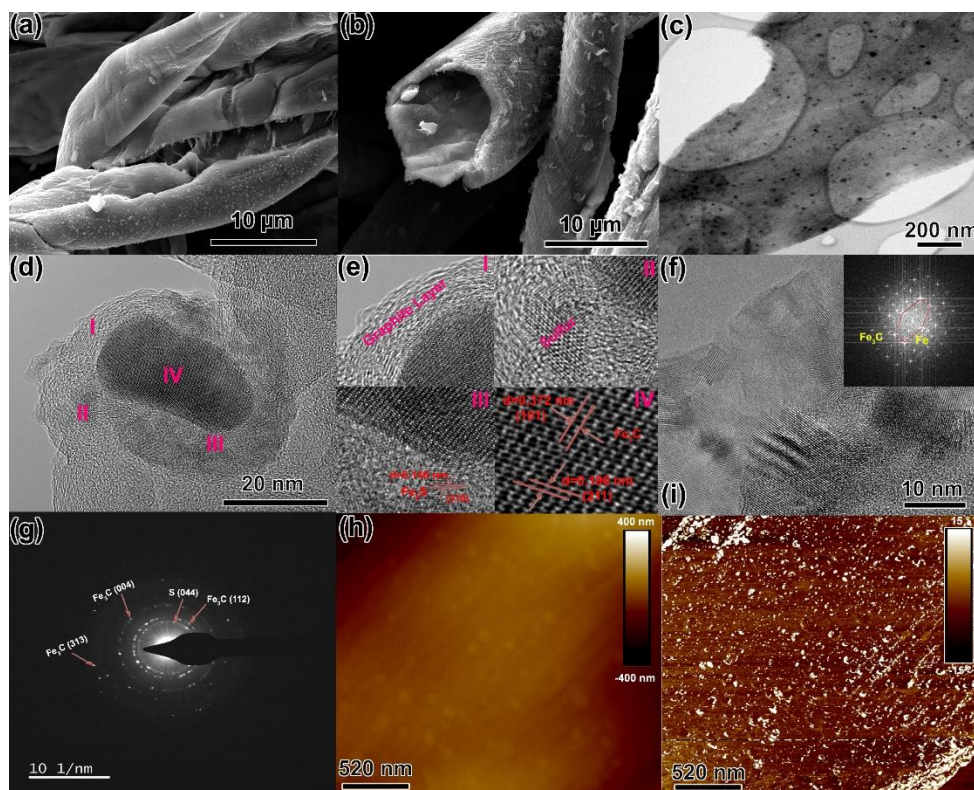


Figure 6.4 (a,b) SEM images of the ACT@Fe/Fe₃C/S composite at different magnifications; (c) TEM image of the ACT@Fe/Fe₃C/S composite; (d) HRTEM images of the core/shell nanostructures in ACT@Fe/Fe₃C/S composite with Fe/Fe₃C NP core and multilayered graphene shell; (e) the corresponding amplified region of (d); (f) HRTEM image of the ACT@Fe/Fe₃C/S composite with random distributed sulfur nanograins; (g) selected area electron diffraction (SAED) pattern of the ACT@Fe/Fe₃C/S composite; (h) AFM height and corresponding phase (i) images of ACT@Fe/Fe₃C/S composite.

The presence of a single layer crystalline carbon (graphene) at 26.4° (JCPD no. 75-0444), cubic α -Fe (JCPD no. 87-0722) and orthorhombic Fe₃C (JCPD no. 76-1877) is verified by the diffraction peaks of ACT@Fe/Fe₃C NPs obtained using XRD (Figure 6.3b). Following the infiltration of sulfur, XRD measurements of the ACT@Fe/Fe₃C/S composite were consistent with the diffraction peaks of graphene, cubic α -Fe and orthorhombic Fe₃C, which indicates a stable phase structure of the Fe/Fe₃C nanoparticles. Any remaining diffraction peaks in the ACT@Fe/Fe₃C/S composite agree well with the standard diffraction peaks of sublimed sulfur (JCPDS no. 08-0247), suggesting that S is embedded into the ACT@Fe/Fe₃C substrate. Comparing the Raman spectrum of ACT@Fe/Fe₃C NPs with the ACT@Fe/Fe₃C/S composite (Figure 6.5) reveals similarities in the characteristic D and G bands of the carbon materials.

Meanwhile, the relatively strong 2D band at 2680 cm^{-1} of ACT@Fe/Fe₃C composite indicates the existence of multilayered graphene. [54] However, the absence of the 2D band and the decreased I_D/I_G ratio of the ACT@Fe/Fe₃C/S Raman peaks suggests that sulfur is embedded into the lattice of multilayered graphene thereby promoting defects in the graphene layer, [55] which agrees well with TEM results above.

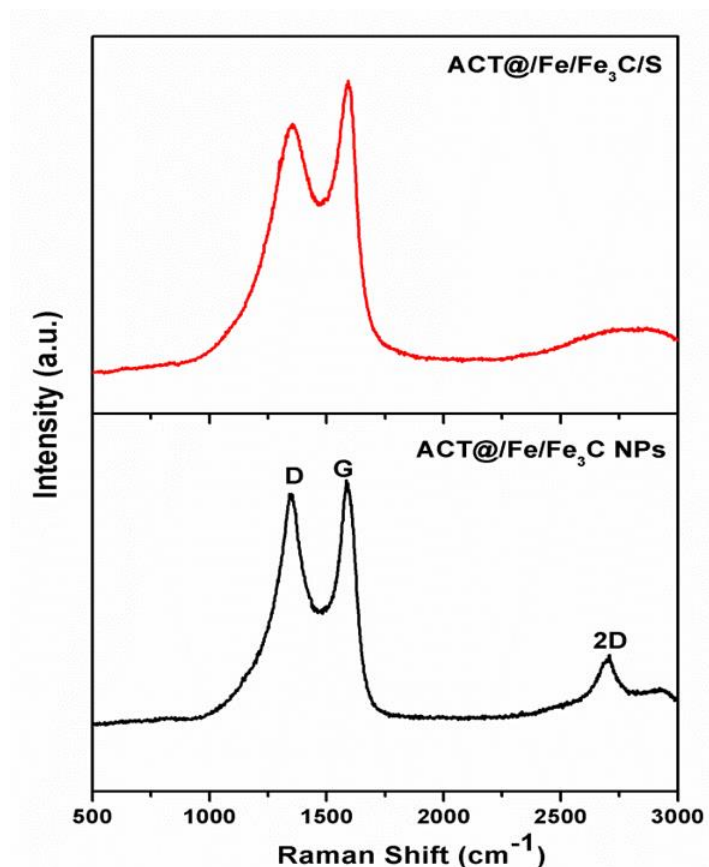


Figure 6.5. Raman spectra of the as-prepared ACT@Fe/Fe₃C NPs and ACT@Fe/Fe₃C/S composite.

In order to map the elemental distribution of C, O, S and Fe in the ACT@Fe/Fe₃C/S composite, Energy Dispersive Spectroscopy (EDS) mapping was utilized, revealing that in addition to the homogeneously deposited S on the outer surface of ACT fibers, it was mainly stored in the inner tubes of the ACT fibers (Figure 6.6d), which enabled higher sulfur loading ($\sim 5.0\text{ mg cm}^{-2}$) than most other reported carbon/sulfur composites ($< 2.0\text{ mg cm}^{-2}$). Analysis with HRTEM and the corresponding EDS spectrum of the ACT@Fe/Fe₃C/S further demonstrates the presence of graphene and sulfur around the ferromagnetic Fe/Fe₃C core (Figure 6.7). The tubular structure

of ACT and the conductive Fe/Fe₃C NPs with a graphene shell also functions as a conductive host for S, which enabled fast electrolyte ion diffusion and electron transfer.

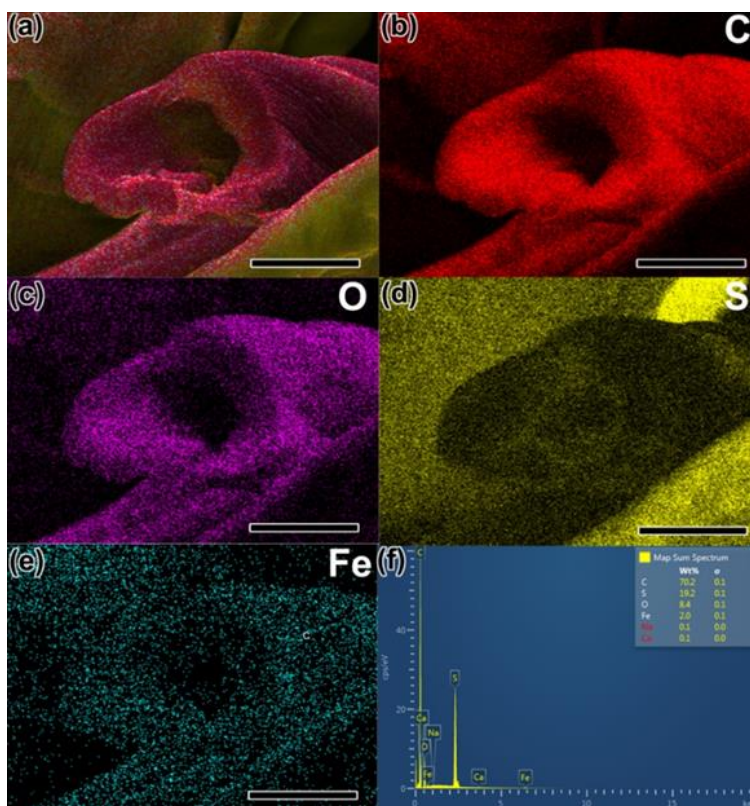


Figure 6.6 (a-e) The EDS element mapping images of the ACT@Fe/Fe₃C/S composite and (f) the elemental spectrum and the relative element ratio of C, O, S, Fe, scale bar 5 μ m.

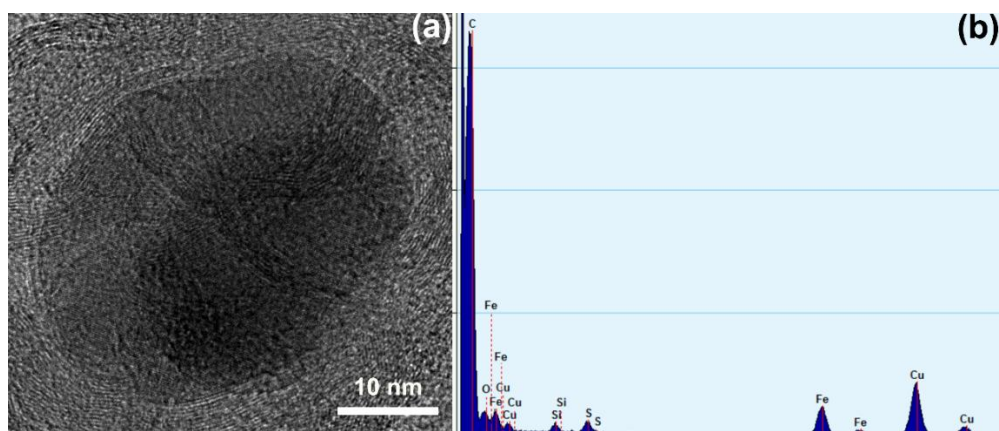


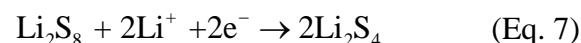
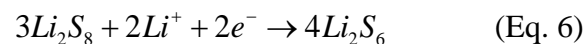
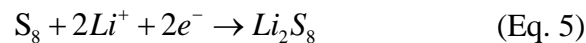
Figure 6.7 (a) Close-up HRTEM image and (b) the corresponding elemental spectrum of the ACT@Fe/Fe₃C/S composite.

6.3.2 Electrochemical Performance

The Li-S cell features two pairs of theoretical reduction-oxidation (redox) peaks, with reduction peaks at ~ 2.35 V and ~ 2.1 V vs. Li⁺/Li and an oxidation peak at ~ 2.5 V vs. Li⁺/Li, which

corresponds to the two-step reaction of sulfur with lithium, as described by the following equations: [56,57]

Step I: formation of easily dissoluble long chain lithium polysulfides (Li_2S_x , $4 \leq x$);



Step II: formation of insoluble Li_2S_2 and Li_2S ;

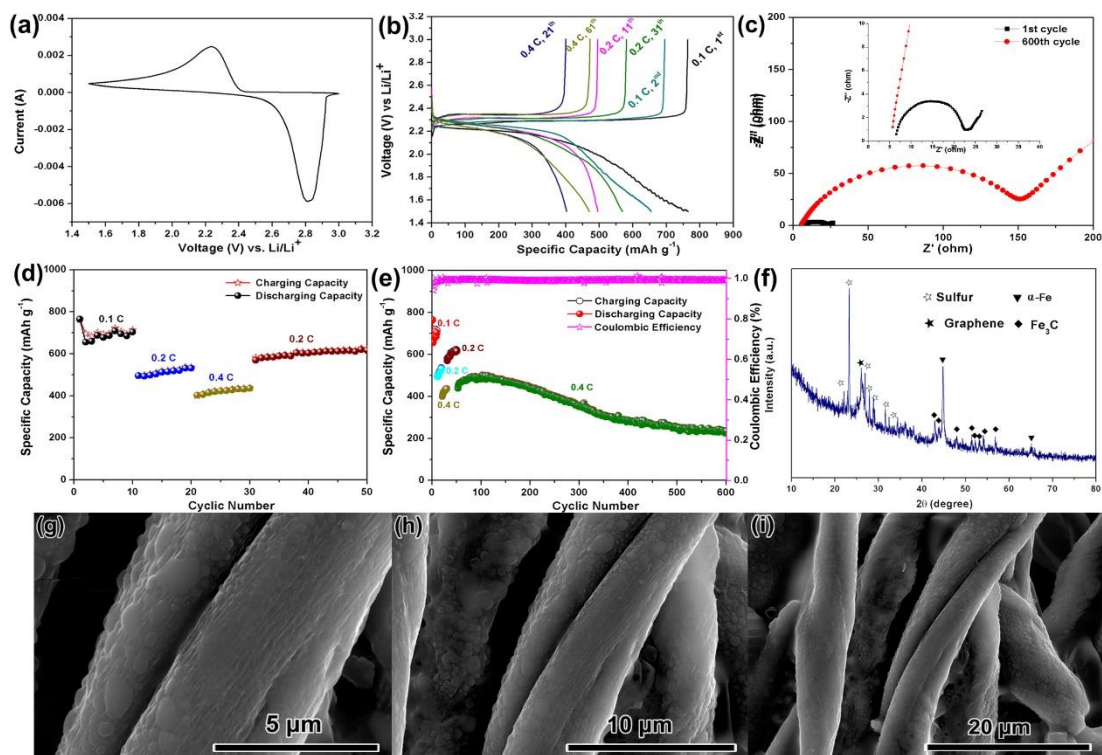
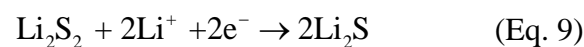
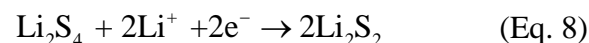


Figure 6.8 (a) Cyclic voltammogram (CV) profile of the prepared ACT@Fe/Fe₃C/S cathode; (b) 1st, 2nd, 11th, 21st, 31st and 61st charge/discharge profiles of ACT@Fe/Fe₃C/S cathode at different current densities (1 C = 3 mA cm⁻²); (c) Electrochemical impedance spectroscopy (EIS) of the prepared ACT@Fe/Fe₃C/S cathode at 1st and 600th cycle; (d) rate performance of ACT@Fe/Fe₃C/S cathode at different current densities in the first 50 cycles; (e) stepwise cycling performance of ACT@Fe/Fe₃C/S cathode and its Coulombic efficiency; (f) XRD pattern and SEM images (g-i) of the ACT@Fe/Fe₃C/S cathode after the cyclic tests.

Unexpectedly, an assembled cell with ACT@Fe/Fe₃C/S cathode exhibited a single pair of redox peaks (Figure 6.8a) measured using cyclic voltammetry (CV), which corresponds to a single, longer plateau in the galvanostatic charge/discharge curves (Figure 6.8b), suggesting that the Fe/Fe₃C NPs disrupt the dissolution of polysulfides. The galvanostatic charge/discharge profiles of the ACT@Fe/Fe₃C/S cathode were measured at varying current densities (Figure 6.8b). Interestingly, a similar trend of a discharge plateau at ~2.2 V and a charge plateau at ~2.35 V has been measured at all current densities. Unlike the double discharge plateaus of the pure ACT/S cathode at ~2.35 V and ~2.1 V (Figure 6.9a), the single discharge plateau at ~2.2 V is in good agreement with the measured CV of the ACT@Fe/Fe₃C/S cathode (Figure 6.8a). The reversible discharge capacity of ACT@Fe/Fe₃C/S cell at 1st (0.1 C), 2nd (0.1 C), 11th (0.2 C), 21st (0.4 C), 31st (0.2 C), 61st (0.4 C) cycles are 763, 656, 501, 404, 568, and 470 mAh g⁻¹, respectively, resulting in a linear trend with increasing current density. However, notable kinetic effects were exhibited by the cell; for instance, at increasing current densities the charge plateau broadened while the discharge plateau shrunk, leading to a higher overpotential and a lower capacity at high current densities.

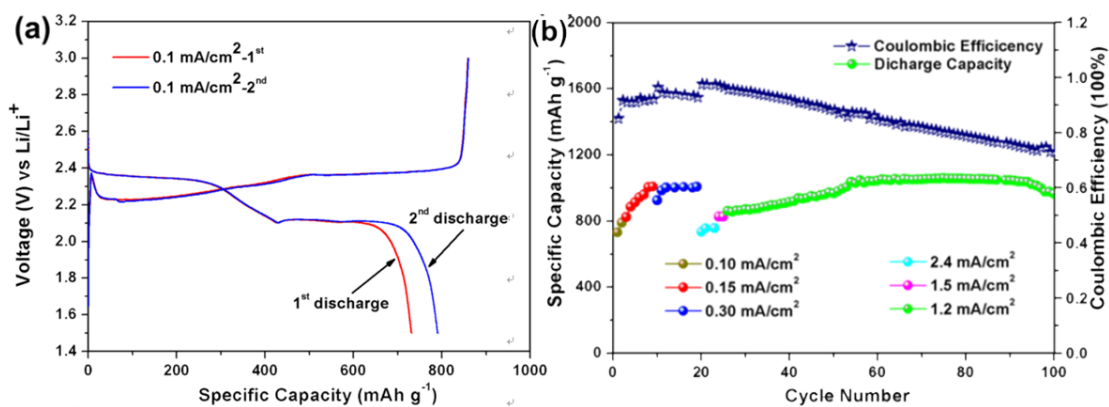


Figure 6.9 (a) The initial charge/discharge curves of the ACT@Fe/Fe₃C/S composite; (b) Cyclic and Coulombic efficiency of the ACT@Fe/Fe₃C/S composite.

To investigate the specific function of Fe/Fe₃C, EIS measurements of the assembled cell were performed at the first cycle and after 600 cycles (Figure 6.8c). A typical Nyquist spectrum of the Li-S battery electrochemistry consists of two semicircles in the high-frequency range and a linear regime in the low-frequency range. The first semicircle in high-frequency range is ascribed to the formation of the passivation layer (Li₂S₂/Li₂S) on the surface of the lithium anode, while the second semicircle in the medium-to-low frequency corresponds to the charge transfer resistance

(R_{ct}), and the line in the low-frequency regime results from the diffusion of lithium ions. [58,59] However, in the spectrum of the ACT@Fe/Fe₃C/S cathode the absence of one semicircle during the initial cycle indicates that the trapping of the polysulfides slows the formation of the passivation layer on the anode. Meanwhile, the reduced semicircle diameter suggests a decreased charge transfer resistance of the ACT@Fe/Fe₃C/S composite. The increased semicircle diameter of the ACT@Fe/Fe₃C/S composite after 600 cycles indicates the increase of charge transfer resistance during cycling. The charge/discharge capacity profile at the current densities ranging from 0.1 C to 0.4 C (Figure 6.8d) is used to evaluate the rate performance of the ACT@Fe/Fe₃C/S cell. Clearly, the capacity is well retained at current densities between 0.1 C and 0.4 C, indicative of excellent rate performance. When the current density is reduced to 0.2 C after 30 cycles, the cell capacity can be recovered to 558 mAh g⁻¹, which is even larger than the 538 mAh g⁻¹ (0.2 C) at the 21st cycle.

The exceptional capacity increase of the ACT@Fe/Fe₃C/S cell is consistent with our previously reported pure ACT/S cathode, [36] wherein hollow tubular structures of ACT fibers (Fig. 6.6) contributed to the favorable performance. Compared to the pure ACT/S cathode (Figure 6.9b), the ACT@Fe/Fe₃C/S cell demonstrated better Coulombic efficiency and a longer lifespan. Unlike the monotonically decreasing efficiency exhibited by the ACT/S cell (~72% at 100th cycle), ACT@Fe/Fe₃C/S remarkably demonstrated an improved Coulombic efficiency, almost 100% throughout the entire cycling process. Excitingly, the lifespan of the ACT@Fe/Fe₃C/S cell reached 600 cycles even at a high sulfur loading of 5 mg cm⁻² (6x longer than ACT/S). Furthermore, at 0.4 C current density, an excellent capacity retention of ~61% was measured after 600 charge/discharge cycles.

In order to identify the mechanistic role of the Fe/Fe₃C NPs in trapping polysulfides during the charge/discharge process, further XRD and SEM analysis of the ACT@Fe/Fe₃C/S cathode after the cycling test was performed. Post-cycling the presence of characteristic peaks of α -Fe and Fe₃C (Figure 6.8f) indicate no reaction between Fe/Fe₃C NPs and S, suggesting the trapping mechanism is not driven by a chemical bonding between Fe/Fe₃C NPs and the polysulfides species. The structural integrity of the ACT@Fe/Fe₃C/S cathode post-cycling remained nominal based on SEM image analysis, indicating the ACT fibers are a mechanically robust sulfur host. Unlike the spherical nanoparticles on the ACT fibers, a compact layer of nanosheets wrapped around the ACT

layer accumulated on the cathode, which is ascribed to the formed $\text{Li}_2\text{S}/\text{Li}_2\text{S}_2$ passivation layer. Based on the single redox peak in the CV profile of ACT@Fe/Fe₃C/S cathode, we conclude that the presence of Fe/Fe₃C NPs is the key factor in preventing the dissolution of the dissolved polysulfides (S_n^{2-} , $n>4$) and the formation of non-soluble $\text{Li}_2\text{S}/\text{Li}_2\text{S}_2$.

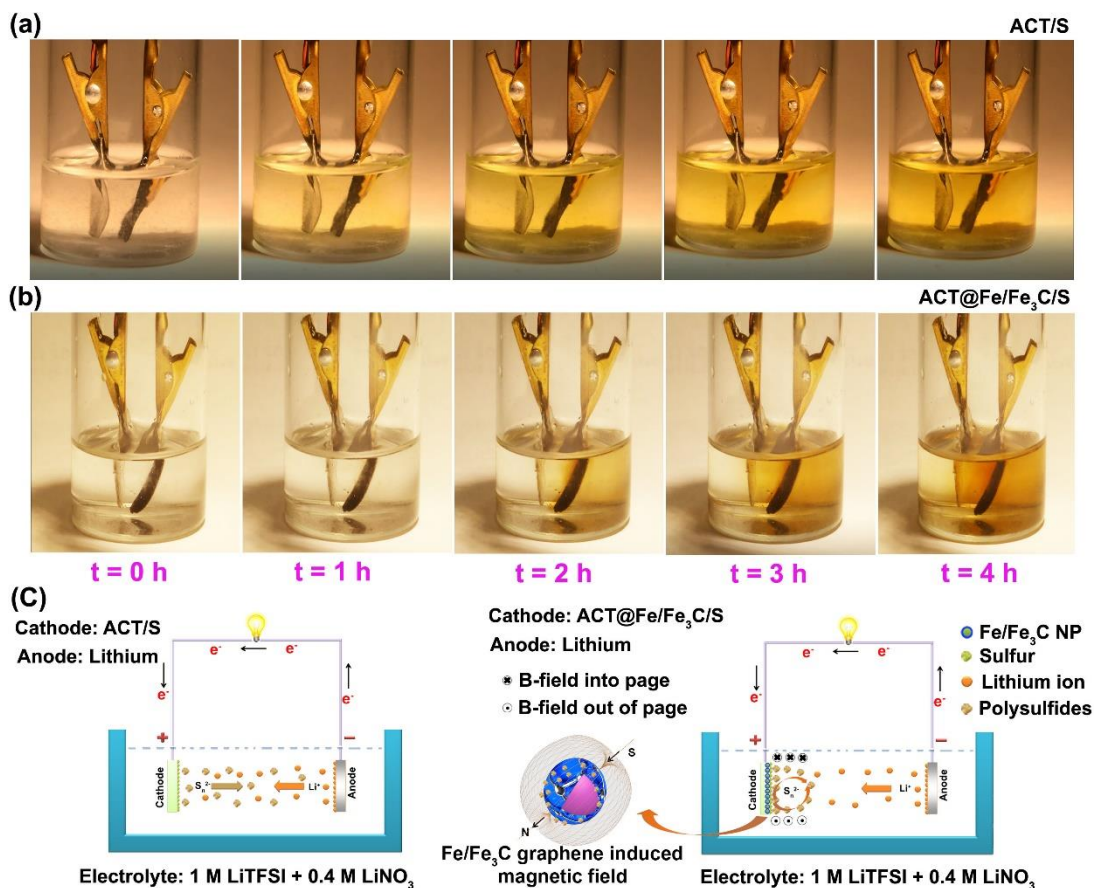


Figure 6.10 Digital images of the ACT/S composite (a) and ACT@Fe/Fe₃C/S composite (b) electrodes during the first discharge cycle in the liquid cell at the current density of 0.1 mA cm^{-2} ; (c) Illustration of the possible polysulfides trapping mechanism by introducing of Fe/Fe₃C NPs in the ACT@Fe/Fe₃C/S cathode.

In order to clarify the trapping mechanism of the Fe/Fe₃C NPs, the color change of the electrolyte in a custom-built liquid cell with both pure ACT/S and the new ACT@Fe/Fe₃C/S cathode was digitally tracked (Figure 6.10). The yellow color indicates the dissolution of sulfur and the formation of long-chain polysulfides (S_n^{2-} , $n>4$). [60] Interestingly, in the absence of Fe/Fe₃C NPs, the electrolyte around the ACT/S cathode changed in color homogeneously (Figure 6.10a, Video S1). With increasing discharge depth (at constant current density) the yellow region darkened substantially. However, with the introduction of Fe/Fe₃C NPs in ACT@Fe/Fe₃C/S the electrolyte around the cathode exhibited an inhomogeneous color distribution and subsequent

dispersion. The electrolyte turned dark brown and concentrated around the cathode disk, with a color gradient reaching the Li anode. After 3 h of constant current discharge, a dark brown region gradually emerged around the surface of ACT@Fe/Fe₃C/S cathode, which further demonstrates the trapping ability of the Fe/Fe₃C NPs (Figure 6.10b).

We postulate that the induced magnetic field from the Fe/Fe₃C NPs is a key factor in the trapping of the dissolved polysulfides (Figure 6.10c). Specifically, during the discharge process, the lithium anode loses an electron to form Li⁺, while the sulfur anode gains two electrons to form S_n²⁻ (1≤n≤8). In the intrinsic electric field between the two active materials, S_n²⁻ (4≤n≤8) ions are attracted to the anode, while the Li⁺ ions are attracted to the cathode via a stable process, which finally reaches a dynamic equilibrium. With the introduction of the Fe/Fe₃C NPs into the ACT matrix, an intrinsic magnetic field (B-field) is formed around the cathode during discharge process, which is enabled by the spontaneous magnetization of Fe/Fe₃C NPs. Through the Lorentz force, the B-field alters the motion of the polysulfide ions by attracting them toward the cathode (Figure 6.10c, right), leading to the darker brown region of the electrolyte around the cathode disk. In fact, a vortex ring was observed during discharge, as demonstrated in the video of the ACT@Fe/Fe₃C/S liquid cell (Video S2). The spontaneously generated intrinsic B-field enabled by the presence of Fe/Fe₃C NPs promotes the trapping of the dissolved polysulfides, improves the utilization of the sulfur cathode, and increases the cyclic performance of the ACT@Fe/Fe₃C/S cathode.

From the above analysis, excellent rate performance, improved Coulombic efficiency together with the significantly enhanced cyclic lifespan of the ACT@Fe/Fe₃C/S composite cathode can all be assigned to the following merits: (1) the porous ACT fiber with a hollow, tubular structure increases sulfur loading, effectively accommodates the volume change of active sulfur and maintains the structural integrity of the electrode during the reversible charge/discharge process; (2) the Fe/Fe₃C NPs with a multilayered graphene coating randomly distributed throughout the active sulfur nanoparticles on the ACT fiber served as conductive sites to facilitate the fast electron transfer and accelerated kinetics; (3) Fe/Fe₃C NPs embedded into the ACT fiber resulted in a spontaneous intrinsic B-field around the ACT@Fe/Fe₃C/S cathode, which altered the path of the dissolved polysulfides, mitigated the “shuttle effect” of polysulfides, and promoted the formation of a cathode electrolyte interface which blocked the dissolution of polysulfides.

6.4 Conclusion

In summary, ferromagnetic Fe/Fe₃C NPs with a graphene shell (ACT@Fe/Fe₃C/graphene) were successfully embedded into the surface of ACT fibers to design a novel sulfur host which prevented the dissolution of polysulfides by a spontaneous magnetization of the intrinsic magnetism of the nanoparticles. After annealing the mixture of ACT@Fe/Fe₃C/graphene and sulfur, the sulfur NPs not only embedded into the inner pores of ACT but also randomly distributed around the Fe/Fe₃C NPs, forming ACT@Fe/Fe₃C/S composite. When used as a cathode, the ACT@Fe/Fe₃C/S composite demonstrated a unique discharge profile with only a single plateau, achieved a high initial discharge capacity of ~764 mAh g⁻¹, with an exceptional capacity increase through the first 120 cycles, an excellent rate performance, and an extended lifespan of 600 cycles. A custom-design liquid cell was used to study the polysulfide trapping mechanism resulting from the spontaneous intrinsic magnetic field caused by the presence of Fe/Fe₃C nanoparticles. Excitingly, the ACT@Fe/Fe₃C/S liquid cell demonstrated a strikingly different polysulfide diffusion behavior compared to the homogeneous polysulfide diffusion exhibited by a pure ACT/S cathode. The magnetic field alters the diffusion path of the negative polysulfides by establishing a favorable diffusion gradient toward the ACT cathode through the Lorentz force. Such a unique polysulfide trapping mechanism has the potential to maximize the utilization of the polysulfides and mitigate the polysulfide shuttle effect, thereby contributing to the prolonged lifespan and increased Coulombic efficiency of the Li-S battery.

Reference

- [1] S. Chu, Y. Cui, N. Liu, *Nat. Mater.* **2016**, *16*, 16.
- [2] A. S. Aricò, P. Bruce, B. Scrosati, J.-M. Tarascon, W. van Schalkwijk, *Nat. Mater.* **2005**, *4*, 366.
- [3] B. Scrosati, J. Hassoun, Y.-K. Sun, *Energy Environ. Sci.* **2011**, *4*, 3287.
- [4] J. B. Goodenough, *Energy Environ. Sci.* **2014**, *7*, 14.
- [5] N. Nitta, F. Wu, J. T. Lee, G. Yushin, *Mater. Today* **2015**, *18*, 252.
- [6] M. Armand, J.-M. Tarascon, *Nature* **2008**, *451*, 652.
- [7] P. G. Bruce, S. a. Freunberger, L. J. Hardwick, J.-M. Tarascon, *Nat. Mater.* **2011**, *11*, 172.
- [8] X. Lou, C. Lin, Q. Luo, J. Zhao, B. Wang, J. Li, Q. Shao, X. Guo, N. Wang, Z. Guo, *ChemElectroChem* **2017**, 3171.
- [9] C. Lin, L. Hu, C. Cheng, K. Sun, X. Guo, Q. Shao, J. Li, N. Wang, Z. Guo, *Electrochim.*

- Acta* **2018**, *260*, 65.
- [10] A. Manthiram, Y. Fu, Y. S. Su, *Acc. Chem. Res.* **2013**, *46*, 1125.
- [11] L. F. Nazar, M. Cuisinier, Q. Pang, *MRS Bull.* **2014**, *39*, 436.
- [12] S. S. Zhang, *J. Power Sources* **2013**, *231*, 153.
- [13] A. Rosenman, E. Markevich, G. Salitra, D. Aurbach, A. Garsuch, F. F. Chesneau, *Adv. Energy Mater.* **2015**, *5*, 1500212.
- [14] Z. W. Seh, Y. Sun, Q. Zhang, Y. Cui, *Chem. Soc. Rev.* **2016**, *45*, 5605.
- [15] S. Evers, L. F. Nazar, *Acc. Chem. Res.* **2013**, *46*, 1135.
- [16] L. Chen, L. L. Shaw, *J. Power Sources* **2014**, *267*, 770.
- [17] X. Ji, K. T. Lee, L. F. Nazar, *Nat. Mater.* **2009**, *8*, 500.
- [18] H. Wang, Y. Yang, Y. Liang, J. T. Robinson, Y. Li, A. Jackson, **2011**, 2644.
- [19] G. Zhou, S. Pei, L. Li, D.-W. Wang, S. Wang, K. Huang, L.-C. Yin, F. Li, H.-M. Cheng, *Adv. Mater.* **2014**, *26*, 625.
- [20] L. Ji, M. Rao, H. Zheng, L. Zhang, Y. Li, W. Duan, J. Guo, E. J. Cairns, Y. Zhang, *J Am Chem Soc* **2011**, *133*, 18522.
- [21] Z. Wang, Y. Dong, H. Li, Z. Zhao, H. Bin Wu, C. Hao, S. Liu, J. Qiu, X. W. (David) Lou, *Nat. Commun.* **2014**, *5*, 5002.
- [22] J. Guo, Y. Xu, C. Wang, *Nano Lett.* **2011**, *11*, 4288.
- [23] M. Li, R. Carter, A. Douglas, L. Oakes, C. L. Pint, *ACS Nano* **2017**, *11*, 4877.
- [24] S. Chen, B. Sun, X. Xie, A. K. Mondal, X. Huang, G. Wang, *Nano Energy* **2015**, *16*, 268.
- [25] Z. Guo, B. Zhang, D. Li, T. Zhao, P. R. Coxon, C. J. Harris, R. Hao, Y. Liu, K. Xi, X. Li, *Electrochim. Acta* **2017**, *230*, 181.
- [26] J. Zhang, J. Xiang, Z. Dong, Y. Liu, Y. Wu, C. Xu, G. Du, *Electrochim. Acta* **2014**, *116*, 146.
- [27] Z. Gao, Y. Zhang, N. Song, X. Li, *Mater. Res. Lett.* **2016**, *3831*, 1.
- [28] W. Li, Q. Zhang, G. Zheng, Z. W. Seh, H. Yao, Y. Cui, *Nano Lett.* **2013**, *13*, 5534.
- [29] W. Zhou, Y. Yu, H. Chen, F. J. Disalvo, H. D. Abru??a, *J. Am. Chem. Soc.* **2013**, *135*, 16736.
- [30] Y. Mao, G. Li, Y. Guo, Z. Li, C. Liang, X. Peng, Z. Lin, *Nat. Commun.* **2017**, *8*, 14628.
- [31] X. Li, Q. Sun, J. Liu, B. Xiao, R. Li, X. Sun, *J. Power Sources* **2016**, *302*, 174.
- [32] X. Wang, G. Li, J. Li, Y. Zhang, A. Wook, A. Yu, Z. Chen, *Energy Environ. Sci.* **2016**, *9*, 2533.
- [33] Z. Li, J. Zhang, X. W. Lou, *Angew. Chemie - Int. Ed.* **2015**, *54*, 12886.

- [34] H. Yao, K. Yan, W. Li, G. Zheng, D. Kong, Z. W. Seh, V. K. Narasimhan, Z. Liang, Y. Cui, *Energy Environ. Sci.* **2014**, *7*, 3381.
- [35] Y.-S. Su, A. Manthiram, *Nat. Commun.* **2012**, *3*, 1166.
- [36] Z. Gao, Y. Zhang, N. Song, X. Li, *Electrochim. Acta* **2017**, *246*, 507.
- [37] A. C. Kozen, C. F. Lin, A. J. Pearse, M. A. Schroeder, X. Han, L. Hu, S. B. Lee, G. W. Rubloff, M. Noked, *ACS Nano* **2015**, *9*, 5884.
- [38] G. Ma, Z. Wen, M. Wu, C. Shen, Q. Wang, J. Jin, X. Wu, *Chem. Commun.* **2014**, *50*, 14209.
- [39] L. Suo, Y.-S. Hu, H. Li, M. Armand, L. Chen, *Nat. Commun.* **2013**, *4*, 1481.
- [40] S. Zhang, K. Ueno, K. Dokko, M. Watanabe, *Adv. Energy Mater.* **2015**, *5*, 1500117.
- [41] W. Li, Z. Liang, Z. Lu, X. Tao, K. Liu, H. Yao, Y. Cui, *Nano Lett.* **2015**, *15*, 7394.
- [42] K. Xie, Y. You, K. Yuan, W. Lu, K. Zhang, F. Xu, M. Ye, S. Ke, *Adv. Mater.* **2017**, 1604724.
- [43] J. Zhu, M. Chen, H. Qu, Z. Luo, S. Wu, H. A. Colorado, S. Wei, Z. Guo, *Energy Environ. Sci.* **2013**, *6*, 194.
- [44] H. Wei, H. Gu, J. Guo, D. Cui, X. Yan, J. Liu, D. Cao, X. Wang, S. Wei, Z. Guo, *Adv. Compos. Hybrid Mater.* **2017**, 127.
- [45] D. L. Huber, *Small* **2005**, *1*, 482.
- [46] A. H. Lu, E. L. Salabas, F. Schüth, *Angew. Chemie - Int. Ed.* **2007**, *46*, 1222.
- [47] H. Wu, Y. Zhang, R. Yin, W. Zhao, X. Li, L. Qian, *Adv. Compos. Hybrid Mater.* **2017**, 168.
- [48] N. Wu, J. Qiao, J. Liu, W. Du, D. Xu, W. Liu, *Adv. Compos. Hybrid Mater.* **2018**, *1*, 149.
- [49] Z. Gao, C. Bumgardner, N. Song, Y. Zhang, J. Li, X. Li, *Nat. Commun.* **2016**, *7*, 11586.
- [50] Z. Gao, N. Song, Y. Zhang, X. Li, *Nano Lett.* **2015**, *15*, 8194.
- [51] Y. Lin, J. Cho, G. a Tompsett, P. R. Westmoreland, G. W. Huber, *Cellulose* **2009**, 20097.
- [52] P. Melnikov, V. A. Nascimento, I. V. Arkhangelsky, L. Z. Zanoni Consolo, L. C. S. De Oliveira, *J. Therm. Anal. Calorim.* **2014**, *115*, 145.
- [53] Y. Xue, B. Wu, Y. Guo, L. Huang, L. Jiang, J. Chen, D. Geng, Y. Liu, W. Hu, G. Yu, *Nano Res.* **2011**, *4*, 1208.
- [54] A. C. Ferrari, J. C. Meyer, V. Scardaci, C. Casiraghi, M. Lazzeri, F. Mauri, S. Piscanec, D. Jiang, K. S. Novoselov, S. Roth, A. K. Geim, *Phys. Rev. Lett.* **2006**, *97*, 1.
- [55] Y. Wang, Q. He, H. Qu, X. Zhang, J. Guo, J. Zhu, G. Zhao, H. a Colorado, J. Yu, L. Sun, S. Bhana, M. a Khan, X. Huang, D. P. Young, H. Wang, X. Wang, S. Wei, Z. Guo, *J.*

- Mater. Chem. C* **2014**, *2*, 9478.
- [56] Y. V. Mikhaylik, J. R. Akridge, *J. Electrochem. Soc.* **2004**, *151*, A1969.
- [57] Z. Lin, C. Liang, *J. Mater. Chem. A* **2015**, *3*, 936.
- [58] W. Zhou, X. Xiao, M. Cai, L. Yang, *Nano Lett.* **2014**, *14*, 5250.
- [59] Y. Mi, W. Liu, Q. Wang, J. Jiang, G. W. Brudvig, H. Zhou, H. Wang, *J. Mater. Chem. A* **2017**, *0*, 1.
- [60] C. Hu, H. Chen, Y. Shen, D. Lu, Y. Zhao, A.-H. Lu, X. Wu, W. Lu, L. Chen, *Nat. Commun.* **2017**, *8*, 479.

Chapter 7. Cotton-Textile-Enabled Self-Sustaining Flexible Power Packs via Roll-to-Roll Fabrication

7.1 Introduction

With ever-increasing global energy consumption and the depletion of fossil fuels, finding a sustainable and clean energy supply has become the most important scientific and technological challenge facing humanity today. [1] Fossil fuels such as coal, oil, and natural gas are limited and non-renewable. With growing energy demand in many urbanizing nations, particularly in India and China, the looming threat of depleting the planet's fossil fuel reserves is more critical than ever. Relief may be as simple as utilizing the most accessible solar energy. Only recently, thanks to the development of less expensive and more efficient photovoltaic cells, solar energy has been harnessed and widely used as an alternative energy source. However, due to the fluctuation of light intensity and the diurnal cycle, the output of a solar cell is non-continuous and unstable. Therefore, there is a clear need to combine solar cells with energy storage devices (serving as a buffer) to mitigate the power-out swing and to allow operation of the cell and storage device as a reliable source of energy. Among various emerging energy storage technologies (batteries, supercapacitors, compressed air, and flywheels), supercapacitors, also named electrochemical capacitors or ultracapacitors, have been regarded as a very promising energy source for next-generation electronics and electric vehicles due to their excellent properties, such as high power density, long lifespan, environment benignancy, safety, and low maintenance cost. [2]

Compared with lithium-ion batteries, the relatively low energy density of supercapacitors limits their wide application. Developing new electrode materials with well-defined nanoarchitecture and high active surface area is the key to improve the electrochemical performance of supercapacitors. To date, according to the different mechanisms of charge storage, typical supercapacitor electrode materials can be categorized into electric double-layer capacitive (EDLC) materials including various carbon materials [3,4] and pseudo-capacitive materials including transition metal oxides, [5-8] and conductive polymers. [9-11] However, different materials have different advantages and disadvantages for supercapacitor applications. For example, carbon materials usually possess higher power density and longer lifespans but lower energy density. Transition metal oxides/hydroxides and conductive polymers possess higher

energy density but poorer cyclic life and lower power density. One intelligent strategy to strengthen the electrochemical performance of supercapacitors is to develop a hybrid material of carbon and metal oxides/hydroxides, which is anticipated to jointly improve the overall performance of supercapacitors in terms of their energy density, power density, and cyclic stability. [12]

Alternatively, a more attractive approach for balancing the contradiction between energy density and power density of supercapacitors is to assemble an asymmetric supercapacitor which consists of a battery-type Faradic electrode as energy source (usually pseudo-capacitive materials) and a capacitor-type electrode as power source (usually carbon materials). [13,14] In the last few decades, metallic layered double hydroxides (LDHs) with the general chemical formula $[M^{II}_1-xM^{III}_x(OH)_2]^{x+}[A^{n-}]_{x/n} \cdot mH_2O$, where M^{II} and M^{III} are divalent and trivalent metal cations and A^{n-} are the charge-balancing anions, [15] have aroused great interest in catalysis, [16] biotechnology, [17] separation, [18] and electrochemistry. [19,20] Moreover, LDHs have been proven to be a very promising class of electrode materials for supercapacitors due to their relatively low cost, high redox activity, and environmentally friendliness. [21,22] For example, Huang *et al.* reported that nickel-aluminum LDH (Ni-Al LDH) deposited on nickel foam exhibited an ultrahigh specific capacitance of 2123 F·g⁻¹ at 1 A g⁻¹. [23] Chen *et al.* also demonstrated that nickel-cobalt LDH (Ni-Co LDH) film had a significantly enhanced specific capacitance of 2682 F g⁻¹ at 3 A g⁻¹. [24] In our previous work, Ni-Al LDH was coupled with graphene nanosheets to prepare a hybrid electrode, which also demonstrated excellent electrochemical performance. [25] Therefore, high-energy LDHs will be ideal candidates for asymmetric supercapacitors. On the other hand, two-dimensional (2D) monolayered graphene has been intensively explored for energy storage application because of its superior electrical conductivity, high specific surface area, outstanding mechanical properties, and relative wide operation windows. [26-29] Graphene-based films and papers have been shown to be ideal “power sources” for flexible, asymmetric supercapacitors. [30-33]

Consumer demand for portable/wearable electronics has triggered a technological race to drive innovation in flexible cell phones, bendable displays, electronic skin, and distributed sensors. [34-36] Many attempts have been devoted to developing safe, lightweight, and flexible power sources to meet the urgent demand for flexible and wearable electronics. [37-40] In addition, “self-

powered nanotechnology” has been proposed to enable the future electronics to operate independently and sustainably without batteries, or with a battery possessing extended lifespan. [41] Self-powered nanosystems with multi-functionalities will be a prominent driving force for future world economies by employing transformative nanomaterials and nanofabrication technologies. [42] To date, many attempts and achievements have been made in developing self-powered nanosystems by combining nanogenerators or solar cells with lithium-ion batteries or supercapacitors. [43-45] However, until now, a streamlined manufacturing process for integrating a flexible energy harvesting unit with a flexible energy storage unit has not been achieved due to the lack of effective packaging technology.

Cotton textile, a source of flexible, green, renewable, breathable clothing, has been proven to be an excellent wearable platform for constructing flexible energy storage devices because activated cotton textiles (ACTs) exhibit eminent flexibility and excellent conductivity. [46,47] In this work, flower-like cobalt-aluminum LDH (Co-Al LDH) nanoarrays consisting of interconnected nano-petals and pompon-like nano-stamens are *in-situ* anchored on flexible ACTs to realize ACT/Co-Al LDH hybrid by a facile hydrothermal method. A highly conductive graphene coating is wrapped onto ACT fibers to form ACT/graphene composite by a simple dipping, drying, and reducing process. A flexible, all-solid-state asymmetric supercapacitor (ACT/Co-Al LDH//ACT/graphene) has been assembled by using the nanostructured ACT/Co-Al LDH as the positive electrode, ACT/graphene as the negative electrode, and PVA-KOH gel as both the solid-state electrolyte and separator. The asymmetric cell works synergically to achieve excellent electrochemical performance in terms of its working potential (1.6 V), energy density (55.04 Wh kg⁻¹), power density (5.44 KW kg⁻¹), and cycling stability (capacitance retention rate of 87.54% after 2000 cycles). Moreover, we demonstrate a practical roll-to-roll manufacturing approach to combine the flexible asymmetric supercapacitor with a flexible solar cell to fabricate an integrated self-sustaining power pack, which is scalable for scalable industrial manufacturing. Importantly, the assembled power pack continuously can power a commercial light-emitting-diode (LED) with or without sunlight, demonstrating its potential for flexible, self-powered energy devices.

7.2 Experimental Section

7.2.1 Preparation of Flexible ACT/Co-Al LDH Positive Electrode

All of the chemicals were used after purchasing without further purification. A piece of the

commercial cotton T-shirt was first cleaned using distilled water in an ultrasonic bath before activation. Activation of the cotton T-shirt was performed as described in detail in our previous report.⁴⁷ First, a piece of cotton T-shirt was dipped into 1 M NaF solution and soaked for 1 h. The wet textile was then dried at 120 °C for 3 h. Second, the NaF-treated cotton textile was transferred into a horizontal tube furnace and kept at 1000 °C for 1 h with a continuous argon gas flow (300 sccm). After cooling down to room temperature, the as-obtained activated cotton textiles (ACTs) were washed with distilled water to remove the residual NaF and then dried at 80 °C for 6 h. Co-Al LDH nanoarrays were grown *in-situ* on ACT fibers via a simple hydrothermal process. Briefly, 0.582 g of Co(NO₃)₂·6H₂O, 0.518 g Al(NO₃)₃·6H₂O, 0.296 g NH₄F, and 0.6 g of urea were dissolved in 36 mL distilled water. The resulting solution was transferred into a 50 mL Teflon-lined stainless autoclave with a piece of vertically suspended ACT (1 cm × 2 cm) in the solution. Then, the autoclave was placed in an electric oven at 100 °C for 24 h. Finally, the as-prepared products were washed thoroughly with ethanol and distilled water and dried at 80 °C overnight to produce ACT/Co-Al LDH composite.

7.2.2 Preparation of Flexible ACT/graphene Negative Electrode

Graphite oxide was synthesized by exfoliating natural graphite flakes using a modified Hummers method. [65] The obtained graphite oxide solution was further exfoliated by ultrasonication in an ultrasonic bath for 1 h to prepare graphene oxide. Then, the above graphene oxide solution was centrifuged at 3000 rpm for 5 min to remove residual aggregates, forming a brown aqueous colloid with a concentration of ~4 mg mL⁻¹. A piece of ACT (1 cm × 2 cm) was then soaked with the graphene oxide aqueous colloid. After drying at 80 °C for 6 h, the as-prepared ACT with graphene oxide coating was heated at 450 °C for 1 h with argon/hydrogen mixture gas (v/v 90/10) to reduce flexible ACT/graphene oxide to ACT/graphene negative electrode.

7.2.3 Characterization Methods

The morphology and microstructure of the as-prepared products were characterized by scanning electron microscopy (SEM; FEI Quanta 650), transmission electron microscopy (TEM; JEOL 2000FX), high-resolution transmission electron microscopy (HRTEM, FEI Titan), and atomic force microscopy (AFM; Nanoscope IIIa). The crystallographic structure of the synthesized materials was determined by a PANalytical X'Pert Pro Multi-Purpose Diffractometer (MPD) equipped with Cu K_α radiation ($\lambda = 0.15406$ nm). The Raman spectra of the ACT/graphene were recorded by a Renishaw InVia Raman microscope at 785 nm. Surface areas of the active materials

were measured by physical adsorption of N₂ at 77 K (Quantachrome Autosorb iQ surface area and pore size analyzer) and calculated by the Brunauer-Emmett-Teller (BET) method.

7.2.4 Fabrication and Characterization of Integrated Flexible Self-Sustaining Power Pack

The electrochemical performances of the prepared ACT, ACT/graphene and ACT/Co-Al LDH electrodes were characterized by both three-electrode and two-electrode systems. The three-electrode tests were carried out in 6 M KOH aqueous electrolyte at room temperature. The prepared ACT, ACT/graphene and ACT/Co-Al LDH were used as the working electrodes, platinum foil (1 cm × 1 cm) and a saturated calomel electrode (SCE) were used as the counter and reference electrodes, respectively. The mass of the ACT, ACT/graphene and ACT/Co-Al LDH was measured to be 2, 3.45, and 4.1 mg cm⁻², respectively. The asymmetric supercapacitor used in this paper was assembled with two pieces of flexible, face-to-face electrodes (ACT/Co-Al LDH positive and ACT/graphene negative) separated by the solid-state, polymer PVA/KOH gel electrolyte (ACT/Co-Al LDH//ACT/graphene). The polymer gel electrolyte was prepared by mixing 3 g KOH and 6 g PVA in 60 mL deionized water by magnetically stirring the solution at 80 °C until the solution became clear. Then, the above solution was transferred into a flat petri-dish to naturally solidify to PVA/KOH gel film electrolyte. Two pieces of flexible electrodes separated by the PVA/KOH gel film were used to assemble the flexible asymmetric cell. The as-obtained solid-state, polymer PVA/KOH gel film served as both the separator and electrolyte. The electrochemical properties of the assembled flexible asymmetric cell were measured using a CHI 660E electrochemical workstation. Cyclic voltammograms (CV), galvanostatic charge/discharge curves, and electrochemical impedance spectroscopy (EIS) in the frequency range from 100 kHz to 0.05 Hz with an AC perturbation of 5 mV were used to evaluate the electrochemical performance of the flexible solid-state asymmetric supercapacitors. The integrated flexible energy conversion and storage unit was assembled by combining a piece of commercial flexible solar panel (with an open circuit potential of 3 V and energy efficiency of 22%, from PowerFilm) with an energy storage unit consisting of two pieces of asymmetric cell connected in series using an electrical rolling machine (MSK-HRP-MR100A, MTI). Two pieces of assembled asymmetric flexible supercapacitors were connected in series and then coated with double-sided adhesive tapes. At the same time, the bottom surface of the flexible solar cell was also coated with double-sided adhesive tapes. As illustrated in Fig. 6a, the flexible supercapacitor, and the flexible

solar cell were integrated together by the roll-to-roll rolling press machine. During the roll-to-roll fabrication process, the top surface of the solar cell (collecting sunlight) was protected by using the soft cloth to obtain a flexible, solar cell/supercapacitor, self-sustaining power pack. The open circuit potential and charge/discharge processes were monitored by the CHI electrochemical workstation.

7.3 Results and Discussion

7.3.1 Positive Electrode Materials

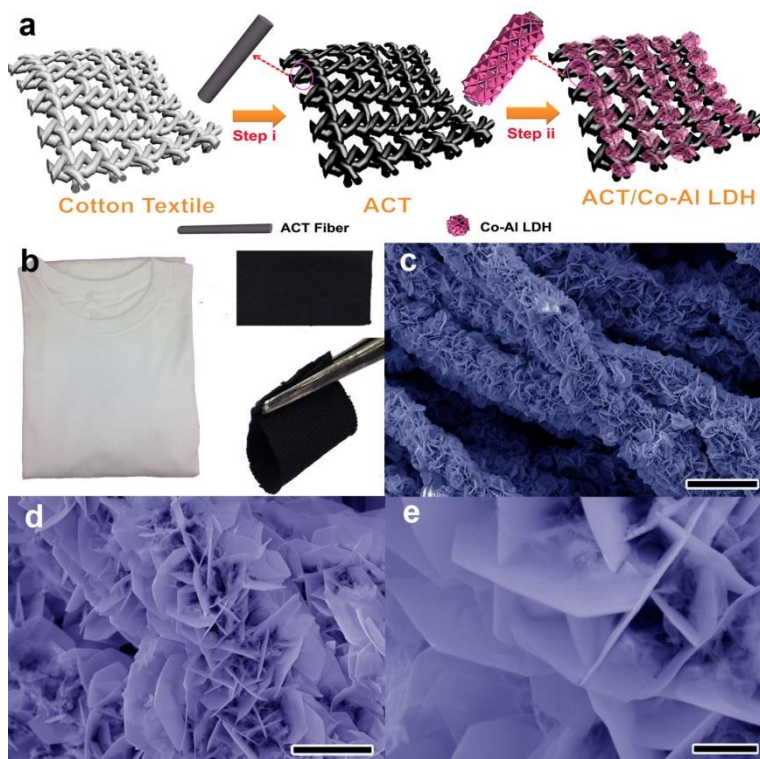


Figure 7.1 (a) Schematic illustration of the formation processes of Co-Al LDH nanostructure on the ACT; (b) Photographs of a cotton T-shirt, a piece of ACT and a piece of ACT under folded state; (c-e) SEM images of Co-Al LDH nanosheets on ACT fibers at different magnifications. Scale bars, 20 μm for (c), 5 μm for (d) and 1 μm for (e).

Figure 7.1a illustrates the two-step design and synthesis procedures of Co-Al LDH nanoarrays on ACT fibers. In a typical experiment, highly conductive and flexible ACTs were first prepared by direct conversion of cotton T-shirt textiles through a dipping, drying and annealing process (step I). Then, flower-like Co-Al LDH nanoarrays were radially grown *in-situ* on ACT fibers using a facile hydrothermal method (step II), which resulted in a pink coating on the surface of ACT fibers. Figure 7.1b shows the digital photographs of the cotton T-shirt and the converted ACT under normal and folded states, demonstrating its mechanical flexibility. Figures 7.1c-e show

the SEM images of the as-synthesized Co-Al LDH nanoarrays on ACT fibers. High-density hexagonal Co-Al LDH nanosheets, with the length of about 2-5 μm and thickness of around 40-70 nm, were radially aligned on individual ACT fibers, forming flower-like nanoarrays that consist of interconnected LDH nano-petals and pompon-like LDH nano-stamens. Such 3D hierarchical, porous nanostructure *in-situ* anchored on ACT fibers not only enhances the contact between the active material and ACT substrate but also serves as a reservoir for electrolyte ions, shortening ion diffusion path and facilitating charge transfer, jointly enhancing the electrochemical performance.

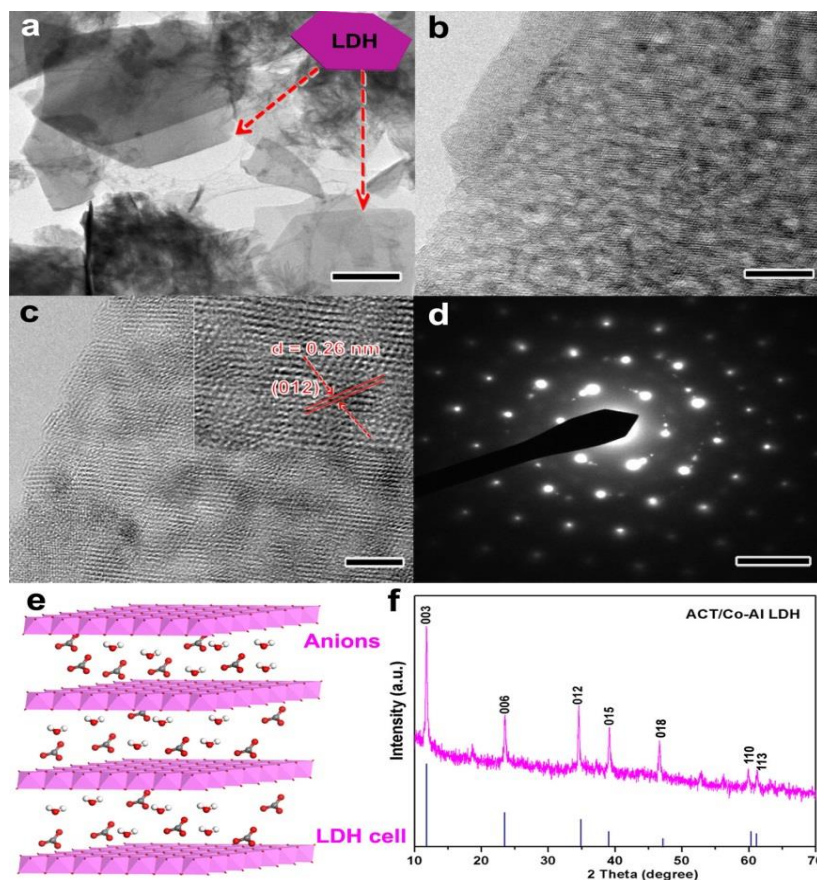


Figure 7.2 (a) TEM image of Co-Al LDH (scale bar, 1 μm), inset is the illustration of LDH; (b-d) HRTEM images of Co-Al LDH and the corresponding SAED pattern. Scale bars, 10 nm for (b), 5 nm for c and 5 $1/\text{nm}$ for (d); (e) Schematic illustration of the molecular structure of Co-Al LDH; (f) XRD patterns of ACT/Co-Al LDH and the standard peaks of Co-Al LDH (JCPDS # 510045).

The structure and morphology of the Co-Al LDH nanosheets were further investigated by transmission electron microscopy (TEM) and X-ray diffraction (XRD). TEM inspection (Fig. 7.2a) reveals that the LDH nanosheets are of hexagonal shape with 2-5 nm sized nanopores on the surface of individual LDH nanosheets (Fig. 7.2b), which is expected to have a higher specific area. The ACT/Co-Al LDH composite achieved a high BET surface area of 814.4 $\text{m}^2 \text{g}^{-1}$. A lattice

spacing of 0.26 nm (Fig. 7.2c) can be ascribed to the (012) crystal plane of Co-Al LDH, which is inconsistent with the XRD results (Fig. 7.2f). The corresponding selected area electron diffraction (SAED) pattern (Fig. 7.2d) shows hexagonally arranged bright spots, indicating the single-crystal nature of LDH nanosheets. The XRD pattern (Fig. 7.2f) shows a series of diffraction peaks at 11.59° , 23.26° , 34.56° , 38.78° and 46.7° , which can be indexed to the (003), (006), (012), (015) and (018) planes of the layered LDH phase (JCPDS #51-0045), respectively. The small peak at $\sim 19^\circ$ probably resulted from cobalt hydroxide impurity in the ACT/Co-Al LDH composite.

7.3.2 Negative Electrode Material

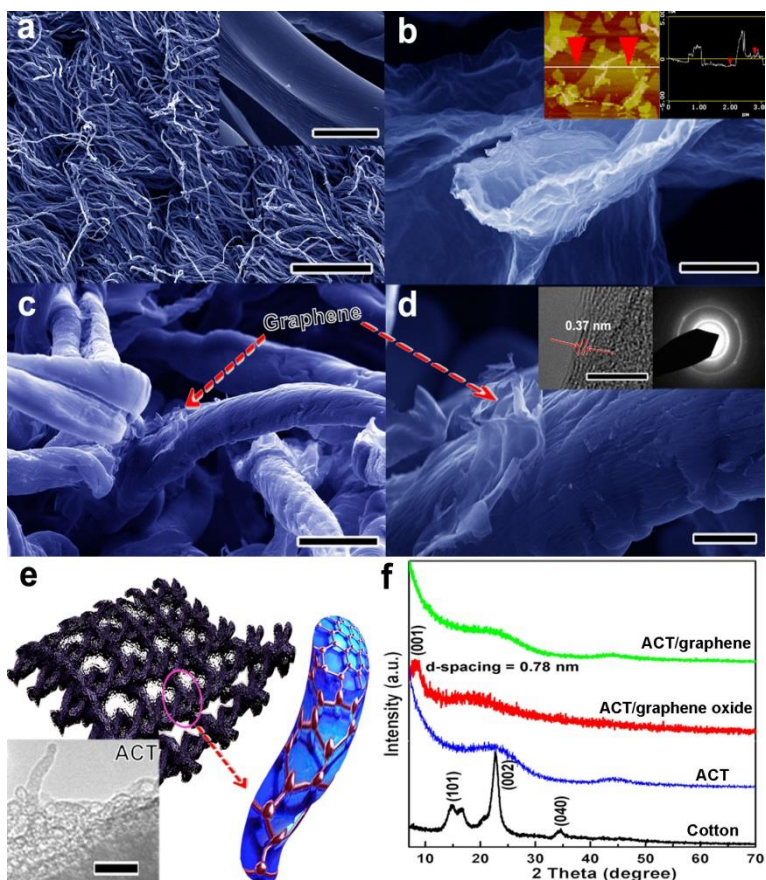


Figure 7.3 (a) SEM image of ACT (scale bar, 250 μm), inset is the amplified SEM image (scale bar, 5 μm); (b) SEM image of graphene oxide, inset is the AFM image of graphene oxide nanosheets (with a height profile showing a step of 1.1 nm marked by the red arrows); (c,d) SEM images of ACT/graphene composite at different magnifications (scale bars, 10 μm for c and 2 μm for (d)), insets of d are the HRTEM image (scale bar, 5 nm) and corresponding SAED pattern of graphene nanosheets; (e) Schematic illustration of the ACT fiber with graphene coating, inset is the TEM image of ACT fiber (scale bar, 25 nm); (f) XRD patterns of pure cotton textile, ACT, ACT/graphene oxide, and ACT/graphene composite.

Highly conductive graphene was coated on flexible ACTs to fabricate negative electrode material for constructing asymmetric supercapacitors. Conductive ACTs (sheet resistance: ~ 10 -20

ohm sq.⁻¹) were first prepared by direct conversion of a cotton T-shirt. As shown in Fig. 7.3a, the ACT fibers have diameters ranging from 5 to 10 μm, which inherit the cellulose fiber structure of the cotton textile. After activation, a piece of ACT was dipped into graphene oxide solution for a few minutes to coat graphene oxide nanosheets. Figure 7.3b shows the typical scanning electron microscopy (SEM) images of the corrugated and scrolled graphene oxide sheets, resembling crumpled silk veil waves. The thickness of the as-synthesized graphene oxide sheets was measured to be 1.1 nm (inset of Fig. 7.3b), which is close to the theoretical value of 0.78 nm for single-layer graphene oxide, indicating that the as-prepared graphene oxide sheets were predominantly in monolayered fashion. [48] Usually, the graphene oxide sheets tend to agglomerate due to the electrostatic interactions of the oxygen-containing functional groups (epoxide, hydroxyl, carbonyl, and carboxyl groups) on the surfaces and the edges of the sheets (inset of Fig. 7.3b). After dipping, individual ACT fibers were wrapped with curled and entangled graphene oxide sheets (a mixture of multilayered/monolayered sheets). During the thermal reduction, the conductivity of the graphene oxide sheets was enhanced due to partial overlapping or coalescing *via* π–π stacking or hydrogen bonding, [49,50] resulting in an interconnected 3D conductive graphene network on the ACT fibers (Figs. 7.3c-e). The insets of Figure 7.3d are the high-resolution transmission electron microscopy (HRTEM) image and corresponding SAED pattern of the graphene nanosheets. The deformed crystal fringes with a d-spacing of ~0.37 nm in the HRTEM image suggest the existence of defects in the graphene nanosheets. The crystalline nature of the graphene nanosheets was validated by the well-defined diffraction spots in the SAED pattern. More importantly, the ACT fibers showed a porous structure as revealed by the TEM image (inset of Fig. 7.3e). The entangled graphene sheets wrapped around the porous ACT fibers, forming a 3D porous conductive net. The BET surface area of the ACT/graphene composite was measured to be ~450 m² g⁻¹. The 3D graphene/fiber conductive net is expected to facilitate electrolyte ion diffusion and electron transport in the charge/discharge processes, improving the overall power density of the asymmetric cell.

Figure 7.3f shows the XRD spectra of cotton, ACT, ACT/graphene oxide and ACT/graphene composites, respectively. The diffraction peaks at 14.8°, 22.7°, and 34.3° can be indexed respectively to the (101), (002) and (040) peaks of the cellulose polymorphs from Cellulose I ingredients in pure cotton. [14,51] After activation, the cotton peaks disappeared, alternately, a broad diffraction peak appeared at ~21° for ACT, indicating the breakage of cellulose

polymorphs and the formation of amorphous carbon during the activation process. The peak at 8.8° for ACT/graphene oxide corresponds to the (001) lattice plane of graphene oxide with an interplanar spacing of 0.78 nm, indicating the complete exfoliation of graphite to graphene oxide. [52] After the thermal reduction process, the peak at 8.8° for the ACT/graphene oxide disappeared, suggesting the oxygen-containing groups on the graphene oxide had been removed, and the conductivity of graphene oxide was restored, [53,54] ensuring the improved electrochemical performance of the assembled asymmetric cell. Raman spectroscopy (Fig. 7.4) was used to further characterize the ACT/graphene composite (reduced from ACT/graphene oxide). Generally, graphene exhibits two characteristic bands in its Raman spectrum: the G band at $\sim 1575\text{ cm}^{-1}$ resulting from the first order scattering of the E_{1g} phonon of sp^2 C atoms and the D band at $\sim 1350\text{ cm}^{-1}$ resulting from a breathing mode of point photons of A_{1g} symmetry. [55] The ACT/graphene showed an increased I_D/I_G ratio (~ 1.21) compared with the ACT/graphene oxide with the I_D/I_G ratio of ~ 1.03 . The increased I_D/I_G ratio is ascribed to the reestablishment of the graphene network during the reduction process, indicating smaller sizes, more defects and disordered structures of the graphene.¹⁴ The XRD and Raman spectroscopy results jointly demonstrate the successful removal of the oxygen-containing groups on the surfaces and edges of graphene oxide sheets during the reduction process.

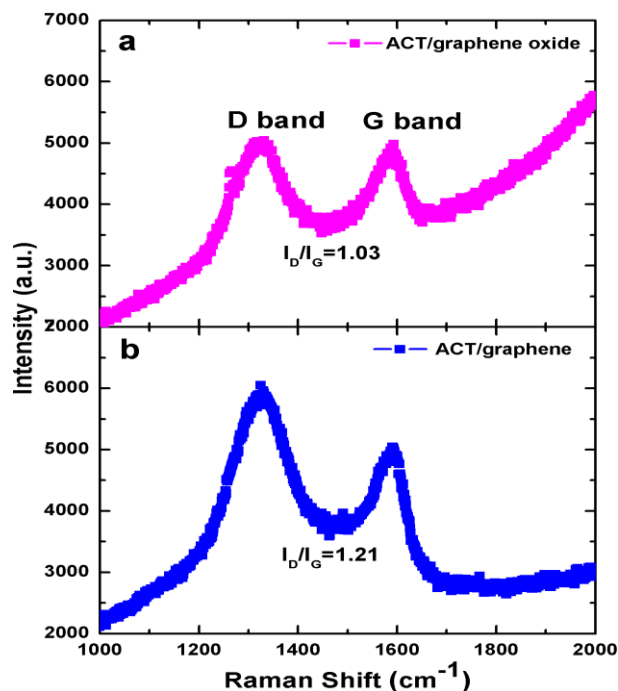


Figure 7.4 Raman spectra of ACT/graphene oxide (a) and ACT/graphene (b) composites.

7.3.3 Cell Performance

The as-prepared ACT/Co-Al LDH was used as the positive electrode, ACT/graphene as the negative electrode and the PVA-KOH gel as both the solid electrolyte and separator to construct a flexible asymmetric supercapacitor. The energy storage performances of the assembled cells and individual electrodes were studied by cyclic voltammetry (CV), galvanostatic charge/discharge and electrochemical impedance spectroscopy (EIS) in both two-electrode and three-electrode testing systems.

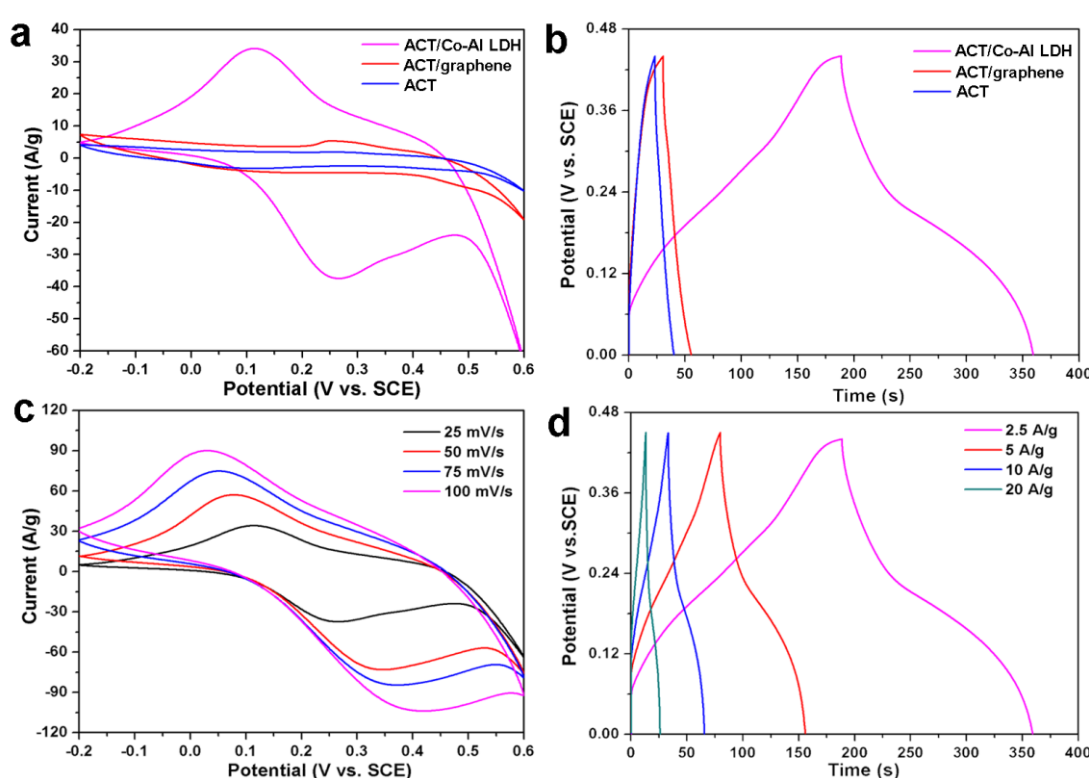


Figure 7.5 (a) CV curves of the ACT, ACT/graphene, and ACT/Co-Al LDH electrodes with the 6 M KOH electrolyte in the potential window of -0.2-0.6 V at a scan rate of 25 mV s⁻¹; (b) Charge/discharge curves of the ACT, ACT/graphene, and ACT/Co-Al LDH electrodes with the 6 M KOH electrolyte in the potential window of 0-0.44 V at a current density of 2.5 A g⁻¹; (c) CV curves of ACT/Co-Al LDH electrode with the 6 M KOH electrolyte in the potential windows of -0.2-0.6 V at different scan rates; (d) Charge/discharge curves of ACT/Co-Al LDH electrode with the 6 M KOH electrolyte in the potential windows of 0-0.44 V at different current densities.

The three-electrode testing system was used to study the electrochemical reaction mechanisms of the as-prepared ACT, ACT/graphene and ACT/Co-Al LDH electrodes. The CV curves of the aforementioned electrodes at the scan rate of 25 mV s⁻¹ with the potential windows ranging from -0.2 to 0.6 V are shown in Fig. 7.5a. Both ACT and ACT/graphene electrodes showed quasi-rectangular shaped CV curves, indicating ideal electrical double

layer capacitive behavior. The small peak at ~ 0.25 V in the CV curve of ACT/graphene electrode is ascribed to the pseudo-capacitive reaction from the residual oxygen-containing groups on graphene sheets, resulting in a higher capacitance. The CV curve of the ACT/Co-Al LDH hybrid electrode showed a more complex shape with two pairs of redox peaks, which resulted from the typical Faradaic redox reactions of Co hydroxides, as described below: [56]

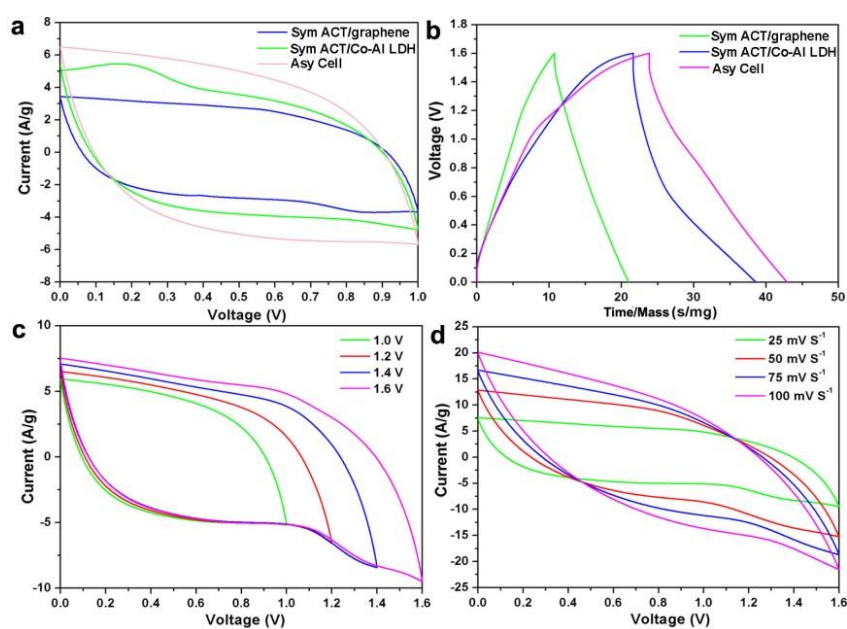


Figure 7.6 (a) CV curves of ACT/graphene//ACT/graphene and ACT/Co-Al LDH//ACT/Co-Al LDH symmetric cells as well as ACT/Co-Al LDH//ACT/graphene asymmetric cell with PVA/KOH polymer gel electrolyte in the voltage window of 1.0 V at a scan rate of 25 mV s^{-1} ; (b) Charge/discharge curves of ACT/graphene//ACT/graphene and ACT/Co-Al LDH//ACT/Co-Al LDH symmetric cells as well as ACT/Co-Al LDH//ACT/graphene asymmetric cell with PVA/KOH polymer gel electrolyte in the voltage window of 1.6 V at a current density of 12.5 mA cm^{-2} (X-axis has been transformed to time/mass, based on the mass of the electrode); (c) CV curves of ACT/Co-Al LDH//ACT/graphene asymmetric cell with PVA/KOH polymer gel electrolyte under the voltage windows of 1, 1.2, 1.4 and 1.6 V at the scan rate of 25 mV s^{-1} , respectively; (d) CV curves of ACT/Co-Al LDH//ACT/graphene asymmetric cell with PVA/KOH polymer gel electrolyte in the voltage windows of 1.6 V at different scan rates.

Fig. 7.5b shows the galvanostatic charge/discharge performances of the ACT, ACT/graphene and ACT/Co-Al LDH electrodes at the current density of 2.5 A g^{-1} . Compared with the triangular-shaped charge/discharge curves of the ACT and ACT/graphene electrodes, the ACT/Co-Al LDH electrode exhibited two charge/discharge voltage plateaus, which are the pseudocapacitive plateaus from the Co-Al LDH. The specific capacitance values of the ACT, ACT/graphene and

ACT/Co-Al LDH electrodes were measured to be 90.1, 136 and 977.3 F/g, respectively. The CV curves of the ACT/Co-Al LDH electrode at the scan rates of 25, 50, 75, and 100 mV s^{-1} in 6 M KOH electrolyte solution are shown in Fig. 7.5c. All of them exhibited similar redox peaks, even at increased scan rates, indicating the quasi-reversible and continuous faradic redox reactions from Co-Al LDH that contributed remarkably to the pseudocapacitance. The galvanostatic charge/discharge curves of the ACT/Co-Al LDH electrode at different current densities are shown in Fig. 7.5d. The specific capacitance values obtained from the ACT/Co-Al LDH at the current densities of 2.5, 5, 10, and 20 A g^{-1} are 977.3, 863, 727, and 545 F g^{-1} , respectively, with a capacitance retention of $\sim 55.8\%$ even when the current density increased from 2.5 to 20 A g^{-1} .

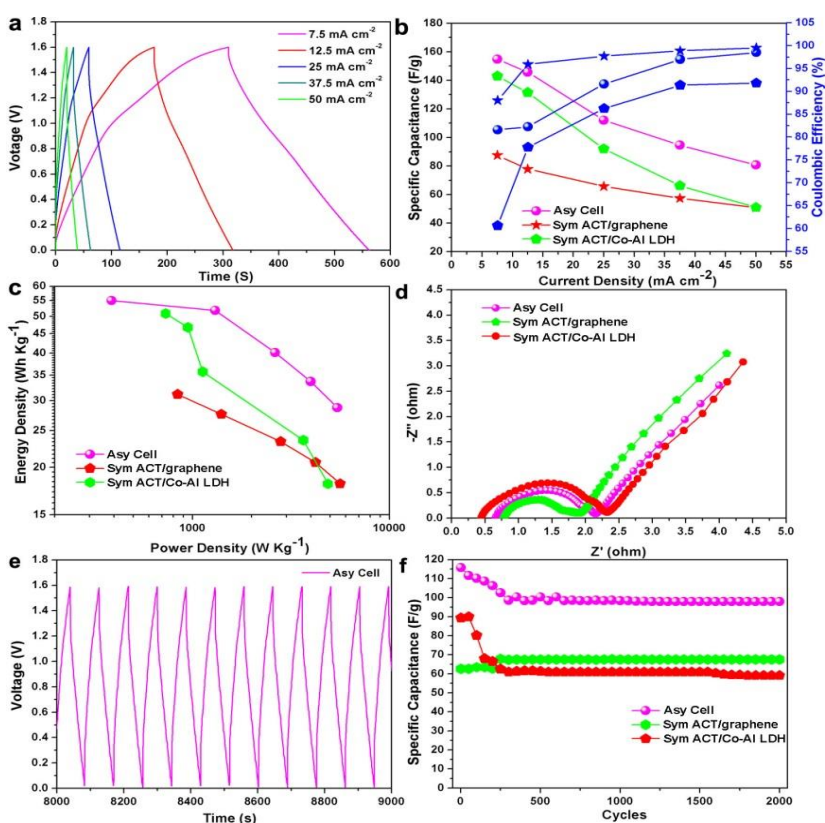


Figure 7.7 (a) Charge/discharge curves of ACT/Co-Al LDH//ACT/graphene asymmetric cell; (b) Specific capacitances and Coulombic efficiency of the ACT/graphene//ACT/graphene and ACT/Co-Al LDH//ACT/Co-Al LDH symmetric cells as well as ACT/Co-Al LDH//ACT/graphene asymmetric cell; (c) Ragone plots of the ACT/graphene//ACT/graphene and ACT/Co-Al LDH//ACT/Co-Al LDH symmetric cells as well as ACT/Co-Al LDH//ACT/graphene asymmetric cell; (d) Nyquist plots of the ACT/graphene//ACT/graphene and ACT/Co-Al LDH//ACT/Co-Al LDH symmetric cells as well as ACT/Co-Al LDH//ACT/graphene asymmetric cell; (e) Representative charge/discharge curve of ACT/Co-Al LDH//ACT/graphene asymmetric cell; (f) Cyclic performance of the ACT/graphene//ACT/graphene and ACT/Co-Al LDH//ACT/Co-Al LDH symmetric cells as well as ACT/Co-Al LDH//ACT/graphene asymmetric cell with PVA/KOH polymer gel electrolyte.

Figure 7.6a shows the CV curves of ACT/graphene//ACT/graphene and ACT/Co-Al

LDH//ACT/Co-Al LDH symmetric cells as well as ACT/Co-Al LDH//ACT/graphene asymmetric cell with PVA/KOH polymer gel electrolyte at the scan rate of 25 mV s^{-1} . The rectangularly shaped CV curves of the ACT/graphene symmetric cell suggest that the ACT/graphene mainly worked as an electrochemical double-layered capacitor. The broad peak at 0.25 V of the ACT/Co-Al LDH symmetric cell indicates the Faradic reaction from the battery-type Co-Al LDH. The CV area of the ACT/Co-Al LDH//ACT/graphene asymmetric cell was much larger than that of the ACT/graphene//ACT/graphene and ACT/Co-Al LDH//ACT/Co-Al LDH symmetric cells, suggesting the larger specific capacitance of ACT/Co-Al LDH//ACT/graphene asymmetric cell resulting from the high accessibility of electrolyte ions. Figure 7.6b shows the charge/discharge curves of the ACT/graphene//ACT/graphene and ACT/Co-Al LDH//ACT/Co-Al LDH symmetric cells as well as ACT/Co-Al LDH//ACT/graphene asymmetric cell. The ACT/graphene symmetric cell exhibited a triangular-shaped charge/discharge curve, implying an ideal capacitor character. Note that the ACT/Co-Al LDH symmetric cell exhibited a distorted charge/discharge profile, indicating the Faradic reaction during the charging/discharging process. The discharging capacities were measured to be 145.8, 131.75 and 77.9 F/g for the ACT/Co-Al LDH//ACT/graphene asymmetric cell, ACT/Co-Al LDH symmetric cell, and ACT/graphene symmetric cell at the current density of 12.5 mA cm^{-2} , respectively. Figure 7.6c shows the CV curves of the ACT/Co-Al LDH//ACT/graphene asymmetric cell with PVA/KOH polymer gel electrolyte in the respective voltage windows of 1.0, 1.2, 1.4 and 1.6 V at the scan rate of 25 mV s^{-1} . The working voltage of the ACT/Co-Al LDH//ACT/graphene asymmetric cell can be extended to 1.6 V, which is essential for practical application. Figure 7.6d shows the CV curves of the ACT/Co-Al LDH//ACT/graphene asymmetric cell at different scan rates ranging from 25 to 100 mV s^{-1} at an operation window of 1.6 V. The current density increases with increasing scan rate. All the CV curves at different scan rates in Fig. 7.7e have a similar shape, indicating stable reversibility and good rate performance of the ACT/Co-Al LDH//ACT/graphene asymmetric cell.

Rate performance and Coulombic efficiency are important factors for the real power application of supercapacitors. Figure 7.7a shows the charge/discharge curves of ACT/Co-Al LDH//ACT/graphene asymmetric supercapacitor at different current densities. A high capacitance retention of 80.78 F g^{-1} was achieved even when the current density increased from 7.5 to 50 mA cm^{-2} , indicating the excellent rate performance of the ACT/Co-Al LDH//ACT/graphene asymmetric cell. The rate performance and corresponding Coulombic efficiency of

ACT/graphene//ACT/graphene and ACT/Co-Al LDH//ACT/Co-Al LDH symmetric cells as well as ACT/Co-Al LDH//ACT/graphene asymmetric cell are comprehensively compared in Fig. 7.7b. The assembled ACT/graphene symmetric cell exhibited an excellent electrochemical stability (58% capacitance retention) and high Coulombic efficiency (99.5% at 50 mA cm^{-2}) in a wide range of current densities ($7.5\text{-}50 \text{ mA cm}^{-2}$). Whereas the ACT/Co-Al LDH symmetric cell showed poor rate performance (35% capacitance retention) and low Coulombic efficiency (91.8% at 50 mA cm^{-2}). Compared with the ACT/Co-Al LDH symmetric cell, the ACT/Co-Al LDH//ACT/graphene asymmetric cell exhibited not only improved capacitance retention (52.3% capacitance retention) but also enhanced Coulombic efficiency (98.5% at 50 mA cm^{-2}). At high charge/discharge rates the ions on electrode decreased rapidly with increasing rate, and the ions in the electrolyte diffused too slowly to satisfy the need of ions near the solid-liquid interface, leading to the decrease of capacitance. [57] The improvements in both rate capability and Coulombic efficiency for the asymmetric cell result from the synergetic effects between the two distinct electrodes where the high conductive ACT/graphene with high rate capacity balanced the poor rate capacity of ACT/Co-Al LDH.

Energy density and power density are important factors for evaluating the practical application of supercapacitors. Figure 7.7c shows the Ragone plots of ACT/graphene//ACT/graphene and ACT/Co-Al LDH//ACT/Co-Al LDH symmetric cells as well as ACT/Co-Al LDH//ACT/graphene asymmetric cell. Compared with the symmetric cells, the ACT/Co-Al LDH//ACT/graphene asymmetric cell exhibited a higher energy density of 55.04 Wh kg^{-1} at the power density of 387.9 W kg^{-1} and maintained 28.72 Wh Kg^{-1} at the power density of 5.44 kW kg^{-1} . For an in-depth understanding of the electrochemical behavior of the assembled symmetric and asymmetric cells, the EIS tests were carried out on the aforementioned cells (Fig. 7.7d). A similar shape can be found for all the impedance spectra, with a straight line at the low-frequency regime and an arc at the high-frequency region. The high-frequency arc is ascribed to the double-layer capacitance (C_{dl}) and the charge transfer resistance (R_{ct}) at the electrode and electrolyte interface, corresponding to the charge transfer limiting process. [58] R_{ct} was directly measured from the diameter of the semicircle arc in the Nyquist plot. Clearly, compared with the ACT/graphene (1.1Ω) and ACT/Co-Al LDH (1.89Ω) symmetric cells, the relatively smaller R_{ct} of the asymmetric cell resulted from the synergistic effect of the ACT/graphene and hierarchical ACT/Co-Al LDH architectures that facilitated the access of electrolyte ions to the active surface

and shortened the ion diffusion path.

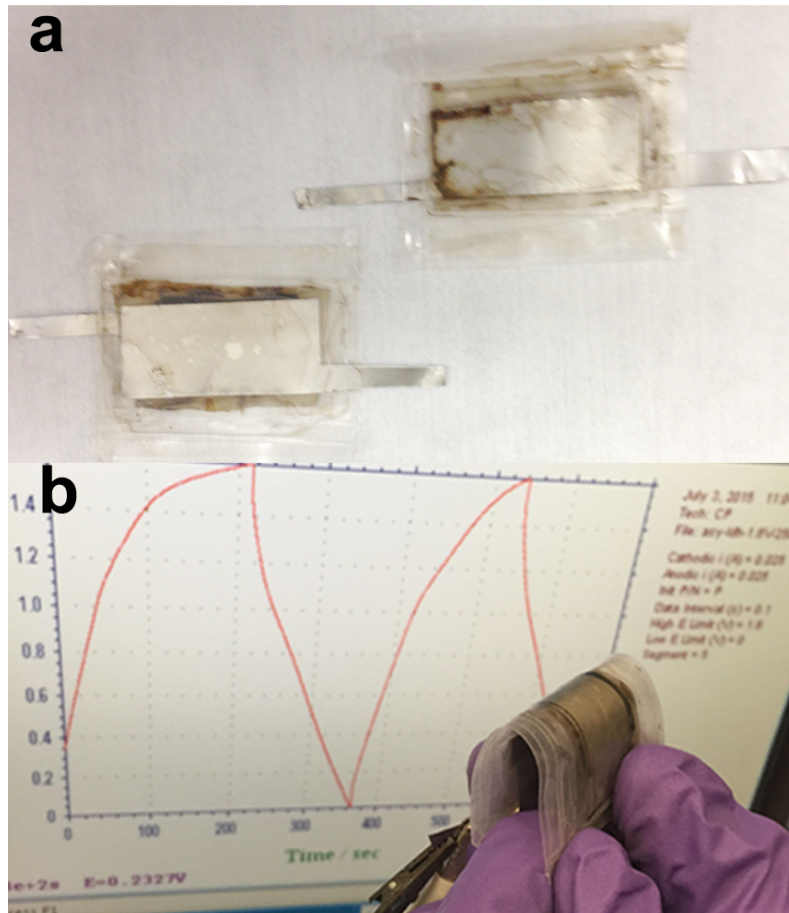


Figure 7.8 (a) The digital photograph of the assembled flexible asymmetric cell under normal state; (b) The digital photograph of the assembled flexible asymmetric cell under folded state, demonstrating its excellent flexibility.

Cycling capability is another crucial requirement for the practical application of supercapacitors. The cyclic performances of ACT/graphene//ACT/graphene and ACT/Co-Al LDH//ACT/Co-Al LDH symmetric cells as well as ACT/Co-Al LDH//ACT/graphene asymmetric cell were evaluated at the current density of 12.5 mA cm^{-2} using a galvanostatic charge-discharge technique. An obvious capacity decay ($\sim 35\%$) was observed for the ACT/Co-Al LDH symmetric cell, while there was a capacity increase ($\sim 8\%$) for the ACT/graphene symmetric cell after 2000 cycles. For the ACT/Co-Al LDH//ACT/graphene asymmetric cell, $\sim 16\%$ decay of its original capacitance was noted after 2000 cycles. The asymmetric cell exhibited linear and symmetrical characteristics in its charge/discharge curves, and no obvious “IR drop” was observed, indicating its low internal resistance (Fig. 7.7e). Compared with previously reported LDH-based asymmetric supercapacitors (see Table 7.1), the electrochemical properties of the ACT/Co-Al LDH//ACT/graphene

asymmetric cell, benefiting from the synergistic effects of ACT/graphene and flower-like ACT/Co-Al LDH, are highly competitive in terms of specific capacity, maximum energy and power densities, and cyclability. The assembled flexible asymmetric cell also worked well under a 180° folded state (Fig. 7.8), a clear indication of the cell's excellent coupled mechanical and electrochemical robustness.

Table 7.1. Comparison of the as-prepared Co-Al LDH asymmetric supercapacitor with previously published results.

<i>Ref.</i>	<i>Electrode materials</i>	<i>Specific capacitance (F/g)</i>	<i>Working potential (V)</i>	<i>Maximum Energy density (Wh/Kg)</i>	<i>Maximum Power density (KW/Kg)</i>	<i>Cyclic performance (retention)</i>
24	Ni-Co LDH//rGO	550	1.6	188	7.32	82% after 5000 cycles
56	GSP/Co-Al LDH//SGC	—	1.6	41.2	9.3	84% after 2000 cycles
59	Ni-Al LDH@CNPs//AC	138	1.6	47.7	51	88.9% after 2000 cycles
60	Ni-Co LDH//AC	125.2	1.2	23.7	5.82	92.7% after 5000 cycles
61	Co-Al LDHs-CNTs//AC	80.6	1.6	28	~6	88.9 % after 1000 cycles
62	Ni-Co LDH//AC	—	1.5	25.3	10.5	91.2% after 10000 cycles
63	NiCo-LDHs@CNT/NF//APDC/NF	210.9	1.8	89.7	8.7	78% after 1200 cycles
Our work	Co-Al LDH/ACT//ACT/graphene	145.8	1.6	55.04	5.4	87.54% after 2000 cycles

*rGO: reduced graphene oxide; GSP: integrated porous Co-Al hydroxide nanosheets; SGC: sandwiched graphene/porous carbon; CNPs: carbon nanoparticles; AC: activated carbon; NF: nickel foam

Supercapacitors have been proven to be efficient and powerful energy storage devices to drive various electronic components. Furthermore, if a renewable energy source can be used to sustain an energy charge, the combined supercapacitor/energy source cell will provide continuous power for consumer electronics, forming a self-sustaining system without need for large, heavy batteries. [64] As the most sustainable and cleanest source of energy in the world, solar energy is usually limited by access to sunlight as restricted by time of day, location, and weather. Combining solar cells with energy storage devices provides a promising solution to extend the practical applications of solar energy beyond the imposed restrictions of sunlight availability. As schematically illustrated in Fig. 7.9a, a flexible thin film solar cell with an open circuit potential of 3 V under light was integrated with the flexible asymmetric cell to realize a combined energy conversion and storage system in a single device by a simple roll-to-roll process.

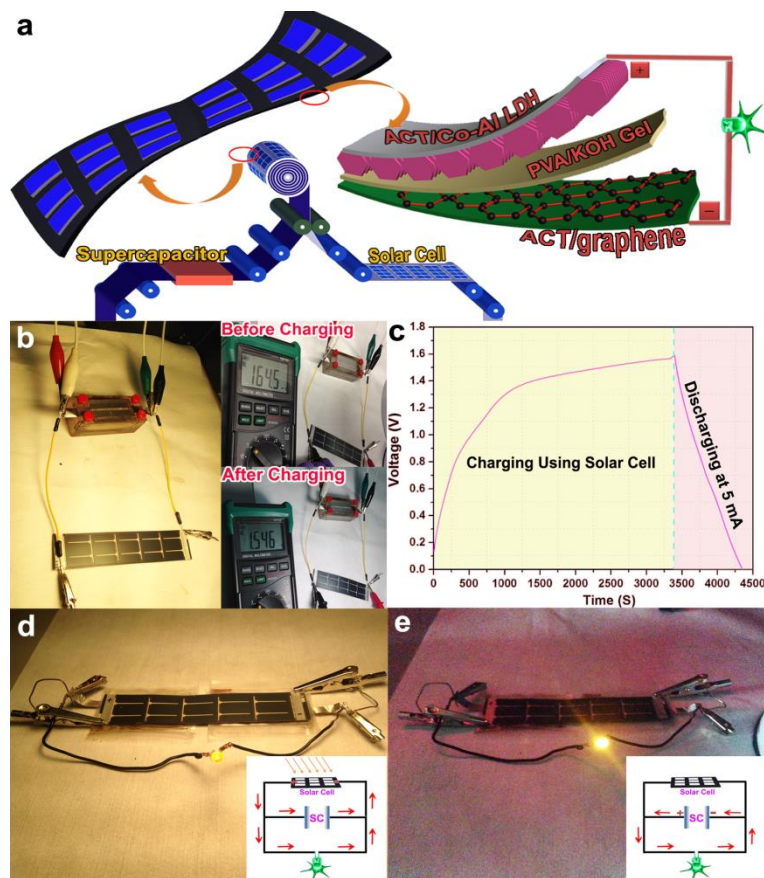


Figure 7.9 (a) Schematic illustration of the roll-to-roll manufacturing process for integrating a flexible solar cell with the supercapacitor into a self-sustaining power pack; (b) Digital photograph of the assembled solar cell/supercapacitor hybrid energy conversion and storage system, insets are the photographs of the open circuit potential of the ACT/Co-Al LDH//ACT/graphene asymmetric cell before and after charging with solar cell; (c) Charging curve of the ACT/Co-Al LDH//ACT/graphene asymmetric cell with solar cell, and discharging curve of the ACT/Co-Al LDH//ACT/graphene asymmetric cell at a current density of 5 mA cm^{-2} ; (d) Digital photograph of the assembled solar cell/supercapacitor hybrid power pack worked under the light, inset shows schematically the working circuit connection; (e) Digital photograph of the assembled solar cell/supercapacitor hybrid power pack worked without the light, inset shows schematically the working circuit connection.

Figure 7.9b illustrates the operation mechanism of the assembled solar cell/supercapacitor hybrid energy conversion and storage system. Insets of Fig. 7.9b are the photographs of the open circuit potential of the ACT/Co-Al LDH//ACT/graphene asymmetric supercapacitor before and after charging with the solar cell. Before charging by the solar cell, the open circuit potential of the asymmetric supercapacitor was 0.1645 V. Under the light source, the solar cell (with an open circuit potential of 3 V) serving as the power source charged the supercapacitor. After charging, the open circuit potential increased to 1.546 V. The corresponding charging (under light) and discharging curves (no light) of the asymmetric supercapacitor at the current density of 5 mA cm^{-2} were recorded by the electrochemical workstation (Fig. 7.9c), demonstrating the self-powered

function of such hybrid energy conversion and storage system. Encouragingly, a high energy transfer efficiency of ~43% was achieved from the solar cell to the capacitor. To further demonstrate the practical application of such integrated flexible energy system, a flexible solar cell was integrated with two flexible asymmetric cells connected in series by a facile roll-to-roll process, which holds a great promise for large-scale manufacturing of such hybrid cells (Figs. 7.9d,e). Insets of Figs. 6d and 6e illustrate the schematics of working circuit connection. Under light, the solar cell served as the power source to provide energy for the supercapacitor and light-emitting-diode (LED). When the light was turned off, the stored energy in the supercapacitor, in turn, served as the power source for the LED, which enabled this hybrid energy system to work continuously for ~10 mins, overcoming the limitation of solar discontinuity. Such flexible, self-sustaining energy systems hold great potential for future portable/wearable electronics where they can reliably power devices as consumers move in and out of sunlight during their normal daily activities.

7.4 Conclusion

Two-dimensional battery-type Co-Al LDH nanosheets were *in-situ* anchored on ACTs by a simple hydrothermal process. Separately, ACT fibers were wrapped with highly conductive graphene coating by a simple dipping, drying, and reducing process (ACT/graphene). A flexible, all-solid-state asymmetric supercapacitor (ACT/Co-Al LDH//ACT/graphene) was assembled using the nanostructured ACT/Co-Al LDH as the positive electrode, ACT/graphene as the negative electrode, and PVA-KOH gel as both the solid-state electrolyte and separator. The hierarchical flower-like Co-Al LDH nanoarrays with interconnected nano-petals and pompon-like nano-stamens provided highly open and porous scaffold-like structure, facilitating the transportation of electrolyte ions. In addition, the wrapped graphene on porous ACTs rendered highly accessible surface area and good electrical conductivity, endowing the flexible asymmetric supercapacitor with higher rate performance. The assembled ACT/Co-Al LDH//ACT/graphene asymmetric supercapacitor exhibited an excellent combination of electrochemical and mechanical performances. Moreover, we demonstrated a low-cost, roll-to-roll manufacturing approach to combine the flexible asymmetric supercapacitor with a flexible solar cell to build an integrated, self-sustaining power pack, which is scalable for industrial manufacturing. Importantly, such hybrid energy storage devices could continuously power a commercial LED, demonstrating a great potential for the future of self-powered nanotechnology.

References

- [1] Lewis, N. S. & Nocera, D. G. Powering the planet: Chemical challenges in solar energy utilization. *Proc. Natl. Acad. Sci.* **103**, 15729–15735 (2007).
- [2] Burke, A. Ultracapacitors: Why, how, and where is the technology. *J. Power Sources* **91**, 37–50 (2000).
- [3] Frackowiak, E. Carbon materials for supercapacitor application. *Phys. Chem. Chem. Phys.* **9**, 1774–1785 (2007).
- [4] Yang, Z. *et al.* Recent advancement of nanostructured carbon for energy applications. *Chem. Rev.* **115**, 5159–5223 (2015).
- [5] Hu, C. C., Chang, K. H., Lin, M. C. & Wu, Y. T. Design and tailoring of the nanotubular arrayed architecture of hydrous RuO₂ for next generation supercapacitors. *Nano Lett.* **6**, 2690–2695 (2006).
- [6] Jiang, J. *et al.* Recent advances in metal oxide-based electrode architecture design for electrochemical energy storage. *Adv. Mater.* **24**, 5166–5180 (2012).
- [7] Lang, X., Hirata, A., Fujita, T. & Chen, M. Nanoporous metal/oxide hybrid electrodes for electrochemical supercapacitors. *Nat. Nanotechnol.* **6**, 232–236 (2011).
- [8] Yang, W. *et al.* Hierarchical NiCo₂O₄@NiO core–shell hetero-structured nanowire arrays on carbon cloth for a high-performance flexible all-solid-state electrochemical capacitor. *J. Mater. Chem. A* **2**, 1448–1457 (2014).
- [9] Fan, L. Z. & Maier, J. High-performance polypyrrole electrode materials for redox supercapacitors. *Electrochem. Commun.* **8**, 937–940 (2006).
- [10] Yang, W. *et al.* Synthesis of hollow polyaniline nano-capsules and their supercapacitor application. *J. Power Sources* **272**, 915–921 (2014).
- [11] Snook, G. A., Kao, P. & Best, A. S. Conducting-polymer-based supercapacitor devices and electrodes. *J. Power Sources* **196**, 1–12 (2011).
- [12] Yu, G., Xie, X., Pan, L., Bao, Z. & Cui, Y. Hybrid nanostructured materials for high-performance electrochemical capacitors. *Nano Energy* **2**, 213–234 (2013).
- [13] Tang, Z., Tang, C. & Gong, H. A high energy density asymmetric supercapacitor from nano-architected Ni(OH)₂/carbon nanotube electrodes. *Adv. Funct. Mater.* **22**, 1272–1278 (2012).

- [14] Gao, Z., Song, N. & Li, X. Microstructural design of hybrid CoO@NiO and graphene nano-architectures for flexible high performance supercapacitors. *J. Mater. Chem. A* **3**, 14833–14844 (2015).
- [15] Wang, Q. & O’Hare, D. Recent advances in the synthesis and application of layered double hydroxide (LDH) nanosheets. *Chem. Rev.* **112**, 4124–4155 (2012).
- [16] Yang, R., Gao, Y., Wang, J. & Wang, Q. Layered double hydroxide (LDH) derived catalysts for simultaneous catalytic removal of soot and NO(x). *Dalton Trans.* **43**, 10317–10327 (2014).
- [17] Ladewig, K., Xu, Z. P. & Lu, G. Q. M. Layered double hydroxide nanoparticles in gene and drug delivery. *Expert Opin. Drug Deliv.* **6**, 907–922 (2009).
- [18] Liu, X., Ge, L., Li, W., Wang, X. & Li, F. Layered double hydroxide functionalized textile for effective oil/water separation and selective oil adsorption. *ACS Appl. Mater. Interfaces* **7**, 791–800 (2015).
- [19] Su, L. H., Zhang, X. G., Mi, C. H. & Liu, Y. Insights into the electrochemistry of layered double hydroxide containing cobalt and aluminum elements in lithium hydroxide aqueous solution. *J. Power Sources* **179**, 388–394 (2008).
- [20] Yang, W. *et al.* Solvothermal one-step synthesis of Ni-Al layered double hydroxide/carbon nanotube/reduced graphene oxide sheet ternary nanocomposite with ultrahigh capacitance for supercapacitors. *ACS Appl. Mater. Interfaces* **5**, 5443–5454 (2013).
- [21] Lu, Z. *et al.* High pseudocapacitive cobalt carbonate hydroxide films derived from CoAl layered double hydroxides. *Nanoscale* **4**, 3640–3643 (2012).
- [22] Vialat, P. *et al.* High-performing monometallic cobalt layered double hydroxide supercapacitor with defined local structure. *Adv. Funct. Mater.* **24**, 4831–4842 (2014).
- [23] Huang, J. *et al.* Effect of Al-doped β -Ni(OH)₂ nanosheets on electrochemical behaviors for high performance supercapacitor application. *J. Power Sources* **232**, 370–375 (2013).
- [24] Chen, H., Hu, L., Chen, M., Yan, Y. & Wu, L. Nickel-cobalt layered double hydroxide nanosheets for high-performance supercapacitor electrode materials. *Adv. Funct. Mater.* **24**, 934–942 (2014).
- [25] Gao, Z. *et al.* Graphene nanosheet/Ni²⁺/Al³⁺ layered double-hydroxide composite as a novel electrode for a supercapacitor. *Chem. Mater.* **23**, 3509–3516 (2011).
- [26] Novoselov, K. S. *et al.* Two-dimensional gas of massless Dirac fermions in graphene. *Nature* **438**, 197–200 (2005).

- [27] Chen, D., Tang, L. & Li, J. Graphene-based materials in electrochemistry. *Chem. Soc. Rev.* **39**, 3157–3180 (2010).
- [28] Stoller, M. D., Park, S., Zhu, Y., An, J. & Ruoff, R. S. Graphene-based ultracapacitors. *Nano Lett.* **8**, 6–10 (2008).
- [29] Zhu, Y. *et al.* Carbon-based supercapacitors produced by activation of graphene. *Science* **332**, 1537–1542 (2011).
- [30] Wu, Z. S. *et al.* High-energy MnO₂ nanowire/graphene and graphene asymmetric electrochemical capacitors. *ACS Nano* **4**, 5835–5842 (2010).
- [31] Films, G. H. *et al.* Flexible solid-state supercapacitors based on three-dimensional. *ACS Nano* **7**, 4042–4049 (2013).
- [32] Ji, J. *et al.* Nanoporous Ni (OH)₂ thin film on 3D ultrathin-graphite foam for asymmetric supercapacitor. *ACS Nano* **7**, 6237–6243 (2013).
- [33] Gao, Z., Yang, W., Wang, J., Song, N. & Li, X. Flexible all-solid-state hierarchical NiCo₂O₄/porous graphene paper asymmetric supercapacitors with an exceptional combination of electrochemical properties. *Nano Energy* **13**, 306–317 (2015).
- [34] Liu, Z., Xu, J., Chen, D. & Shen, G. Flexible electronics based on inorganic nanowires. *Chem. Soc. Rev.* **44**, 161–192 (2015).
- [35] Jung, Y. H. *et al.* High-performance green flexible electronics based on biodegradable cellulose nanofibril paper. *Nat. Commun.* **6**, 7170 (2015).
- [36] Gao, Z., Song, N., Zhang, Y. & Li, X. Cotton textile enabled, all-solid-state flexible supercapacitors. *RSC Adv.* **5**, 15438–15447 (2015).
- [37] Huang, Y. *et al.* From industrially weavable and knittable highly conductive yarns to large wearable energy storage textiles. *ACS Nano* **9**, 4766–4775 (2015).
- [38] Gao, P. X., Song, J., Liu, J. & Wang, Z. L. Nanowire piezoelectric nanogenerators on plastic substrates as flexible power sources for nanodevices. *Adv. Mater.* **19**, 67–72 (2007).
- [39] Jost, K. *et al.* Natural fiber welded electrode yarns for knittable textile supercapacitors. *Adv. Energy Mater.* **5**, 1401286 (2015).
- [40] Xiao, X. *et al.* High-strain sensors based on ZnO nanowire/polystyrene hybridized flexible films. *Adv. Mater.* **23**, 5440–5444 (2011).
- [41] Xu, S. *et al.* Self-powered nanowire devices. *Nat. Nanotechnol.* **5**, 366–373 (2010).

- [42] Wang, X. *et al.* Fiber-based all-solid-state flexible supercapacitors for self-powered systems. *Adv Mater* **3**, 6790–6797 (2014).
- [43] Yang, P. *et al.* Hydrogenated ZnO core-shell nanocables for flexible supercapacitors and self-powered systems. *ACS Nano* **7**, 2617–2626 (2013).
- [44] Xu, X. *et al.* A power pack based on organometallic perovskite solar cell and supercapacitor. *ACS Nano* **9**, 1782–1787 (2015).
- [45] Wang, Z., Chen, J. & Lin, L. Progress in triboelectric nanogenerators as new energy technology and self-powered sensors. *Energy Environ. Sci.* **8**, 2250–2282 (2015).
- [46] Liu, Y., Wang, X., Qi, K. & Xin, J. H. Functionalization of cotton with carbon nanotubes. *J. Mater. Chem.* **18**, 3454 (2008).
- [47] Bao, L. & Li, X. Towards textile energy storage from cotton T-shirts. *Adv. Mater.* **24**, 3246–52 (2012).
- [48] Dreyer, D. R., Park, S., Bielawski, C. W. & Ruoff, R. S. The chemistry of graphene oxide. *Chem. Soc. Rev.* **39**, 228–240 (2010).
- [49] Bai, H., Li, C., Wang, X. & Shi, G. On the gelation of graphene oxide. *J. Phys. Chem. C* **115**, 5545–5551 (2011).
- [50] Chen, W. & Yan, L. In situ self-assembly of mild chemical reduction graphene for three-dimensional architectures. *Nanoscale* **3**, 3132–3137 (2011).
- [51] Ford, E. N. J.; Mendon, S. K.; Thames, S. F.; Ph, D.; Rawlins, J. W. X-ray diffraction of cotton treated with neutralized vegetable oil-based macromolecular crosslinkers. *J. Eng. Fiber. Fabr.* **2010**, 5, 10–20.
- [52] Liu, Z. H., Wang, Z. M., Yang, X. & Ooi, K. Intercalation of organic ammonium ions into layered graphite oxide. *Langmuir* **18**, 4926–4932 (2002).
- [53] Hassan, H. M. a. *et al.* Microwave synthesis of graphene sheets supporting metal nanocrystals in aqueous and organic media. *J. Mater. Chem.* **19**, 3832–3837 (2009).
- [54] Mcallister, M. J. *et al.* Single sheet functionalized graphene by oxidation and thermal expansion of graphite. *Chem. Mater.* **19**, 4396–4404 (2007).
- [55] Wang, Y. *et al.* Magnetic graphene oxide nanocomposites: nanoparticles growth mechanism and property analysis. *J. Mater. Chem. C* **2**, 9478–9488 (2014).
- [56] Wu, X., Jiang, L., Long, C., Wei, T. & Fan, Z. Dual support system ensuring porous Co-Al hydroxide nanosheets with ultrahigh rate performance and high energy density for supercapacitors. *Adv. Funct. Mater.* **25**, 1648–1655 (2015).

- [57] Di Fabio, A., Giorgi, A., Mastragostino, M. & Soavi, F. Carbon-Poly(3-methylthiophene) Hybrid Supercapacitors. *J. Electrochem. Soc.* **148**, A845–A850 (2001).
- [58] Wang, J.; Gao, Z.; Li, Z.; Wang, B.; Yan, Y.; Liu, Q.; Mann, T.; Zhang, M.; Jiang, Z. Green Synthesis of Graphene nanosheets/ZnO Composites and Electrochemical Properties. *J. Solid State Chem.* **2011**, *184*, 1421–1427.
- [59] Liu, X. *et al.* A Ni-Al layered double hydroxide@carbon nanoparticles hybrid electrode for high-performance asymmetric supercapacitors. *J. Mater. Chem. A* **2**, 1682–1685 (2014).
- [60] Wang, X., Sumboja, A., Lin, M., Yan, J. & Lee, P. S. Enhancing electrochemical reaction sites in nickel–cobalt layered double hydroxides on zinc tin oxide nanowires: a hybrid material for an asymmetric supercapacitor device. *Nanoscale* **4**, 7266 (2012).
- [61] Yu, L. *et al.* Facile synthesis of exfoliated Co–Al LDH–carbon nanotube composites with high performance as supercapacitor electrodes. *Phys. Chem. Chem. Phys.* **16**, 17936 (2014).
- [62] Jing, M. *et al.* Alternating Voltage Introduced NiCo Double Hydroxide Layered Nanoflakes for an Asymmetric Supercapacitor. *ACS Appl. Mater. Interfaces* **7**, 22741–22744 (2015).
- [63] Li, X. *et al.* An asymmetric supercapacitor with super-high energy density based on 3D core-shell structured NiCo-layered double hydroxide@carbon nanotube and activated polyaniline-derived carbon electrodes with commercial level mass loading. *J. Mater. Chem. A* 13244–13253 (2015).
- [64] Wang, Z. L. Toward self-powered sensor networks. *Nano Today* **5**, 512–514 (2010).
- [65] William S. Hummers, J. & Offeman, R. E. Preparation of graphitic oxide. *J. Am. Chem. Soc.* **80**, 1339 (1958).

Chapter 8 Summary and Recommendations

In this dissertation, cotton textile, as the commonly overlooked everyday household, has been chosen as the starting precursor material to fabricate renewable flexible conductive substrates for different energy storage systems. Based on their different applications and different emphases, in this dissertation, research thrusts were placed on the following aspects: (1) cotton textile-enabled flexible supercapacitors; (2) cotton textile-enabled flexible lithium-ion batteries; (3) cotton textile-enabled flexible lithium-sulfur batteries; (4) cotton textile-enabled nanoparticle-assisted new polysulfide trapping mechanism; (5) cotton textile enabled self-sustaining solar/supercapacitor hybrid power packs. These research activities brought new insights on the renewable carbon materials derived from natural abundant biomass resources and will boost the design and fabrication of next-generation flexible energy-storage devices from natural abundant biomass materials.

8.1 Summary of Contributions and Significance

In Chapter 2 and 3, natural abundant cotton textiles were first converted to flexible, conductive activated cotton textiles (ACTs). Because of the excellent flexibility and conductivity, ACTs were chosen as a flexible substrate to design and fabricate flexible supercapacitors. However, the energy storage capability of the pure ACTs is not high enough to be used alone to construct supercapacitors, in order to push up the capacity of the flexible supercapacitors, high energy density metal oxides, such as core/shell $\text{NiCo}_2\text{O}_4@\text{NiCo}_2\text{O}_4$, 3D porous $\text{CoO}@\text{NiO}$, were controllably deposited on the ACT fibers with desired microstructure.

Specifically, in Chapter 2, hierarchical $\text{NiCo}_2\text{O}_4@\text{NiCo}_2\text{O}_4$ core/shell nanostructure was grown on flexible cotton activated carbon textiles (ACTs) to fabricate $\text{NiCo}_2\text{O}_4@\text{NiCo}_2\text{O}_4/\text{ACT}$ electrodes. After dipped with PVA-KOH polymer gel which served as both the solid-state electrolyte and separator, the flexible $\text{NiCo}_2\text{O}_4@\text{NiCo}_2\text{O}_4/\text{ACT}$ hybrid electrode exhibited an exceptional combination of electrochemical and mechanical properties in terms of specific

capacitance (1929 F/g, based on the mass of NiCo_2O_4), energy density (83.6 Wh/kg), power density (8.4 KW/kg), cycling stability, and mechanical robustness (the tensile strength is 6.4 times higher than that of pure ACT). The outstanding electrochemical performance is ascribed to the unique core/shell nanostructure with the high active-surface area, morphological stability, and short ion transport path.

In Chapter 3, we demonstrated the rational design and fabrication of CoO nano-architectures with different morphologies (sheet-like, petal-like and urchin-like) on flexible activated carbon textiles (ACT) by simply changing the reactant solution concentration. We further unveiled that the electrochemical properties of CoO nanostructures are morphology-dependent. The specific capacitance increased exponentially with the surface/volume ratio of nanostructures. The architecture with higher surface area exhibited better electrochemical performance. Due to its higher surface/volume ratio and better electrochemical performance, urchin-like CoO nanostructure was further chosen as a backbone to deposit NiO nanoflakes to construct a hierarchical core/shell CoO@NiO hybrid nanostructure. Flexible ACT wrapped with conductive graphene was used as the negative electrode material. After coated with PVA-KOH polymer gel which served as both the solid-state electrolyte and separator, the flexible core/shell CoO@NiO/ACT//ACT/graphene asymmetric cell exhibited an exceptional combination of electrochemical properties in terms of working potential (1.6 V), energy density (52.26 Wh kg^{-1}), maximum power density (9.53 KW kg^{-1}), and cycling stability (97.53% capacitance retention after 2000 cycles even under harsh working condition). The strategy by controllable synthesis of hierarchical nanostructure on the cotton-enabled flexible textile substrate should find more applications in next-generation flexible solid-state power sources for future wearable electronics.

Inspired by the application of flexible ACTs for supercapacitor applications, we kept thinking whether we could rationally design battery materials on flexible ACT substrate to fabricate binder-free flexible lithium-ion batteries by taking the advantages that ACTs possess excellent flexibility, superior conductivity, and exceptional mechanical robustness. In Chapter 4, we found that ACT has fantastic 3D porous tubular microstructure. Battery active materials NiS_2 nanobowls wrapped with conductive graphene sheets (ACT/ NiS_2 -graphene) deposited on ACT fiber by a simple two-step heat treatment method. When used as a binder-free electrode, the ACT/ NiS_2 -graphene electrode exhibited an exceptional electrochemical performance including ultrahigh initial

discharge capacity ($\sim 1710 \text{ mAh g}^{-1}$ at 0.01 C), magnificent rate performance (the discharge capacitance retained at $\sim 645 \text{ mAh g}^{-1}$ at 1 C after 100 cycles) and excellent cyclic stability (the discharge capacitance recovered to $\sim 1016 \text{ mAh g}^{-1}$ at 0.1 C after 400 cycles). This is the first time, ACT was adopted as flexible substrates to design flexible battery.

Encouraged by the success of the design and fabrication of flexible lithium-ion batteries by using flexible ACTs, we extended the application of flexible ACTs to lithium-sulfur battery applications. The porous and tubular structure of ACTs are desirable for trapping the polysulfides. In Chapter 5, the conductive ACT with porous tubular structure was first derived from natural cotton textile to load sulfur, which was further wrapped with partially reduced graphene oxide (ACT/S-rGO) to immobilize lithium polysulfides. Meanwhile, the partially reduced graphene oxide nanosheets served as a conductive coating, which further mitigated the poor conductivity of sulfur and enabled fast electron transportation along ACT fibers. Furthermore, a KOH-activated ACT with micropore size distribution was inserted between cathode and separator to mitigate the “shuttle effect” of polysulfides. Finally, the assembled ACT/S-rGO cathode with porous ACT interlayer exhibited an exceptional rate capability and durable cyclic performance (with a well-retained capacity of $\sim 1016 \text{ mAh g}^{-1}$ even after 200 cycles). A flexible Li-S cell with ACT/S-rGO as a cathode was also assembled to demonstrate its superior potential as flexible power sources for future wearable electronic devices.

The excellent capacity and rate performance of the ACT-enabled lithium-sulfur batteries indicated the potential of using the porous ACT to design next-generation high-energy batteries. However, the lifespan of 200 cycles is still far from the practical application, which mainly results from the dissolution of polysulfides and the corresponding “shuttle effect”. To mitigate this plaguing problem, here, in Chapter 6, a new built-in magnetic field enhanced polysulfide trapping mechanism was discovered and realized by introducing ferromagnetic iron/iron carbide (Fe/Fe₃C) nanoparticles with a graphene shell (Fe/Fe₃C/graphene) onto a flexible ACT fiber to prepare the ACT@Fe/Fe₃C/graphene sulfur host. The novel trapping mechanism was demonstrated by significant differences in the diffusion behavior of polysulfides in a custom-designed liquid cell compared to a pure ACT/S cathode. Furthermore, a cell assembled by using the ACT@Fe/Fe₃C/S cathode exhibited a high initial discharge capacity of $\sim 764 \text{ mAh g}^{-1}$, excellent rate performance, and a remarkably long lifespan of 600 cycles using ACT@Fe/Fe₃C/S (whereas only 100 cycles

were achieved using pure ACT/S). The new magnetic field-enhanced trapping mechanism provides not only novel insight but unveils new possibilities for mitigating the “shuttle effect” of polysulfides, thereby promoting the practical applications of Li-S batteries.

With the goal of tackling the forthcoming energy crisis, efficient energy conversion and storage devices are urgently needed to provide a sustainable, green energy supply. Solar cells hold great promise as energy conversion devices for their utilization of readily accessible solar energy; however, the output of solar cells is non-continuous and unstable. Therefore, it is necessary to combine solar cells with compatible energy storage devices to realize a stable power supply. To achieve this goal, supercapacitors, as highly efficient energy storage devices, were integrated with solar cells to mitigate the power-out swing. Based on our work on the design of various activated cotton-textile-enabled flexible energy storage systems with excellent electrochemical performance and exceptional mechanical robustness, in Chapter 7, we proposed a scalable roll-to-roll manufacturing approach to fabricate a novel solar cell-supercapacitor hybrid device as a solution to the impending huge energy need. A high performance, cotton textile-enabled asymmetric supercapacitor was integrated with a flexible solar cell via the scalable roll-to-roll fashion to assemble a self-powered hybrid device, which not only transforms the way of manufacturing hybrid flexible energy storage devices but also provides a new path how we can collect and store renewable energy more efficiently.

8.2 Recommendations for Future Research

While this dissertation conducted a comprehensive research on the potential of using activated cotton textile to design and construct various types flexible energy storage systems, including flexible supercapacitors, flexible lithium-ion batteries and flexible lithium-sulfur batteries, which provide rich information on how we can natural cotton textiles and what we can do functionalization of ACT in order to realize better energy storage capability, it also raises questions and opportunities for future studies. Here, I will summarize several future research opportunities in the following aspects:

- 1) How to realize a high-performance flexible energy system?

From the practical perspective, a flexible energy system not only needs good electrochemical performance, such as high energy storage capability and stable energy output, but

also requires high mechanical robustness, which means the assembled energy systems should bear the arbitrary mechanical deformation and simultaneously maintain its electrochemical performance. For flexible energy systems, it is still a big challenge to maintain its electrochemical performance under the continuously mechanical loading, such as bent, fold, and twisted states. The mechanical issues caused by mechanical deformation, fracture, debonding, breakage, cavitation, and disintegration, will accelerate the failure of the battery. Most of the metal oxides, are brittle and can be easily failed upon mechanical loading, which is one of the main reasons for the failure of the battery. Unfortunately, there is still a lack of understanding on how these mechanical issues affect the electrochemical performance of the flexible energy storage systems. Therefore, it is a great opportunity to investigate the failure mechanism of battery by coupling the mechanical deformation and electrochemistry.

- 2) How to design and fabricate a flexible substrate with good conductivity, mechanical stability and desired functionalities?

Although ACT has been proven to be an excellent flexible platform for flexible energy storage systems design, there is still a critical issue that needs to be pointed out – the reduced mechanical properties after activation. It is known that natural cotton textiles have fantastic mechanical strength yet poor conductivity, hindering their application in energy storage. In order to realize good conductivity, in this work, we used a high-temperature process to activate cotton textile, converting it to the activated cotton textile with good conductivity. In fact, the high temperature activation process also damaged the mechanical properties of cotton textile to some extent, leading to the relatively poor mechanical properties of the ACT. To improve the mechanical strength of ACT, we hybridized ACT with PVA polymer, which worked for some certain systems with adding PAV-gel electrolyte. One promising direction will be how to improve the conductivity of cotton textile without using high-temperature activation. The metal coating, such as nickel, stainless steel, or cobalt, is suggested to be coated/deposited on pure cotton textile to solve this problem. At the same time, how to functionalize the substrate with the desirable capability to hold/anchor active nanomaterials is also important.

- 3) How to derive advanced carbon materials from other biomass materials and what is the universal conversion mechanism?

The extension of this work is how we derive more advanced carbon materials from natural abundant biomass resources for energy storage and other applications. Currently, we are

consuming more and more nonrenewable resources, such as graphite and cobalt, for lithium-ion batteries, which not only brings serious environmental problems but also increases the pressure on the supply of sustainable battery materials, especially with rapidly swelling battery market. To realize a sustainable development, we need to explore more renewable materials from natural abundant biomass materials. Therefore, it will be promising and practical to derive renewable carbon materials from biomass, especially, appropriate approaches need to be exploited to derive advanced carbon materials, such as CNTs and graphene. Excitingly, our recent research found that CNTs can be derived from the yeast-fermented wheat flour without using any extra catalysts and carbon sources, which encourages us to explore more on how we convert more biomass to carbon materials, identify the conversion mechanism, and find more universal approaches to use biomass materials.